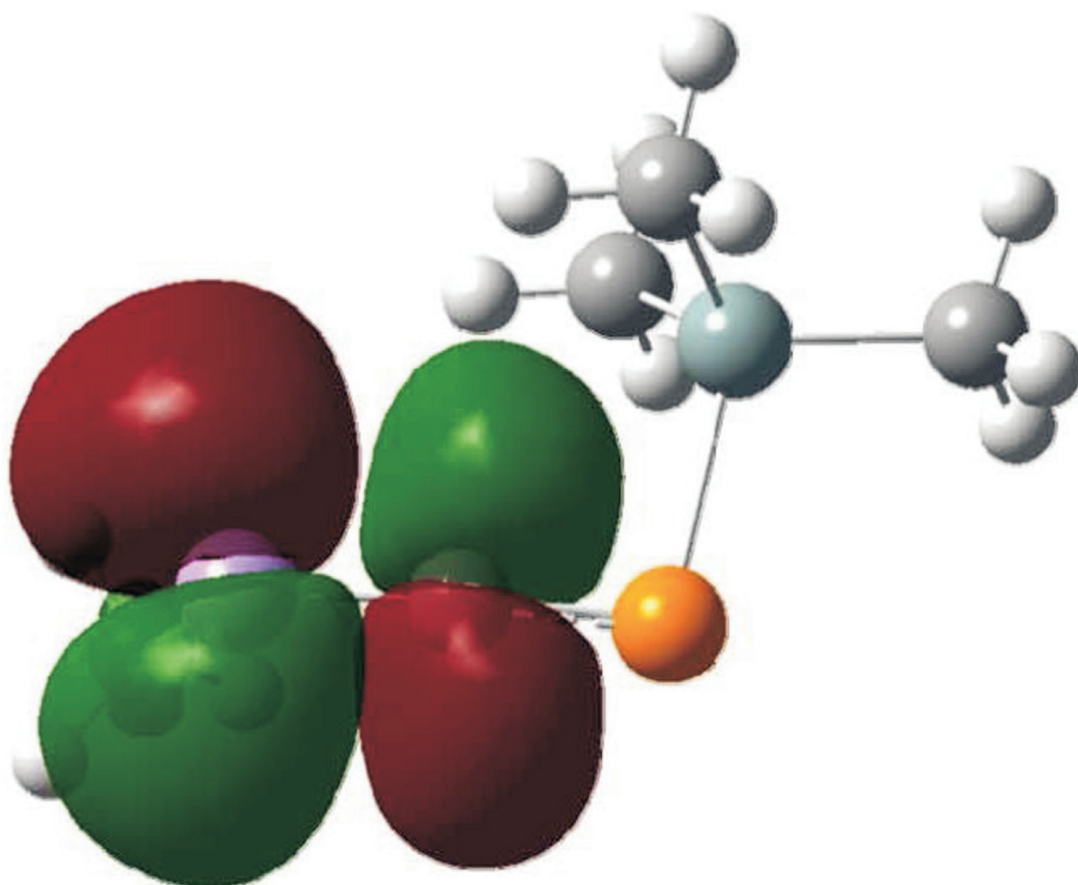




STUDIA UNIVERSITATIS
BABEŞ-BOLYAI



CHEMIA

2/2010
tom I

S T U D I A
UNIVERSITATIS BABEȘ-BOLYAI
CHEMIA

2

tom I

Desktop Editing Office: 51ST B.P. Hasdeu Street, Cluj-Napoca, Romania, Phone + 40 264-405352

CONTENT – SOMMAIRE – INHALT – CUPRINS

| | |
|--|----|
| IOAN SILAGHI-DUMITRESCU 1950-2009 | 5 |
| LIST OF PUBLICATIONS..... | 7 |
| P.M. PETRAR, G. NEMES, L. SILAGHI-DUMITRESCU, A Theoretical Approach on the Structure of Arsaallenes -As=C=C< and Arsaphosphaallenes -As=C=P- | 25 |
| A.-L. SEFF, S. PILBÁK, I. SILAGHI-DUMITRESCU , L. POPPE, Zinc-Containing Active Site in a Partially Modified 1GKM Crystal Structure of Histidine Ammonia-Lyase: a Computational Investigation | 37 |
| M.V. PUTZ, Chemical Hardness: Quantum Observable? | 47 |
| V. MAXIM, C.-C. CORMOȘ, P.Ș. AGACHI, Mathematical Modeling and Simulation of Coal Co-Gasification with Waste/Biomass in an Entrained-Flow Gasifier..... | 51 |

| | |
|--|-----|
| R. SILAGHI-DUMITRESCU, Computational Analysis of Bonding in PhIO and Related 'Hypervalent' Iodine Complexes..... | 63 |
| M. FERBINTEANU, F. CIMPOESU, On the Multiple Facets of Aromaticity: Organic, Inorganic, Organometallic, Coordination and Supramolecular Case Studies | 69 |
| E.M. MOSOARCA, I. LABADI, L. SAJTI, R. TUDOSE, V. SIMULESCU, W. LINERT, O. COSTISOR, Synthesis and Thermal Behavior of Copper(II) Complexes Containing N,N'-tetra(4-antipyrilmethyl)-1,2 diaminoethane as Ligand | 89 |
| L. GĂINĂ, T. DALLOS, C. CRISTEA, T. LOVASZ, I. PERETEANU, M. SURDUCAN, L. SILAGHI-DUMITRESCU, Microwaves Asssited N-Alkylation of Phenothiazine..... | 97 |
| Z. GARBAN, A.-E. AVACOVICI, G. GARBAN, F. PETER., G.-D. GHIBU, M. BOTOCA, A. CUMPĂNAȘ, Purine Metabolism Dyshomeostasis and the Heterogenous Nucleation of Uroconcrements Note I. Alkaline and Alkaline-Earth Metals in Purine Urolithiasis..... | 103 |
| C. MAJDIK, A. MĂICĂNEANU, C. INDOLEAN, S. BURCĂ, M. STANCA, Phenol Contaminated Water Remediation Using Commercial Immobilized Bentonites as Adsorbents | 115 |
| B. MIHÁLY, A.-ZS. KUN, E. FORIZS, A. PATRUT, <u>I. SILAGHI-DUMITRESCU</u> , Geometry Optimization and Comparative DFT Study of (Diethylenetriamine)bis(Theophyllinato)Zinc(II) Dihydrate | 125 |
| A. SAPONAR, E.-J. POPOVICI, I. PERHAIȚA, N. POPOVICI, <u>I. SILAGHI-DUMITRESCU</u> , Studies on the Europium and Palladium Extraction with some calix[6]arene Derivatives | 133 |
| A. GHIRIȘAN, S. DRĂGAN, The Influence of Coagulants in Colloidal Particles Removal from Dispersions..... | 145 |
| L. COPOLOVICI, I. BALDEA, Kinetics of the Phenol Oxidation by Permanganate in Acidic Media. The Intermediate Oxidized Species 4,4'-biphenquinone Evolution | 155 |
| E. BICA, E.-J. POPOVICI, M. ȘTEFAN, I. PERHAIȚA, I. C. POPESCU, Synthesis of Tungsten Trioxide Mesoporous Powders Prepared by Inorganic Sol-Gel Route | 169 |
| V. R. DEJEU, R. BARABÁS, A.-M. CORMOȘ, E. S. BOGYA, P.-Ș. AGACHI, Growth Rate of Hydroxyapatite Crystals Obtained by Precipitation..... | 179 |
| L. VARVARI, G. SZABÓ, A. NICOARĂ, Kinetic Investigation in Trolox-DPPH• System | 189 |

Studia Universitatis Babes-Bolyai Chemia has been selected for coverage in Thomson Reuters products and custom information services. Beginning with V. 53 (1) 2008, this publication is indexed and abstracted in the following:

- Science Citation Index Expanded (also known as SciSearch®)
- Chemistry Citation Index®
- Journal Citation Reports/Science Edition



IOAN SILAGHI-DUMITRESCU
1950-2009

Corresponding member of the Romanian Academy

Born in 1950, he attended primary school in his home village (Botiz, Satu Mare county) and followed on with highschool in Satu-Mare.

Graduated in 1974 from the Inorganic Chemistry of the Department of Chemistry of the Babes-Bolyai University at Cluj-Napoca, Romania, he obtained his PhD from the same university in 1981. After three years spent in the industry at the Sanex Enterprise for Fine Ceramics in Construction (1974-1977), he joined the faculty at the Department of Chemistry and Chemical Engineering of the Babes-Bolyai University, where he eventually became a full professor in 1994; here, he served as head of the Inorganic Chemistry Chair (1994-2007) and as Dean of the Department (2008-2009).

Professor Ioan Silaghi-Dumitrescu's research contributions were in the fields of inorganic and organometallic chemistry, with synthesis and structural characterization of transition metal compounds as well as of compounds involving elements from main groups 13, 14 and 15 (e.g., cumulene and heterocumulene systems with heavy elements, biologically-active compounds).

IOAN SILAGHI-DUMITRESCU
1950-2009

He was among the first researchers in Romania to approach chemistry with computational techniques, starting very early on from force constant calculations and spectrum simulations to offer general principles for assigning coordination modes with thiophosphoric ligands at a time when structural analysis with X-ray diffraction was not available in Romania. He then evolved towards quantum chemistry, where he provided notable contributions with molecular modeling studies. His results on the structure of clusters involving main group (post-transition) elements, organometallic clusters, cumulenenic and heterocumulenenic systems, nanotubes and calixarenes, were reported in journals among the most prestigious in the field of chemistry. Much of his research was aimed not solely at obtaining structural information, but also at understanding and guiding experiments performed in his own research group as well as by collaborators from various countries, thereby allowing for establishing strategies in synthesis and for explanation and prediction of properties for a wide range of inorganic, organometallic and organic compounds. His results have been reported in 182 scientific articles in relevant journals across the world (December 2009).

The Center for Molecular Modeling and Quantum Chemistry founded by him in 2007 (developed from the Laboratory for Structure and Molecular Modeling established in 1996), featuring an internationally-competitive computational infrastructure, has consolidated the school of theoretical chemistry in Cluj and has provided a sound basis for high-level collaborations with prominent researchers from the United States of America and from China.

He was a visiting professor at the National Autonomous University in Mexico (UNAM) in the Theoretical Chemistry Group at the Institute of Chemistry (1995-1996) and at the University of Georgia, Athens, Georgia (USA) (2000-2008, for 1-2 months each year). He also had research-related stays at the University of Nottingham (1992) and Heidelberg University (1993-1994), and was engaged in active collaborations with groups from the Universities in Toulouse, Rouen, Lille, Leipzig, Braunschweig, Köln, Budapest, Pecs, Beijing, Guanjou, Moskow (Idaho).

He received the "*Gheorghe Spacu*" prize from the Romanian Academy for his "Research in structure and molecular topology" in 1989 and the "*Gheorghe Spacu*" Medal and "Diploma de Onoare" from the Romanian Society of Chemistry (2009).

Editorial Board

Ioan Silaghi-Dumitrescu - List of Publications

Binuclear cyclopentadienylcobalt sulfur and phosphinidene complexes $Cp_2Co_2E_2$ ($E = S, PX$): Comparison with their Iron carbonyl analogues, Li, Guoliang; Li, Qian-Shu; Silaghi-Dumitrescu, Ioan; King, Bruce R.; Schaefer, Henry F, *Journal of Organometallic Chemistry* (2010), 695(6), 804-808.

On the microwave-assisted synthesis of acylphenothiazine derivatives- Experiment versus theory synergism, Gaina, Luiza; Porumb, Dan; Silaghi-Dumitrescu, Ioan; Cristea, Castelia; Silaghi-Dumitrescu, Luminita, *Canadian Journal of Chemistry* (2010), 88(1), 42-49.

(Diethylenetriamine)bis(theophyllinato)zinc(II) dihydrate. Mihaly, Bela; Forizs, Edit; Kun, Attila-Zsolt; Silaghi-Dumitrescu, Ioan, *Acta Crystallographica, Section E: Structure Reports Online* (2009), E65(5), m579.

An insight into the structure of model germaphosphaallenes, Petrar, P. M.; Nemes, G.; Silaghi-Dumitrescu, I.; Escudie, J.; Ranaivonjatovo, *Molecular Physics* (2009), 107(8-12), 1161-1167

Butterfly and rhombus structures for binuclear cobalt carbonyl sulfur and phosphinidene complexes of the type $Co_2(CO)_6E_2$ ($E = S, PX$), Li, Guoliang; Li, Qian-Shu; Silaghi-Dumitrescu, Ioan; King, R. Bruce; Schaefer, Henry F., III, *Dalton Transactions* (2009), (47), 10474-10480.

Endohedral Nickel, Palladium, and Platinum Atoms in 10-Vertex Germanium Clusters: Competition between Bicapped Square Antiprismatic and Pentagonal Prismatic Structures, King, R. B.; Silaghi-Dumitrescu, I.; Uta, M. M, *Journal of Physical Chemistry A* (2009), 113(3), 527-533.

From closo to isocloso structures and beyond in cobaltaboranes with 9 to 12 vertices, King R Bruce; Silaghi-Dumitrescu Ioan; Sovago Ioana, *Inorganic chemistry* (2009), 48(21), 10117-25.

Kinetic versus thermodynamic isomers of the deltahedral cobaltadiboraboranes, King R Bruce; Silaghi-Dumitrescu Ioan; Sovago Ioana, *Inorganic chemistry* (2009), 48(12), 5088-95.

N,N' and N,O chelated phosphonium cations containing aminotroponimate or aminotroponate units, Pop, Lucian-Cristian; Katir, Nadia; Castel, Annie; Silaghi-Dumitrescu, Luminita; Delpech, Fabien; Silaghi-Dumitrescu, Ioan; Gornitzka, Heinz; MacLeod-Carey, Desmond; Saffon, Nathalie, *Journal of Organometallic Chemistry* (2009), 694(9-10), 1562-1566.

Narrow-rim alkenyl calix[n]arene. Synthesis and spectral characterization, Saponar, Alina; Popovici, Elisabeth-Jeanne; Popovici, Nicolae; Bica, Ecaterina; Nemes, Gabriela; Petrar, Petronela; Silaghi-Dumitrescu, Ioan, *Revista de Chimie* (2009), 60(3), 278-282.

Stabilisation of an inorganic digallane by the phosphinobisthiolato P,S,S pincer ligand PPh(2-SC₆H₄)₂, Valean, Ana-Maria; Gomez-Ruiz, Santiago; Loennecke, Peter; Silaghi-Dumitrescu, Ioan; Silaghi-Dumitrescu, Luminita; Hey-Hawkins, Evamarie, *New Journal of Chemistry* (2009), 33(8), 1771-1779.

The unique palladium-centered pentagonal antiprismatic cationic bismuth cluster: a comparison of related metal-centered 10-vertex pnictogen cluster structures by density functional theory, King R B; Silaghi-Dumitrescu I; Uta M M, *Inorganic chemistry* (2009), 48(17), 8508-14.

Lower Rim Silyl Substituted Calix[8]Arenes, Fleuret, Nathan; Paic, Sebastian; Nemes, Gabriela; Septelean, Raluca; Petrar, Petronela; Silaghi-Dumitrescu, Ioan, *Studia Universitatis Babes-Bolyai, Chemia* (2009), 54(3), 81-88.

Theoretical aspects of main group multiple bonded systems, Silaghi-Dumitrescu, Ioan; Petrar, Petronela; Nemes, Gabriela; King, R. Bruce, *Computational Inorganic and Bioinorganic Chemistry* (2009), 563-575.

vic-Dichlorodiphosphapropenes - synthesis and coordination ability, Septelean, Raluca; Nemes, Gabriela; Escudie, Jean; Silaghi-Dumitrescu, Ioan; Ranaivonjatovo, Henri; Petrar, Petronela; Gornitzka, Heinz; Silaghi-Dumitrescu, Luminita; Saffon, Nathalie, *European Journal of Inorganic Chemistry* (2009), (5), 628-634.

Beyond the icosahedron: a density functional theory study of 14-atom germanium clusters, King, R. Bruce; Silaghi-Dumitrescu, Ioan; Uta, Matei M, *European Journal of Inorganic Chemistry* (2008), (25), 3996-4003.

Beyond the Wade-Mingos Rules in Bare 10- and 12-Vertex Germanium Clusters: Transition States for Symmetry Breaking Processes, King, R. B.; Silaghi-Dumitrescu, I.; Uta, M. M, *Journal of Chemical Theory and Computation* (2008), 4(1), 209-215.

Bis(phosphanyl-amino)benzene ligands: a zinc(II) complex and an unusual nickel(I) complex with a Dewar-benzene-type Ni₂P₂N₂ backbone, Majoum-Mbe, F.; Kuehl, O.; Loennecke, P.; Silaghi-Dumitrescu, I.; Hey-Hawkins, E, *Dalton Transactions* (2008), (23), 3107-3114.

Germanium cluster polyhedral, Silaghi-Dumitrescu, Ioan; King, Bruce, *Studia Universitatis Babes-Bolyai, Chemia* (2008), 53(2), 83-88.

Interplay among Tetrahedrane, Butterfly Diradical, and Planar Rhombus Structures in the Chemistry of the Binuclear Iron Carbonyl Phosphinidene Complexes Fe₂(CO)₆(PX)₂, Silaghi-Dumitrescu, Ioan; Bitterwolf, Thomas E.; King, R. Bruce, *Journal of the American Chemical Society* (2008), 130(3), 901-906.

Palladium(II) and Platinum(II) Complexes with Heteroditopic 10-(Aryl)phenoxarsine (Aryl = 2-C₆H₄OR, R = H, Me, Pri) Ligands: Solvent-Oriented Crystallization of cis Isomers, Moldovan, Natalia; Loennecke, Peter; Silaghi-Dumitrescu, Ioan; Silaghi-Dumitrescu, Luminita; Hey-Hawkins, Evamarie, *Inorganic Chemistry* (2008), 47(5), 1524-1531.

Polyhedral structures with three-, four-, and five fold symmetry in metal-centered ten-vertex germanium clusters, King R Bruce; Silaghi-Dumitrescu Ioan; Uta Matei-Maria (2008), 14(15), 4542-50.

Process for preparation of calixarene derivatives for the extraction of rare earth metal ions, Ursales, Traian; Popovici, Nicolae; Popovici, Elisabeth-Jeanne; Silaghi-Dumitrescu, Ioan; Palibroda, Nicolae. 121691 B1 20080228 Patent written in Romanian. Application: RO 2003-200300816 20031003. Priority: CAN 150:35528 AN 2008:361932.

Serinolic amino-s-triazines: iterative synthesis and rotational stereochemistry phenomena as N-substituted derivatives of 2-aminopropane-1,3-diols, Pinteau, Monica; Fazekas, Marijana; Lameiras, Pedro; Cadis, Ionut; Berghian, Camelia; Silaghi-Dumitrescu, Ioan; Popa, Flavia; Bele, Constantin; Ple, Nelly; Darabantu, Mircea, *Tetrahedron* (2008), 64(37), 8851-8870.

Synthesis and characterisation of some copper oxide catalysts for ozone decomposition, Dan, C.; Popovici, E.-J.; Imre-Lucaci, F.; Popovici, N.; Marginean, P.; Silaghi-Dumitrescu, I, *Journal of Optoelectronics and Advanced Materials* (2008), 10(9), 2234-2236.

Temperature induced rotation in a [4.4]cyclophane, Bogdan, Niculina D.; Condamine, Eric; Toupet, Loic; Ramondenc, Yvan; Silaghi-Dumitrescu, Ioan; Grosu, Ion, *Tetrahedron Letters* (2008), 49(35), 5204-5207. **Abstract**

The role of "external" lone pairs in the chemical bonding of bare post-transition element clusters: the Wade-Mingos rules versus the jellium model, King, R. B.; Silaghi-Dumitrescu, I, *Dalton Transactions* (2008), (44), 6083-6088.

When Arsine Makes the Difference: Chelating Phosphino and Bridging Arsenoarylthiolato Gallium, Valean, Ana Maria; Gomez-Ruiz, Santiago; Loncke, Peter; Silaghi-Dumitrescu, Ioan; Silaghi-Dumitrescu, Luminita; Hey-Hawkins, Evamarie, *Inorganic Chemistry* (2008), 47(23), 11284-11293.

1,1,4,4-Tetrabenzyl-1,4-diphosphinane-1,4-dium dibromide deuteriochloroform disolvate, Fild, Manfred; Krueger, Oana N.; Silaghi-Dumitrescu, Ioan; Thoene, Carsten, *Acta Crystallographica, Section E: Structure Reports Online* (2007), E63(12), o4525, o4525/1-o4525/8.

1,3-Digermacyclobutanes with exocyclic C:P and C:P:S double bonds, Petrar, Petronela Maria; Nemes, Gabriela; Silaghi-Dumitrescu, Ioan; Ranaivonjatovo, Henri; Gornitzka, Heinz; Escudie, Jean, *Chemical Communications* (2007), (40), 4149-4151

Calix[n]arene derivatives with binding properties toward Eu³⁺, Saponar, Alina; Silaghi-Dumitrescu, Ioan; Popovici, Elisabeth-Jeanne; Popovici, Nicolae, *Studia Universitatis Babes-Bolyai, Chemia* (2007), 52(4), 67-74.

Synthesis of Ester Derivatives of Calix[n]arene, Saponar, Alina; Popovici, Elisabeth-Jeanne; Grecu, Rodica; Silaghi-Dumitrescu, Ioan; Popovici, Nicolae, *Studia Universitatis Babes-Bolyai, Chemia* (2009), 54(4), 203-210.

cis- -1,4-Diphenyl-1,4-diphosphorinane- 2P:P'-bis[pentacarbonylchromium(0)] deuteriochloroform solvate, Fild, Manfred; Krueger, Oana N.; Silaghi-Dumitrescu, Ioan; Thoene, Carsten; Weinkauff, Andreas, *Acta Crystallographica, Section E: Structure Reports Online* (2007), E63(12), m3011, m3011/1-m3011/9.

Density functional theory study of twelve-atom germanium clusters: conflict between the Wade-Mingos rules and optimum vertex degrees, King, R. Bruce; Silaghi-Dumitrescu, Ioan; Uta, Matei M, Dalton Transactions (2007), (3), 364-372.

New [4.4]cyclophane diketals, monoketones, and diketones: design, synthesis, and structural analysis, Bogdan, Niculina; Grosu, Ion; Condamine, Eric; Toupet, Loiec; Ramondenc, Yvan; Silaghi-Dumitrescu, Ioan; Ple, Gerard; Bogdan, Elena, European Journal of Organic Chemistry (2007), (28), 4674-4687.

New Digermylalkenes and Digermylalkynes: [1,3]-Chlorine Shifts in Organogermanium Chemistry? Nemes, Gabriela; Escudie, Jean; Silaghi-Dumitrescu, Ioan; Ranaivonjatovo, Henri; Silaghi-Dumitrescu, Luminita; Gornitzka, Heinz, Organometallics (2007), 26(21), 5136-5139.

Secondary interactions in heteroallenic systems with P:C-E units, Nemes, G.; Silaghi-Dumitrescu, I.; Petrar, P. M.; Septelean, R.; Silaghi-Dumitrescu, L, Studia Universitatis Babes-Bolyai, Chemia (2007), 52(1), 3-9.

Silatropic migration in (1-trimethylsilylindenyl)(indenyl)dimethylsilane, bis(1-trimethylsilylindenyl)dimethylsilane and related compounds, Nemes, Gabriela; Silaghi-Dumitrescu, Luminita; Silaghi-Dumitrescu, Ioan; Escudie, Jean; Ranaivonjatovo, Henri; Zukerman-Schpector, Julio, Revue Roumaine de Chimie (2007), 52(8-9), 809-816.

Studies on some ozone decomposition catalysts based on nickel oxide, Dan, Crina; Popovici, Elisabeth-Jeanne; Imre, Florica; Indrea, Emil; Marginean, Petre; Silaghi-Dumitrescu, Ioan, Studia Universitatis Babes-Bolyai, Chemia (2007), 52(1), 91-95.

Synthesis and characterization of calix[4]arene with different donor groups at the "narrow" rim, Saponar, Alina; Silaghi-Dumitrescu, Ioan; Popovici, Elisabeth-Jeanne; Popovici, Nicolae, Revista de Chimie (2007), 58(5), 481-483.

Synthesis and characterization of some mixed ligand zinc(II) complexes of theophylline, Mihaly, Bela; Forizs, Edit; Silaghi-Dumitrescu, Ioan, Studia Universitatis Babes-Bolyai, Chemia (2007), 52(4), 111-116.

Synthesis and characterization of the first arsanylbis(methylene)phosphorane (Me₃Si)₂C:P(Mes*)₂:C(Cl)As(F)Mes*, Petrar, Petronela Maria; Nemes, Gabriela; Silaghi-Dumitrescu, Luminita; Silaghi-Dumitrescu, Ioan; Escudie, Jean; Gornitzka, Heinz; Ranaivonjatovo, Henri, Revue Roumaine de Chimie (2007), 52(1-2), 45-49.

Synthesis and properties of organogermanium and organotin dithiophosphonate complexes; crystal structures of (C₆H₅)₂Sn(Cl)[(p-MeOC₆H₄)(EtO)PS₂-S, S'], Me₂Sn[(p-MeOC₆H₄)(MeO)PS₂-S]₂, Me₂Sn[(p-MeOC₆H₄)(iPrO)PS₂-S]₂, and Me₂Ge{[(C₆H₅)₃SiO](p-MeOC₆H₄)PS₂-S]₂, Fild, Manfred; Krueger, Oana; Silaghi-Dumitrescu, Ioan; Thoene, Carsten; Weinkauff, Andreas, Phosphorus, Sulfur and Silicon and the Related Elements (2007), 182(10), 2283-2310.

Synthesis and spectral characterization of some calix[4]pyrogallolarenes, Popovici, N.; Ursales, T. N.; Silaghi-Dumitrescu, I.; Saponar, Alina; Popovici, Elisabeth-Jeanne, Acta Universitatis Cibiniensis, Seria F: Chemia (2007), 10(2), 51-57.

The formylation of bis-(N-alkyl-phenothiazinyl)-methane; a theoretical approach, Porumb, Dan; Silaghi-Dumitrescu, Ioan; Gaina, Luiza; Silaghi-Dumitrescu, Luminita; Cristea, Castelia; Cormos, Gabriela, *Studia Universitatis Babes-Bolyai, Chemia* (2007), 52(4), 39-42.

Towards new double-bonded organophosphorus derivatives of C:P:C:P type, Nemes, Gabriela; Septelean, Raluca; Petrar, Petronela M.; Silaghi-Dumitrescu, Luminita; Silaghi-Dumitrescu, Ioan, *Studia Universitatis Babes-Bolyai, Chemia* (2007), 52(4), 89-94.

α -(3,7-Dioxo-r-1-azabicyclo[3.3.0]oct-c-5-ylmethoxy)-diazines. Part 2: Functionalization via directed ortho-metalation and cross-coupling reactions, Berghian, Camelia; Condamine, Eric; Ple, Nelly; Turck, Alain; Silaghi-Dumitrescu, Ioan; Maieranu, Carmen; Darabantu, Mircea, *Tetrahedron* (2006), 62(31), 7339-7354.

A quantum chemical conformational analysis of p-tert-butyl/pentyl/octyl-calix[8]arenes, Lupan, Alexandru; Saponar, Alina; Silaghi-Dumitrescu, Ioan; Kun, Attila; Silaghi-Dumitrescu, Luminita; Popovici, Elisabeth Jeanne, *Studia Universitatis Babes-Bolyai, Chemia* (2006), 51(2), 27-34.

Butterfly Diradical Intermediates in Photochemical Reactions of Fe₂(CO)₆(μ -S₂), Silaghi-Dumitrescu, Ioan; Bitterwolf, Thomas E.; King, R. Bruce, *Journal of the American Chemical Society* (2006), 128(16), 5342-5343.

Co-complexes of ortho-dilithiated thiophenol or 2-trimethylsilylthiophenol with lithiated TMEDA molecules: synthesis, crystal structures and theoretical studies (TMEDA = N,N,N',N'-tetramethylethylenediamine), Hildebrand, Alexandra; Loennecke, Peter; Silaghi-Dumitrescu, Luminita; Silaghi-Dumitrescu, Ioan; Hey-Hawkins, Evamarie, *Dalton Transactions* (2006), (7), 967-974.

Density Functional Theory Study of 10-Atom Germanium Clusters: Effect of Electron Count on Cluster Geometry. King, R. B.; Silaghi-Dumitrescu, I.; Uta, M. M, *Inorganic Chemistry* (2006), 45(13), 4974-4981.

DFT and the electromerism in complexes of iron with diatomic ligands, Silaghi-Dumitrescu, Radu; Silaghi-Dumitrescu, Ioan., *Journal of Inorganic Biochemistry* (2006), 100(1), 161-166.

First synthesis of a G-2 melamine dendrimer with serinolic peripheral groups, Darabantu, Mircea; Pinteau, Monica; Fazekas, Marijana; Lameiras, Pedro; Berghian, Camelia; Delhom, Isabelle; Silaghi-Dumitrescu, Ioan; Ple, Nelly; Turck, Alain, *Letters in Organic Chemistry* (2006), 3(12), 905-910.

Molecular Rotors: Design, Synthesis, Structural Analysis, and Silver Complex of New [7.7]Cyclophanes, Bogdan, Niculina; Grosu, Ion; Benoit, Guillaume; Toupet, Loic; Ramondenc, Yvan; Condamine, Eric; Silaghi-Dumitrescu, Ioan; Ple, Gerard, *Organic Letters* (2006), 8(12), 2619-2622.

New halo compounds of silicon and tin, potential precursors of >E=C=P-heteroallenic systems, Petrar, Petronela Maria; Nemes, Gabriela; Silaghi-Dumitrescu, Ioan; Silaghi-Dumitrescu, Luminita, *Studia Universitatis Babes-Bolyai, Chemia* (2006), 51(1), 77-82

New low symmetry low energy structures of 11-atom bare germanium clusters: A density functional theory study, King, R. B.; Silaghi-Dumitrescu, I.; Lupan, A, *Chemical Physics* (2006), 327(2-3), 344-350.

Phosphavinylidene(oxo)phosphorane Mes*P(O):C:PMes*: a diphosphaallene featuring λ 5 σ 3- and λ 3 σ 2-phosphorus atoms, Septelean, Raluca; Ranaivonjatovo, Henri; Nemes, Gabriela; Escudie, Jean; Silaghi-Dumitrescu, Ioan; Gornitzka, Heinz; Silaghi-Dumitrescu, Luminita; Massou, Stephane, *European Journal of Inorganic Chemistry* (2006), (21), 4237-4241.

Special issue: Computational inorganic chemistry - Part 3 of 3. [In: Chemtracts; 2006, 19(2)], Silaghi-Dumitrescu, Radu; Silaghi-Dumitrescu, Ioan. USA. (2006), 41 pp. Publisher: (Data Trace Publishing Co., Baltimore, Md.) Book written in English. CAN 146:175448 AN 2007:

Special theme issue inorganic computational chemistry, Part I. [In: Chemtracts, 2006; 18(11)], Silaghi-Dumitrescu, Radu; Silaghi-Dumitrescu, Ioan; Editors. USA. (2006), 41 pp. Publisher: (Data Trace Publishing Co., Baltimore, Md.) Book written in English. CAN 146:175447 AN 2006:1324965

Structural, energetic and electronic characterization of the chiral carbon-nitride nanotubes, Rada, Simona; Silaghi-Dumitrescu, Ioan, *Revue Roumaine de Chimie* (2006), 51(2), 141-145.

Synthesis of new bromo-stannanes: toward unsaturated tin derivatives, Petrar, Petronela Maria; Nemes, Gabriela; Silaghi-Dumitrescu, Ioan; Silaghi-Dumitrescu, Luminita, *Studia Universitatis Babes-Bolyai, Chemia* (2006), 51(2), 35-40.

A quantum chemical study on boron nitride and carbon nitride nanotubes., Rada, Simona; Dumitrescu, Ioan Silaghi, *Studia Universitatis Babes-Bolyai, Chemia* (2005), 50(2), 155-158.

A surprisingly stable 1-(chlorosilyl)-2-phosphaethenyllithium compound, RCI2SiC(Li):PMes*, Nemes, Gabriela Cretiu; Ranaivonjatovo, Henri; Escudie, Jean; Silaghi-Dumitrescu, Ioan; Silaghi-Dumitrescu, Luminita; Gornitzka, Heinz, *European Journal of Inorganic Chemistry* (2005), (6), 1109-1113.

Adsorption of 6-mercaptopurine and 6-mercaptopurine riboside on silver colloid: a pH dependent surface enhanced Raman spectroscopy and density functional theory study. Part I. 6-Mercaptopurine, Szeghalmi, A. V.; Leopold, L.; Pinzaru, S.; Chis, V.; Silaghi-Dumitrescu, I.; Schmitt, M.; Popp, J.; Kiefer, W, *Journal of Molecular Structure* (2005), 735-736 103-113.

Anodic oxidation of difluorenyls bridged through a dimethylsilyl group and of the 9-trimethylsilyl fluorene: Towards new three-dimensional polyfluorenes, Silaghi-Dumitrescu, Ioan; Escudie, Jean; Cretiu-Nemes, Gabriela; Raoult, Eugene; Rault-Berthelot, Joelle, *Synthetic Metals* (2005), 151(2), 114-119

Applications of carbon-nitride nanotubes to molecular engines photochemically engineered, Rada, Simona; Dumitrescu, Ioan Silaghi; Maties, Vistrian; Rada, Marius, *Revista de Chimie (Bucharest, Romania)* (2005), 56(5), 490-494.

Computational inorganic chemistry - a useful tool and more, Silaghi-Dumitrescu, Radu; Silaghi-Dumitrescu, Ioan, *Chemtracts* (2005), 18(11), 595-619.

Density Functional Study of 8- and 11-Vertex Polyhedral Borane Structures: Comparison with Bare Germanium Clusters, King, R. B.; Silaghi-Dumitrescu, I.; Lupan, A, *Inorganic Chemistry* (2005), 44(22), 7819-7824.

Density Functional Theory Study of 11-Atom Germanium Clusters: Effect of Electron Count on Cluster Geometry, King, R. B.; Silaghi-Dumitrescu, I.; Lupan, A, *Inorganic Chemistry* (2005), 44(10), 3579-3588.

Density functional theory study of eight-atom germanium clusters: effect of electron count on cluster geometry, King, R. B.; Silaghi-Dumitrescu, I.; Lupan, A, *Dalton Transactions* (2005), (10), 1858-1864

Difluorenylsilanes, -germanes, and -stannanes Exhibiting an Unprecedented Parallel Arrangement of the Fluorene Units, Nemes, Gabriela Cretiu; Silaghi-Dumitrescu, Luminita; Silaghi-Dumitrescu, Ioan; Escudie, Jean; Ranaivonjatovo, Henri; Molloy, Kieran C.; Mahon, Mary F.; Zukerman-Schpector, Julio, *Organometallics* (2005), 24(6), 1134-1144.

Discontinuum between ferrous-superoxo and ferric-peroxo in heme [FeO₂]⁹ complexes? Silaghi-Dumitrescu, Radu; Silaghi-Dumitrescu, Ioan, *Studia Universitatis Babes-Bolyai, Chemia* (2005), 50(1), 11-15.

Electronic properties of C₈₀-xN_x tubes with chair geometry, Rada, Simona; Dumitrescu, Ioan Silaghi; Maties, Vistrian; Rada, Marius, *Revista de Chimie* (2005), 56(2), 144-147.

Germanium cluster polyhedra: a density functional theory study, Silaghi-Dumitrescu, Ioan; Kun, Attila; Lupan, Alex; King, R. Bruce, *Lecture Series on Computer and Computational Sciences* (2005), 4 A(Advances in Computational Methods in Sciences and Engineering), 804-806. Publisher: Brill Academic Publishers, ISSN: 1573-4196.

Periodic Cages, Diudea, Mircea V.; Nagy, Csaba L.; Silaghi-Dumitrescu, Ioan; Graovac, Ante; Janezic, Dusanka; Vikić-Topić, Drazen, *Journal of Chemical Information and Modeling* (2005), 45(2), 293-299

75. Structural, energetic and electronic properties of pure/doped BN nanotubes, Rada, Simona; Dumitrescu, Ioan Silaghi, *Studia Universitatis Babes-Bolyai, Chemia* (2005), 50(1), 297-306.

Synthesis and Stereochemistry of New Bis(1,3-Oxathian-2-yl) Derivatives: Epimerisation and Chair-Twist Equilibria, Cismas, C.; Grosu, I.; Ple, G.; Condamine, E.; Ramondenc, Y.; Toupet, L.; Silaghi-Dumitrescu, I.; Nemes, G.; Terec, A.; Muntean, L *Structural Chemistry* (2005), 16(4), 369-377.

The first evidence for a transient stiballene ArSbCCR₂, Baiget, Lise; Ranaivonjatovo, Henri; Escudie, Jean; Nemes, Gabriela Cretiu; Silaghi-Dumitrescu, Ioan; Silaghi-Dumitrescu, Luminita, *Journal of Organometallic Chemistry* (2005), 690(2), 307-312.

The shapes of hypoelectronic six-vertex anionic bare boron clusters: effects of the counteractions, King, R. B.; Silaghi-Dumitrescu, I.; Lupan, A.; Kun, A, *Main Group Chemistry* (2005), 4(4), 291-302

3,7-dioxa-1-azabicyclo[3.3.0]octanes substituted at the C-5 position - >From local to global stereochemistry, Darabantu, Mircea; Maioreanu, Carmen; Silaghi-Dumitrescu, Ioan; Toupet, Loic; Condamine, Eric; Ramondenc, Yvan; Berghian, Camelia; Ple, Gerard; Ple, Nelly, *European Journal of Organic Chemistry* (2004), (12), 2644-2661.

A complex problem of diastereoisomerism: Synthesis and stereochemistry of 1,4-bis-{r-1-aza-c-5-ethyl-3,7-dioxabicyclo[3.3.0]octane-c-2-yl}-benzene, Maioreanu, Carmen; Toupet, Loic; Condamine, Eric; Silaghi-Dumitrescu, Ioan; Ple, Gerard; Ramondenc, Yvan; Darabantu, Mircea, *Revue Roumaine de Chimie* (2004), 49(7), 595-602.

A novel disiloxanediolato-derivative of tin(IV), Petrar, Petronela M.; Nemes, Gabriela Cretiu; Silaghi-Dumitrescu, Ioan. *Studia Universitatis Babes-Bolyai, Chemia* (2004), 49(2), 209-216.

Conformational and configurational analysis on some calix[4]resorcinarenes functionalized with organo-phosphorus groups, Ursales, Traian-Nicolae; Silaghi-Dumitrescu, Ioan, *Revue Roumaine de Chimie* (2004), 49(2), 143-147.

Electronic properties of the zigzag carbon-nitride nanotubes, Rada, Simona; Dumitrescu, Ioan Silaghi. *Studia Universitatis Babes-Bolyai, Chemia* (2004), 49(2), 217-222.

Hemes revisited by density functional approaches. 1: The axial ligand and the dioxygen-peroxo chemistry, Silaghi-Dumitrescu, Radu; Silaghi-Dumitrescu, Ioan *Revue Roumaine de Chimie* (2004), 49(3-4), 257-268.

New materials based on phosphorylated calix[n]arenes, Ursales, T. N.; Silaghi-Dumitrescu, I.; Popovici, E.-J.; Ursales, A.; Popovici, N *Journal of Optoelectronics and Advanced Materials* (2004), 6(1), 307-313.

Possible hybrids between polyoxometalates and calixarenes, Ursales, T. N.; Silaghi-Dumitrescu, I.; Grecu, R.; Silaghi-Dumitrescu, L.; Popovici, N.; Popovici, E.-J, *Journal of Optoelectronics and Advanced Materials* (2004), 6(2), 471-476.

Synthesis of calix[n]arenes with pendant diphenyl phosphate functionalities at the "narrow rim", Ursales, T.-N.; Popovici, N.; Silaghi-Dumitrescu, I.; Popovici, E.-J, *Acta Universitatis Cibiniensis, Seria F: Chemia* (2004), 7(1), 71-75.

Synthesis of some new O-alkenyl calix[6]arene and calix[8]arene derivatives, Ursales, Traian-Nicolae; Silaghi-Dumitrescu, Ioan; Ciocan, Cristina; Palibroda, Nicolae; Popovici, Nicolae; Popovici, Elisabeth-Jeanne. *Revue Roumaine de Chimie* (2004), 49(9), 741-745.

The conformational analysis of some calix[4]arenes substituted at the "lower rim" with organo-phosphorus groups, Ursales, Traian-Nicolae; Silaghi-Dumitrescu, Ioan, *Revue Roumaine de Chimie* (2004), 49(5), 437-441.

Tin(IV) halide complexes of AsPh₃) The structures of trans-SnCl₄(AsPh₃)₂ and SnBr₄(AsPh₃)₂, Mahon Mary F; Moldovan Natalia L; Molloy Kieran C; Muresan Alexandra; Silaghi-Dumitrescu Ioan; Silaghi-Dumitrescu Luminita, *Dalton transactions* (2004), (23), 4017-21.

1-Aza-5-hydroxymethyl-3,7-dioxabicyclo[3.3.0]octanes: Chelating properties related to their conformational chirality, Maieranu, Carmen; Condamine, Eric; Silaghi-Dumitrescu, Ioan; Darabantu, Mircea, *Studia Universitatis Babes-Bolyai, Chemia* (2003), 48(2), 91-101.

Azocoupling products. Part IV. The structure of dyes obtained by azo-coupling reaction of 1-(4-hydroxy-6-methylpyrimidin-2-yl)-3-methylpyrazolin-5-one with aromatic diazonium salts, Panea, Ioan; Ghirisan, Adina; Baldea, Ioan; Silaghi-Dumitrescu, Ioan; Craciun, Liliana; Silberg, Ioan A, *Studia Universitatis Babes-Bolyai, Chemia* (2003), 48(2), 67-83.

Computational Study of the Non-Heme Iron Active Site in Superoxide Reductase and Its Reaction with Superoxide, Silaghi-Dumitrescu, Radu; Silaghi-Dumitrescu, Ioan; Coulter, Eric D.; Kurtz, Donald M., Jr. *Inorganic Chemistry* (2003), 42(2), 446-456

Computational study of the non-heme iron active site in superoxide reductase and its reaction with superoxide, Silaghi-Dumitrescu Radu; Silaghi-Dumitrescu Ioan; Coulter Eric D; Kurtz Donald M Jr, *Inorganic chemistry* (2003), 42(2), 446-56.

Density Functional Theory Study of Nine-Atom Germanium Clusters: Effect of Electron Count on Cluster Geometry, King, R. B.; Silaghi-Dumitrescu, I, *Inorganic Chemistry* (2003), 42(21), 6701-6708.

Density functional theory study of nine-atom germanium clusters: effect of electron count on cluster geometry, King R B; Silaghi-Dumitrescu I, *Inorganic chemistry* (2003), 42(21), 6701-8.

Influences of Changes in Multitopic Tris(pyrazolyl)methane Ligand Topology on Silver(I) Supramolecular Structures, Reger, Daniel L.; Semeniuc, Radu F.; Silaghi-Dumitrescu, Ioan; Smith, Mark D *Inorganic Chemistry* (2003), 42(12), 3751-3764.

Influences of changes in multitopic tris(pyrazolyl)methane ligand topology on silver(I) supramolecular structures, Reger Daniel L; Semeniuc Radu F; Silaghi-Dumitrescu Ioan; Smith Mark D, *Inorganic chemistry* (2003), 42(12), 3751-64

Molecular structure and infrared spectra of 2-bromopropane by ab initio HF and post HF calculations, Greco, Rodica; Kun, Attila; Silaghi-Dumitrescu, Ioan, *Revue Roumaine de Chimie* (2003), Volume Date 2002, 47(10-11), 1055-1061.

New halo compounds of Si, P, As, and Sb bearing a bulky substituted fluorenyl group, Baiget, L.; Bouslikhane, M.; Escudie, J.; Nemes, G. Cretiu; Silaghi-Dumitrescu, I.; Silaghi-Dumitrescu, L, *Phosphorus, Sulfur and Silicon and the Related Elements* (2003), 178(9), 1949-1961.

One pot synthesis a new calix[n]arene derivatives, Ursales, T.-N.; Popovici, E.-J.; Silaghi-Dumitrescu, I.; Popovici, N, Acta Universitatis Cibiniensis, Seria F: Chemia (2003), 6(2), 9-13

Relative stability of conformers of some organophosphorus calix[4]arenes, Ursales, Traian-Nicolae; Silaghi-Dumitrescu, Ioan, Revista de Chimie, (2003), 54(9), 756-758

Small fullerenes, Diudea, Mircea V.; Silaghi-Dumitrescu, Ioan, Studia Universitatis Babes-Bolyai, Chemia (2003), 48(1), 21-30.

Stereocontrolled synthesis by anomeric effects of substituted 1-aza-3,7-dioxabicyclo[3.3.0]octanes, Maieranu, Carmen; Silaghi-Dumitrescu, Ioan; Berghian, Camelia; Pinteau, Monica; Fazekas, Marijana; Darabantu, Mircea, Studia Universitatis Babes-Bolyai, Chemia (2003), 48(2), 103-112.

Synthesis and characterization of some new phosphorylated cavitands from calix[4]resorcinarenes, Ursales, Traian-Nicolae; Silaghi-Dumitrescu, Ioan, Revista de Chimie, (2003), 54(11), 888-889.

Synthesis and reactivity of difluoromethylene bridged diphospha-derivatives, Toetes, R.; Silaghi-Dumitrescu, I, Studia Universitatis Babes-Bolyai, Chemia (2003), 48(2), 149-163.

Synthesis, characterization and conformational analysis of methyl-, propyl-, and isopropylcalix[4]resorcinarenes, Ursales, Traian-Nicolae; Ursales, Adina; Silaghi-Dumitrescu, Ioan. Revista de Chimie) (2003), 54(3), 229-231.

A density functional theory study of five-, six- and seven-atom germanium clusters: distortions from ideal bipyramidal deltahedra in hypoelectronic structures, King, R. B.; Silaghi-Dumitrescu, I.; Kun, A, Journal of the Chemical Society, Dalton Transactions (2002), (21), 3999-4004.

Ring-chain tautomerism and other versatile behaviour of 1,4-diimino- and 1,2-phenylene derivatives of some C-substituted serinols. Maieranu, Carmen; Darabantu, Mircea; Ple, Gerard; Berghian, Camelia; Condamine, Eric; Ramondenc, Yvan; Silaghi-Dumitrescu, Ioan; Mager, Sorin. Tetrahedron (2002), 58(13), 2681-2693

Crystal, molecular, and electronic structure of 9,9'-bis(trimethylsilyl)fluorene, Silaghi-Dumitrescu, Ioan; Cretiu, Gabriela; Silaghi-Dumitrescu, Luminita; Haiduc, Ionel; Toscano, Alfredo; Cea-Olivares, Raymundo, Revue Roumaine de Chimie 2001, 46(4), 289-295.

Crystal, molecular, and electronic structure of 9,9'-bis(trimethylsilyl)fluorene, Silaghi-Dumitrescu, Ioan; Cretiu, Gabriela; Silaghi-Dumitrescu, Luminita; Haiduc, Ionel; Toscano, Alfredo; Cea-Olivares, Raymundo, Revue Roumaine de Chimie (2002), 46(4), 289-295.

Difluorenylsilane derivatives, a class of compounds exhibiting strong intra- and intermolecular C-H... π interactions. Crystal and molecular structures of bis(9-methylfluoren-9-yl)dimethylsilane and (9-methylfluoren-9-yl)(fluoren-9-yl)dimethylsilane, Cretiu, Gabriela; Silaghi-Dumitrescu, Luminita; Silaghi-Dumitrescu, Ioan; Escudie, Jean; Toscano, Alfredo; Hernandez, Simon; Cea-Olivares, Raymundo, Journal of Organometallic Chemistry (2002), 659(1-2), 95-101.

Electronic structure of hypervalent organoarsenic bromo derivatives. An ab initio RHF and DFT-B3LYP investigation of H5-XAsBr_x systems, Silaghi-Dumitrescu, L.; Silaghi-Dumitrescu, I, *Studia Universitatis Babes-Bolyai, Chemia* (2002), 47(1-2), 203-211.

Toroidal fullerenes from squared tiled tori, Diudea, Mircea V.; Silaghi-Dumitrescu, Ioan; Parv, Bazil, *Internet Electronic Journal of Molecular Design* [online computer file] (2002), 1(1), 10-22.

Toroidal fullerenes from squared tiled tori, Diudea, Mircea V.; Silaghi-Dumitrescu, Ioan; Parv, Bazil. *Internet Electronic Journal of Molecular Design* [online computer file] (2002), 1(1), 10-22

Distortions from octahedral symmetry in hypoelectronic six-vertex polyhedral clusters of the group 13 elements boron, indium, and thallium as studied by density functional theory, King, R. Bruce; Silaghi-Dumitrescu, Ioan; Kun, Attila, *Inorganic chemistry* (2001), 40(10), 2450-2.

Electronic and magnetic properties of (tetrakis(2-pyridylmethyl)-ethylenediamine)iron(II) perchlorate. A comparison of different computational methods, Chen, Guangju; Liu, Ruozhuang; Silaghi-Dumitrescu, I.; Espinosa-Perez, G.; Zentella-Dehesa, A.; Lara-Ochoa, F, *International Journal of Quantum Chemistry* (2001), 83(2), 60-69.

Solvent effects in infrared spectra and ab initio calculations of 2-bromopropane, Grecu, R.; Kun, A.; Silaghi-Dumitrescu, I, *Journal of Molecular Structure* (2001), 565-566 39-42

Structural distortions in homoleptic (RE)4A (E = O, S, Se; A = C, Si, Ge, Sn): implications for the CVD of tin sulfides, Barone, Giampaolo; Hibbert, Thomas G.; Mahon, Mary F.; Molloy, Kieran C.; Parkin, Ivan P.; Price, Louise S.; Silaghi-Dumitrescu, Ioan, *Journal of the Chemical Society, Dalton Transactions* (2001), (23), 3435-3445.

Toranes versus torenes, Diudea, Mircea V.; Silaghi-Dumitrescu, Ioan; Parv, Bazil, *MATCH* (2001), 44 117-133.

Voltammetric behaviour of 1,4-benzothiazino[2,3-b]phenothiazine and some of its derivatives. II. The influence of N-substitution and S-oxidation, Cristea, Castelia; Filip, Cecilia; Silaghi-Dumitrescu, Ioan; Silberg, Ioan A, *Revue Roumaine de Chimie* (2001), 45(7-8), 639-642.

(Tetrakis(2-pyridylmethyl)ethylenediamine)iron(II) Perchlorate. Study of Density Functional Methods, Chen, Guangju; Espinosa-Perez, G.; Zentella-Dehesa, A.; Silaghi-Dumitrescu, I.; Lara-Ochoa, F, *Inorganic Chemistry* (2000), 39(16), 3440-3448.

(Tetrakis(2-pyridylmethyl)ethylenediamine)iron(II) perchlorate. Study of density functional methods, Chen G; Espinosa-Perez G; Zentella-Dehesa A; Silaghi-Dumitrescu I; Lara-Ochoa F, *Inorganic chemistry* (2000), 39(16), 3440-8.

A new tubular arrangement of a dimethylsilyl bridged calix[4]resorcinarene, Lara-Ochoa, F.; Garcia, M. Martinez; Teran, R.; Cruz-Almanza, R.; Espinosa-Perez, G.; Chen, G.; Silaghi-Dumitrescu, I, *Supramolecular Chemistry* (2000), 11(4), 263-273.

Bromination of (AsPh₂)₂O: the structure of tribromo-diphenylarsenic(V), Silaghi-Dumitrescu, Luminita; Silaghi-Dumitrescu, Ioan; Silaghi-Dumitrescu, Radu; Haiduc, Ionel; Blake, Alexander J.; Sowerby, D. Bryan. *Revista de la Sociedad Quimica de Mexico* (2000), 44(2), 134-138.

Synthesis and stereochemistry of some new spiro-1,3-perhydrooxazines, Muntean, Luminita; Grosu, Ion; Ple, Gerard; Mager, Sorin; Silaghi-Dumitrescu, Ioan, *Monatshefte fuer Chemie* (2000), 131(9), 975-983.

Synthesis and stereochemistry of some 1,3-oxazolidine systems based on TRIS (α, α, α -trimethylolaminomethane) and related aminopolyols skeleton. Part 2: 1-aza-3,7-dioxabicyclo[3.3.0]octanes. Darabantu, Mircea; Ple, Gerard; Maieranu, Carmen; Silaghi-Dumitrescu, Ion; Ramondenc, Yvan; Mager, Sorin. *Tetrahedron* (2000), 56(23), 3799-3816

Synthesis and stereochemistry of some 1,3-oxazolidine systems based on TRIS (α, α, α -trimethylolaminomethane) and related aminopolyols skeleton. Part 1: (Di)spiro-1,3-oxazolidines. Darabantu, Mircea; Ple, Gerard; Silaghi-Dumitrescu, Ion; Maieranu, Carmen; Tuross, Istvan; Silberg, Ioan A.; Mager, Sorin. *Tetrahedron* (2000), 56(23), 3785-3798

Is the trigonal prismatic distortion the answer for the geometry of In(III) four members dithiochelate compounds? The crystal and molecular structure of In(S₂AsR₂)₃ (R = Me, Ph). Silaghi-Dumitrescu, Luminita; Silaghi-Dumitrescu, Ion; Haiduc, Ionel; Toscano, Ruben-Alfredo; Garcia-Montalvo, Veronica; Cea-Olivares, Raymundo. *Zeitschrift fuer Anorganische und Allgemeine Chemie* (1999), 625(2), 347-351

The crystal and molecular structure of the 2,4,6,8-tetra-t-Bu-phenothiazine 0.5 benzene adduct, Silaghi-Dumitrescu, I.; Silberg, I. A.; Filip, S.; Vlassa, M.; Silaghi-Dumitrescu, L.; Hernandez-Ortega, S, *Journal of Molecular Structure* (2000), 526 279-286.

An interactive workstation for molecular-mechanics modeling of chemical structures. Horvat, Dragos; Silaghi-Dumitrescu, Ion. *Revue Roumaine de Chimie* (1992), 37(10), 1165-74

1-(Acridin-9'-yl)-pyrazolin-3- and -5-ones. A new class of heterocycles with potential biological activity, Cristea, Ioan; Popovici, Mariana M.; Mendel, Maria T.; Silaghi-Dumitrescu, Ioan; Kozma, Erika, *Heterocyclic Communications* (1999), 5(6), 543-548.

A new organodithiophosphoric derivative; synthesis and structural characterization of bis(diphenylborano)dithiophosphoric [(C₆H₅)₂BO]₂P(S)SH, Gabriela, Cretiu; Reka, Torok; Delia, Bugnariu; Oxana, Jeman; Silaghi-Dumitrescu, Ioan, *Studia Universitatis Babes-Bolyai, Chemia* (1999), 44(1-2), 177-182.

An AM1 investigation of the structures of C₆₀:tBu-calix[8]arene 1:1 adducts, Lara-Ochoa, F.; Cogordan, J. A.; Cruz, R.; Martinez, M.; Silaghi-Dumitrescu, I, *Fullerene Science and Technology* (1999), 7(3), 411-419.

Molecular orbital calculations and physical properties of 1,4-benzothiazino[2,3-b]phenothiazine and its substituted derivatives, Silberg, I. A.; Silaghi-Dumitrescu, I.; Cristea, C.; Tordo, P.; Gignes, D, *Heterocyclic Communications* (1999), 5(2), 147-150.

Stable isomers of sila- and germadodecahedrane. A semiempirical (AM1) investigation of the structure of 4/6 and 4/5/6 ring containing E20 (E=Si,Ge) systems, Silaghi-Dumitrescu, Ioan; Kun, Attila; Haiduc, Ionel, *Fullerene Science and Technology* (1999), 7(5), 841-854.

Why does the yellow isomer of [Sn{(PPh₂Se)₂-Se,Se'}₂] present a square planar four-co-ordinated tin(II)? A molecular orbital approach, Silaghi-Dumitrescu, Ioan; Silaghi-Dumitrescu, Luminita; Cea-Olivares, Raymundo, *Main Group Metal Chemistry* (1999), 22(1), 5-8.

Synthesis and ring-ring tautomerism of some spirooxazolidines based on i-p-nitrophenylserinol skeleton. Darabantu, Mircea; Ple, Gerard; Gaina, Luiza; Maieran, Carmen; Silaghi-Dumitrescu, Ion. *Studia Universitatis Babes-Bolyai, Chemia* (1998), 43(1-2), 179-192

Cis and/or trans dioxaphosphetanes. A molecular orbital study of some model (RPO)₂ systems, Silaghi-Dumitrescu, Ioan; Horea, Alin, *Revue Roumaine de Chimie* (1997), 42(7), 599-604.

Comparative PM3-MO study of the E2O2 and E2N2 (E = P, As) four-membered-ring systems, Silaghi-Dumitrescu, Ioan; Horea, Alin; Pascu, Sofia; Silaghi-Dumitrescu, Luminita; Haiduc, Ionel, *Phosphorus, Sulfur and Silicon and the Related Elements* (1997), 124 & 125 441-444.

Ion-molecule interactions in organic electrochemical systems. I. NMR investigations of electrolyte solutions used in lithium anode batteries, Silberg, Ioan Alexandru; Oniciu, Liviu; Bobos, Liviu-Dorel; Silaghi-Dumitrescu, Ioan; Avram, Silvia; Cuius, Cristina. *Revue Roumaine de Chimie* (1997), 42(7), 535-542.

On the formation of cyclodisilazanes via the coordination of bis(dialkylamino)silanes to halosilanes: an ab initio and AM1 molecular orbital study of the 4644 R₂Si(NR'₂)₂:SiX₄ ring systems, Silaghi-Dumitrescu, Ioan; Lara-Ochoa, Francisco; Haiduc, Ionel, *THEOCHEM* (1997), 397 213-222.

On the structure of bis(9-fluorenyl)dimethylsilane: a sterically crowded molecule with relatively low barriers of rotations around the Si-C(fluorenyl) bonds X-ray diffraction analysis and AM1 molecular orbital calculations, Silaghi-Dumitrescu, Luminita; Haiduc, Ionel; Cea-Olivares, Raymundo; Silaghi-Dumitrescu, Ioan; Escudie, Jean; Couret, Claude, *Journal of Organometallic Chemistry* (1997), 545-546 1-7.

Structural studies of tetrazoles. Crystal and molecular structure and ab initio calculations of 1-phenyl-1H-tetrazole-5-thiolate, as its [diaqua(18-crown-6)sodium] salt: an anionic tetrazole free of direct metal interactions, Jimenez-Sandoval, Omar; Cea-Olivares, Raymundo; Hernandez-Ortega, Simon; Silaghi-Dumitrescu, Ioan, *Heteroatom Chemistry* (1997), 8(4), 351-359.

The first oxygen-bridged diorganoarsenic(V) compound: the crystal structure of $\text{AsMe}_2(\text{S})\text{OAs}(\text{S})\text{Me}_2$, Silaghi-Dumitrescu, Luminita; Pascu, Sofia; Silaghi-Dumitrescu, Ioan; Haiduc, Ionel; Gibbons, Martin N.; Sowerby, D. Bryan, *Journal of Organometallic Chemistry* (1997), 549(1-2), 187-192.

A12B12 (A = B,Al; B = N,P) 4/6 fullerene-like cages and their hydrogenated forms stabilized by exohedral bonds. An AM1 molecular orbital study, Silaghi-Dumitrescu, Ioan; Lara-Ochoa, Francisco; Haiduc, Ionel, *THEOCHEM* (1996), 370(1), 17-23.

Coordinative dimerization of aminosilanes. Model MNDO and ab initio molecular orbital calculations, Lara-Ochoa, Francisco; Silaghi-Dumitrescu, Ioan; Haiduc, Ionel. *Main Group Chemistry* (1996), 1(4), 387-398.

Interactions between calix[8]arenes and fullerenes. Molecular dynamics and molecular mechanics simulation of the 1:1 and 1:2 complexes, Lara-Ochoa, Francisco; Cogordan, Juan Antonio; Silaghi-Dumitrescu, Ioan *Fullerene Science and Technology* (1996), 4(5), 887-896

Ion molecule interaction in organic electrochemical systems III. Acrylonitrile-quaternary ammonium cations adducts and their possible implications in electrohydrodimerization processes, Silberg, I. A.; Ciomos, Forentina; Silaghi-Dumitrescu, I, *Studia Universitatis Babes-Bolyai, Chemia* (1996), 41(2), 167-172.

More about boron-nitrogen B12+3nN12+3n fullerene-like cages. An ab initio and AM1 investigation of some 4/6 isomers, Silaghi-Dumitrescu, Ioan; Lara-Ochoa, Francisco; Bishof, Peter; Haiduc, Ionel, *THEOCHEM* (1996), 367 47-54.

Oxidation of $(\text{AsPh}_2)_2\text{E}$ (E = O or S); supramolecular hydrogen-bonded self-assembly of an unusual tetranuclear adduct and crystal structure of $[\text{AsPh}_2(\text{O})\text{OH} \cdot \text{AsPh}_2(\text{S})\text{OH}]_2$, Silaghi-Dumitrescu, Luminita; Gibbons, Martin N.; Silaghi-Dumitrescu, Ioan; Zukerman-Schpector, Julio; Haiduc, Ionel; Sowerby, D. Bryan, *Journal of Organometallic Chemistry* (1996), 517(1-2), 101-106.

On the geometries and electronic structures of XH_2SiNH_2 (X = F, Cl, Br) silanes. MNDO molecular orbital calculations, Silaghi-Dumitrescu, Ioan; Haiduc, Ionel, *Studia Universitatis Babes-Bolyai, Chemia* (1995), 40(1-2), 91-98.

An improved first-order optimization of molecular structure taking account of molecular topology, Horvath, Dragos; Silaghi-Dumitrescu, Ioan, *Studia Universitatis Babes-Bolyai, Chemia* (1994), 39(1-2), 15-27.

An old ligand in a new environment: triply bridged O,O'-dimethyldithiophosphate in the organosamarium complex $[(\text{C}_5\text{Me}_5)_2\text{Sm}\{\text{S}_2\text{P}(\text{OMe})_2\}_2]_2$, Rieckhoff, Melanie; Noltemeyer, Mathias; Edelmann, Frank T.; Haiduc, Ionel; Silaghi-Dumitrescu, Ioan, *Journal of Organometallic Chemistry* (1994), 469(1), C22-C23.

Chelating versus bridging coordination of dithiophosphates in copper complexes. An EHMO study, Silaghi-Dumitrescu, Ioan; Serban, Liliana; Silaghi-Dumitrescu, Luminita; Haiduc, Ionel, *Revue Roumaine de Chimie* (1994), 39(12), 1397-405.

On the geometry of 1,3-diazadiphosphetidines. The cis-trans isomerism, Silaghi-Dumitrescu, Ioan; Haiduc, Ionel, Phosphorus, Sulfur and Silicon and the Related Elements (1994), 91(1-4), 21-36.

ansa-Metallocene derivatives of samarium and ytterbium with soft donor ligands, Edelmann, Frank T.; Rieckhoff, Melanie; Haiduc, Ionel; Silaghi-Dumitrescu, Ioan, Journal of Organometallic Chemistry (1993), 447(2), 203-8.

Fully inorganic (carbon-free) fullerenes? The boron-nitrogen case, Silaghi-Dumitrescu, Ioan; Haiduc, Ionel; Sowerby, D. Bryan, Inorganic Chemistry (1993), 32(17), 3755-8.

On the ring angles in the four-membered cyclodiphosphazanes, Silaghi-Dumitrescu, Ioan; Haiduc, Ionel, Studia Universitatis Babes-Bolyai, Chemia (1993), 38(1-2), 183-186.

Molecular topology. 2. A computer program for multiple bond, cycle and radical approximations of DS index, Diudea, Mircea V.; Silaghi-Dumitrescu, Ioan, Revue Roumaine de Chimie (1991), 36(1-3), 263-9.

Molecular topology. 2. A computer program for multiple bond, cycle and radical approximations of DS index, Diudea, Mircea V.; Silaghi-Dumitrescu, Ioan, Revue Roumaine de Chimie (1991), 36(8), 975-82.

The richness of structures available to P₂N₂ inorganic heterocycles. A topological and molecular orbital (EHMO) analysis, Haiduc, Ionel; Silaghi-Dumitrescu, Ioan, Revue Roumaine de Chimie (1991), 36(4-7), 527-44.

The electronic structure of silyl amide ([H₃SiNSiH₃]⁻) anion. A simple molecular orbital treatment, Silaghi-Dumitrescu, Ioan; Haiduc, Ionel, Revue Roumaine de Chimie (1990), 35(3), 475-84.

The infrared spectra of methyl(O-methyl)dithiophosphonic acid. Multiplicity of some bands due to different conformers, Grecu, Rodica; Constantinescu, Rodica; Silaghi-Dumitrescu, I.; Haiduc, I, Journal of Molecular Structure (1990), 218 111-16.

Molecular structure modeling by using a basic line formula interpreter, Horvath, D.; Silaghi-Dumitrescu, I, Studia Universitatis Babes-Bolyai, Chemia (1989), 34(2), 41-5.

Molecular topology. I. Valence group electronegativity as a vertex discriminator, Diudea, Mircea V.; Silaghi-Dumitrescu, Ioan, Revue Roumaine de Chimie (1989), 34(5), 1175-82.

The sulfotropic molecular rearrangement of tetraorganodiarsine disulfides, Silaghi-Dumitrescu, Luminita; Silaghi-Dumitrescu, Ioan; Haiduc, Ionel, Revue Roumaine de Chimie (1989), 34(1), 305-15.

Vibrational spectra and coordination behavior of organo-dithiophosphorus ligands, Silaghi-Dumitrescu, Ioan; Grecu, Rodica; Silaghi-Dumitrescu, Luminita; Haiduc, Ionel, Studia Universitatis Babes-Bolyai, Chemia (1989), 34(1), 97-101.

Electronic structure and bonding in diamidoboron cations. A molecular orbital study of diamidoboron(1+) [H₂NBNH₂]⁺, Silaghi-Dumitrescu, Ioan; Haiduc, Ionel, *Revue Roumaine de Chimie* (1988), 33(9-10), 851-6.

Linear versus bent bis(diphosphine)iminium cations. A molecular orbital discussion of the bonding in [H₃PNPH₃]⁺ and related species, Silaghi-Dumitrescu, I.; Haiduc, I, *Revue Roumaine de Chimie* (1988), 33(2), 133-42.

Inorganic (carbon-free) chelate rings, Haiduc, Ionel; Silaghi-Dumitrescu, Ioan *Coordination Chemistry Reviews* (1986), 74 127-270.

The bonding in dialkyldithiophosphinato metal complexes. A molecular orbital study of bis(dimethyldithiophosphinato)nickel(II), Silaghi-Dumitrescu, Ioan; Haiduc, Ionel, *Revue Roumaine de Chimie* (1986), 31(11-12), 955-62.

Why are cyclodisilazane rings more stable than cyclodisiloxanes? A qualitative molecular orbital approach to the bonding in cyclodisilazanes and cyclodisiloxanes, Silaghi-Dumitrescu, Ioan; Haiduc, Ionel, *Inorganica Chimica Acta* (1986), 112(2), 159-65.

The crystal and molecular structure of a versatile bidentate ligand: tetraphenyldithioimidodiphosphinate, Ph₂(S)PNHP(S)Ph₂, Hitchcock, Peter B.; Nixon, John F.; Silaghi-Dumitrescu, Ioan; Haiduc, Ionel, *Inorganica Chimica Acta* (1985), 96(1), 77-80.

The electronic structure and bonding in the thiophosphoryl cation PS⁺, Silaghi-Dumitrescu, I.; Haiduc, I, *Phosphorus and Sulfur and the Related Elements* (1985), 22(1), 85-91.

Electronic structure and force constants of the dithionitronium cation NS₂⁻, Silaghi-Dumitrescu, I.; Haiduc, I, *THEOCHEM* (1984), 15(3-4), 217-23.

Vibrational spectra of phosphorodithioic metal complexes. Normal coordinate treatment of bis(O-isopropyl ethyldithiophosphonato)nickel(II), Haiduc, I.; Silaghi-Dumitrescu, I.; Grecu, Rodica; Constantinescu, Rodica; Silaghi-Dumitrescu, Luminita, *Journal of Molecular Structure* (1984), 114 467-70.

Bonding in organophosphorus dithio acids. A CNDO/2 calculation of electronic structure, Silaghi-Dumitrescu, Ioan; Haiduc, Ionel, *Phosphorus and Sulfur and the Related Elements* (1982), 12(2), 205-12.

Normal coordinate analysis of the vibrational spectrum of dimethyldithioarsinato anion, (CH₃)₂AsS₂⁻, Silaghi-Dumitrescu, Ioan; Silaghi-Dumitrescu, Luminita; Haiduc, Ionel, *Revue Roumaine de Chimie* (1982), 27(8), 911-16.

A simple topology-based method for estimating stretching force constants of AB_n molecules, Silaghi-Dumitrescu, I *Revue Roumaine de Chimie* (1981), 26(11-12), 1441-5.

IOAN SILAGHI-DUMITRESCU
1950-2009

The infrared spectrum of dimethyldithiophosphinato anion $(\text{CH}_3)_2 \text{PS}_2^-$. Normal coordinate analysis and Urey-Bradley force field calculation, Silaghi-Dumitrescu, Ioan; Haiduc, Ionel, *Revue Roumaine de Chimie* (1980), 25(6), 815-21.

Vibrational characteristics of nickel(II) dithiophosphinato chelates. Normal coordinate analysis and Urey-Bradley force field calculation of $\text{Ni}[\text{S}_2\text{P}(\text{CH}_3)_2]_2$, Silaghi-Dumitrescu, Ioan; Haiduc, Ionel *Revue Roumaine de Chimie* (1980), 25(6), 823-30.

Dedicated to the memory of Prof. dr. Ioan Silaghi-Dumitrescu marking 60 years from his birth

A THEORETICAL APPROACH ON THE STRUCTURE OF ARSAALLENES -As=C=C< AND ARSAPHOSPHAALLENES -As=C=P-

PETRONELA M. PETRAR*, GABRIELA NEMES,
LUMINITA SILAGHI-DUMITRESCU

ABSTRACT. Calculations at the B3LYP/6-311 level were performed on a series of arsaallenes and arsaphosphaallenes of the type RAs=C=CR₂ and RAs=C=PR in order to evaluate the nature of the As=C bond. The influence of several substituents (F, Cl, OMe, SiMe₃) on the order of the bond was also investigated.

Keywords: arsaallenes, arsaphosphaallenes, DFT calculations

INTRODUCTION

Derivatives of the type E=C=E' (E, E' = group 14 and 15 elements) have become the focus of research only in the last decades [1]. So far, only a few heteroallenic derivatives of the type -As=C=E (E = CR₂ [2], PR [3], AsR [4]) have been isolated and structurally investigated. The arsenic – carbon distance has a small value of 1.758 Å as reported in Mes*As=C=AsMes* (Mes* = 2,4,6-tri-*tert* butylphenyl) [4] and Mes*As=C=CR₂ (CR₂ = fluorenyl) [2]. The As-C-C bond angle for this derivative is 169.7°, with the central carbon atom deviated from the expected linearity. The supermesityl group lies at a 102° angle from the As=C double bond. For the arsaphosphaallene Mes*As=C=PMes*, problems of symmetry in the X-ray diffraction did not allow to determine exactly the bond lengths and bond angles [3].

We have previously investigated the nature of the As-C bond in heteroallenic derivatives of the type As(V)=C=E (As(V) = $\lambda^5\sigma^4$ As), where E=C, P(III) (P(III) = $\lambda^3\sigma^2$ P), [5]. A model for the structure of H₃As=C=CH₂ according to NBO analysis at the B3LYP/6-311G(d, p) level was proposed, in which As has a lone pair in an *sp* type orbital.

* Universitatea Babeș-Bolyai, Facultatea de Chimie și Inginerie Chimică, Str. Kogălniceanu Nr. 1, RO-400084 Cluj-Napoca, Romania; ppetrar@chem.ubbcluj.ro

A comparison with the analogues in which As has the formal oxidation state III can be very interesting, especially since there are more As(III) ($\text{As(III)} = \lambda^3\sigma^2 \text{As}$), derivatives of this type reported in the literature and the experimental data for doubly bonded As(V) is very scarce.

In order to assess the nature of the As-C bond in arsaallenes -As=C=C< and arsaphosphaallenes -As=C=P-, a theoretical investigation was carried out at the B3LYP/6-311G(d, p) level of the theory. Model compounds of the type RAs=C=CR₂ (R= H, Me, Ph), were studied as well as those in which one or two R groups have been replaced by one or two R' groups (R'= F, Cl, OMe, SiMe₃) on the As or the C atom. The same R' substituents were used for the arsaphosphaallenes. All geometries were optimized and a frequency calculation was run in order to verify if the obtained structures are indeed global minima. An NBO analysis was performed, in order to evaluate the nature of the orbitals involved in bonding and the Wiberg bond order for the As=C and C=C bonds was calculated for each case.

RESULTS AND DISCUSSION

For the model compound HAs=C=CH₂, the As=C bond has a length of 1.77 Å, in agreement with the experimental data obtained for the arsaallene Mes*As=C=CR₂ (1.758 Å) [2], and a bond order of 1.85. (The calculated bond order in the case of H₃As=C=CH₂ at the same level of theory was found to be 1.07). The calculated C=C bond length is 1.30 Å (1.314 Å by X-ray [2]). The geometry around the arsenic in HAs=C=CH₂ is angular, with the H-As-C bond angle of 94°. This suggests that the bonding involves the valence $4s^24p^3$ arsenic orbitals rather than hybrid ones, as expected for heavier main group elements. An NBO analysis shows that the lone pair on the As atom lies in an orbital with strong s character, and that almost pure p orbitals are contributing to the formation of the σ and π bonding to the carbon atom. The same is expected for the other arsaallenes investigated.

As for the only arsaallene characterized experimentally, Mes*As=C=CR₂, (As-C-C bond angle of 169.7°) the value of the angle As-C-C for HAs=C=CH₂ is not 180° but 173.8°. We can thus conclude that the deviation from the linearity of the allenic unit is not the result of steric hindrance or crystal-packing effects, but is inherent to the nature of the arsaallene. Moreover, the most significant second order interaction involves the As(III) lone pair as a donor and the antibonding s orbital of the C-C bond, which is also present for all the derivatives discussed below (figure 1). This interaction could account for the slight narrowing of the angle.

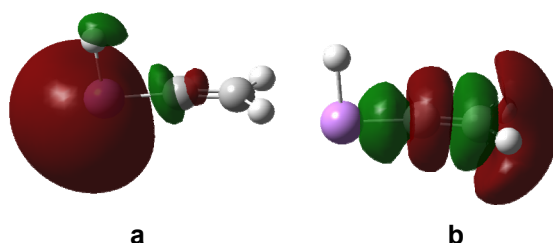


Figure 1. NB orbitals involved in second order perturbation interactions for $\text{HAs}=\text{C}=\text{CH}_2$. (a) lone pair electrons on As; (b) anti-bonding non-Lewis orbital on the C-C bond

I. Monosubstituted arsaallenes $\text{R}'\text{As}=\text{C}=\text{CR}_2$ and $\text{RAs}=\text{C}=\text{CRR}'$

In the case of substitution with one R' group ($\text{R}' = \text{F}, \text{Cl}, \text{OMe}$ and SiMe_3), two types of derivatives were considered: with R' on the arsenic, and on the terminal carbon atom of the allenic unit. The group R was either H, Me or Ph . The results obtained from the geometry optimization and NBO analysis are given in table 1.

It can be noticed that in every case the isomer bearing the R' group on the arsenic atom is more stable. However, in the case of substitution with SiMe_3 , the energy difference is significantly smaller. As in the case of As(V) derivatives, substitution of arsenic with an electron-withdrawing group or atom leads to a decrease in the bond order of the $\text{As}=\text{C}$ bond.

For the $\text{H}_2\text{AsC}_2\text{R}'$ isomers, there is a decrease of the bond order when going from $\text{HAs}=\text{C}=\text{CR}'\text{H}$ to $\text{R}'\text{As}=\text{C}=\text{CH}_2$, for $\text{R}' = \text{F}, \text{Cl}$, and OMe . This is explained by charge donation from the lone pairs of the R' to a vacant antibonding orbital of π symmetry on the $\text{As}-\text{C}$ bond. The value of the second order perturbation energy is 7.31 for $\text{R}' = \text{F}$, 5.15 for Cl and 11.30 for $\text{R}' = \text{OMe}$, which also reflects the magnitude of the bond order decrease. The two natural bonding orbitals involved in the interaction are illustrated in figure 2 for the case $\text{R}' = \text{OMe}$.

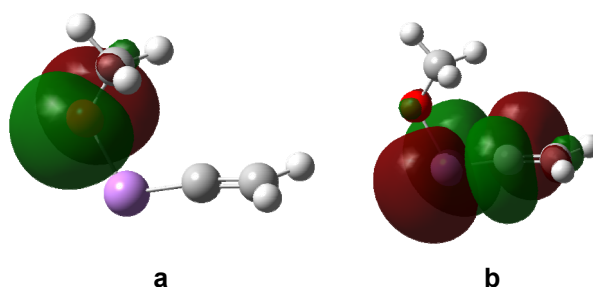


Figure 2. NB orbitals involved in second order perturbation interactions for $(\text{MeO})\text{As}=\text{C}=\text{CH}_2$. (a) lone pair electrons on O; (b) anti-bonding non-Lewis orbital on the C-C bond

However, for $R' = \text{SiMe}_3$, the bond order of the arsenic-carbon bond is higher in the case of $\text{Me}_3\text{SiAs}=\text{C}=\text{CH}_2$ (1.86, close to the bond order calculated for $\text{HAs}=\text{C}=\text{CH}_2$) than for the corresponding isomer, substituted at the terminal carbon atom, $\text{HAs}=\text{C}=\text{CH}(\text{SiMe}_3)$ (1.80). This is because in the case of the latter, there is a charge transfer from an orbital localized on $\text{C}_2\text{-Si}$ and the antibonding orbital of π symmetry of the As-C_1 bond. The two orbitals are shown in figure 3. The same phenomenon is observed for all SiMe_3 substituted derivatives.

Table 1. Selective data for $R'\text{As}=\text{C}=\text{CR}_2$ and $\text{RAs}=\text{C}=\text{CRR}'$, calculated at the B3LYP/6-311G(d, p) level (bond lengths in Å, bond angles in degrees). The Wiberg bond orders for As=C and C=C are also given.

| Molecule | Energy (a.u.) | ΔE (kcal/mol) | As=C | C1=C2 | As-C-C | W BO As=C | W BO C=C |
|---|---------------|-----------------------|------|-------|--------|-------------|----------|
| $\text{HAs}=\text{C}=\text{CH}_2$ | -2313.843087 | - | 1.77 | 1.30 | 173.8 | 1.85 | 2.02 |
| $\text{MeAs}=\text{C}=\text{CMe}_2$ | -2431.831534 | - | 1.76 | 1.31 | 173.5 | 1.84 | 1.88 |
| $\text{PhAs}=\text{C}=\text{CPh}_2$ | -3007.169658 | - | 1.76 | 1.32 | 172.7 | 1.81 | 1.80 |
| $\text{HAs}=\text{C}=\text{CHF}$ | -2413.096739 | 20.5 | 1.76 | 1.31 | 172.6 | 1.87 | 1.92 |
| $\text{FAs}=\text{C}=\text{CH}_2$ | -2413.129358 | 0.0 | 1.76 | 1.31 | 174.8 | 1.78 | 2.03 |
| $\text{HAs}=\text{C}=\text{CHCl}$ | -2773.461680 | 24.7 | 1.76 | 1.30 | 173.1 | 1.84 | 1.95 |
| $\text{ClAs}=\text{C}=\text{CH}_2$ | -2773.501019 | 0.0 | 1.76 | 1.31 | 174.1 | 1.81 | 2.01 |
| $\text{HAs}=\text{C}=\text{CH}(\text{OMe})$ | -2428.389328 | 11.8 | 1.76 | 1.31 | 170.5 | 1.88 | 1.87 |
| $(\text{MeO})\text{As}=\text{C}=\text{CH}_2$ | -2428.408053 | 0.0 | 1.76 | 1.31 | 172.6 | 1.74 | 2.03 |
| $\text{HAs}=\text{C}=\text{CH}(\text{SiH}_3)$ | -2722.591752 | 3.1 | 1.78 | 1.30 | 173.8 | 1.80 | 2.03 |
| $(\text{Me}_3\text{Si})\text{As}=\text{C}=\text{CH}_2$ | -2722.596750 | 0.0 | 1.76 | 1.31 | 176.1 | 1.86 | 1.98 |
| $\text{MeAs}=\text{C}=\text{CMeF}$ | -2491.763808 | 17.8 | 1.75 | 1.31 | 172.4 | 1.83 | 1.86 |
| $\text{FAs}=\text{C}=\text{CMe}_2$ | -2491.792168 | 0.0 | 1.75 | 1.32 | 175.4 | 1.81 | 1.87 |
| $\text{MeAs}=\text{C}=\text{CMeCl}$ | -2852.125134 | 24.3 | 1.76 | 1.30 | 173.2 | 1.80 | 1.90 |
| $\text{ClAs}=\text{C}=\text{CMe}_2$ | -2852.163852 | 0.0 | 1.75 | 1.31 | 175.1 | 1.84 | 1.85 |
| $\text{MeAs}=\text{C}=\text{CMe}(\text{OMe})$ | -2507.048261 | 13.2 | 1.75 | 1.32 | 175.1 | 1.86 | 1.82 |
| $\text{MeOAs}=\text{C}=\text{CMe}_2$ | -2507.069265 | 0.0 | 1.76 | 1.32 | 171.9 | 1.77 | 1.87 |
| $\text{MeAs}=\text{C}=\text{CMe}(\text{SiMe}_3)$ | -2801.246316 | 4.9 | 1.77 | 1.31 | 174.1 | 1.79 | 1.96 |
| $(\text{Me}_3\text{Si})\text{As}=\text{C}=\text{CMe}_2$ | -2801.254090 | 0.0 | 1.77 | 1.31 | 174.9 | 1.86 | 1.85 |
| $\text{PhAs}=\text{C}=\text{CPhF}$ | -2875.324550 | 17.4 | 1.75 | 1.32 | 170.4 | 1.79 | 1.80 |
| $\text{FAs}=\text{C}=\text{CPh}_2$ | -2875.352230 | 0.0 | 1.75 | 1.33 | 175.5 | 1.82 | 1.78 |
| $\text{PhAs}=\text{C}=\text{CPhCl}$ | -3235.682429 | 25.9 | 1.76 | 1.31 | 171.8 | 1.75 | 1.85 |
| $\text{ClAs}=\text{C}=\text{CPh}_2$ | -3235.723670 | 0.0 | 1.74 | 1.33 | 176.0 | 1.86 | 1.76 |
| $\text{PhAs}=\text{C}=\text{CPh}(\text{OMe})$ | -2890.618419 | 4.3 | 1.75 | 1.33 | 170.1 | 1.81 | 1.73 |
| $\text{MeOAs}=\text{C}=\text{CPh}_2$ | -2890.625224 | 0.0 | 1.75 | 1.32 | 174.0 | 1.81 | 1.79 |
| $\text{PhAs}=\text{C}=\text{CPh}(\text{SiMe}_3)$ | -3184.803748 | 6.8 | 1.77 | 1.31 | 174.8 | 1.75 | 1.92 |
| $\text{Ph}(\text{SiMe}_3)\text{As}=\text{C}=\text{CPh}_2$ | -3184.814571 | 0.0 | 1.76 | 1.32 | 174.2 | 1.89 | 1.76 |

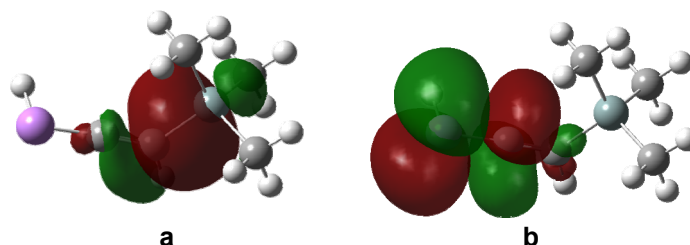


Figure 3. NB orbitals involved in second order perturbation interactions for $\text{HAs}=\text{C}=\text{CH}(\text{SiMe}_3)$. (a) σ orbital on the $\text{C}_2\text{-Si}$ bond; (b) π anti-bonding non-Lewis orbital on the $\text{As}=\text{C}_1$ bond

Going from the hydrogen to the methyl-substituted series, it can be noticed that the bond order for the fluorinated derivative decreases. The NBO analysis shows second order interactions between the π orbital situated on the As-C bond and a $\text{C}_2\text{-C}_3$ (from methyl) antibonding orbital, which lowers the bond order. The chlorinated species also display different values when $\text{R} = \text{Me}$. Thus, $\text{MeAs}=\text{C}=\text{CMeCl}$ has a lower bond order for the As-C bond than $\text{ClAs}=\text{C}=\text{CMe}_2$, in contrast with the hydrogen-substituted analogues. When the chlorine is on the carbon atom, a charge transfer occurs from the π orbital situated on the As-C and a σ^* (C-Cl) orbital, which was not present for $\text{HAs}=\text{C}=\text{CHCl}$. Also, the donation from the lone pairs of the Cl to the vacant antibonding orbital of π symmetry on the As-C bond is not present for the isomer $\text{ClAs}=\text{C}=\text{CMe}_2$, contrary to the case when $\text{R} = \text{H}$. The OMe and SiMe_3 -substituted derivatives behave like their analogues with hydrogen instead of methyl.

The only other notable exception is for the isomers $\text{PhAs}=\text{C}=\text{CPhF}$ (with a bond order of the As=C bond of 1.79) and $\text{FAs}=\text{C}=\text{CPh}_2$ (1.82). In this case, an interaction of the kind described for $\text{ClAs}=\text{C}=\text{CMe}_2$ influences the difference between the two values.

II. Disubstituted arsaallenes $\text{R}'\text{As}=\text{C}=\text{CRR}'$ and $\text{RAs}=\text{C}=\text{CR}'_2$

The same groups were considered in the case of the disubstitution by two R' groups. From the calculated energies presented in table 2, there can be noticed that the $\text{RAs}=\text{C}=\text{CR}'_2$ isomer is always energetically favored, but that in the case of $\text{R}' = \text{OMe}$ and SiMe_3 , the difference between the two types of derivatives is smaller. The bond order of the As=C bond is generally higher for $\text{R}'\text{As}=\text{C}=\text{CRR}'$ compounds, except when $\text{R} = \text{H}$, Me and $\text{R}' = \text{F}$, OMe and $\text{R} = \text{H}$, $\text{R}' = \text{Cl}$. This is due to donations from the lone pairs of F, Cl and O respectively to bonding orbitals on the As=C bond (mainly the one of π symmetry), similar to those described for $\text{R}'\text{As}=\text{C}=\text{CR}'_2$ (see figure 2 for the shape of the orbitals involved). The same considerations as before can be applied to explain the variation of the As=C bond order for the derivatives

with $R' = F, Cl$ and OMe . The silyl group is a special case, mainly because of the lack of lone pairs on the silicon, so it will be discussed in detail. From table 2, it can be seen that the $As=C$ bond order in is always smaller than in the corresponding isomer $Me_3SiAs=C=C(SiMe_3)R$. The explanation is similar as for the monosubstituted derivative, with a charge transfer from the bonding C_2-Si orbital (figure 4a, for $R = Me$) to both the σ (figure 4b) and the π anti-bonding orbitals localized on the $As-C$ bond. Only two such interactions are possible for $(Me_3Si)As=C=CR(SiMe_3)$, as opposed to four in the case of $RA_s=C=C(SiMe_3)_2$ derivatives (from both $C-Si$ bonding orbitals), which thus display a lower bond order.

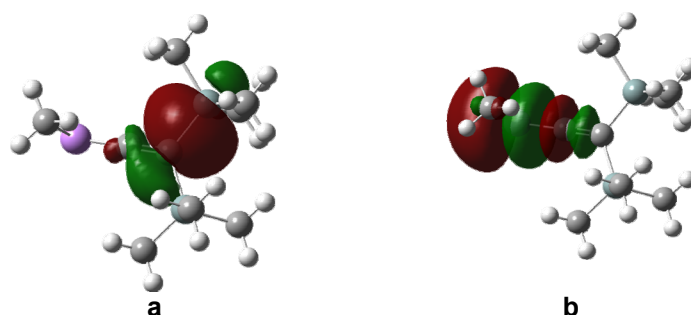


Figure 4. NB orbitals involved in second order perturbation interactions for $MeAs=C=C(SiMe_3)_2$. (a) σ -orbital on the C_2-Si bond; (b) σ -anti-bonding non-Lewis orbital on the $As=C_1$ bond

This bond order is even lower for $PhAs=C=C(SiMe_3)_2$. The NBO analysis shows that in this case, a supplementary charge transfer occurs from the p-symmetry bonding orbital on the $As-C$ bond to an antibonding orbital situated on a bond of the phenyl ring (see figure 5). This leads to a bond order of 1.67, the lowest for the entire series analyzed. However, $As-C$ distance is not greatly influenced.

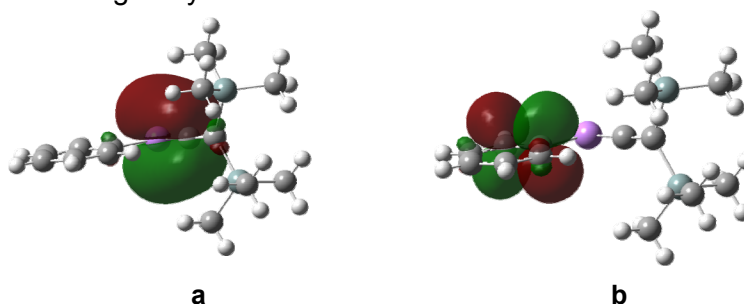


Figure 5. NB orbitals involved in second order perturbation interactions for $PhAs=C=C(SiMe_3)_2$. (a) π -orbital on the C_2-Si bond; (b) π -anti-bonding non-Lewis orbital on a $C=C$ bond of the phenyl ring

Table 2. Selective data for R'As=C=CRR' and RAs=C=CR'₂, calculated at the B3LYP/6-311G(d, p) level (bond lengths in Å, bond angles in degrees). The Wiberg bond orders for As=C and C=C are also given.

| Molecule | Energy (a.u.) | ΔE (kcal/mol) | As=C | C1=C2 | As-C-C | WBO As=C | WBO C=C |
|--|---------------|---------------|------|-------|--------|-------------|---------|
| FAs=C=CHF | -2512.387693 | 0.0 | 1.74 | 1.31 | 173.6 | 1.79 | 1.91 |
| HAs=C=CF ₂ | -2512.360844 | 16.8 | 1.75 | 1.30 | 170.9 | 1.86 | 1.84 |
| ClAs=C=CHCl | -3233.120327 | 0.0 | 1.75 | 1.30 | 173.3 | 1.79 | 1.93 |
| HAs=C=CCl ₂ | -3233.075782 | 28.0 | 1.76 | 1.30 | 172.6 | 1.81 | 1.87 |
| (MeO)As=C=CH(OMe) | -2542.956023 | 0.0 | 1.74 | 1.32 | 171.4 | 1.81 | 1.85 |
| HAs=C=C(OMe) ₂ | -2542.948974 | 4.4 | 1.75 | 1.33 | 162.8 | 1.88 | 1.73 |
| (SiMe ₃)As=C=CH(SiMe ₃) | -3131.345021 | 0.0 | 1.77 | 1.31 | 175.1 | 1.80 | 1.98 |
| HAs=C=C(SiMe ₃) ₂ | -3131.339292 | 3.6 | 1.79 | 1.30 | 174.3 | 1.72 | 2.05 |
| FAs=C=CMeF | -2551.724813 | 0.0 | 1.74 | 1.31 | 174.5 | 1.80 | 1.84 |
| MeAs=C=CF ₂ | -2551.693708 | 19.5 | 1.75 | 1.30 | 171.0 | 1.81 | 1.85 |
| ClAs=C=CMeCl | -3272.454314 | 0.0 | 1.75 | 1.31 | 174.0 | 1.79 | 1.86 |
| MeAs=C=CCl ₂ | -3272.408031 | 29.0 | 1.75 | 1.30 | 172.9 | 1.77 | 1.89 |
| (MeO)As=C=CMe(OMe) | -2582.284328 | 0.0 | 1.74 | 1.32 | 170.0 | 1.82 | 1.79 |
| MeAs=C=C(OMe) ₂ | -2582.274268 | 6.3 | 1.75 | 1.32 | 171.9 | 1.84 | 1.81 |
| (SiMe ₃)As=C=CMe(SiMe ₃) | -3170.670114 | 0.0 | 1.77 | 1.31 | 175.1 | 1.80 | 1.93 |
| MeAs=C=C(SiMe ₃) ₂ | -3170.666509 | 2.3 | 1.78 | 1.30 | 174.6 | 1.72 | 2.03 |
| FAs=C=CPhF | -2743.507094 | 0.0 | 1.74 | 1.32 | 171.9 | 1.81 | 1.77 |
| PhAs=C=CF ₂ | -2743.472533 | 21.7 | 1.75 | 1.30 | 168.9 | 1.76 | 1.85 |
| ClAs=C=CPhCl | -3464.233759 | 0.0 | 1.74 | 1.31 | 173.6 | 1.80 | 1.80 |
| PhAs=C=CCl ₂ | -3464.186502 | 29.7 | 1.76 | 1.30 | 172.5 | 1.71 | 1.90 |
| (MeO)As=C=CPh(OMe) | -2774.066178 | 0.0 | 1.74 | 1.32 | 169.6 | 1.81 | 1.79 |
| PhAs=C=C(OMe) ₂ | -2774.05281 | 8.4 | 1.75 | 1.32 | 170.8 | 1.80 | 1.81 |
| (SiMe ₃)As=C=CPh(SiMe ₃) | -3362.450222 | 0.0 | 1.77 | 1.31 | 175.2 | 1.82 | 1.87 |
| PhAs=C=C(SiMe ₃) ₂ | -3362.444627 | 3.5 | 1.78 | 1.30 | 174.6 | 1.67 | 2.05 |

III. Arsaphosphaallenes R'As=C=PR and RAs=C=PR'

In the case of arsaphosphaallenes, the bond order of the As=C bond is lower than that of the corresponding arsaallenes (e.g., 1.82 for HAs=C=PH and 1.84 for HAs=C=CH₂; for complete data see table 3). This is readily explained by the NBO analysis: there is electron donation from the lone pair of the phosphorus atom in the σ-symmetry antibonding orbital localized on the As-C bond. The orbitals involved are shown in figure 6 for MeAs=C=PMe. In addition, charge transfer from the As lone pair to vacant orbitals on the P-C is present, similarly to the case of arsaallenes. The bond order of the P-C bond varies from 1.80 to 1.98.

The calculated energies for the model compounds show that for R' = Cl, SiMe₃, the RAs=C=PR' isomer is energetically favored, while in the case of F and OMe, R'As=C=PR have lower energies. In both cases though, the

difference in energy is not significant, going up to only 7.1 kcal for $R' = \text{Cl}$ and $R = \text{Ph}$. This relatively low value comparatively to that calculated for arsaallenes can be accounted by close values of bond energies of R-P and R-As, which are significantly different for R-As and C-R [6].

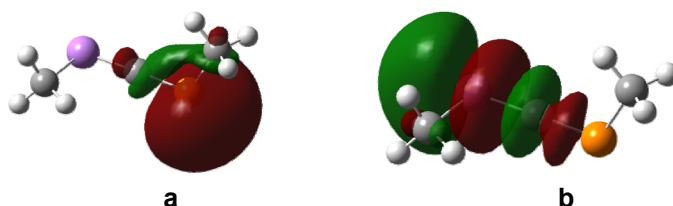


Figure 6. NB orbitals involved in second order perturbation interactions for $\text{MeAs}=\text{C}=\text{PMe}$. (a) lone pair on the P atom; (b) σ -anti-bonding non-Lewis orbital on the C=P bond

The value of the Wiberg bond order for the As=C is always much lower for the $\text{RAs}=\text{C}=\text{P}(\text{SiMe}_3)$ derivatives than for $(\text{Me}_3\text{Si})\text{As}=\text{C}=\text{PR}$. This is explained by the NBO analysis in terms of a charge transfer from a P-Si bonding orbital to an antibonding orbital localized on the As=C bond (see figure 7 for the shape of the NB orbitals involved). The values of the second order interactions are 18.70 for $R = \text{H}$, 15.96 for $R = \text{Me}$ and 14.72 for $R = \text{Ph}$. On the contrary, when Me_3Si group is on the arsenic atom, then the electron donation occurs from an As-Si orbital to an antibonding C-P orbital, which reduces the bond order of this bond for the $(\text{Me}_3\text{Si})\text{As}=\text{C}=\text{PR}$ compared to their isomers. The lack of this interaction explains the higher bond orders for $(\text{Me}_3\text{Si})\text{As}=\text{C}=\text{PR}$: 1.98 for $R=\text{H}$, 1.96 for $R=\text{Me}$ and 1.97 for $R=\text{Ph}$.

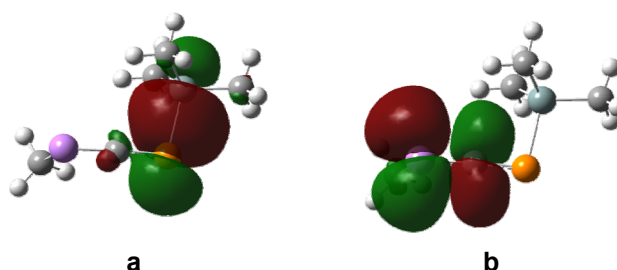


Figure 7. NB orbitals involved in second order perturbation interactions for $\text{MeAs}=\text{C}=\text{PSiMe}_3$. (a) σ -bonding orbital on the P-Si bond; (b) π -anti-bonding non-Lewis orbital on the As=C bond

As in the case of the arsaallenes, when R = H, R' = F, Cl, OMe, the lone pairs of the R' group play an important role in the value of the bond order of the As=C bond. Thus, when the groups are bonded to arsenic, the donation of electrons from lone pairs to an antibonding orbital of p symmetry on the As-C bond is present. For the HAs=C=PR' isomers, this charge transfer occurs to the more available P=C antibonding orbitals, leading to a decrease of the P=C bond order when compared to its isomer or the simplest model compound, HAs=C=PH.

Table 3. Selective data for RAs=C=PR' and R'As=C=PR, calculated at the B3LYP/6-311G(d, p) level (bond lengths in Å, bond angles in degrees). The Wiberg bond orders for As=C and C=C are also given.

| Molecule | Energy (a.u.) | ΔE (kcal/mol) | As=C | C=P | As-C-P | W BO As=C | W BO C=P |
|--------------------------------|---------------|--------------------------|------|------|--------|--------------|-------------|
| HAs=C=PH | -2616.496293 | - | 1.77 | 1.64 | 170.1 | 1.82 | 1.94 |
| MeAs=C=PMe | -2695.159405 | - | 1.76 | 1.64 | 170.5 | 1.79 | 1.89 |
| PhAs=C=PPh | -3078.717049 | - | 1.76 | 1.64 | 168.6 | 1.74 | 1.84 |
| HAs=C=PF | -2715.785965 | 0.0 | 1.76 | 1.64 | 168.0 | 1.83 | 1.83 |
| FAs=C=PH | -2715.782567 | 2.1 | 1.76 | 1.64 | 170.2 | 1.73 | 1.94 |
| HAs=C=PCl | -3076.145363 | 5.5 | 1.77 | 1.63 | 168.6 | 1.79 | 1.89 |
| ClAs=C=PH | -3076.154206 | 0.0 | 1.76 | 1.64 | 169.6 | 1.76 | 1.92 |
| HAs=C=P(OMe) | -2731.064527 | 0.0 | 1.76 | 1.64 | 166.8 | 1.84 | 1.81 |
| (MeO)As=C=PH | -2731.058053 | 4.1 | 1.76 | 1.64 | 167.8 | 1.72 | 1.95 |
| HAs=C=P(SiMe ₃) | -3025.251322 | 1.1 | 1.78 | 1.63 | 172.2 | 1.72 | 1.98 |
| (Me ₃ Si)As=C=PH | -3025.253113 | 0.0 | 1.76 | 1.65 | 171.7 | 1.85 | 1.86 |
| MeAs=C=PF | -2755.119568 | 0.0 | 1.76 | 1.63 | 168.1 | 1.77 | 1.84 |
| FAs=C=PMe | -2755.117374 | 1.4 | 1.76 | 1.64 | 170.3 | 1.74 | 1.88 |
| MeAs=C=PCl | -3115.478872 | 6.2 | 1.76 | 1.63 | 169.0 | 1.74 | 1.89 |
| ClAs=C=PMe | -3115.488827 | 0.0 | 1.76 | 1.64 | 169.7 | 1.78 | 1.86 |
| MeAs=C=P(OMe) | -2770.397116 | 0.0 | 1.76 | 1.64 | 167.9 | 1.80 | 1.81 |
| MeOAs=C=PMe | -2770.392069 | 3.2 | 1.76 | 1.64 | 168.4 | 1.73 | 1.89 |
| MeAs=C=P(SiMe ₃) | -3064.580612 | 2.0 | 1.78 | 1.64 | 172.3 | 1.71 | 1.96 |
| (Me ₃ Si)As=C=PMe | -3064.583753 | 0.0 | 1.76 | 1.65 | 171.8 | 1.83 | 1.84 |
| PhAs=C=PF | -2946.898555 | 0.0 | 1.76 | 1.63 | 156.3 | 1.71 | 1.85 |
| FAs=C=PPh | -2946.897732 | 0.5 | 1.76 | 1.64 | 167.7 | 1.75 | 1.81 |
| PhAs=C=PCl | -3307.257729 | 7.1 | 1.77 | 1.63 | 168.0 | 1.68 | 1.91 |
| ClAs=C=PPh | -3307.269059 | 0.0 | 1.75 | 1.64 | 168.6 | 1.79 | 1.79 |
| PhAs=C=P(OMe) | -2962.176075 | 0.0 | 1.76 | 1.64 | 165.5 | 1.74 | 1.81 |
| MeOAs=C=PPh | -2962.172192 | 2.4 | 1.76 | 1.64 | 166.4 | 1.73 | 1.83 |
| PhAs=C=P(SiMe ₃) | -3256.35854 | 3.0 | 1.78 | 1.64 | 171.8 | 1.67 | 1.97 |
| Ph(SiMe ₃)As=C=PPh | -3256.363293 | 0.0 | 1.76 | 1.65 | 171.1 | 1.84 | 1.79 |

For $\text{MeAs}=\text{C}=\text{PCl}$, electron donation from the $\text{As}=\text{C}$ bond to an orbital situated on the $\text{P}-\text{Cl}$ bond occurs, which lowers the bond order. This interaction is present for $\text{R} = \text{Ph}$, but not for $\text{R} = \text{H}$, which explains the difference in the values of the $\text{As}-\text{C}$ bond order when changing the R group.

CONCLUSIONS

The $\text{As}-\text{C}$ bond in arsa- and arsaphosphaallenes has a calculated bond order between 1.67 and 1.90. The bonding of the arsenic in such derivatives involves the 'pure' atomic shell orbitals $4s$ and $4p$, with the lone pair being situated in the s orbital. The strength of the bond is influenced by functionalization on both the arsenic and the terminal element of the $\text{As}=\text{C}=\text{E}$ ($\text{E} = \text{C}, \text{P}$) unit. Substituents bearing lone pairs can influence it significantly, by charge transfer from the lone pairs to anti-bonding orbitals of the bond. The calculations indicate that increase of the bond order is favored by the presence of silyl groups on the arsenic atom, which can also afford the steric protection needed.

Whatever the group on As , C and P , the $\text{As}=\text{C}$, $\text{C}=\text{C}$ and $\text{C}=\text{P}$ bond lengths are about the same within 2 or 3 pm.

ACKNOWLEDGEMENT

The authors are grateful to Dr. Jean Escudié (Paul Sabatier University, Toulouse) for useful discussions on the manuscript. Through these, Dr. Escudie joins the authors in paying homage to the memory of Prof. Dr. Ioan Silaghi-Dumitrescu.

The computational resources acquired through the CMMCCC program (Capacitati, modul I, 130/14.09.2007) were employed.

COMPUTATIONAL DETAILS

The calculations were performed using the Gaussian 09 package [7], at the B3LYP [8]/6-311G (d, p) level of the theory. The results were visualized with GaussView 4.1. The input geometry was also built with GaussView; in every case the starting geometry included the $\text{As}=\text{C}$ double bond. The structures were optimized and a vibrational analysis was performed in every case. Negative frequencies higher than -20 cm^{-1} were ignored. An NBO analysis was requested, together with a calculation of the Wiberg bond order, which was listed for the $\text{As}=\text{C}$ and $\text{C}=\text{C}/\text{P}$ bonds.

REFERENCES

- For reviews on heteroallenes E=C=E' (E, E' = Si, Ge, Sn; $\lambda^3\sigma^2$ P and As) see: (a) J. Escudié, H. Ranaivonjatovo and L. Rigon, *Chem. Rev.* **2000**, *100*, 3639; (b) R. Appel, in *Multiple Bonds and Low Coordination in Phosphorus Chemistry*, Georg Thieme Verlag: Stuttgart, Germany, **1990**, 157; (c) B. Eichler and R. West, *Adv. Organomet. Chem.* **2001**, *46*, 1; (d) M. Yoshifuji and K. Toyota, in *The Chemistry of Organosilicon Compounds*; Rappoport, Z., Apeloig, Y., Eds.: John Wiley and Sons: Chichester, UK, **2001**, *3*, 491; (e) J. Escudié, H. Ranaivonjatovo, M. Bouslikhane, Y. El Harouch, L. Baiget and G. Cretiu Nemes, *Russ. Chem. Bull.* **2004**, *5*, 1020; (f) J. Escudié and H. Ranaivonjatovo, *Organometallics* **2007**, *26*, 1542.
- M. Bouslikhane, H. Gornitzka, H. Ranaivonjatovo and J. Escudié, *Organometallics*, **2002**, *21*, 1531.
- H. Ranaivonjatovo, H. Ramdane, H. Gornitzka, J. Escudié and J. Satgé, *Organometallics*, **1998**, *17*, 1631.
- M. Bouslikhane, H. Gornitzka, J. Escudié, H. Ranaivonjatovo and H. Ramdane, *J. Am. Chem. Soc.*, **2000**, *122*, 12880.
- P. M. Petrar, G. Nemes, R. Septelean, L. Silaghi-Dumitrescu and J. Escudié, *Rev. Roum. Chimie*, submitted for publication.
- C. D. Schaeffer, C. A. Strausser, M. W. Thomsen and C. H. Yoder, *Data for General Organic and Physical Chemistry*, Franklin & Marshall College, **1989**, Table 6.
- Gaussian 09, Revision A.02, M. J. Frisch, G. W. Trucks, H. B. Schlegel, G. E. Scuseria, M. A. Robb, J. R. Cheeseman, G. Scalmani, V. Barone, B. Mennucci, G. A. Petersson, H. Nakatsuji, M. Caricato, X. Li, H. P. Hratchian, A. F. Izmaylov, J. Bloino, G. Zheng, J. L. Sonnenberg, M. Hada, M. Ehara, K. Toyota, R. Fukuda, J. Hasegawa, M. Ishida, T. Nakajima, Y. Honda, O. Kitao, H. Nakai, T. Vreven, J. A. Montgomery, Jr., J. E. Peralta, F. Ogliaro, M. Bearpark, J. J. Heyd, E. Brothers, K. N. Kudin, V. N. Staroverov, R. Kobayashi, J. Normand, K. Raghavachari, A. Rendell, J. C. Burant, S. S. Iyengar, J. Tomasi, M. Cossi, N. Rega, J. M. Millam, M. Klene, J. E. Knox, J. B. Cross, V. Bakken, C. Adamo, J. Jaramillo, R. Gomperts, R. E. Stratmann, O. Yazyev, A. J. Austin, R. Cammi, C. Pomelli, J. W. Ochterski, R. L. Martin, K. Morokuma, V. G. Zakrzewski, G. A. Voth, P. Salvador, J. J. Dannenberg, S. Dapprich, A. D. Daniels, Ö. Farkas, J. B. Foresman, J. V. Ortiz, J. Cioslowski, and D. J. Fox, Gaussian, Inc., Wallingford CT, 2009.
- a) A.D. Becke, *J.Chem.Phys.*, **1993**, *98*, 5648; b) C. Lee, W. Yang and R. G. Parr, *Phys. Rev. B*, **1988**, *37*, 785; c) S.H. Vosko, L. Wilk and M. Nusair, *Can. J. Phys.*, **1980**, *58*, 1200; d) P.J. Stephens, F.J. Devlin, C.F. Chabalowski and M.J. Frisch, *J. Phys. Chem.*, **1994**, *98*, 11623.

Dedicated to the memory of Prof. dr. Ioan Silaghi-Dumitrescu marking 60 years from his birth

ZINC-CONTAINING ACTIVE SITE IN A PARTIALLY MODIFIED 1GKM CRYSTAL STRUCTURE OF HISTIDINE AMMONIA-LYASE: A COMPUTATIONAL INVESTIGATION

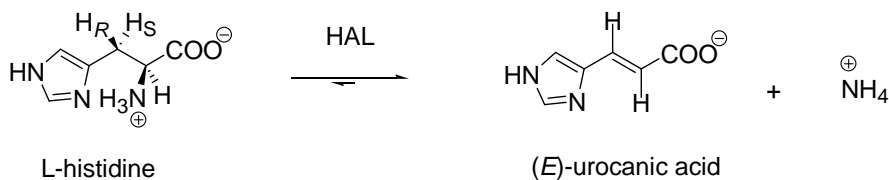
AMALIA-LAURA SEFF^a, SAROLTA PILBÁK^b,
IOAN SILAGHI-DUMITRESCU^a, LÁSZLÓ POPPE^b

ABSTRACT. The histidine ammonia-lyase (HAL) biocatalyst has an important role in the formation of (*E*)-urocanic acid from L-histidine eliminating ammonia. In order to investigate the active center of HAL, we have prepared "*in silico*" a HAL model with a compact active center on the basis of the recently appeared phenylalanine ammonia-lyase (PAL) structure (PDB code: 3CZO). Furthermore, to have a better view on the orientation of a key reaction intermediate within the active site, systematic conformational analysis has been performed. Furthermore, the possible positions of the L-histidine/(*E*)-urocanic acid were evaluated by optimization and docking.

Keywords: *histidine ammonia-lyase, homology modeling, conformational analysis, docking, Zr²⁺*

INTRODUCTION

The degradation pathway of histidine in various organisms proceeds in a different way than for most of the other amino acids [1]. The histidine ammonia-lyase (HAL, EC 4.3.1.3) catalyzes the first step of the degradation with ammonia elimination from the L-histidine substrate forming the product (*E*)-urocanic acid (Scheme 1).



Scheme 1

^a Faculty of Chemistry and Chemical Engineering, Babeș-Bolyai University, Kogălniceanu Str. No. 1, RO-400084 Cluj-Napoca, Romania, samalia@chem.ubbcluj.ro

^b Department of Organic Chemistry and Technology, Budapest University of Technology and Economics, H-1111 Budapest, Gellért tér 4, Hungary, poppe@mail.bme.hu

The aforementioned product was identified as a component of human sweat [2] and a condition named histidinemia appears in case of the lack of HAL in humans [3]. Histidine ammonia-lyase together with the phenylalanine ammonia-lyase (PAL, EC 4.3.1.24) and tyrosine ammonia-lyase (TAL, EC 4.3.1.23) are a part of the family of ammonia-lyases. PAL and TAL as members of this family catalyze the elimination of ammonia from the corresponding L-amino acid forming unsaturated products as (*E*)-cinnamic acid and (*E*)-coumaric acid. These products have important biological roles from the amino acid catabolism to the formation of intermediates in different biosyntheses. HAL, PAL and TAL catalyze the ammonia elimination by the aid of the 5-methylene-3,5-dihydroimidazol-4-one (MIO) prosthetic group [4].

It was observed that cations, like Zn^{2+} , Cd^{2+} or Mn^{2+} can increase the activity of the HAL enzyme [5]. After elucidation of the X-ray structure of HAL [6], the importance of several amino acid residues at the active center (Tyr53, His83, Asn195, Gln277, Tyr280, Arg283, Phe329 and Glu414) for catalysis and substrate binding was evaluated by site-directed mutagenesis and it was supposed that Zn^{2+} may play a role in catalysis [7].

The present work describes the "*in silico*" preparation of the partially modified HAL structure (1GKM*mod*) from the crystal structure (1GKM) [8] of *Pseudomonas putida* HAL (*Pp*HAL), including modeling of a closed Tyr53-loop region which was necessary to obtain a closed active site. A systematic conformational analysis of the substrate covalently bound to the MIO prosthetic group (*N*-MIO intermediate) taking into account the presence of a Zn^{2+} cation and ligand docking results are also presented.

RESULTS AND DISCUSSION

Selection and modeling of the HAL crystal structure

According to the study with active site mutants of HAL [7], Tyr53, Glu414 and Tyr280 residues may have an important role in the abstraction of the pro-(S) β -proton from the L-histidine substrate. A comparison of the structure of *Pp*HAL to other ammonia-lyases showed that the loop with the essential Tyr53 adopts a partially open conformation (Figure 1).

The X-ray structure of plant PAL from *Petroselinum crispum* (PDB code: 1W27) determined at 1.7 Å resolution [9] has an opened, solvent accessible active site (Figure 1A). The bacterial *Pp*HAL (PDB code: 1GKM) structure reveals a partially opened, solvent accessible active site (Figure 1B). All the six crystal structures determined for HAL so far contain the catalytically essential Tyr53 in a partially open loop conformation. This may be the reason why these structures could not retain substrate or product related ligands. Therefore, none of them could be used for theoretical investigation of the compact active center. Only the 1GKM crystal structure of HAL (inhibited with L-cysteine) was determined in the presence of an inhibitor in the active center.

The recently published ammonia-lyase crystal structure (PDB code: 3CZO) [10], determined for *Anabaena variabilis* PAL (AvPAL), contains the most compact active center in which the essential Tyr78 and the MIO prosthetic group are deeply buried and not solvent accessible (Figure 1C).

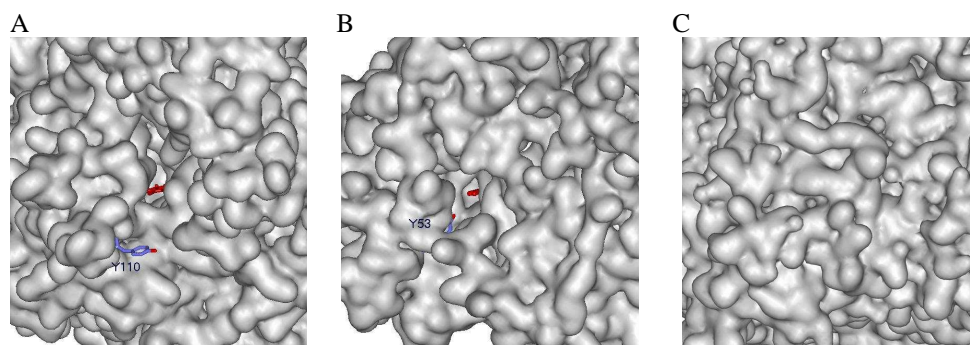


Figure 1. Comparison of the substrate entrance channel towards MIO group (red) in several ammonia-lyase structures. Representation of molecular surface of (A) *Pc*PAL (PDB code 1W27), (B) *Pp*HAL (PDB code 1GKM) and (C) *Av*PAL (PDB code 3CZO) crystal structures. The analogous Tyr110 (A) and Tyr53 (B) residues are seen as stick models in the partially opened ammonia-lyase structures.

Our motivation to select the 1GKM HAL structure for further calculations was the presence of an inhibitor and the unique orientation of the side chain of Met382 amino acid within the active site.

Modification of the essential Tyr-containing loop region (39-80 amino acid sequence) of 1GKM HAL was based on the 3CZO PAL structure using homology modeling (Figure 2). The new (1GKM_{mod}) model contains a tightly closed active site and thus provides a well defined enzymic ambience for further theoretical investigation and calculations.

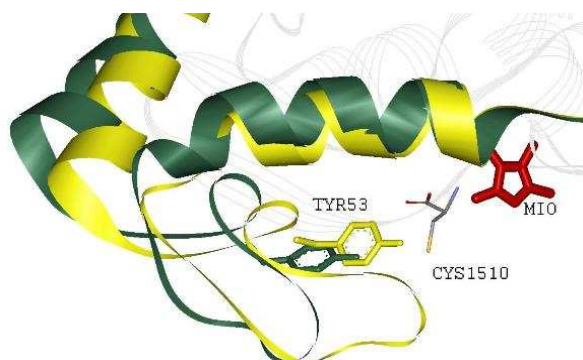


Figure 2. Overlay of the important Tyr53 loop regions of *Pp*HAL (1GKM, green chain; including the L-cysteine inhibitor in CPK color) and of the partially modified 1GKM_{mod} (yellow chain) structures.

Conformational analysis of the *N*-MIO intermediate

The arrangement of L-cysteine inhibitor within the active center of 1GKM crystal structure provided the opportunity to replace the inhibitor with the natural substrate (L-histidine). In the *N*-MIO intermediate of the HAL reaction, the L-histidine is covalently bound to the MIO prosthetic group through its amino group. The carboxyl group of the histidine substrate may point towards the Arg283 amino acid residue and the imidazole ring of the substrate may be in the hydrophobic part of the active site close to the His83 residue. In order to get the geometries of the possible orientation of the intermediate within the active site, the systematic conformational analysis search (CS) method has been used. The active center of the HAL structure was proposed to contain a Zn²⁺ ion [7]. Concerning on the Zn-binding site, the S atom of Met382 could be one of the coordinating ligand of the Zn²⁺ ion together with the imidazole group of His83 and substrate. The W544 water molecule was moved as the fourth ligand of Zn²⁺.

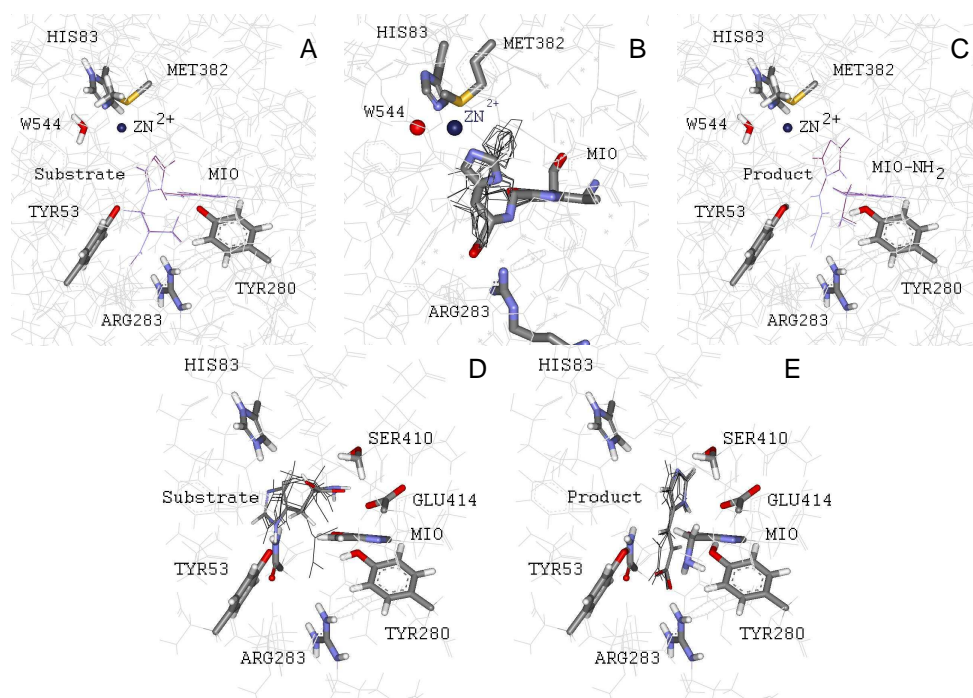


Figure 3. Optimized arrangements of substrate (A) and product (C), conformational analysis of the covalent intermediate (B), and docking results for the substrate (D) and product (E) in the modified HAL structure.

For the covalent intermediate model (Figure 3B), the best ligand energy conformation was selected and highlighted as stick model (imidazole group points towards His83 and carboxylate is in the close vicinity of Arg283) which was also in correspondence with the overall arrangement of the ligands found in the experimental structures of *Rhodobacter sphaeroides* TAL. The Zn²⁺ coordination set is formed by the imidazole group of His83 and of the substrate, the Met382 and a water molecule. The geometrical characterization of the optimized substrate, covalent intermediate and product structures is presented in the Table 1.

Table 1. Geometrical parameters resulted after optimization of the substrate/product structure and after conformational search of the covalent intermediate structure.

| | Distances (Å) | | | |
|--------------|---|---|---|--|
| | d(Zn-N3 _{H83}) | d(Zn-N3 _{Lig}) | d(Zn-O _{W544}) | d(Zn-S _{M382}) |
| substrate | 1.91 | 2.90 | 2.91 | 3.76 |
| intermediate | 1.91 | 2.67 | 2.91 | 3.76 |
| product | 1.91 | 3.05 | 2.91 | 3.76 |
| | d(H _{O-Y53} -Cβ _{Lig}) | d(βH _{Lig} -O _{Y53}) | d(O _{Lig} -H _{R283}) | d(H _{N1-Lig} -O _{E414}) |
| subst./prod. | <u>2.21</u> | 2.20 | 1.85/ <u>2.01</u> | 3.00/ <u>3.28</u> |
| | Angles(°) | | | |
| | N3 _{H83} -Zn-N3 _{Lig} | N3 _{Lig} -Zn-O _{W544} | O _{W544} -Zn-S _{M382} | S _{M382} -Zn-N3 _{H83} |
| substrate | 165.5 | 113.7 | 47.1 | 84.8 |
| intermediate | 164.0 | 86.8 | 47.1 | 66.6 |
| product | 147.2 | 117.6 | 47.1 | 70.4 |

Geometry optimization and ligand docking of the substrate/product

Geometry optimization of the substrate/product ligands within the active site of 1GKM_{mod} was necessary because none of the crystal structures determined for HAL contain the natural L-histidine substrate or the (*E*)-urocanic acid product of the reaction.

For a good evaluation of the substrate/product position within the active site, molecular mechanics (MM+) optimization (Figure 3A and 3C) of the ligands derived from the best covalent *N*-MIO intermediate using HyperChem program [11] and ligand docking (Figure 3D and 3E) within the active center of 1GKM_{mod} structure using AutoDock software [12, 13] were carried out.

CONCLUSIONS

Taking into account that partial modification of the 1W27 PcPAL crystal structure by homology modeling [14, 15, 16] was already applied for computational investigation within the active site of the reaction mechanism, it can be considered that our novel HAL model (1GKM_{mod}) is eligible for further computational investigation of the possible geometry orientation of the L-histidine substrate/*N*-MIO intermediate/*(E)*-urocanic acid product.

Although the ligand docking is a computational tool which is dedicated to the evaluation of the possible positions of the ligand within the active site using different algorithms, the results obtained at the L-histidine and *(E)*-urocanate docking within the 1GKM_{mod} active center revealed only for the *(E)*-urocanate product the following interactions: the carboxylate moiety establishes an interaction with the Arg283 and the imidazole ring points towards the His83 amino acid residue through its *N*₃ atom.

EXPERIMENTAL SECTION

Selection of the HAL crystal structure for modification and modeling

There are six crystal structures determined for *Pseudomonas putida* histidine ammonia-lyase enzyme (Brookhaven Protein Data Bank codes: 1B8F, 1EB4, 1GK2, 1GK3, 1GKJ, 1GKM). Among the available structures the 1GKM structure was selected for computational investigation of HAL. This is the only structure which contains a ligand (L-cysteine) inside the active center and revealed a unique orientation of the side chain of Met382 amino acid within the active site compared to the other structures determined for HAL. The distance between the N atom of the amino moiety in L-cysteine and the C atom of the methylene group in MIO was 1.31 Å.

The 3CZO AvPAL crystal structure has the inner Tyr loop region (containing the essential Tyr53 amino acid) in a fully closed form. The 39-80 amino acid sequence of 1GKM HAL, which contains the important Tyr53 amino acid in a partially open loop conformation, was replaced by the corresponding homology model sequence of the 1GKM HAL based on 3CZO PAL. The resulted 1GKM_{mod} model structure seemed to be eligible for calculations within the enzymic ambience taking into account the new position of the Tyr53 amino acid in comparison with the one from the crystal structure of PpHAL within the active site (Figure 2).

Conformational analysis of the N-MIO intermediate

The initial ligand structures for the CS were built from the L-cysteine inhibitor (Cys1510) of the 1GKM crystal structure of PpHAL. Therefore, the L-cysteine of the 1GKM was replaced by L-histidine in the 1GKM_{mod} HAL structure. In the resulted starting conformation the carboxyl group of the MIO-bound L-histidine pointed towards the Arg283 residue and the imidazole

ring of the substrate occupied a relative hydrophobic part of the active site close to the His83 residue. From the resulted 1GKM_{mod} structure a region defined by a sphere of 15 Å radius around the C atom of the original L-cysteine (Cys1510) and a sphere of 12 Å radius around the O atom of a highly conserved water (W544 – close to the place where we propose the presence of the Zn²⁺ ion) was cut off for CS calculations as a closed active site model of HAL (including 146 amino acids and 43 water molecules). Next, by a HyperChem [11] standard procedure, hydrogen atoms were added to the amino acid moieties. In the starting structure, the C- and N-termini at cuttings were completed to neutral aldehyde and amino parts. The resulted overall structure and the hydrogen additions were verified and corrected [17]. From this verified raw PpHAL active site model (partially modified 1GKM crystal structure including L-histidine), only one initial active site construct involving the substrate covalently bound to MIO through the amino moiety (N-MIO model) was built. In this active site model a Zn²⁺ ion was included at a 1.9 Å distance from the N3 atom of His83 amino acid residue (as found in many Zn-containing protein structures). During CS on the covalently bound histidine and the imidazolone ring of the MIO in rigid enzymic environment (including 41 water molecules), 3 of the ligand torsion angles were varied for the N-MIO model. CS's were performed by HyperChem implemented CS module [11] using default settings (MM+ forcefield; gradient: 0.1 kcal/mol; Polak-Ribiere method; limits: 300 iterations, 150 optimizations, 15 conformations; test options: "skip if atoms are closer than 0.3 Å").

For the covalent intermediate model, the best ligand energy conformation was selected which was also in agreement with the overall arrangement (imidazole group points towards His83 and carboxylate is in the close vicinity of Arg283) found in the experimental inhibited structures of *Rhodobacter sphaeroides* RstAL.

Several N-MIO active site models were constructed by replacing the substrate-MIO part of the initial PpHAL (1GKM_{mod})/ L-histidine active site construct with the ligand arrangements resulted from the CS.

Geometry optimization and docking of L-histidine/(E)-urocanic acid in the active site model of PpHAL

In order to construct the L-histidine/(E)-urocanate ligand-containing starting structures, six different conformers resulted from the CS were used. The covalent bond (Figure 4) between the methylene group of the MIO and the amino moiety was cut in case of the substrate (indicated by the green line). The bond between the amino moiety and the carbon atom of the ligand was cut in case of the product (indicated by the blue line) and the structure was completed with the necessary olefinic bond to get (E)-urocanate.

Next, the 6×2 L-histidine/(*E*)-urocanate ligand structures were optimized within rigid enzymic environment, by the HyperChem implemented *Geometry optimization* using the default settings (MM+ forcefield; gradient: 0.1 kcal/mol; Polak-Ribiere method). From the resulted set of models, the two lowest energy substrate and product structures (ones obtained from the c12 and c14 optimizations) were used for further optimizations in which the essential parts of the active site (including the MIO-NH₂, the aromatic part of the His83, Tyr280, Tyr53, the -CH₂-CO-NH₂ part of Asn195, Asn313, Gln277, Gln413, the -CH₂-COO⁻ part of the Glu414, the -CH₂-OH part of Ser410 and the Zn²⁺ ion) were included.

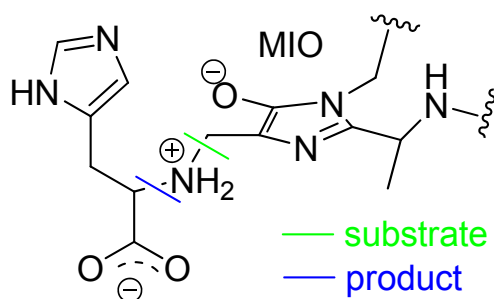


Figure 4. The bond cuts of the *N*-MIO intermediate to construct the L-histidine substrate (green) and (*E*)-urocanate product (blue) containing HAL models

The starting structures for the docking calculations were constructed from the active site model of *Pp*HAL 1GKM_{mod} structure used for CS calculations. Only 29 amino acid residues (including the essential amino acid residues like His83, Arg283, Met382, Tyr53, Tyr280, Asn195 and Glu414, determined by mutagenesis) and the MIO prosthetic electrophilic group were used as environment for the substrate/product docking. We used separate initial active site models for the substrate (4 torsion angle were selected from the substrate using flexible-rigid docking) and for the product. For the docking process of L-histidine/(*E*)-urocanic acid in the 1GKM_{mod} active site models, the AutoDock software [12, 13] was used. The Grid Parameter File was established with the default settings (Total Grid Pts per map: 77326; number of points 40 for x- and y-dimensions, 45 for z-dimension; spacing: 0.375 Å; center on ligand). The docking process of the L-histidine/(*E*)-urocanic acid in 1GKM_{mod} active site model was performed by the AutoDockTools implemented Docking module using default settings (Lamarckian Genetic Algorithm also known as a Genetic Algorithm-Local Search: 10 runs; population size: 150; maximum number of energy evaluations: short setting).

For the product-containing 1GKM_{mod} active site model, a set of the best docking energy poses were selected (Figure 3E), which were also in correspondence to the overall arrangement found for (*E*)-coumarate in wild-type *Rhodobacter sphaeroides bacterial* TAL (PDB code: 2O7B).

ACKNOWLEDGMENTS

ALS thanks the financial support of Romanian National University Research Council (CNCSIS, PNII-TD-400). PL thanks OTKA T048854 for financial support.

Supporting information available:

The coordinates of the 1GKM_{mod} structure.

REFERENCES

1. L. Poppe, J. Rétey, *Angewandte Chemie, International Edition English*, **2005**, *44*, 3668.
2. H. Morrison, C. Bernasconi, G. Pandey, *Photochemistry and Photobiology*, **1984**, *40*, 549.
3. R.G. Taylor, H.L. Levy, R.R. McInnes, *Molecular Biology and Medicine*, **1991**, *8*, 101.
4. L. Poppe, *Current Opinion in Chemical Biology*, **2001**, *5*, 512.
5. C.B. Klee, *The Journal of Biological Chemistry*, **1972**, *247*, 1398.
6. T.F. Schwede, J. Rétey, G.E. Schulz, *Biochemistry*, **1999**, *38*, 5355.
7. D. Röther, L. Poppe, S. Viergutz, B. Langer, J. Rétey, *European Journal of Biochemistry*, **2001**, *268*, 6011.
8. M. Baedeker, G.E. Schulz, *European Journal of Biochemistry*, **2002**, *269*, 1790.
9. H. Ritter, G.E. Schulz, *Plant Cell*, **2004**, *16*, 3426.
10. L. Wang, A. Gamez, et al., *Journal of Molecular Biology*, **2008**, *380*, 623.
11. HyperChem version 7.0 (Hypercube, Inc. <http://www.hyper.com/>).
12. G.M. Morris, D.S. Goodsell, et al., *Journal of Computational Chemistry*, **1998**, *19*, 1639.
13. R. Huey, G.M. Morris, et al., *Journal of Computational Chemistry*, **2007**, *28*, 1145.
14. S. Pilbák, A. Tomin, J. Rétey, L. Poppe, *The FEBS Journal*, **2006**, *273*, 1004.
15. A.L. Seff, S. Pilbák, L. Poppe, *Studia Universitatis Babeş-Bolyai, Chemia LIII*, **2008**, *2*, 67.
16. S. Bartsch, U.T. Bornscheuer, *Angewandte Chemie, International Edition English*, **2009**, *48*, 3362.
17. Molfunction, Institute of Molecular Function (<http://www.molfunction.com/>).

Dedicated to the memory of Prof. dr. Ioan Silaghi-Dumitrescu marking 60 years from his birth

CHEMICAL HARDNESS: QUANTUM OBSERVABLE?

MIHAI V. PUTZ*

ABSTRACT. The question whether chemical hardness may be regarded as ordinary quantum observable is responded in negative employing the second quantification within fermionic Fock space.

Keywords: *annihilation and creation particle operators, valence energy, electronic density, ionization and affinity energies*

INTRODUCTION

In modern quantum chemistry the chemical reactivity is conceptualized throughout specific indices, among which the chemical hardness stands a pre-eminent one, often seen as a companion of the electronegativity [1,2]. However, the phenomenological and analytical definitions of chemical hardness together with its principles, i.e. hard and soft-acids and bases HSAB and maximum hardness principles MHP, are systematically presented within the density functional theory framework and applied on paradigmatic atomic and molecular systems [3-6]. Despite this, the recent proof on the two decades question about the quantum nature of the electronegativity [7] opens the natural similar question about chemical hardness; this communication likes to offer an analytical answer in this regard.

INTRODUCING QUANTUM CHEMICAL HARDNESS

The fermionic Fock space is build by the aid of the creation and annihilation particle operators

$$\mathbf{a}^+ = |1\rangle\langle 0|, \mathbf{a} = |0\rangle\langle 1|, \quad (1)$$

such that the vacuum and uni-particle sectors cover the entire particle projection space:

* West University of Timișoara, Chemistry Department, Str. Pestalozzi No. 16, RO-300115 Timișoara, Romania, mvputz@cbq.uvt.ro

$$\mathbf{1} = |0\rangle\langle 0| + |1\rangle\langle 1| = \mathbf{a}\mathbf{a}^+ + \mathbf{a}^+\mathbf{a} = \{\mathbf{a}, \mathbf{a}^+\}, \quad (2)$$

that allows for the equivalent density normalization relationships

$$\begin{aligned} 1 &= \langle \psi_0 | \psi_0 \rangle = \langle \psi_0 | \mathbf{1} | \psi_0 \rangle = \langle \psi_0 | (\mathbf{a}\mathbf{a}^+ + \mathbf{a}^+\mathbf{a}) | \psi_0 \rangle = \langle \psi_0 | \mathbf{a}\mathbf{a}^+ | \psi_0 \rangle + \langle \psi_0 | \mathbf{a}^+\mathbf{a} | \psi_0 \rangle \\ &= |\langle 0 | \psi_0 \rangle|^2 + |\langle 1 | \psi_0 \rangle|^2 = (1 - \rho_0) + \rho_0, \quad \rho_0 \in [0, 1], \end{aligned} \quad (3)$$

for unperturbed state $|\psi_0\rangle$ with associated eigen-energy E_0 for a given atomic or molecular valence system.

In these conditions, the chemical processes of electronic exchange with environment (releasing by ionization or accepting through affinity) are modelled by the associate ionization and affinity second quantized wave-functions

$$|\psi_\lambda^I\rangle = (1 + \lambda\mathbf{a}\mathbf{a}^+)|\psi_0\rangle = |\psi_0\rangle + \lambda|0\rangle\langle 1|1\rangle\langle 0|\psi_0\rangle = |\psi_0\rangle + \lambda\sqrt{1 - \rho_0}|0\rangle, \quad (4a)$$

$$|\psi_\lambda^A\rangle = (1 + \lambda\mathbf{a}^+\mathbf{a})|\psi_0\rangle = |\psi_0\rangle + \lambda|1\rangle\langle 0|0\rangle\langle 1|\psi_0\rangle = |\psi_0\rangle + \lambda\sqrt{\rho_0}|1\rangle \quad (4b)$$

by means of the perturbation factor λ ; they enter in calculation of the perturbed energy

$$\langle E_{\lambda \in \mathbb{R}}^{I \leftrightarrow A} \rangle = \frac{\langle \psi_\lambda^I | H | \psi_\lambda^A \rangle}{\langle \psi_\lambda^I | \psi_\lambda^A \rangle} \quad (5)$$

and electronic density

$$\rho_{\lambda \in \mathbb{R}}^{I \leftrightarrow A} = \frac{\langle \psi_\lambda^I | \mathbf{a}^+\mathbf{a} | \psi_\lambda^A \rangle}{\langle \psi_\lambda^I | \psi_\lambda^A \rangle} \quad (6)$$

that finally provide the chemical hardness realization as

$$\eta_\lambda = \frac{1}{2} \frac{\partial^2 \langle E_\lambda \rangle}{\partial \rho_\lambda^2} \quad (7)$$

By considering the basic chain-derivation rule

$$\frac{\partial \bullet}{\partial \rho_\lambda} = \frac{\partial \bullet}{\partial \lambda} \cdot \frac{\partial \lambda}{\partial \rho_\lambda} \quad (8)$$

chemical hardness of Eq. (7) unfolds as

$$\eta_\lambda = \frac{1}{2} \left\{ \left[\frac{\partial}{\partial \lambda} \left(\frac{\partial \langle E_\lambda \rangle}{\partial \lambda} \right) \right] \frac{\partial \lambda}{\partial \rho_\lambda} + \frac{\partial \langle E_\lambda \rangle}{\partial \lambda} \left[\frac{\partial}{\partial \lambda} \left(\frac{\partial \lambda}{\partial \rho_\lambda} \right) \right] \right\} \frac{\partial \lambda}{\partial \rho_\lambda} \quad (9)$$

to be in next evaluated.

QUANTUM VALUES OF CHEMICAL HARDNESS

Equation (9) may be further expressed by employing the inverse density and energy gradients respecting the chemical perturbation factor λ , see Ref. [7]:

$$\frac{\partial \lambda}{\partial \rho_\lambda} = \frac{(1 + \lambda \rho_0)^2}{\rho_0 (1 - \rho_0)}, \quad (10a)$$

$$\frac{\partial \langle E_\lambda \rangle}{\partial \lambda} = E_0 \frac{1 - \rho_0}{(1 + \lambda \rho_0)^2} \quad (10b)$$

toward the second order perturbation terms

$$\frac{\partial}{\partial \lambda} \left(\frac{\partial \lambda}{\partial \rho_\lambda} \right) = 2 \frac{1 + \lambda \rho_0}{1 - \rho_0}, \quad (11a)$$

$$\frac{\partial}{\partial \lambda} \left(\frac{\partial \langle E_\lambda \rangle}{\partial \lambda} \right) = -2 E_0 \rho_0 \frac{1 - \rho_0}{(1 + \lambda \rho_0)^3} \quad (11b)$$

leading with the chemical hardness limits

$$\eta_\lambda = 0 \cdot E_0 \frac{1 + \lambda \rho_0}{\rho_0 (1 - \rho_0)} = \begin{cases} 0, & \rho_0 \in (0,1) \\ 0 \cdot \infty = ?, & \rho_0 \rightarrow 0 \\ 0 \cdot \infty = ?, & \rho_0 \rightarrow 1 \end{cases} \quad (12)$$

The results of Eq. (12) give the answer that the chemical hardness is *not* an observable, having neither a *non-zero* nor a *definite* value for any electronic density realization or limit, respectively. Such a behavior is somehow explained by the energetic nature of chemical hardness usually associated with the HOMO-LUMO gap for a molecular system, i.e. with an energy interval (or energy difference) rather than with an eigen-energy (or an energy level) of a spectrum.

However, the result (12) does not exclude the “real”, even as “hidden” or dispersed, values of chemical hardness: for the fractional occupied states – the first upper branch of Eq. (12) – are assessed to the open states of

chemical bonding, while the empty or fully occupied valence states – the middle and lower branches of Eq. (12) – are described by the not definite (in eigen-value sense) of chemical hardness, since is uncertain it will allow fully engagement or inert chemical response in reactivity and bonding, respectively.

CONCLUSIONS

In modeling of chemical reactivity by means of electronegativity and chemical hardness, there was proofed that while electronegativity may be assumed as a quantum observable with an eigen-value equating the chemical potential [7], the chemical hardness, although as driving the chemical force in bonding through the electronegativity change with engaged charge change of a given (valence) system [2], cannot be associated with a non-zero or a definite energetic value for fractional or fully empty/filled electronic states in interacting states. However, the hidden quantum nature of chemical hardness may be appropriately fitted with the non-locality electronic measures of chemical bond accompanying any localized charge in bonding, being thus susceptible to be further considered in elucidation of aromaticity chemical concept, for instance. Yet, related studies in the second quantization framework are expected to be very fruitful in elucidating quantum aspects of chemical reactivity and bonding and will be addressed in the years to come and in subsequent communications.

REFERENCES

1. M. V. Putz, "Absolute and Chemical Electronegativity and Hardness", Nova Publishers Inc., New York, **2008**.
2. M. V. Putz, *International Journal of Molecular Sciences*, **2008**, 9, 1050.
3. M. V. Putz, *MATCH Communication in Mathematical and in Computer Chemistry*, **2008**, 60, 845.
4. M. V. Putz, N. Russo, E. Sicilia, *Journal of Computational Chemistry*, **2004**, 25, 994.
5. M. V. Putz, *Journal of Theoretical and Computational Chemistry*, **2007**, 6, 33.
6. M. V. Putz, *International Journal of Quantum Chemistry*, **2006**, 106, 361.
7. M. V. Putz, *International Journal of Quantum Chemistry*, **2009**, 109, 733.

Dedicated to the memory of Prof. dr. Ioan Silaghi-Dumitrescu marking 60 years from his birth

MATHEMATICAL MODELING AND SIMULATION OF COAL CO-GASIFICATION WITH WASTE/BIO MASS IN AN ENTRAINED-FLOW GASIFIER

VICTORIA MAXIM^a, CĂLIN-CRISTIAN CORMOȘ^a,
PAUL ȘERBAN AGACHI^a

ABSTRACT. The aim of this paper is to evaluate the ways to use coal alone or in addition with biomass (sawdust, agricultural wastes etc.) or solid waste (animal residue, municipal solid wastes, waste paper etc.) through co-gasification to supply syngas for energy vectors poly generation in an Integrated Gasification Combined Cycle (IGCC) with Carbon Capture and Storage (CCS).

This paper analyses various cases of blending coal with different renewable energy sources by means of mathematical modeling and simulation of the gasification process using the process flow modeling software ChemCAD.

The effect of varying the feedstock and the effect of varying the blending ratio coal vs. alternative fuel on the cold gas efficiency and hydrogen production potential is studied for the gasifier performance optimization.

Keywords: *Co-gasification, Coal, Renewable energy sources, Solid wastes, Mathematical modelling and simulation*

INTRODUCTION

The climate change and the reduction of greenhouse emissions are very important and actual in the context of modern society. There are many greenhouse gases sources: transport, agriculture, power generation plants, industry etc., but the larger contributor is the power generation field, with a percentage around 24% of all greenhouse gases emissions and is set to grow by 2030 around 40% [1]. Coal accounts for around one-third of the EU's electricity production and its utilization is regarded with concern because of the larger greenhouse emissions compared with other fossil fuels (e.g. natural gas and oil).

^a *Universitatea Babeș-Bolyai, Facultatea de Chimie și Inginerie Chimică, Str. Kogălniceanu Nr. 1, RO-400084 Cluj-Napoca, Romania,
Emails: vgoaia@chem.ubbcluj.ro, cormos@chem.ubbcluj.ro, sagachi@staff.ubbcluj.ro*

The most powerful greenhouse gas is the carbon dioxide CO₂ which is produced by the transportation, industrial and energy generating sectors. In order to prevent the increasing trend of greenhouse gas emissions the carbon capture and storage technology was developed. The carbon capture and storage (CCS) is a way of mitigating the contribution of fossil fuel emission to global warming. This is based on capturing the carbon dioxide and storing it away either in deep geological formations, in deep ocean masses, or in the form of mineral carbonates [2, 3].

In close co-operation with industries and Member States, the EU government presently supports the development of CCS (Carbon Capture and Storage) technologies in coal-fired power plants [4]. The aim is to make zero emission power generation plants using CCS commercially feasible by 2020 [1,4].

Gasification of solid fuels is a process which converts the solid feedstock by partial oxidation with oxygen and steam into syngas. The syngas can be used in a large number of applications as: power generation, manufacture of various chemicals and fuels (e.g.. hydrogen, methanol, ammonia, fertilizers etc.). The gasifiers may be designed for wide variety of solid feedstock: fossil fuels (e.g. coal, lignite peat etc.), various biomass types (sawdust, agricultural wastes etc.) and solid waste (e.g. animal residue, municipal solid wastes, waste paper etc.). The chemical composition of syngas varies based on many factors: coal composition, size and rank, feeding system (dry or slurry), gasification agent used for oxidation (air or oxygen), temperature, pressure, residence time in the gasifier, heating rate, gasification island configuration, etc. [5,6].

The conventional Integrated Gasification Combined Cycle (IGCC) is a concept regarding the conversion of solid fuels into syngas, meaning that a mixture of carbon monoxide and hydrogen, which after ash removal and desulphurization is burned in a conventional Combined Cycle Gas Turbine (CCGT) to generate electrical power. A unit can be considered capture-ready if, at some point in the future, it can be retrofitted for CO₂ capture and sequestration and still be economical to operate [7]. IGCC is a carbon capture ready technology. The design for a modified IGCC scheme for poly-generation of electricity and hydrogen with CCS is presented in Figure1.

The core of the IGCC technology is the gasification process of a solid fuel either fossil fuels alone or in addition with various biomass types and solid waste having energetically value. The IGCC is one of the power generation technologies having the highest potential to capture CO₂ with the lowest penalties in energy efficiency and cost. The IGCC technology is very attractive for energy vectors poly-generation: electricity, hydrogen, heat and chemicals [8, 9].

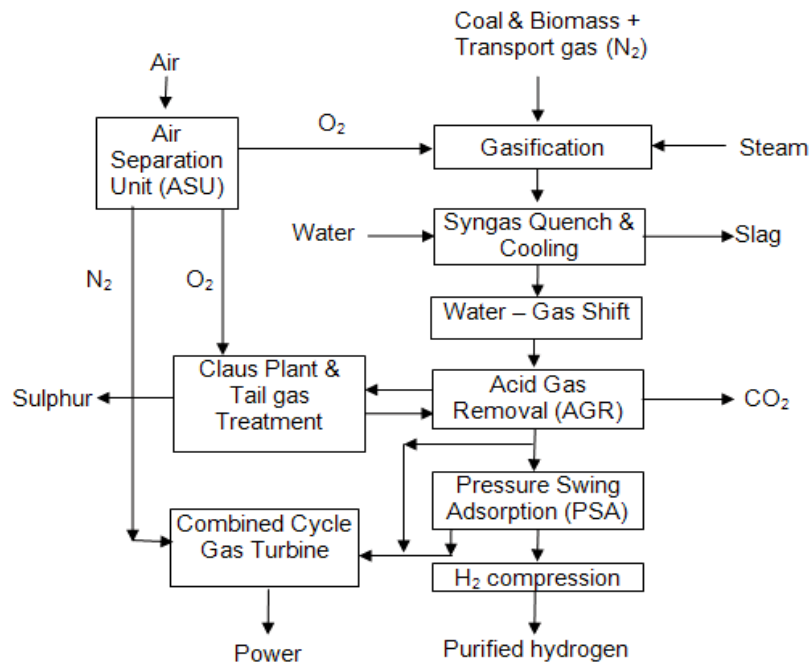


Figure 1. The IGCC scheme modified for poly-generation of electricity and hydrogen with carbon capture and storage (CCS)

The next section of this paper presents the gasifier concept, the feedstock characteristics and the modeling and simulation of gasification process. The co-gasification of coal alone or in addition with biomass (sawdust, agricultural wastes) or solid waste (animal residue, municipal solid wastes, waste paper) will be analyzed by mathematical modeling and simulation using the process flow modeling software ChemCAD. The most appropriate mixture will be chosen by analyzing the syngas composition, Cold Gas Efficiency (CGE) and the hydrogen production potential. The behavior of co-gasification of coal with various sorts of biomass or solid wastes will be studied by varying the blending ratio.

RESULTS AND DISCUSSION

The main system component of the gasification process is the gasifier. It is a pressure vessel in which a fuel (coal or biomass/waste) together with air (or oxygen) and water are heated to high temperatures, above 900°C, to produce syngas (mainly a mixture of hydrogen and carbon monoxide). The syngas after cleaning is used to generate electricity in a gas turbine [10].

The gasification reactors can be grouped in one of the three main categories: moving-bed gasifiers, fluidised-bed gasifiers, and entrained-flow gasifiers. The characteristics of these reactors can be found in the literature [6,11].

Based on several criteria such as: oxygen purity, gasifier throughputs, reliability and experience, cold gas efficiency (CGE), carbon conversion efficiency (CCE), syngas cooling options, influence of oxygen purity and gasifier feed system for hydrogen purification step, hydrogen production potential, capital cost etc., from the large range of gasifiers, as the most promising reactor for energy vectors poly-generation (mainly hydrogen and electricity) with Carbon Capture and Storage, a Shell gasifier has been chosen.

Table 1. Design assumptions for Shell gasifier

| Parameters | Shell gasifier |
|------------------------|-----------------------|
| Maximum pressure (bar) | 40 |
| Temperature (°C) | 1400-1600 |
| Carbon conversion (%) | >99 |

The Shell gasifier is a carbon steel vessel that contains a gasification chamber enclosed by a non-refractory membrane wall, which operates at 30-40 bar pressure, temperature range of 1500-1600°C, dry feed and one stage. The pulverized coal is stored under nitrogen, where it is pressurized and then pneumatically transported into the gasifier. The syngas is quenched with cooled recycled product gas and further cooled in a syngas cooler. Raw gas is cleaned in ceramic filters. A Shell gasifier configuration is shown in Figure 2. The image represents a dry-feed, pressurized, entrained-flow, slagging gasifier which can be operated on a wide variety of feedstocks [12].

The Shell gasifier used for the coal co-gasification with waste/biomass considered was the Gibbs Free Energy Reactor (GIBS). The Gibbs reactor model uses an equilibrium model based on equilibrium constants. Product rates, compositions, and thermal conditions are calculated by the minimization of Gibbs free energy. This method has to define the specific chemical reactions used in the calculation [13].

The gasifier is operating at high temperatures with a high fuel conversion. Other gasifier design assumptions are: pressure drop 1 bar, operating pressure 40 bar and heat duty -22990 MJ/h.

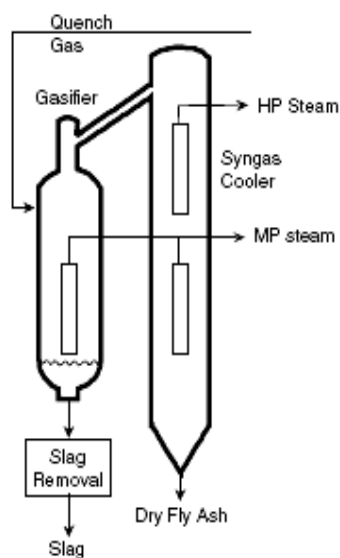


Figure 2. Schematic diagram of Shell gasifier

Figure 3 represents the flowsheet for a Shell gasification block mathematically modeled and simulated using ChemCAD software.

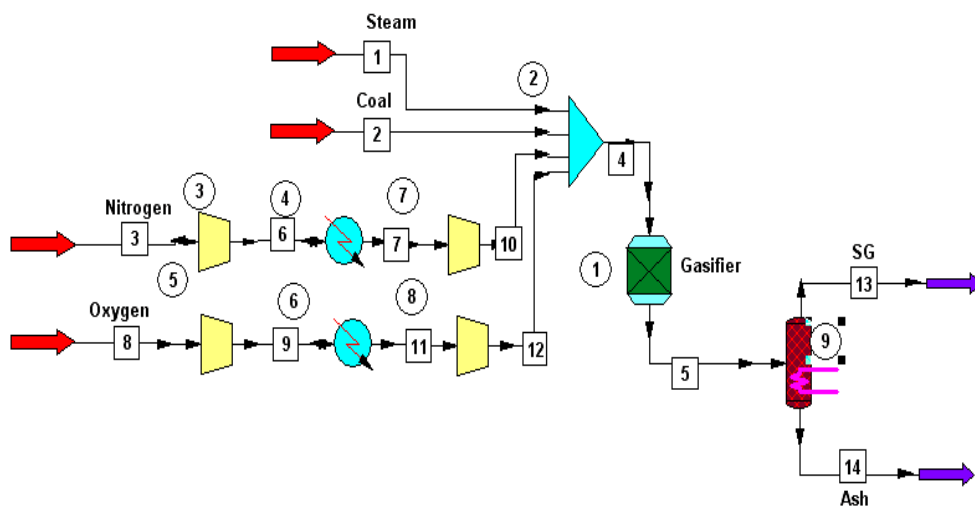


Figure 3. The Shell gasification diagram

Feedstocks

Coal is mainly the result of slow anaerobic transformation of biomass (wood, vegetation etc.) over millions of years. Coal is often classified in terms of its rank, which is determined by the degree of this anaerobic transformation from brown coal to anthracite [6, 14].

The most important biomass fuel is wood, but the trees are too valuable to be burned, instead residues from the woodworking industries as sawdust, could be a very valuable feedstock. Another biomass fuels are the agricultural residues such as: wheat straw, corn stalks, husks from rice, coconuts etc. Different solid wastes, such as: municipal solid wastes, waste paper, sewage, animal residues, can be used as feedstock to a gasification process as well.

For the gasification process the proximate analysis (fixed carbon, volatile matter, moisture, ash), the ultimate analysis (elemental, apart from ash) and ash composition must be known prior evaluation. These fuel characteristics mainly determine the key performance indicators of the gasification process (e.g. cold gas efficiency, oxygen and steam consumptions, hydrogen production potential etc.)

Case studies

This paper analyses eight different case studies of coal blending with different renewable energy sources, which use the same configuration for the gasification process, as follows:

- Case 1 - coal alone used as feedstock;
- Case 2 – coal in addition with sawdust (SWD) blending ratio 80/20% wt.;
- Case 3 – coal in addition with wheat straw (WS) blending ratio 80/20% wt.;
- Case 4 – coal in addition with corn stalks (CS) blending ratio 80/20% wt.;
- Case 5 – coal in addition with municipal solid wastes (MSW) blending ratio 80/20% wt.;
- Case 6 – coal in addition with waste paper (WP) blending ratio 80/20% wt.;
- Case 7 – coal in addition with sewage sludge (SWG) blending ratio 80/20% wt.;
- Case 8 – coal in addition with meat and bone meal (MBM) blending ratio 80/20% wt.

The fuel characteristics are presented in Table 2 [15].

Table 2. Fuel characteristics

| Parameter | Coal | SWD | WS | CS | MSW | WP | SWG | MBM |
|-------------------------------------|--------|--------|--------|--------|--------|--------|--------|--------|
| Proximate analysis (% wt) | | | | | | | | |
| Moisture (a.r.) | 8.10 | 10.00 | 10.00 | 8.00 | 10.00 | 6.00 | 10.00 | 1.90 |
| Volatile matter (dry) | 28.51 | 80.05 | 69.94 | 73.40 | 72.70 | 82.50 | 54.50 | 73.40 |
| Ash | 14.19 | 0.98 | 14.48 | 7.00 | 13.90 | 8.21 | 37.56 | 18.80 |
| Ultimate analysis (% wt dry) | | | | | | | | |
| Carbon | 72.04 | 49.20 | 41.11 | 44.80 | 41.20 | 49.25 | 36.19 | 46.20 |
| Hydrogen | 4.08 | 5.99 | 5.20 | 5.39 | 5.50 | 6.97 | 4.46 | 6.70 |
| Nitrogen | 1.67 | 0.82 | 1.01 | 0.85 | 0.50 | 0.34 | 5.63 | 9.70 |
| Oxygen | 7.36 | 42.98 | 37.36 | 41.75 | 38.70 | 35.00 | 15.00 | 17.07 |
| Sulphur | 0.65 | 0.03 | 0.24 | 0.21 | 0.20 | 0.20 | 1.06 | 0.65 |
| Chlorine | 0.01 | 0.00 | 0.60 | 0.00 | 0.00 | 0.03 | 0.10 | 0.88 |
| Ash | 14.19 | 0.98 | 14.48 | 7.00 | 13.90 | 8.21 | 37.56 | 18.80 |
| Calorific value (MJ/kg dry) | | | | | | | | |
| HHV – Gross | 28.704 | 19.436 | 16.091 | 17.206 | 16.425 | 21.664 | 15.264 | 21.163 |
| LHV – Net | 27.803 | 18.113 | 14.943 | 16.016 | 15.211 | 20.125 | 14.279 | 19.683 |
| Ash composition (%wt) | | | | | | | | |
| SiO ₂ | 52.20 | 9.44 | 54.64 | 63.30 | 52.45 | 19.44 | 39.80 | 0.00 |
| Al ₂ O ₃ | 27.30 | 1.56 | 5.73 | 0.00 | 16.21 | 63.97 | 11.70 | 0.00 |
| Fe ₂ O ₃ | 5.10 | 1.88 | 6.16 | 4.70 | 7.17 | 0.42 | 14.20 | 2.90 |
| CaO | 6.40 | 62.00 | 5.02 | 0.60 | 16.92 | 8.37 | 8.00 | 66.28 |
| MgO | 2.10 | 2.18 | 2.45 | 4.80 | 0.00 | 1.68 | 0.00 | 0.00 |
| TiO ₂ | 1.50 | 0.10 | 0.23 | 0.00 | 0.00 | 3.81 | 0.00 | 0.00 |
| K ₂ O | 1.00 | 15.00 | 14.09 | 8.40 | 0.00 | 0.23 | 0.80 | 13.00 |
| Na ₂ O | 0.30 | 0.61 | 2.16 | 0.50 | 7.25 | 0.83 | 0.60 | 17.82 |
| SO ₃ | 2.40 | 2.72 | 3.03 | 7.20 | 0.00 | 1.14 | 0.00 | 0.00 |
| P ₂ O ₅ | 1.30 | 1.23 | 2.43 | 2.10 | 0.00 | 0.10 | 0.00 | 0.00 |
| SrO | 0.00 | 0.15 | 0.00 | 0.00 | 0.00 | 0.00 | 0.00 | 0.00 |

The effects of coal blending with renewable energy sources (wood, agricultural wastes etc.) or alternative fuels (various wastes) are analyzed using the following key gasification process parameters[6,16]:

- **Cold gas efficiency (CGE):** is desirable that this indicator to be as high as possible on condition that hydrocarbons (mainly methane) present in syngas must be as low as possible (hydrocarbons negative influence the carbon capture plant capabilities). CGE represents the energy efficiency of the gasification process and it is defined as follow:

$$CGE = \frac{\text{Syngas thermal energy [MW]}}{\text{Feedstock thermal energy [MW]}} * 100 \quad (1)$$

- **Hydrogen production potential:** similar to CGE, it is defined as the sum of carbon monoxide and hydrogen content in the syngas and it must be as high as possible. It gives a better idea of how much of the thermal energy of coal can be converted into hydrogen and it is calculated with the formula:

$$\text{Hydrogen production potential} = \frac{\text{CO and H}_2 \text{ thermal energy [MW]}}{\text{Feedstock thermal energy [MW]}} * 100 \quad (2)$$

All the cases from 1 to 8 were simulated using the process flow modelling software ChemCAD. Table 3 presents the results of blending coal with renewable energy sources and solid wastes.

On the basis of the Cold Gas Efficiency (CGE) and the hydrogen production potential the following four cases have the highest efficiencies: Case 1 (coal alone), Case 2 (coal in addition with sawdust), Case 6 (coal in addition with waste paper) and Case 8 (coal in addition with meat and bone meal).

For Case 8 must be mentioned that the cold gas efficiency is higher on behalf of the good thermal properties of the alternative fuel used - MBM (high calorific value and carbon content, low moisture content), the relatively high methane content in the syngas compared with other cases. Figure 4 present the changes in the Cold Gas Efficiency for the considered case studies.

Table 3. The performance indicators

| | UM | Case 1 | Case 2 | Case 3 | Case 4 | Case 5 | Case 6 | Case 7 | Case 8 |
|--------------------------------|------------------|--------------------|---------|---------|---------|---------|---------|---------|---------|
| Solid fuel flowrate | t/h | | | | 165.4 | | | | |
| Solid fuel energy | MW _{th} | 1164.7 | 1079.29 | 1053.08 | 1061.95 | 1055.29 | 1095.94 | 1047.59 | 1092.29 |
| Steam/fuel | | 0.072 | 0.036 | 0.036 | 0.036 | 0.036 | 0.036 | 0.036 | 0.091 |
| O2/fuel | | 0.848 | 0.788 | 0.788 | 0.788 | 0.776 | 0.788 | 0.788 | 0.727 |
| N2/Fuel | | | | | 0.09 | | | | |
| Syngas flowrate | t/h | 310.94 | 299.02 | 294.61 | 292.5 | 288.15 | 291.83 | 283.08 | 285.04 |
| | | Syngas composition | | | | | | | |
| CO | % vol | 59.79 | 57.39 | 56.88 | 57.88 | 57.41 | 58.23 | 57.91 | 60.00 |
| H ₂ | % vol | 25.42 | 24.5 | 23.86 | 24.16 | 24.89 | 26.41 | 25.13 | 29.88 |
| CH ₄ | % vol | 0 | 0 | 0 | 0 | 0 | 0 | 0 | 0.06 |
| H ₂ S | % vol | 0.19 | 0.16 | 0.17 | 0.17 | 0.17 | 0.17 | 0.23 | 0.22 |
| H ₂ O | % vol | 5.2 | 6.29 | 8.11 | 7.90 | 7.65 | 6.54 | 6.73 | 4.28 |
| Ar | % vol | 0.9 | 0.81 | 0.90 | 0 | 0 | 0 | 0 | 0.62 |
| Others | % vol | 8.5 | 10.85 | 10.08 | 8.99 | 9.88 | 8.65 | 10.00 | 4.94 |
| Syngas energy | MW _{th} | 928.41 | 850.9 | 820.13 | 833.89 | 829.96 | 880.63 | 824.79 | 940.95 |
| CGE | % | 79.71 | 78.84 | 77.88 | 78.52 | 78.65 | 80.35 | 78.73 | 86.14 |
| CO + H ₂ energy | MW _{th} | 924.46 | 847.73 | 816.84 | 830.59 | 826.68 | 877.25 | 820.43 | 935.45 |
| H ₂ prod. potential | % | 79.37 | 78.54 | 77.57 | 78.21 | 78.34 | 80.05 | 78.32 | 85.64 |

As can be noticed in Figure 4, the Cold Gas Efficiency increases with the increase of the carbon percent in the feedstock. Case 2 (coal in addition with sawdust), Case 6 (coal in addition with waste paper) and Case 8 (coal in addition with meat and bone meal) have a higher carbon percent, hence a higher Cold Gas Efficiency.

Analyzing the syngas composition, the Cold Gas Efficiency (CGE) and the hydrogen production potential can be noticed that Case 8 is the most appropriate mixture, which could contribute to the reduction of fossil fuels dependency and CO₂ emissions. As a result, Case 8 was chosen for a further case study: the effect of varying the blending ratio of coal with MBM on the cold gas efficiency and syngas composition.

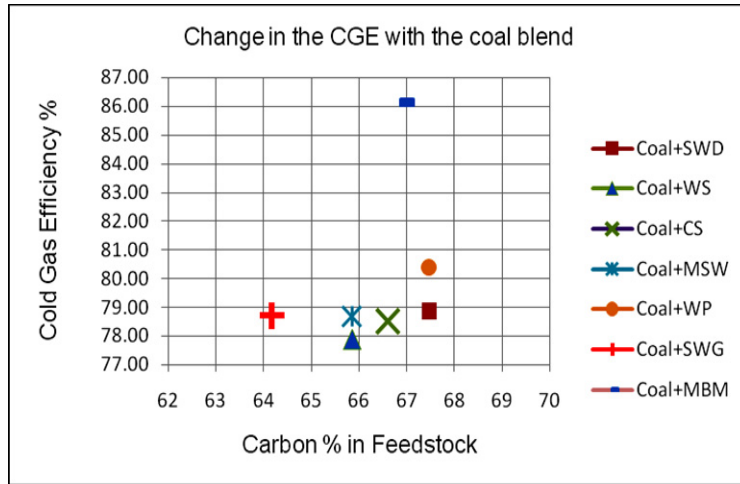


Figure 4. Changes in the CGE with the coal blend options

The blending ratio was varied from 0.1 to 0.5 (wt./wt. ratio on as received basis) and is defined by the following equation [17]:

$$\text{Blending ratio} = \frac{\text{Biomass feed rate [Kg / h]}}{\text{Total feed rate [Kg / h]}} \quad (3)$$

Figure 5 shows the change in the syngas composition with the blending ratio for Case 8 (coal in addition with meat and bone meal). With the increasing of blending ratio, the CO composition decreased from 59.79% to 52.51% and the H₂ composition increased from 25.42% to 34.84% (all syngas composition figures are expressed in molar percentages).

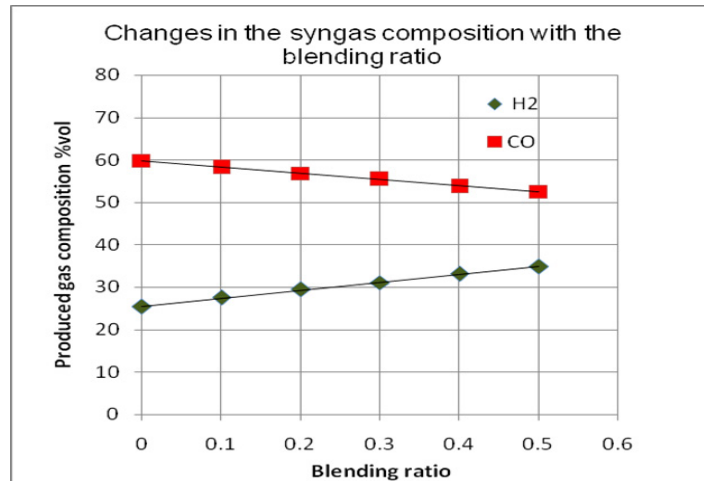


Figure 5. Change in the syngas composition with the blending ratio for Case 8

Figure 6 shows the change in the cold gas efficiency with the blending ratio for Case 8 (coal in addition with meat and bone meal), with the increasing of biomass ratio, cold gas efficiency increases from 79.71% to 90.35%.

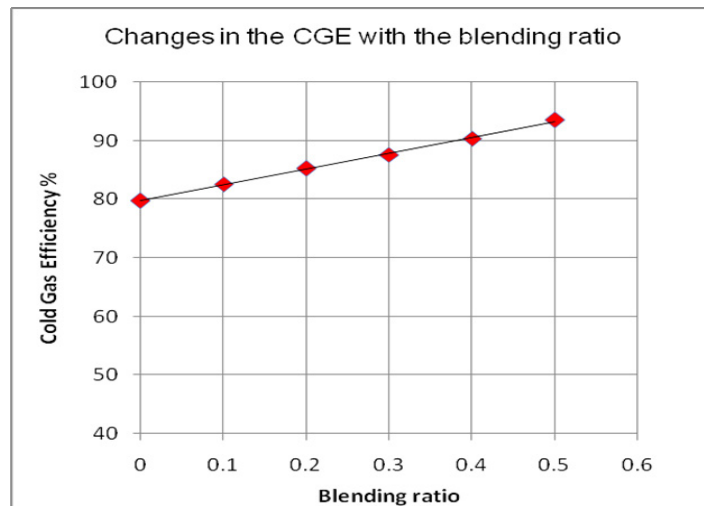


Figure 6. Change in the CGE with the blending ratio for Case 8

The results also indicate that blending coal with biomass or waste, besides the environmental benefits (conservation of fossil fuel resources and reduced CO₂ emissions with 3.58% to 17.93%, depending of the blending ratio) could provide a higher cold gas efficiency and hydrogen production potential.

CONCLUSIONS

The aim of this paper was to evaluate the coal co-gasification with various alternative and renewable solid fuels like wastes (animal residue, municipal solid wastes, waste paper etc.) or biomass (sawdust, agricultural wastes etc.) to supply syngas for energy vectors poly generation in an Integrated Gasification Combined Cycle (IGCC) with Carbon Capture and Storage (CCS).

In this paper was presented a study of the effect of varying different blends of feedstock (coal alone or in addition with biomass or solid waste) on the cold gas efficiency and hydrogen production potential in a entrained-flow gasifier (Shell technology was chosen based on best performances compared with other entrained-flow gasifiers). The best performances of the gasifier have been obtained for the following blends: coal in addition with meat and bone meal (MBM), coal in addition with waste paper and coal in addition with sawdust.

The technology of co-gasification of coal with renewable energy sources as waste and biomass can result in a very clean power plants using a wide range of feedstock. The use of renewable energy sources has real and tangible environmental benefits such as: the conservation of fossil fuel resources and the reduction of the CO₂ emissions with 3.58% to 17.93%, depending of the blending ratio used.

ACKNOWLEDGMENTS

The authors wish to thank for the financial support provided from the programs: (i) Investing in people! PhD scholarship, Project co-financed by the Sectoral Operational Programme Human Resources Development Contract POSDRU 6/1.5/S/3 – „Doctoral studies: through science towards society" and (ii) Romanian National University Research Council (CNCSIS) through grant no. 2455: "Innovative systems for poly-generation of energy vectors with carbon dioxide capture and storage based on co-gasification processes of coal and renewable energy sources (biomass) or solid waste".

REFERENCES

1. European Commission, <http://ec.europa.eu/energy>
2. M. M. Maroto-Valer, C. Song, Y. Soong, "Environmental Challenges and Greenhouse Gas Control for Fossil Fuel Utilization in the 21st Century", Kluwer Academic/Plenum, **2002**

3. S. Lombardi, L.K. Altunina, S.E. Beaubien, "Advances in the Geological Storage of Carbon Dioxide International Approaches to Reduce Anthropogenic Greenhouse Gas Emissions", Springer, **2006**
4. Statistical Review of World Energy BP, www.bp.com
5. A.G. Collot, *International Journal of Coal Geology*, **2006**, 65, 191
6. C. Higman, M. Van Der Burgt, **2008**, "Gasification", Elsevier Science, Second edition
7. Massachusetts Institute of Technology, "The future of coal an interdisciplinary study", **2007**
8. E. Tzimas, A. Mercier, C.C. Cormos, S. Peteves, *Energy Policy*, **2007**, 35, 3991
9. C. C. Cormos, *Studia Universitatis Babeș-Bolyai, Chemia*, **2009**, LIV, 1, 81
10. National Energy Technology Laboratory, <http://www.netl.doe.gov/>
11. C.C. Cormos, "Decarbonizarea combustibililor fosili solizi prin gazeificare", Cluj University Press, **2008**
12. B. G. Miller, "Coal Energy Systems", Elsevier Academic Press, **2005**, chapter 5
13. Z.A. Zainal, R. Ali, C.H. Lean, K.N. Seetharamu, *Energy Convers Manage* **2001**, 42:1499
14. M. L. de Souza-Santos, "Solid Fuels Combustion and Gasification Modeling, Simulation, and Equipment Operation", Marcel Dekker Inc, New York, **2005**, chapter 2
15. Energy Research Centre of the Netherlands, **2010**, www.ecn.nl
16. J.C. Meerman, A.P.Faaij, W.C. Turkenburg, *Energy Procedia*, **2009**, 1, 4241
17. K. Kumabe, T. Hanaoka, S. Fujimoto, T. Minowa, K. Sakanishi, *Fuel*, **2007**, 86, 684

Dedicated to the memory of Prof. dr. Ioan Silaghi-Dumitrescu marking 60 years from his birth

COMPUTATIONAL ANALYSIS OF BONDING IN PhIO AND RELATED 'HYPERVALENT' IODINE COMPLEXES

RADU SILAGHI-DUMITRESCU^a

ABSTRACT. Iodosylbenzene (iodosobenzene, PhIO) is a known oxygen atom transfer agent with interesting bioinorganic applications (e.g., formation of high-valent iron species), and is regarded as a representative member of a class of hypervalent iodine complexes. Iodine-oxygen bonding is analyzed in this and related complexes, based on molecular orbitals and Mulliken population analyses obtained from density functional theory (DFT) calculations. All data is seen to be straightforwardly interpretable in terms of a sigma dative bond between neutral iodine and oxygen units, as opposed to any alternative explanations involving iodine d-orbitals or hypervalence at the iodine.

Keywords: hypervalence, iodosylbenzene, density functional, iodine

INTRODUCTION

Iodosylbenzene (iodosobenzene, PhIO) is a known oxygen atom transfer agent with interesting bioinorganic applications, especially in formation of high-valent iron species with heme proteins/enzymes (e.g., peroxidases, cytochromes P450) and their models.[1-5] PhIO is regarded as a representative member of a class of hypervalent iodine complexes;[2] the term 'hypervalence' is rigorously defined as a situation where the number of valence electrons formally assignable to an atom exceeds the number of electrons that can be nominally accommodated within its valence shell. In particular, for iodine as well as for other main-group elements, 'hypervalence' would mean the presence of more than eight electrons within the valence shell. PhIO is often represented as Ph-I=O,[2] a formulation which clearly breaks the octet rule at the iodine. To avoid the apparent physical non-sense of breaking the octet rule, an alternative explanation has previously been proposed involving participation of the d-orbitals. In most cases however, it is advocated that X→O formulations be used instead of X=O. Nevertheless, the Ph-I=O notation is still widely used[2] and a clear formulation of the electronic structure of

^a *Universitatea Babeș-Bolyai, Facultatea de Chimie și Inginerie Chimică, Str. Kogălniceanu, Nr. 1, RO-400084 Cluj-Napoca, Romania, rsilaghi@chem.ubbcluj.ro*

this compound would be useful, among others, in establishing reaction mechanisms and electronic structures in bioinorganic problems of general applicability.

Here, the iodine-oxygen bonding is analyzed in PhIO and related complexes, based on molecular orbitals and Mulliken population analyses obtained from density functional theory (DFT) calculations. All data is seen to be straightforwardly interpretable in terms of a sigma dative bond between neutral iodine and oxygen units, as opposed to any alternative explanations involving iodine d-orbitals or hypervalence at the iodine.

RESULTS AND DISCUSSION

Figure 1 shows relevant frontier molecular orbitals computed for PhIO employing DFT procedures (full geometry optimization with BP86/6-31G**, a standard approach for bioinorganic centers for which these results shall be relevant, as detailed in Refs.[6-9]). The C-I-O angle is computed to be 106° , indicative of an sp^3 -type spatial arrangement of the orbitals at the iodine. LUMO and HOMO-7 clearly illustrate a single σ bond between I and O. HOMO-4 and HOMO also clearly illustrate no net π interaction between the two elements. The 'pseudo- σ ' (or, two-electron three-center) interaction (HOMO-5 and HOMO-1) also offers no net bonding. Thus, the I-O bond has a clean σ character, and the bond order is 1.

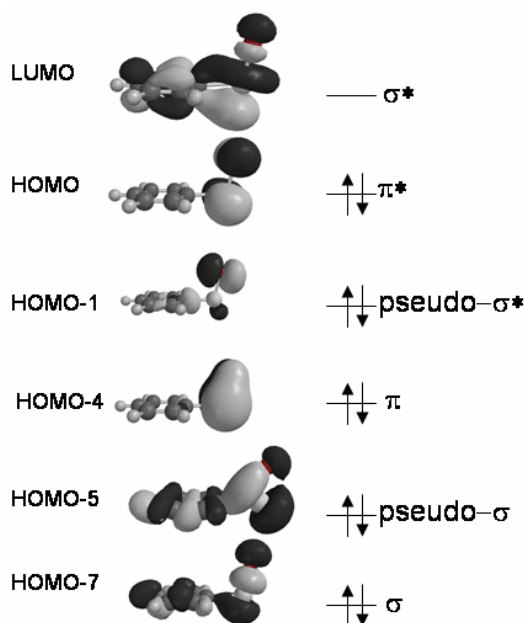


Figure 1. Bonding and anti-bonding orbitals for the I-O bond in PhIO.

The Mulliken population analysis shows that the oxygen atom in Figure 1 formally contains two electrons in each of its 2s, 2p_x and 2 p_y orbitals (assuming the z-axis to be along the I-O bond), with occupancies of 1.96, 1.61, and 1.87, respectively. In addition to these six electrons, the oxygen 2p_z orbital contains 1.17 electrons (equally distributed between the spin-up and spin-down orbitals). This data can be taken as indication of dative bonding between neutral PhI and an oxygen atom, PhI:→O; within this dative bond, the electrons are almost equally shared between the iodine and the oxygen, as illustrated in Figure 1 and by the -0.60 partial atomic charge on the oxygen atom. Gradual elongation of the I-O bond from the equilibrium length of 1.90 Å to 2.50 Å led to a gradual decrease in partial atomic charge on the oxygen, from -0.60 to -0.49; an *increase* would have been expected if the oxygen in PhIO was formally charged, O²⁻ or O⁻ - although one can also simply interpret these changes as evidence that heterolytic cleavage of the bond to generate an oxo moiety is not favoured. Such electronic structure description is completely consistent with the ability of PhIO to function as oxygen *atom* donor.

A similar situation is seen in the simpler aliphatic analogue, CH₃IO. The oxygen atom features a partial atomic charge of -0.61, and the orbital picture (not shown) is similar to that of Figure 1.

In the related CH₃I(OH)₂ species, the oxygen atoms feature partial atomic charges of -0.62 and -0.63, respectively, i.e. very similar to the oxygen atom in CH₃IO and in turn very similar to the water oxygen. CH₃I(OH)₂ formally results from CH₃I and two neutral hydroxyl radicals, HO, as opposed to CH₃IO resulting formally from CH₃I and a neutral oxygen atom. As the CH₃I iodine already has a formally closed-shell configuration, it can only engage in dative bonding. With a 2s² 2p⁴ oxygen atom, such dative bonding is straightforward, as the oxygen can engage with an empty p orbital. On the other hand, with a hydroxyl radical-type oxygen (2s² 2p⁵), the I-O bond will contain one extra electron; in CH₃I(OH)₂, there will be a total of two extra electrons in the I-O σ systems, leading to a formal bond order of 0.5, and an expectedly longer I-O distance compared to CH₃IO. Indeed, the I-OH distances in CH₃I(OH)₂ are 2.16 Å and 2.17 Å, respectively, as opposed to 1.90 Å in CH₃IO. These two extra electrons in the σ system of CH₃I(OH)₂ also explain why although iodine engages in two dative bonds as opposed to only one in CH₃IO, the partial atomic charge on I is essentially the same in the two systems (0.47 vs 0.49, respectively).

In the related CH₃I(O)(OH)₂ species, the oxygen atoms feature partial atomic charges of -0.60 (on the OH oxygens) and -0.58 (on the non-protonated oxygen), respectively, suggesting that the three oxygen atoms have identical oxidation states. As expected (see above discussion on CH₃I(OH)₂), in CH₃I(O)(OH)₂ the I-OH bond lengths are distinctly longer than I-O, i.e.

2.10 Å, vs. 1.85 Å. The partial atomic charge on the iodine in $\text{CH}_3\text{I}(\text{O})(\text{OH})_2$ is 0.93, essentially double compared to CH_3IO or $\text{CH}_3\text{I}(\text{OH})_2$ and reflecting a cumulative effect of the three dative bonds towards oxygenic ligands.

CONCLUSIONS

The partial atomic charges and bond lengths are consistent with an assignment of the I-O bond in PhIO as single dative, i.e. $\text{I}\rightarrow\text{O}$. Within this bond, the electrons are distributed evenly between iodine and oxygen. An important point is that in none of the complexes examined is the octet rule *effectively* violated: there are indeed more than eight electrons in the non-participating and bonding orbitals around the iodine, but of all these electrons only 8 can be effectively assigned to iodine while the others effectively belong to oxygen. The I-O system holds 11 electrons (i.e., 10 electrons as shown in Figure 1, plus one electron of iodine involved in I-C bonding). We, therefore, see no need for the use of the term 'hypervalent' in connection to the complexes of this class (i.e., RIO , $\text{RIO}(\text{OH})_2$, etc., where R is an organic substituent). The situation seen here appears in no way different from what is seen with other oxyanions (e.g. sulfate, nitrate), for all of which we advocate against the use of the term 'hypervalent' as well as against the use of a double-bond symbol, i.e., $\text{X}\rightarrow\text{O}$ with an oxygen atom accepting the dative bond, rather than $\text{X}=\text{O}$.

EXPERIMENTAL SECTION

The models were subjected to full geometry optimizations unless otherwise specified. Geometries were optimized for each spin state without any geometrical constraints, with the BP86 functional, which uses the gradient-corrected exchange functional proposed by Becke (1988),^[10] the correlation functional by Perdew (1986),^[11] and the DN** numerical basis set (comparable in size to 6-31G**), as implemented in Spartan.^[12] For the SCF calculations, a fine grid was used, and the convergence criteria were set to 10^{-6} (for the root-mean square of electron density) and 10^{-8} (energy), respectively. For geometry optimization, convergence criteria were set to 0.001 au (maximum gradient criterion) and 0.0003 (maximum displacement criterion). Charges and spin densities were derived from Mulliken population analyses after DFT geometry optimization.

ACKNOWLEDGMENTS

This work was supported by CNCSIS –UEFISCSU, project PNII – IDEI code 565/2007.

REFERENCES

1. M. Sono; M.P. Roach; E.D. Coulter; J.H. Dawson. *Chem. Rev.*, **1996**, 96, 2841.
2. L. Leman; L. Sanière; P. Dauban, R.H. Dodd. *ARKIVOC*, **2003**, 126.
3. T.L. Macdonald; W.G. Gutheim; R.B. Martin, F.P. Guengerich. *Biochemistry*, **1989**, 28, 2071.
4. I.H. Hanna; J.A. Krauser; H. Cai; M.-S. Kim, F.P. Guengerich. *J. Biol. Chem.*, **2001**, 276, 39553.
5. R.C. Blake, M.J. Coon. *J. Biol. Chem.*, **1989**, 264, 3694.
6. R. Silaghi-Dumitrescu; B.J. Reeder; P. Nicholls; C.E. Cooper, M.T. Wilson. *Biochem. J.*, **2007**, 403, 391.
7. R. Silaghi-Dumitrescu. *J. Biol. Inorg. Chem.*, **2004**, 9, 471.
8. R. Silaghi-Dumitrescu, C.E. Cooper. *Dalton Trans.*, **2005**, 3477.
9. R. Silaghi-Dumitrescu, I. Silaghi-Dumitrescu. *Chemtracts - Inorganic Chemistry*, **2005**, 684.
10. A.D. Becke. *Phys. Rev.*, **1988**, 3098.
11. J.P. Perdew. *Phys. Rev.*, **1986**, B33, 8822.
12. *Spartan 5.0*, Wavefunction, Inc., 18401 Von Karman Avenue Suite 370, Irvine, CA 92612 U.S.A.

Dedicated to the memory of Prof. dr. Ioan Silaghi-Dumitrescu marking 60 years from his birth

ON THE MULTIPLE FACETS OF AROMATICITY: ORGANIC, INORGANIC, ORGANOMETALLIC, COORDINATION AND SUPRAMOLECULAR CASE STUDIES

MARILENA FERBINTEANU^a, FANICA CIMPOESU^b

ABSTRACT. This work is an original synopsis over different structural patterns, from different areas of chemistry, unified under the broadened paradigm of the aromaticity. Cluster, coordination and supramolecular systems selected from our own work, as well as correlated literature examples are gathered together and revisited with state of the art electron structure methods and post-computational analyses. Methodological innovations, such as the vibronic approach and the simulation of resonance structures by enforced electron population of correspondingly prepared natural bond orbitals afforded the revealing of new keys for the old keyword of aromaticity.

Keywords: *aromaticity, ab initio calculations, vibronic models, resonance structures, natural bond orbitals, coordination chemistry, organometallic chemistry, supramolecular assembling.*

INTRODUCTION

The aromaticity [1,2] concept is a perennial asset in the heuristic panoply of chemistry, a valuable currency for exchanging ideas between experimental and theoretical sides of communities exploring structure-property correlations, in both fundamental and application respects. Aside the usefulness of the term for taxonomy and reactivity thumb rules in the organic chemistry, [3] its relevance goes up to the advanced material science issues. Thus, the delocalization effects that determine the molecular aromaticity share the same causal reasons with those driving the optical and electrical properties of polymeric conducting polyenes [4,5] and the special properties of nanoscale graphenes. [6]

^a *University of Bucharest, Faculty of Chemistry, Inorganic Chemistry Department, Dumbrava Rosie 23, Bucharest 020462, Romania. marilena.cimpoesu@g.unibuc.ro*

^b *Institute of Physical Chemistry, Splaiul Independentei 202, Bucharest 060021, Romania. cfanica@yahoo.com*

As offers-and-demands balance, there is a large variety of models devoted to the aromaticity, in answer to the general appeal of this topic, along the time-line of modern and contemporary chemistry. The models address, at various levels, electron structure parameters, going from semi-empirical conventions, such as the TREPE indexing (Topological Resonance Energy Per Electron) [7] to criteria worked by *ab initio* procedures, as the NICS case (Nucleus Independent Chemical Shifts) [8], keeping also correlations with instrumental checking *via* NMR shifts. [9] The above mentioned methods are usable also in the generalized purposes, for assessing the aromaticity in non-organic systems, going then beyond the classical early outline of the concept (namely, the Kekule-Erlenmeyer identification with the presence of benzene rings, [10] and the pioneering Hückel rules [11] of $(4n+2)\pi$ electron count in planar conjugated hydrocarbons).

Once the structural patterns of the extremely large variety of cluster systems started to be rationalized with the help of electron-count Wade-Mingos rules, [12] it became clear that aromaticity has rich manifestations in the realm inorganic and organometallic rings and clusters.[13,14] From its initial limitation to planar molecules, the aromaticity was generalized to three-dimensional and spherical patterns. [15]

In the key of such paradigms, the chemistry offers large open and uncharted areas, tempting audacious prospectors with promising new treasures. To answer this challenge, a good general culture in intricacies of cluster chemistry and structural methods is demanded. Fulfilling such commandments, a fine collection of correlations between cluster stereochemistry and electron counting concepts is offered by the works of Professor Ioan Silaghi-Dumitrescu. [16] At the same time, several aspects marked at the study of clusters with distorted polyhedral frames [17] can be presented as inquires open to the anti-aromaticity case studies. The puzzling case of electron Ge_{12}^{2-} cluster [18] showing high symmetry combined with antiaromatic-type NICS indices, i.e. putting in sheer contradiction the criteria of bond length distribution vs. ring-current determinations, proves the challenge of the running paradigms and the value of the heritage offered by professor's Silaghi-Dumitrescu works, his topics pointing the way to new exploratory paths. Honoring such achievements, we will present selected parts from our investigations on several systems proposed as prototypic examples, illustrating the variety of landscapes in the realm of aromaticity concepts.

RESULTS AND DISCUSSION

1. Revisiting the basic organic prototypes: aromaticity in C_6H_6 and the antiaromaticity of C_4H_4

We will set our starting point with the most celebrated representatives of the aromaticity-antiaromaticity dyad, namely the benzene and cyclobutadiene, respectively. In complex polyaromatic hydrocarbons,[3] the existence of aromatic

type behaviour and properties is usually associated with the presence of blocks made of conjugated six-membered rings. For anti-aromaticity the situation is different, since there are no notorious cases of globally antiaromatic molecules assigned to the presence of smaller antiaromatic building blocks. The anti-aromatic behaviour is manifested in different ways, most generally characterized by the presence of a distortion (C=C and C-C bond length alternation and the eventual non-planarity of the rings). Conversely, the aromaticity can be generally presented as resistance to distortion, the system adopting the most symmetrical molecular geometry, with respect of the given topology. The anti-aromatic bond length distortion can be considered a pseudo-Jahn Teller effect [19] and the aromaticity itself can be outlined as balance of factors related to the π -distortivity effects.[2a] We revisited [20] the antiaromaticity of these two systems combining state of the art CASSCF (Complete Active Space Self Consistent Field) calculations and the vibronic modelling, a complex approach taking into account the coupling between vibration and electronic factors. [21] The methodological procedures are not trivial, since, even though the computer codes for structural chemistry have become increasingly accessible, powerful and user-friendly, it is not a simple task to recover from the massive black box of an *ab initio* calculation the pieces needed to recover a picture in line with the chemical intuition perspectives. For instance, the general knowledge takes the π problem at benzene as a frontier MO picture, while using Hartree-Fock (HF) as starting procedure, and 6-311+G* basis set we must retrieve the set of six π -type molecular orbitals (belonging to the a_{1u} , e_{1g} , e_{2u} , b_{2g} , representations of the D_{6h} point group) from the positions 12, 15, 16, 22, 23, 48, respectively (the HOMO-LUMO couple being located at the 21-22 sequence).

Therefore, to set-up a CASSCF procedure one must construct the active space with carefully selected molecular orbitals, the use of chemical intuition being a key step in the art of this kind of multi-configuration calculations. The CASSCF(6,6) calculation (where the numbers in brackets specify the use of 6 electrons in 6 orbitals) produces 175 spin singlet states. We identified the series of 1,3,9,10, 22 levels as being relevant for interpreting the results in terms resonance concepts. Thus, the mentioned series of states can be presented as superposition of the celebrated resonance structures of Kekule and Dewar type. As suggested on Fig.1b chart also, the first two states (the $^1A_{1g}$ groundstate and the $^1B_{2u}$ excited one) can be presented, respectively, as the *in-phase* (sum) and *out-of-phase* (difference) of Kekule-type resonance structures. The upper three levels are combination of Dewar-type resonances (a degenerate couple $^1E_{2g}$ and a totally symmetric combination with equal weights of all three components). We have selected 5 relevant states out of the many CASSCF levels, to span their making from 5 resonance structures, the identification of the adequation to this phenomenology being checked by rather complicate succession of steps.

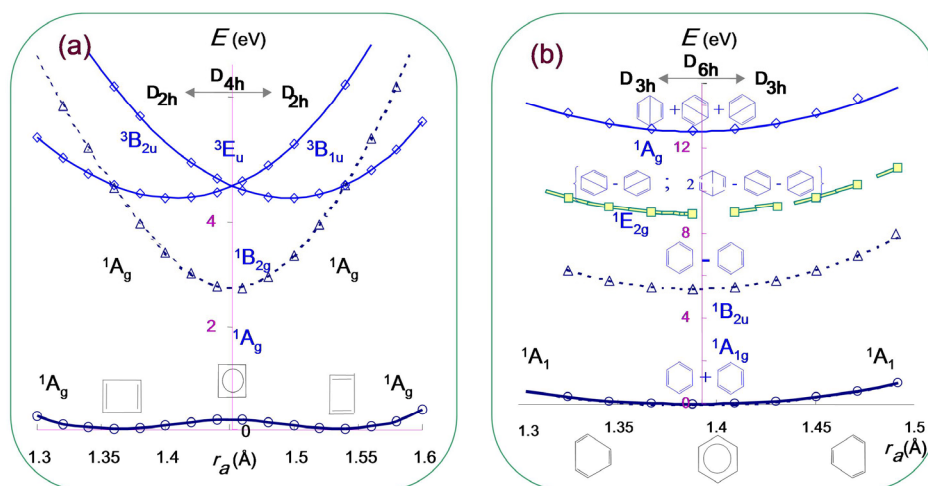


Figure 1. Energy profiles, as function of bond alternating distortion, for selected ground and excited states of: a) cyclobutadiene b) benzene. One observes the pseudo Jahn-Teller effect (double well potential energy of the ground state) that correspond to the anti-aromaticity. The aromaticity is interpreted as resistance against distortion trend (parabola profile). The states were selected from the set of CASSCF calculations to correspond to the interpretation in terms of resonance structures.

The resonance ideas are sometimes presented in as puzzling, suggesting the physical non-reality of separate resonance structures. In fact, the resonance structures are not so imaginary things, neither bogus nor counterfeit. These are the quite concretely writable wave-functions, serving to obtain a given set of states, by their linear combination. In both C_6H_6 and C_4H_4 cases, the ground state can be taken, at the point of high symmetry, as the $\Psi_{\text{sym}} \propto (K_1 + K_2)$ superposition of the two Kekule resonances, while the first excited one is the $\Psi_{\text{asym}} \propto (K_1 - K_2)$ combination. The aromaticity is then characterized by keeping the high molecular symmetry and the correspondingly symmetrical superposition of resonance components. The antiaromaticity can be considered as the trend toward a distorted state, by adopting a pattern adequate for a given single resonance component (i.e. having alternating bonds according to the single vs. double character), i.e. either K_1 or K_2 , as shown in different extremes of the panel a of Figure 1.

Conversely, the individual resonance structures can be presented as a mixing between ground and excited states, as these were defined in the high symmetry point, e.g. $K_1 \propto (\Psi_{\text{sym}} + \Psi_{\text{asym}})$ or $K_2 \propto (\Psi_{\text{sym}} - \Psi_{\text{asym}})$. Then, the antiaromaticity can be formulated as this kind of interstate coupling, promoted by a distortion coordinate. It is, therefore, a case of vibronic coupling or, in other words, a pseudo Jahn-Teller effect. The pseudo Jahn-Teller effect,[19]

i.e. the spontaneous distortion of a symmetrical system with non-degenerate groundstate, is a balance of two opposite terms: a so-called vibronic part, that cumulates all the effects due to the mixing between ground and excited states, and a non-vibronic element that contains all the remaining effects.

The vibronic modeling, comprising terms that account for the dynamic factors, has more general virtues even in cases when there is no distortion of Jahn-Teller or pseudo Jahn-Teller type. The force constant for any given nuclear coordinate can be put as a sum of non-vibronic and vibronic terms, $k=k_0+k_v$. The non-vibronic term can be intuitively interpreted as a sort of mechanical resistance of the molecular skeleton against the given distortion. The pseudo Jahn-Teller distortion becomes visible when the vibronic term ($k_v < 0$, that gives negative contribution to the force constant with respect of a nuclear distortion coordinate) dominates the non-vibronic one ($k_0 > 0$, a positive contribution). In the frame of vibronic modeling the aromaticity and antiaromaticity can be then presented as two cases of a common mechanism, based on the mixing of two states $\Psi_{\text{sym}} \propto (K_1+K_2)$ and $\Psi_{\text{asym}} \propto (K_1-K_2)$ which yields a $k > 0$ parameter for aromaticity and $k < 0$ for antiaromaticity. Our analyses showed that the π subsystem contributes in both aromatic and antiaromatic cases to the vibronic component $k_v < 0$, while the nonvibronic one can be mostly assigned as due to the σ skeleton. Or, in other words, if only the π system existed, even the benzene would have been distorted. The σ skeleton is stronger in the case of benzene, because of in-plane hybrids matching perfectly the 120° bond angles. Then, k_0 predominates, leading to the conservation of the symmetric frame. The 90° bond angles in cyclobutadiene can be obtained only with pure p orbitals, loosing then the cohesive supplement from the s shell. Having a smaller positive k_0 , determined by the weaker skeleton, the cyclobutadiene becomes the subject of the pseudo Jahn-Teller distortion. The energy profile of the ground state along the bond-alternating distortion shows two minima, corresponding to molecular frame distorted in rectangular way, the symmetrical square configuration being metastable, as transition point between these rectangular optimal geometries. Conversely, the energy profile for the benzene ground state is a parabola with minimum in the hexagonal symmetry.

Since the CASSCF, as electron structure calculation method, implies certain intricacies, we will attempt to commute now in presenting the aromaticity issue in more affordable frames, such as the Density Functional Theory (DFT).[22] In this view, *a posteriori*, to a B3LYP/6-311G* calculation for benzene, which is a straightforward task, we employed several steps worked with the help of Natural Bond Orbital (NBO) method.[23] Namely, localized orbital functions were obtained by corresponding input specification of the desired atom pairs. Thus, in one case we specified the three double bonds located between C1-C2, C3-C4 and C5-C6 couples, in order to mimic one Kekule structure (See panel a in Figure 2).

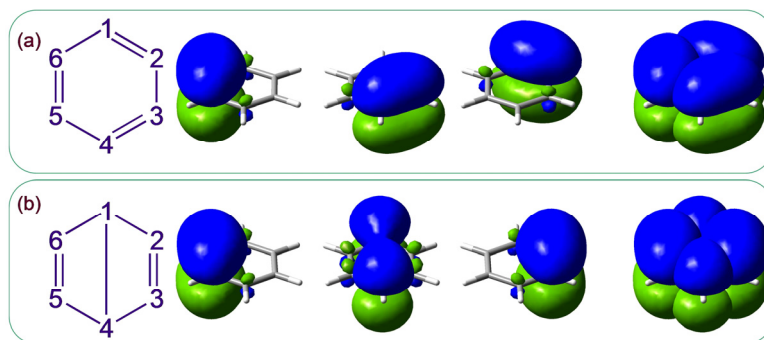


Figure 2. Computational experiments simulating the (a) Kekule and (b) Dewar resonance structures with the help of localized bond orbitals and enforced occupation of each state with a pair of electrons. In the right side, the superpositions of three individual orbitals from each set are presented.

Aiming for a Dewar structure, we succeeded in producing a distant C1-C4 weak bond, aside the regular C2-C3 and C5-C6 double bonds (See Figure 2b). This result is a non-standard approach, but at the same time can be worked in user-friendly manner, since the NBO code[24] can be easily controlled by specifying the desired connectivities and formal bond orders. If one imposes the double occupation of these localized bond orbitals, the total density breaks the hexagonal symmetry, showing the Kekule or Dewar π alternation patterns. One must point that this approach is different from the the so-called Natural Resonance Theory (NRT) [25] also related to the NBO frame. Another computational experiment consisted in taking these broken symmetry total densities and doing a non-iterative DFT calculation with the imposed frozen functions. The resulted energies are higher than those from regular DFT calculation, the gap measuring the stabilization gained by the molecular orbital delocalization. If one s the energy gap by 6, one obtains an equivalent of topological resonance energy per electron (TREPE). While the standard TREPE [7] is a semiempirical procedure based on Hückel-type approach, our computation experiment offers quantities resulted from state of the art DFT techniques. The corresponding amounts (per electron) are 0.10 a.u. (60.8 kcal) for the Kekule state and 0.42 a.u. (265.3 kcal) for the Dewar case. The above revisiting of the very classical prototypic systems of the aromaticity paradigm gave us the opportunity to present and assess methodological issues that can be applied on other examples of general aromaticity, as we will proceed in the following.

II. The spherical aromaticity in inorganic systems. The icosahedral borane

The $B_nH_n^{2-}$ dianions were assigned as aromatic[26] with the help of NICS indices,[8] having a new manifestation, i.e. the spherical aromaticity. This happens because the orbitals of the clusters having the atoms averagely distributed on the surface of a sphere, start to approximate, progressively with the increase of nuclearity, certain regularities similar to a giant atom virtually placed in the center of the cluster and carrying in its shells the valence (bonding and nonbonding) electrons of the constituents. The sign of the orbital components resemble the pattern known for atomic orbitals, or more precisely, the Spherical Harmonics angular functions. In Figure 3 a comparison of classical planar aromaticity with the 3D generalization is suggested. The aromaticity in rings is related to the circular symmetry, whose representations are driven by the $\exp(\pm iM\phi)$ functions, or equivalently, by the $\{\cos(M\phi), \sin(M\phi)\}$ couples. These form doubly degenerate shells, except the $M=0$ element, which is the trivial total symmetrical representation. Filling progressively the $M=0,1,2, \text{ etc}$ sub-shells drawn in the panel (a) of Figure 3, one obtains the 2,6,10,... electron count, spanning the $4n+2$ Hückel rule. In clusters, we go to higher spherical patterns. Here, the irreducible representations are Spherical Harmonics with $L=0,1,2, \dots$ parameters, that are similar to the atomic shells, i.e. having a $2L+1$ multiplicity and L nodal planes in each subset. The lobes of the MOs constructing a pseudo-spherical cluster are "painted" in "colors" borrowed from the pattern of the Spherical Harmonics depicted in the panel (b) of Figure 3. More precisely, the LCAO components of an AO located at a given position on the sphere are proportional in sign and magnitude with the Spherical Harmonics at that coordinate. Then, the MOs are grouped in quasi-degenerate sets spanning the $2L+1$ multiplicities of an appropriate L number. Then, progressively filling such sub-shells one obtains a 2, 8, 18, series, i.e. a $2(L+1)^2$ count. Such a regularity is called the Hirsch rule. [27] Since in many cases the effective symmetry is not so high, to completely match the spherical approximation, and also because the full complexity of electron structure is realized with the help of supplementary functions taken as derivatives of Spherical Harmonics, there are alternate regularities, such as Wade's electron count, which specifies the need of $2n+2$ polyhedral skeleton electron pairs [28] to achieve a good stability and therefore to claim the aromaticity case. Counting the valence electrons in the $B_{12}H_{12}^{2-}$ as follows, 12×5 from boron atoms, 12 from hydrogens and 2 from dianion charge, one obtains a total of 50 electrons, apparently favorable to the Hirsch rule (with $L=4$). Counting the skeletal electron pairs (i.e. ignoring the 12×2 electrons comprised in the outer B-H bonds) one obtains a 26 count that satisfies Wade's rule for the electron pairs devoted to the cluster itself.

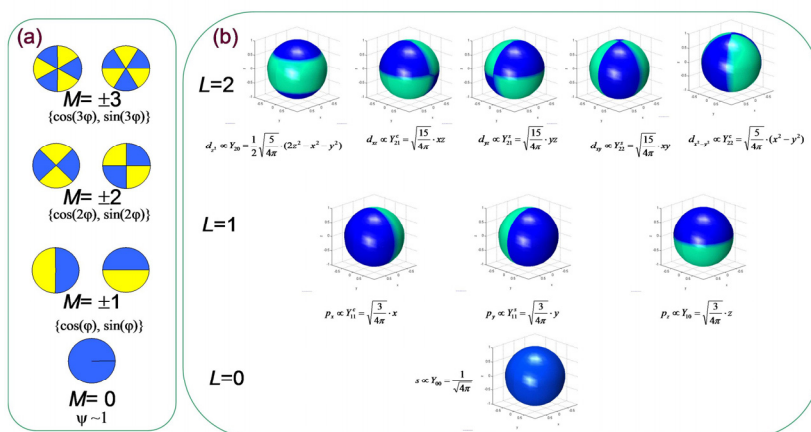


Figure 3. Symmetry regularities determining the aromaticity in (a) rings and (b) clusters, according to the patterns of cyclical and spherical symmetry, respectively. The different colors mark the different signs of the functions and nodal planes around a cycle and on the surface of a sphere.

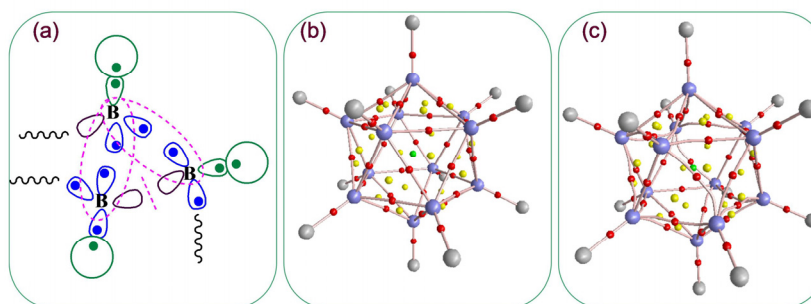


Figure 4. The bonding regime in boranes. a) the scheme of local electron deficiency, each B atom contributing with two electrons for the cluster; the possibility to assign formal localized bonds on and electron void areas is suggested. (b) The $B_{12}H_{12}^{2-}$ dianion with its critical points and bond paths. (c) The bond paths in the neutral $B_{12}H_{12}$ appear curved and distorted, as expression of the fact that the electron count of the neutral molecule is incompatible with a stable closed shell icosahedral configuration.

Besides, looking at point group symmetry reasons, one observes that the dianion realizes the completion of a four-degenerate HOMO level. This is why the dianion status is required, because otherwise the non-closed degenerate shell would lead to pseudo Jahn-Teller distortions. From this point of view, the neutral $B_{12}H_{12}$ could be called anti-aromatic. However, the things are a bit more complicated.

Another view on the aromaticity of boranes is the electron deficient nature of the boron. This implies a large delocalization, in order to spread the electron density over all the interatomic contacts. Employing the analysis of density distribution with the help of Bader's theory of Atoms in Molecules (AIM) [29, 30] one obtains the so called (3,-1) critical points, certifying the formation of a bond for each B-H unit and also for all the 30 B-B edges of the icosahedron, both in case of the dianion $B_{12}H_{12}^{2-}$ and for the neutral $B_{12}H_{12}$. The number of established bonds is larger than the available electron pairs (13 for dianion, 12 for the neutral molecule). It is interesting to compare the bond paths of the two related systems (depicted in Figures 4b and 4c). The bond paths are gradient lines joining points of maximal density located at nuclei, passing via the (3,-1) bond points. Regular bond paths are almost linear, while in certain cases these appear curved, as is visible for the neutral $B_{12}H_{12}$. Because of incomplete degenerate HOMO shell, the neutral $B_{12}H_{12}$ is unstable in the icosahedral symmetry, but we will discard for the moment the question of optimal geometry and the comparison of distortion isomers. In turn, the bond path bending resulted by taking the enforced icosahedral symmetry for $B_{12}H_{12}$ can be interpreted as a sign of the inner trends for distortion.

In the following we will try to transcribe the electron deficient boranes in terms of resonance structures. Because the number of electron pairs is larger than the number of interatomic bonds, the groundstate must be conceived as a superposition of many configurations. Each boron atom participates with two electrons to the cluster delocalization, while one electron per boron should be reserved for firm bonds with the outer hydrogen atoms. Each boron has 5 immediate neighbors, but is able to share Lewis-type electron pairs only with two of them. Each B atom has formally an empty valence orbital (See the the panel a of Figure 3).

Therefore, if draw a line for an electron pair shared by a B-B couple, each boron vertex of the B_{12} polyhedron has two emerging lines. The resonance structures can be then formulated as lines running over a total of 12 edges in the case of $B_{12}H_{12}$ and over 13 edges in the case of $B_{12}H_{12}^{2-}$ dianion. It is particularly more convenient to discuss the resonance structures of the neutral molecule. We will not detail now their complete count, which is a matter of specialized graph theory. We will confine ourselves in noticing that, marking by ticker lines the bonds, these can be grouped in a number of closed walks, ranging from 1 to 4 independent circuits (See Figures 5-7).

These circuits do not cross each-other and comprise, in ensemble, all the vertices of the icosahedron. In the case of the dianion $B_{12}H_{12}^{2-}$ one supplementary line can be drawn at any of the 18 remaining empty B-B lines (out of the 30 B-B edges) to which no previous line was assigned (12 edges being occupied by the mentioned bond lines). Each possibility to design such walks can be considered as a resonance structure. The superposition of such resonance structures resolves the problem of electron

deficiency and consequently offers a suggestion for the aromaticity of these systems, if accepting that aromaticity can be defined as the need for resonance superposition, in order to describe a stable structure. In this perspective, even the neutral $B_{12}H_{12}$ can be presented as aromatic while $B_{12}H_{12}^{2-}$ is the most aromatic, since it has more resonance structures, multiplied by a factor of 18 as compared to the $B_{12}H_{12}$ count as seen above.

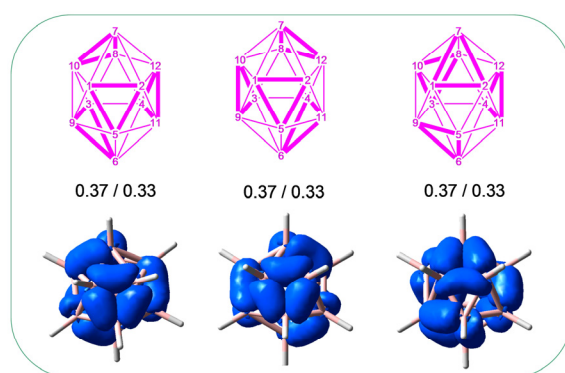


Figure 5. Selected equivalent resonance structures for $B_{12}H_{12}$, spanning 4 islands of 3-membered circuits, marked with bold lines in the graphs depicted in the upper part. The lower part contains the simulation of this resonance structure with the help of superposed correspondingly prepared and occupied localized bond orbitals. The numbers written in couples on the middle line are designed as a measure of resonance effect: the first number of each couple is estimated for dianion and the second for the neutral molecule. Each values represents the DFT energy gap (in a.u.) of between the localized resonance structure and the delocalized state, divided by 24, the number of cluster electrons, in order to have a resemblance with TREPE indices.

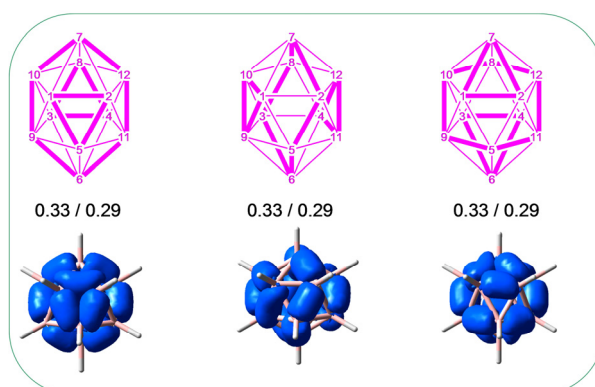


Figure 6. Selected equivalent resonance structures spanning 3 islands with 3,6,3 members. The interpretation is similar to the precedent figure.

The neutral system can be presented, at this stage, as intermediately aromatic, since, even letting it to relax at a lower symmetry the presence of resonance superposition will still be required to resolve its intrinsic electron deficiency. The complete picture will not be developed now. We will proceed, in turn, to an interesting computational experiment, mimicking the above mentioned types of resonance structures with the help of localized natural bond orbitals, using the same procedures as explained in the above section for benzene. This simulation of the resonance structures is a rather inedited deal, as well as, to the best of our knowledge, the whole explained picture of resonating bonds in boranes. The procedure offers also certain indices similar to the traditional TREPE, as explained above in the benzene case. We recall that, to be distinguished from TREPE, which are based on empirical methods, our approach is based on energy amounts primarily obtained at DFT level. Thus, the energy gap between the DFT energies of delocalized molecule and enforcedly localized resonance structure, divided by the number of electrons in the cluster, i.e. 24, stands for the values printed along with the resonance structures from figures 5-7. The values are presented in couples, the first one devoted to the dianion, the second to the neutral molecules. The resonance structures are, in fact drawn for the neutral molecule, the dianion presenting a supplementary number of resonances, due to the added electron pair. In our calculations the dianion was taken by a resonance structure obtained adding a lone pair, conventionally, on the first atom, B1. The definition as lone pair is convenient because in this way it appears delocalized towards the remaining boron neighbours and offers in this way a sort of simulated averaging over the three resonance structures obtainable by separate localization procedures. One observes that the defined indices show larger magnitudes for the dianion, as a measure of its larger aromaticity. At the same time, even though the resonance patterns differ very much in topological respects, their indices are comparable, suggesting that the resonance in borane may use such various patterns on almost equal footing. The pictures 5 and 6 offer, altogether with the formal resonance structures, the realistic electron density superposition realized with the localization approach. The figure 7 is confined to drawing only the formal graphs of several other selected resonances, altogether with their corresponding indices. In panel 7a is illustrated another topology with 3 rings of bond circuits, in 7b patterns with two 6-membered circuits, in 7c selected shapes with two unequal circuits (3 and 9 membered) and in 7d the case of single 12 member circuits. The classification of the resonance structures in the above suggested style is a challenging matter in itself, as graph theory issue, committing our interests in further developments in this sense.

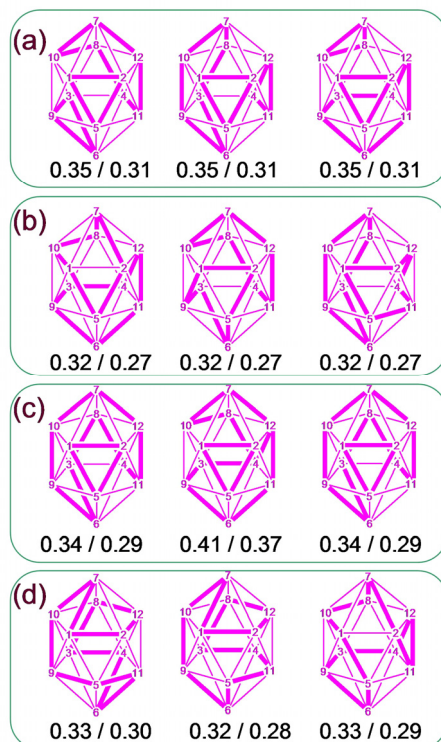


Figure 7. Selected equivalent resonance structures of $B_{12}H_{12}$, belonging different topological patterns : a) 3 circuits with 3,6,3 members; b) two circuits with 6,6 members; c) two circuits with 3,9 members; d) a single circuit with 12 members. The value couples below each graph are resonance indices for dianion and neutral cases, respectively.

III. The aromaticity in coordination systems. The diketonate ligands

The diketonate anions can be proposed as subject for inquires on aromaticity, since their structure with delocalized negative charge imply the use of resonance structures. We will address this issue in both the free anion and also coordination complexes with diketonates as ligand, using in this purpose the the so-called Natural Resonance Theory [25] which is a part of the NBO methods and computer codes.[23] The procedure is a bit different from our previously exposed methodology with localized orbitals and is distinct also from the genuine frame that imposed the concept of resonance, namely the Valence Bond theory (VB). [31] The NRT is not a multiconfigurational method. It offers a sort of surrogate for the effect of

superposed resonance structures, fitting the total density from a regular DFT calculation (i.e. with delocalized MOs) in terms of contributions from occupation schemes with imposed localizations. This procedure offers a convenient user-friendly access to the resonance concepts.

We will take as study case a coordination system from our own synthetic results,[32] $[\text{Ni}(\text{tmen})(\text{NO}_2)(\text{dbm})]$, where *tmen* is tetra-methylene-diamine and *dbm* is dibenzoyl-methanate, i.e. the diketonate taken in our focus. In Figure 8 we comparatively show the weights of main resonance structures for the free ligand and the coordinated one. The presented amounts do not complete a 100% total, since there are several other discarded small terms, assignable to hyperconjugation effects. The free ligand is less aromatic, since the contribution of the keto-enolate forms are smaller, being in competition with a carbanionic resonance. In the coordinated mode, the two keto-enolate resonance structures become the dominating contributors. In the presented case, the two twin diketonate resonances have slightly differing weights because of the asymmetry induced by the mixed ligand environment. The chelate can be interpreted as aromatic, since it can be presented as superposition of two equivalent resonance structures.

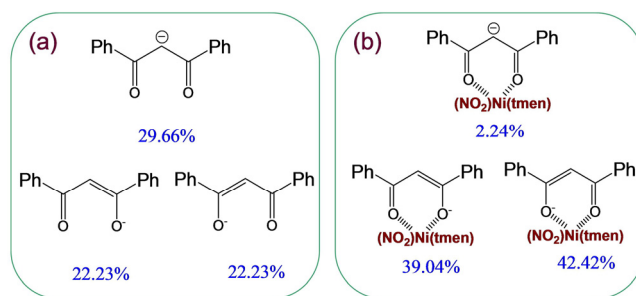


Figure 8. The resonance weights computed with the NRT (post DFT) method for the: (a) free and (b) coordinated, dibenzoyl-methanate ligand.

IV. Surface aromaticity in organometallic clusters

We will propose as example for this entry a system belonging to our previous work, a carbalane cluster with $\{\text{Al}_8\text{C}_6\}$ cubo-octahedral pattern.[33] Not only the theoretical analysis, but also the chemical tests suggested this system as aromatic, since the cluster core resisted well at several reactions that affected only its terminal groups, in a manner resembling the stability of benzene core against substitutions and additions. This cluster is electron deficient (like boranes), since the analysis of critical points of density identified implying the superposition of resonance structures, as suggested by panel more bonds than the available electron pairs, as seen in Figure 9a, the situation 9b.

There are $4^6 = 4096$ resonance structures, figure 9b presenting only a selected portion. Without entering the details, we point that there exist two different types of Al-C bonds, differing by certain overlap factors, one marked with full line, the others with dashed line. From each C site emerges one tick line and two dashed ones.

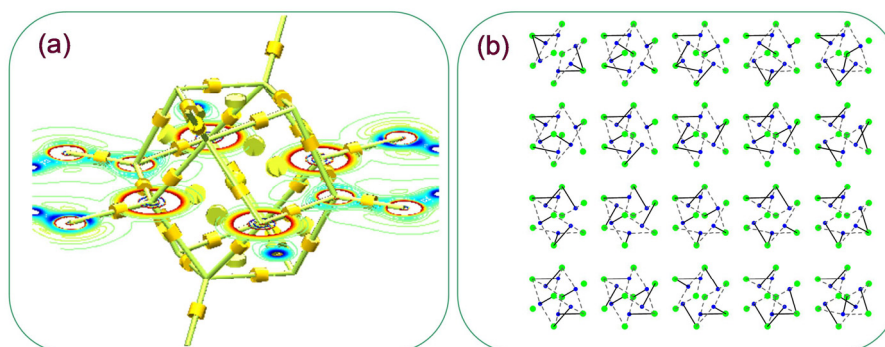


Figure 9. Synopsis of the delocalization and resonance effects in the carbalane with $\{Al_8C_6\}$ core, as images of surface aromaticity effects. The skeleton drawn in (a) corresponds to computed bond paths, with bond critical points marked with ticker cylinders. The C atoms are penta-conexe (with 4 bonds inside the cluster and one outer one, while the aluminum are represented as triconexe). The Laplacian of electron density is represented in a molecular section. In (b) one shows a selected part of the resonance structures with linkages between the the Al_8 and C_6 subsystems.

The resonance structures at one $\{Al_4C\}$ face of the cluster are obtained rotating the set of three bonds around the square frame, letting one Al site non-bonded. The rule for obtaining the resonance structures can be presented as decrypting the monomials resulted after expanding the following product:

$$(y_1x_2y_3 + x_1y_2y_4 + y_1y_3x_4 + y_2x_3y_4) \cdot (y_5x_6y_7 + x_5y_6y_8 + y_5y_7x_8 + y_6x_7y_8) \cdot \\ (x_1y_2y_5 + y_1x_2y_6 + y_1x_5y_6 + y_2y_5x_6) \cdot (x_2y_3y_6 + y_2x_3y_7 + y_2x_6y_7 + y_3y_6x_7) \cdot \\ (x_3y_4y_7 + y_3x_4y_8 + y_3x_7y_8 + y_4y_7x_8) \cdot (x_1y_4y_5 + y_1x_4y_8 + y_1x_5y_8 + y_4y_5x_8) .$$

The x_i (with $i = 1$ to 8) stand for the aluminum the Al-C bonds conventionally marked by tick line, while the x_j represent the dashed ones. The subscript indices mark the Al atom touched by the bonds of the presented types.

V. An inedited case of supramolecular antiaromaticity

We present now a system with radicalic character that can be exploited as an unprecedented case of antiaromatic-type distortion in a supramolecular ordered network. The compound was synthesized[34] and explored by us for sake of magneto-structural correlations, the antiaromatic features remaining yet incompletely explored, presenting here an excerpt of the ongoing detailed analysis. The system is an octa-coordinated yttrium complex $K[Y(QT)_4]$ with QT (Quinoline-Tempo) a diketonate chelatic ligand that has also a radical tail. The interaction between the NO radical groups of the ligand tails and the lattice potassium ions determines a supramolecular ordering with nodes made of K^+ ions surrounded by four radicals. The set of four interacting radicals resembles the configurational problem from the cyclobutadiene prototype (4 electrons in 4 orbitals). Even though here there is not the case of similar genuine π system, the same factors that determine the rectangular shape of C_4H_4 , are imposing the distortion in the actual $\{K(QT)_4\}$ moieties of our system.

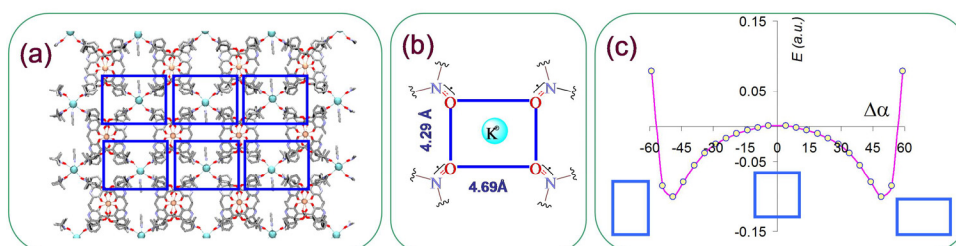


Figure 10. (a) The antiaromatic-type rectangular distortions in the supramolecular assemblies of the $K[Y(QT)_4]$ complex with radicalic ligands. (b) The scheme of the $\{K(QT)_4\}$ node with four-radical character and rectangular pattern. (c) A simplified simulation of the preference for distortion in the idealized model $[K(ONH_2)_4]^+$ of the four radical complex node. The $\Delta\alpha$ coordinate measures the deviation of one O-K-O angle from the 90° perfect square value. Namely, at the perfect square geometry $\Delta\alpha=0$, the energy profile shows a metastable transition point, the system spontaneously breaking its symmetry toward the minima corresponding to antiaromatic pattern.

The rectangular pattern of the whole supramolecular ordering is shown in Figure 10a, with the scheme of rectangular $\{K(QT)_4\}$ nodes in 10b. In 11c we present a simulation of the preference for distortion, taken on a simplified model $[K(ONH_2)_4]^+$ with B3LYP/6-311G* DFT potential energy surface procedures. The double well potential proves the trend for the antiaromatic type of distortion in the four radical system, an effect which is cooperatively transmitted to the whole supramolecular network.

The system is interesting also from magneto-structural point of view, being a challenging detective story. Namely, the attempts to fit the experimental magnetic susceptibility with standard procedures lead systematically to results incompatible with the experimentally observed rectangular topology. The cause was a sort of accidental local minimum comprised in the standard phenomenological modeling. A clear cut of the question was done with the help of *ab initio* calculations, that helped us in choosing the right parametric balance, the situation being illustrative for the role of theoretical approaches, as valuable complements to experiments.

CONCLUSIONS

We presented a broad perspective on the aromaticity paradigm, analyzing prototypic molecules such as benzene and icosahedral boranes, as examples for organic and inorganic cases, and systems from our own results, to illustrate the coordination, [32] organometallic [33] and supramolecular [34] varieties. The aromaticity is a very generalizing and fruitful keyword, that catalyzes interdisciplinary results, establishing natural bonds between the experimental and theoretical sides. It is important to safeguard these links and the role of intuition, since with the advent of modern electron structure methods and codes, the thesaurus of heuristic ideas like hybridization, hypervalence, aromaticity, started to loose terrain in the front of accurate *ab initio* reproduction of structural parameters. The brute-force computational approach does not need, apparently, the *a priori* guidelines of these heuristic concepts originating from the experimental chemistry, but a real understanding is realized when we can find a simple meaning behind the output bulk information. It is a challenge to rebuild *a posteriori*, from the bare output of the electronic structure methods, the information matching the major keywords with *aprioric* virtues. The revisiting of the basic concepts is a steady temptation and a challenging task, with a rewarding outcome. In spite of its longstanding history, the aromaticity is still an active and appealing concept, that triggers theoretical debates and marks the way to new lands of experimental chemistry.

EXPERIMENTAL SECTION

The synthetic and structural details of the compounds belonging to our synthetic works were presented elsewhere. [33, 34]. The calculations were performed using the Gaussian 03,[35] Gamess [36] and NBO [24] software packages.

ACKNOWLEDGMENTS

Parts of this work were supported by the CNCSIS-UEFISCSU grant "Idei" 174/2007.

REFERENCES

-
1. (a) L. Salem, "The Molecular Orbital Theory of Conjugated Systems", Benjamin, New York, **1966**. (b) V. I. Minkin, M. N. Glukhovtsev, B. Y. Simkin, "Aromaticity and Antiaromaticity", Wiley, New York, **1994**.
 2. (a) S. Shaik, A. Shurki, D. Danovich, P. C. Hiberty, *Chem. Rev.*, **2001**, *101*, 1501. (b) P. v. R. Schleyer, H. Jiao, *Pure Appl. Chem.*, **1996**, *68*, 209.
 3. (a) E. Clar, "Polycyclic Hydrocarbons", Academic Press, London, **1964**. (b) T. M. Krygowski, M. K. Cyranski, Z. Czarnocki, G. Häfelinger, Alan R. Katritzky, *Tetrahedron*, **2000**, *56*, 1783.
 4. (a) Z. Shuai, J. L. Bredas, *Physical Review*, **2000**, *B 62*, 15452. (b) W. Barford, R. J. Bursill, *Physical Review*, **2006**, *B 73*, 045106.
 5. Y. Geerts, G. Klärner, K. Müllen, "In Electronic Materials: The Oligomer Approach", K. Müllen, G. Wagner, Eds.; Wiley-VCH:Weinheim, Germany, **1998**.
 6. J.-N. Fuchs, P. Lederer, *Physical Review Letters*, **2007**, *98*, 016803. (b) B. Trauzettel, D. V. Bulaev, D. Loss, G. Burkard, *Nature Physics*, **2007**, *3*, 192.
 7. (a) I. Gutman, M. Milun, N. Trinajstić, *J. Am. Chem. Soc.*, **1977**, *99*, 1692. (b) J. Aihara, *J. Am. Chem. Soc.*, **1976**, *98*, 2750; **1977**, *99*, 2048. (c) M. S. J. Dewar, C. de Llano, *J. Am. Chem. Soc.*, **1969**, *91*, 789. (d) A. Graovac, I. Gutman, M. Randić, N. Trinajstić, *J. Am. Chem. Soc.*, **1973**, *95*, 6267. (e) A. R. Katritzky, K. Jug, D. C. Oniciu, *Chem. Rev.*, **2001**, *101*, 1421.
 8. P. v. R. Schleyer, C. Maerker, A. Dransfeld, H. Jiao, N. J. R. v. E. Hommes, *J. Am. Chem. Soc.*, **1996**, *118*, 6317.
 9. (a) P. v. R. Schleyer, H. Jiao, *Pure Appl. Chem.* **1996**, *68*, 209. (b) T. M. Krygowski, M. K. Cyranski, Z. Czarnocki, G. Häfelinger, A. R. Katritzky, *Tetrahedron*, **2000**, *56*, 1783.
 10. (a) A. Kekule', *Bull. Soc. Chim. Fr.*, **1865**, *3*, 98. (b) E. Erlenmeyer, *Liebigs Ann. Chem.*, **1866**, *137*, 327.
 11. E. Hückel, *Z. Physik*, **1931**, *70*, 204; *Z. Physik*, **1931**, *72*, 310; *Z. Physik*, **1932**, *76*, 628.
 12. (a) K. Wade, *Chem. Commun.*, **1971**, 792. (b) D. M. P. Mingos, *Acc. Chem. Res.*, **1984**, *17*, 311.
 13. (a) R. B. King, *Chem. Rev.*, **2001**, *101*, 1119, and references therein. (b) R.B. King, *Inorg. Chim. Acta*, **2003**, *350*, 126. (c) H. Tanaka, S. Neukermans, E. Janssens, R. E. Silverans, P. Lievens, *J. Am. Chem. Soc.*, **2003**, *125*, 2862.
 14. (a) A. I. Boldyrev, J. Simons, *J. Am. Chem. Soc.*, **1998**, *120*, 7967. (b) X. Li, A. E. Kuznetsov, H. F. Zhang, A. I. Boldyrev, L.-S. Wang, *Science*, **2001**, *291*, 859. (c) A. Hirsch, Z. Chen, H. Jiao, *Angew. Chem.*, **2001**, *113*, 2916; *Angew. Chem., Int. Ed.*, **2001**, *40*, 2834.

-
15. (a) A. Hirsch, Z. Chen, H. Jiao, *Angew. Chem., Int. Ed.*, **2001**, *40*, 2834. (b) M. Bühl, A. Hirsch, *Chem. Rev.*, **2001**, *101*, 1153.
16. (a) R. B. King, I. Silaghi-Dumitrescu, *Inorg. Chem.*, **2003**, *42*, 6701. (b) R. B. King, I. Silaghi-Dumitrescu, A. Lupan, *Inorg. Chem.*, **2005**, *44*, 3579. (c) R. B. King, I. Silaghi-Dumitrescu, A. Lupan, *Inorg. Chem.*, **2005**, *44*, 7819. (d) R. B. King, I. Silaghi-Dumitrescu, M. M. Uță, *Inorg. Chem.*, **2006**, *45*, 4974.
17. (a) R. B. King, I. Silaghi-Dumitrescu, A. Kun, *Inorg. Chem.*, **2001**, *40*, 2450. (b) R. B. King, I. Silaghi-Dumitrescu, M. M. Uță, *J. Chem. Theory Comput.*, **2008**, *4*, 209.
18. (a) R. B. King, I. Silaghi-Dumitrescu, M. M. Uță, *Dalton Trans.*, **2007**, 364. (b) R. B. King, T. Heine, C. Corminboeuf, P. v. R. Schleyer, *J. Am. Chem. Soc.*, **2004**, *126*, 430.
19. I. B. Bersuker, *Chem. Rev.*, **2001**, *101*, 1067.
20. (a) F. Cimpoesu, K. Hirao, M. Ferbinteanu, Y. Fukuda, W. Linert, *Monatshefte für Chemie*, **2005**, *136*, 1071. (b) F. Cimpoesu, V. Chihaiia, N. Stanica, K. Hirao, *Advances In Quantum Chemistry*, **2003**, *44*, 273.
21. (a) I. B. Bersuker, "The Jahn-Teller Effect and Vibronic Interactions in Modern Chemistry", New-York, Plenum Press, 1984. (b) F. Cimpoesu, K. Hirao, "The Ab Initio Analytical Approach of Vibronic Quantities: Application to Inorganic Stereochemistry", *Advances In Quantum Chemistry*, **2003**, *44*, 370.
22. W. Koch, M. C. Holthausen, "A Chemist's Guide to Density Functional Theory", Wiley-VCH, Berlin, **2001**.
23. A. E. Reed, L. A. Curtiss, F. Weinhold, *Chem. Rev.*, **1988**, *88*, 899; the NBO3.0 program, E. D. Glendening, A. E. Reed, J. E. Carpenter, F. Weinhold.
24. NBO 5.0 Glendening E. D., Badenhoop J. K., Reed A. E., Carpenter J. E., Bohmann J. A., Morales C. M., Weinhold F., <http://www.chem.wisc.edu/~nbo>
25. (a) E. D. Glendening, F. Weinhold, *J. Comput. Chem.*, **1998**, *19*, 593; *19*, 610. (b) E. D. Glendening, J. K. Badenhoop, F. Weinhold, *J. Comput. Chem.*, **1998**, *19*, 628. (b) S. Feldgus, C. R. Landis, E. D. Glendening, F. Weinhold, *J. Comput. Chem.*, **2000**, *21*, 11.
26. (a) P. v. R. Schleyer, K. Najafian, "In The Borane, Carborane, Carbocation Continuum", J. Casanova, Ed., Wiley, New York, **1994**. (b) P. v. R. Schleyer, K. Najafian, *Inorg. Chem.*, **1998**, *37*, 3454. (c) M.L. McKee, Z.-X. Wang, P. v. R. Schleyer, *J. Am. Chem. Soc.*, **2000**, *122*, 4781.
27. A. Hirsch, Z. Chen, H. Jiao, *Angew. Chem., Int. Ed.*, **2001**, *40*, 2834.
28. (a) K. Wade, *Adv. Inorg. Chem. Radiochem.*, **1976**, *18*, 1. (b) E. D. Jemmis, M. M. Balakrishnarajan, D. Rabcharatna, *Chem. Rev.*, **2002**, *102*, 93.
29. (a) R. F. W. Bader "Atoms in Molecules - A Quantum Theory", University Press, Oxford, **1990**; (b) R. F. W. Bader, *Acc. Chem. Res.*, **1985**, *18*, 9.
30. F. Biegler-König, "AIM2000" computer code, Bielefeld, **2000**.
31. (a) D. J. Klein, N. Trinajstić (Eds) "Valence Bond Theory and Chemical Structure", Elsevier, Amsterdam, **1990**; (b) D. L. Cooper, J. Gerratt, M. Raimondi, *Chem. Rev.*, **1991**, *91*, 929.

-
32. M. Ferbinteanu unpublished results.
33. A. Stasch, M. Ferbinteanu, J. Prust, W. Zheng, F. Cimpoesu, H. W. Roesky, J. Magull, H.-G. Schmidt, M. Noltemeyer, *J. Am. Chem. Soc.*, **2002**, *124*, 5441.
34. L. Maretti, M. Ferbinteanu, F. Cimpoesu, S. M. Islam, Y. Ohba, T. Kajiwara, M. Yamashita, S. Yamauchi, *Inorg. Chem.*, **2007**, *46*, 660.
35. M. J. Frisch, G. W. Trucks, H. B. Schlegel, G. E. Scuseria, M. A. Robb, J. R. Cheeseman, J. A. Montgomery, Jr., T. Vreven, K. N. Kudin, J. C. Burant, J. M. Millam, S. S. Iyengar, J. Tomasi, V. Barone, B. Mennucci, M. Cossi, G. Scalmani, N. Rega, G. A. Petersson, H. Nakatsuji, M. Hada, M. Ehara, K. Toyota, R. Fukuda, J. Hasegawa, M. Ishida, T. Nakajima, Y. Honda, O. Kitao, H. Nakai, M. Klene, X. Li, J. E. Knox, H. P. Hratchian, J. B. Cross, V. Bakken, C. Adamo, J. Jaramillo, R. Gomperts, R. E. Stratmann, O. Yazyev, A. J. Austin, R. Cammi, C. Pomelli, J. W. Ochterski, P. Y. Ayala, K. Morokuma, G. A. Voth, P. Salvador, J. J. Dannenberg, V. G. Zakrzewski, S. Dapprich, A. D. Daniels, M. C. Strain, O. Farkas, D. K. Malick, A. D. Rabuck, K. Raghavachari, J. B. Foresman, J. V. Ortiz, Q. Cui, A. G. Baboul, S. Clifford, J. Cioslowski, B. B. Stefanov, G. Liu, A. Liashenko, P. Piskorz, I. Komaromi, R. L. Martin, D. J. Fox, T. Keith, M. A. Al-Laham, C. Y. Peng, A. Nanayakkara, M. Challacombe, P. M. W. Gill, B. Johnson, W. Chen, M. W. Wong, C. Gonzalez, and J. A. Pople, "*Gaussian 03*", Gaussian, Inc., Wallingford, **2004**.
36. M. W. Schmidt; K. K. Baldridge; J. A. Boatz, S. T. Elbert, M. S. Gordon, J. H. Jensen, S. Koseki, N. Matsunaga, K. A. Nguyen, S. J. Su, T. L. Windus, M. Dupuis, J. A. Montgomery, *J. Comput. Chem.*, **1993**, *14*, 1347.

Dedicated to the memory of Prof. dr. Ioan Silaghi-Dumitrescu marking 60 years from his birth

SYNTHESIS AND THERMAL BEHAVIOR OF COPPER(II) COMPLEXES CONTAINING N,N'-TETRA(4-ANTIPYRILMETHYL)-1,2 DIAMINOETHANE AS LIGAND

ELENA MARIA MOSOARCA^a, IMRE LABADI^b,
LUDOVIC SAJTI^a, RAMONA TUDOSE^a, VASILE SIMULESCU^a,
WOLFGANG LINERT^c AND OTILIA COSTISOR^{a,*}

ABSTRACT. The synthesis of new complexes [Cu(TAMEN)][Zn(NCS)₄] and [Cu(TAMEN)ZnCl₄(H₂O)], where TAMEN stand for the Mannich base N,N'-tetra(4-antipirylmethyl)-1,2-diaminoethane are reported. The molecular formulas are proposed on the basis of elemental analysis, mass spectra, molar conductivity values, UV-VIS and IR spectra. The thermal behavior of the complexes was also investigated.

Keywords: antipyrine, copper(II), zinc(II), Mannich base, thermal analysis.

INTRODUCTION

Antipyrine and its derivatives are reported to exhibit analgesic and anti-inflammatory effects, antiviral, antibacterial and herbicidal activities [1-12]. Formation of complexes with some oligoelements may explain their pharmaceutical activity [13]. Antipyrine complexes with certain metal ions, including Pt(II) and Co(II) ions, have been shown to act as antitumor agents. In order to extend this class of pharmaceuticals, Mannich bases containing two or four antipyrine fragments have been obtained [14]. Considering that more antipyrine active fragments would lead to a more efficient antipyretic and analgesic medicine, we synthesized and structurally characterized 3d metal complexes of antipyrine Mannich bases, namely, N,N'-bis(4-antipirylmethyl)-piperazine (BAMP) [15-16] and N,N'-tetra(4-antipirylmethyl)-1,2 diaminoethane (TAMEN) [17]. Some of them have been biologically investigated as antimicrobial and antitumoral agents [18-21].

^a Institute of Chemistry Timisoara of Romanian Academy, 24 Mihai Viteazu Bd., 300223, Timisoara, Romania

^b University of Szeged, Department of Inorganic and Analytical Chemistry, H-6701 Szeged, P.O. Box 440, Hungary

^c Institute of Applied Synthetic Chemistry, Vienna University of Technology, Getreidemarkt, 9/163-AC, A-1060 Vienna, Austria

* Author for correspondence: ocostisor@acad-icht.tm.edu.ro

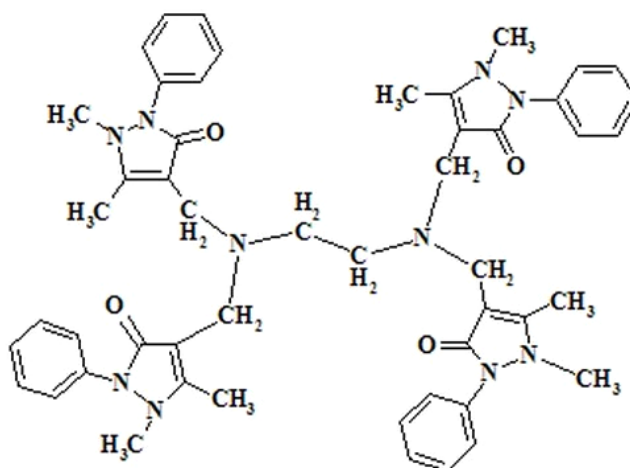


Figure 1. N,N'-tetra-(4-antipyrilmethyl)-1,2-ethanediamine (TAMEN)

The Mannich base, N,N'-tetra-(4-antipyrilmethyl)1,2-ethanediamine (TAMEN) has a symmetric molecule with two groups of potential donor atoms separated by the ethylenediamine bridge (Figure 1). Thanks to the flexibility of the ethylenediamine bridge, TAMEN show a great versatility. Thus, when it acts as bis-tridentate ligand, binuclear complexes have been obtained [22]. Mononuclear complexes have been obtained when TAMEN acts as hexa- or tetradentate ligand [23-25]. The thermal behavior of some monometallic complexes containing TAMEN as ligands have been investigated and the decomposition mechanism for the studied complexes has been established [26-30]. As a continuous work in this field, the new bimetallic complexes $[\text{Cu}(\text{TAMEN})][\text{Zn}(\text{NCS})_4]$ and $[\text{Cu}(\text{TAMEN})\text{ZnCl}_4(\text{H}_2\text{O})]$ are reported along with their thermal behavior.

RESULTS AND DISCUSSION

The complexes $[\text{Cu}(\text{TAMEN})][\text{Zn}(\text{NCS})_4]$ and $[\text{Cu}(\text{TAMEN})\text{ZnCl}_4(\text{H}_2\text{O})]$ were obtained as microcrystalline powders, stable in air, insoluble in most common organic solvents like acetone, chloromethane or benzene, and soluble in DMSO, DMF, acetonitrile. Molar conductivity values of the two complexes in acetonitrile are quite different. Thus, $[\text{Cu}(\text{TAMEN})][\text{Zn}(\text{NCS})_4]$ shows an 1:1 electrolyte type behaviour whereas $[\text{Cu}(\text{TAMEN})\text{ZnCl}_4(\text{H}_2\text{O})]$ is a non-electrolyte [31].

The electronic spectrum of the free ligand shows bands at 244 and 280 nm assigned to the $\pi \rightarrow \pi^*$ and $n \rightarrow \pi^*$ transitions, respectively. In the spectra of the complexes, these are shifted to the higher values denoting

the coordination of the ligand to the metal ion. An intense new band appears around 420 nm in the spectra of the complexes which is attributable to a charge transfer process. Further, the spectra show bands of low intensity in the quite similar region, around 700 nm denoting a similar geometry of the metal ion. According to the literature data, these bands can be assigned to the d-d transitions of copper(II) in a distorted octahedral ligand field [32-34].

The FT-IR spectra of the complexes were recorded and compared with that of the free ligand. Some important differences were noticed. First, the strong band at 1656 cm^{-1} due to the $\nu(\text{C}=\text{O})$ mode in the spectrum of the free ligand is shifted to 1630 and 1631 cm^{-1} for the complexes $[\text{Cu}(\text{TAMEN})][\text{Zn}(\text{NCS})_4]$ and $[\text{Cu}(\text{TAMEN})\text{ZnCl}_4(\text{H}_2\text{O})]$, respectively, proving coordination through antipyrine carbonyl oxygens, which further affect the pyrazolonic ring. Thus, in the spectrum of the free ligand bands assigned to the pyrazolone ring appear in the region $1347\text{-}1494\text{ cm}^{-1}$. They are shifted to $1374\text{-}1493\text{ cm}^{-1}$ in the spectra of the complexes. New bands appear at $1573\text{-}1593\text{ cm}^{-1}$ in the IR spectra also and they are assigned to a combination of the $\nu(\text{C}=\text{O})$ and $\nu(\text{C}=\text{N})$ stretching modes. These changes can be explained by an important contribution of the mesomeric structures II and III of the antipyrine moiety [35].

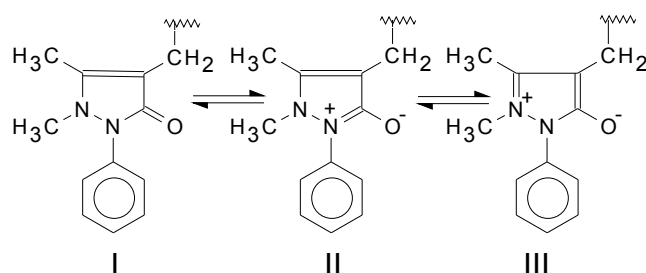


Figure 2. Mesomeric forms of the antipyrine fragment

Bands attributable to $\nu(\text{Cu}-\text{O})$ and $\nu(\text{Cu}-\text{N})$ can be identified in the spectra of both complexes. Thus, for $[\text{Cu}(\text{TAMEN})][\text{Zn}(\text{NCS})_4]$ the weak band at 526 cm^{-1} is assigned to $\nu(\text{Cu}-\text{O})$ and that at 412 cm^{-1} to $\nu(\text{Cu}-\text{N})$. For $[\text{Cu}(\text{TAMEN})\text{ZnCl}_4(\text{H}_2\text{O})]$ these modes appear at 439 cm^{-1} for $\nu(\text{Cu}-\text{O})$ and at 411 cm^{-1} for $\nu(\text{Cu}-\text{N})$, respectively [36, 37]. In the spectrum of this compound a band attributable to $\nu(\text{Zn}-\text{O})$ at 521 cm^{-1} can be noticed. Infrared spectra demonstrate that TAMEN acts as a hexadentate ligand in the $[\text{Cu}(\text{TAMEN})][\text{Zn}(\text{NCS})_4]$ complex. The behaviour of TAMEN as a hexadentate ligand through N_2O_4 donor set in the chromophore $[\text{Cu}(\text{TAMEN})]^{2+}$ has already been demonstrated [24] on the basis of crystallographic analyses. However, the differences between the positions and intensities of the stretching modes

denote that TAMEN acts in a different mode in $[\text{Cu}(\text{TAMEN})\text{ZnCl}_4(\text{H}_2\text{O})]$. Based on our previous results, we assume that TAMEN acts here as a binucleating ligand with copper(II) coordinated by the NO_2 donor set and zinc(II) by O atoms of two antipyrine moieties. The six coordination number of copper(II) is achieved by coordination of two chloride ions and a water molecule. For Zn(II), the usual coordination number 4 is reached by two chloride ions. Crystallographic studies are in progress for this compound. The complex $[\text{Cu}(\text{TAMEN})][\text{Zn}(\text{NCS})_4]$ exhibits a $\nu(\text{CN})$ vibration at 2074 cm^{-1} and $\nu(\text{CS})$ bands at 861 cm^{-1} and 446 cm^{-1} [$\delta(\text{NCS})$], characteristic to the M-NCS bond. Mass spectra showed the molecular peak for both compounds. For $[\text{Cu}(\text{TAMEN})][\text{Zn}(\text{NCS})_4]$, the molecular peak was found at m/z 1222. Together with this signal, were observed as well other two isotopic signals at m/z 1223 and 1224 in the positive mode. In the same time in the negative mode the molecular peak appear at m/z 1222, together with several isotopic peaks from m/z 1215 to 1221. All of these data proved that the assumed structure of $[\text{Cu}(\text{TAMEN})][\text{Zn}(\text{NCS})_4]$ is correct. The mass spectra obtained for the compound $[\text{Cu}(\text{TAMEN})\text{ZnCl}_4(\text{H}_2\text{O})]$ showed the molecular peak (m/z 1149) both in the positive and in the negative mode, with a smaller intensity, probably due to the lower ionization process. As in the previous compound, the mass spectra confirmed the proposed structure for $[\text{Cu}(\text{TAMEN})\text{ZnCl}_4(\text{H}_2\text{O})]$.

Thermoanalytical studies of complexes

The decomposition curves in the case of $[\text{Cu}(\text{TAMEN})][\text{Zn}(\text{NCS})_4]$ shows that below 200°C there is no definite peak on DTG and endothermic peak on DTA curve, so it could be concluded that there are no coordinated water molecules in the complex compound. In the temperature range $200\text{--}340^\circ\text{C}$, a mass loss of 32.52% correspond to a partial loss of ligand, accompanied by an exothermic process. In the temperature range $340\text{--}600^\circ\text{C}$ the mass loss of 45.45% corresponds to the loss of the rest of the ligand and a deposit of $\text{CuO}+\text{Zn}(\text{SCN})_2$ is formed. On DTA curves the exothermic process is observed. Between $620\text{--}1000^\circ\text{C}$ from the $\text{Zn}(\text{SCN})_2$, ZnO is formed. The mass loss is about 7.08 %.

The decomposition curves of complex $[\text{Cu}(\text{TAMEN})\text{ZnCl}_4(\text{H}_2\text{O})]$ shows below the temperature of 150°C a mass loss of about 1.70% that corresponds to the loss of one water molecule. This process is accompanied by an endothermic process on the DTA curve. The second stage of decomposition takes place between the temperature range $150\text{--}250^\circ\text{C}$ with a loss of two chlorine atoms (the mass loss about 6.25%) and a loss of 0.47 molecule of TAMEN. On DTA curve a large exothermic peak are started in this temperature range with two small maxima. Between $250\text{--}450^\circ\text{C}$ a part of ligand release the solid matter and an exothermic process appears on the DTA curve, corresponding to a 34.96% mass loss. The fourth stage of decomposition

process occurs in the temperature range 450-1000°C, corresponding to the mass loss of the rest of the ligand, about 45.84%, and to the formation of a deposit of CuO and ZnO. On the DTA curve a continuous exothermic process appears.

EXPERIMENTAL

All chemicals have been purchased from commercial sources and were used without further purification. Analytical data were obtained by a Perkin-Elmer model 240C elemental analyzer. Metal ions analysis was performed by atomic absorption spectroscopy with a GBC SENSAA spectrophotometer. IR spectra were recorded in KBr pellets with a JASCO 430 FT-IR spectrometer (4000–400 cm^{-1}). Electric conductivities were measured at room temperature in acetonitrile solutions with a WTW conductivity meter. Electronic absorption spectra of freshly prepared acetonitrile solutions (10^{-3} M) were measured on a Perkin Elmer Lambda 12 spectrophotometer. The mass spectra were obtained using a mass spectrometer Esquire 6000 ESI (electrospray ionization) from Bruker Daltonics. All the compounds analyzed were diluted before measurements at 10^{-5} M, in acetonitrile. A small syringe pump is included with the instrument system to provide the introduction of samples directly to either the electrospray. The solution was injected into the spray chamber by a Hamilton syringe, with a constant flow of 250 $\mu\text{l/h}$. The API-ESI (Atmospheric Pressure Interface-ElectroSpray Ionization) generates ions, focuses and transports them into the ion trap mass analyzer. The thermal analysis was performed with a computer-controlled MOM derivatograph. The mass of the investigated samples was 30-60 mg. The measurements were made between room temperature and 1000°C at a heating rate of 5°C/min, in ceramic crucibles under static atmosphere of air, with $\alpha\text{-Al}_2\text{O}_3$ as reference substance.

Synthesis of the ligand and the complexes

The ligand TAMEN has been obtained following a Mannich type condensation between antipyrine, 1,2-ethandiamine and formaldehyde [14].

[Cu(TAMEN)][Zn(NCS)₄]

$\text{CuCl}_2 \cdot 2\text{H}_2\text{O}$ (0.17 g, 1 mmol) dissolved in 5 ml ethanol was mixed with TAMEN (0.86 g, 1 mmol) dissolved in 10 ml ethanol at 45°C and stirred for 30 min. Further, $\text{Zn}(\text{CH}_3\text{COO})_2 \cdot 2\text{H}_2\text{O}$ (0.22 g, 1 mmol) and NH_4SCN (0.37g (4.75 mmol) dissolved in 5 ml EtOH was slowly added to the reaction mixture and stirred for 2 hours. The resulting green product was filtered, washed with ether and dried over CaCl_2 in air. Yield: (0.94 g) 77 %; UV-VIS (CH_3CN) spectrum: $\lambda_{\text{max}}(\epsilon) = 269 (4\ 940), 295 (3110), 422 (480), 685 (50)$ nm. IR spectrum (KBr), ν / cm^{-1} : 2917 m, 2352 w, 2103 sh, 2074 s, 1630 m, 1593 w, 1564 m, 1488 m, 1453 m, 1429 m, 1374 m, 1304 s, 1247 w,

1172 w, 1144 m, 1108 m, 1077 w, 1025 m, 901 m, 861 w, 808 w, 762 s, 695 s, 648 m, 607 m, 526 w, 505 w, 479 w. 446 w, 412 w. Molar conductivity in CH₃CN ($\Omega^{-1}\text{mol}^{-1}\text{cm}^2$):120. *Anal.* Calcd. mass fractions of elements, w/%, for CuZnC₅₄H₅₆O₄N₁₄S₄ (MW 1222.30 g/mol) are: C 53.06, H 4.62, N 16.04, O 5.24, S 10.49, Cu 5.20, Zn 5.35; found: C 53.10, H 4.58, N 15.99, O 5.29, S 10.45, Cu 5.19, Zn 5.40. MS+: m/z 1222, 1223, 1224. MS-: m/z.1215, 1216, 1217, 1218, 1219, 1220, 1221, 1222

[Cu(TAMEN)ZnCl₄(H₂O)]

CuCl₂·2H₂O (0.17 g, 1 mmol) dissolved in 2 ml ethanol and Zn(CH₃COO)₂ (0.22 g, 1 mmol) was mixed with TAMEN (0.86 g, 1 mmol) dissolved in 20 ml ethanol under vigorous stirring. The green mixture was further stirred for 2 hours and the resulted blue product was filtered, washed with ether and dried over CaCl₂ in air. Yield: (0.88 g) 69%; UV-VIS spectrum (CH₃CN): $\lambda_{\text{max}}/\text{nm}$ 269, 299, 416 (240), 706, $\epsilon/\text{l mol}^{-1}\text{cm}^{-1}$ 4940, 3150 (30). IR spectrum (KBr) ν/cm^{-1} : 3465m, 2921 m, 2352 w, 1631m, 1573 s, 1493 m, 1457 m, 1431 m, 1379 w, 1299 m, 1249 w, 1145 w, 1107 m, 1078 m, 1026 m, 930w, 903 m, 864 w, 762 s, 696 s, 653 m, 607 m, 521w, 507 w, 461 w; 439 w, 411 w. Molar conductivity(CH₃CN) $\Lambda/\Omega^{-1}\text{mol}^{-1}\text{cm}^2$: 20. *Anal.* Calcd. mass fractions of elements, w/%, for CuZnC₅₀H₅₈O₅N₁₀Cl₄ (MW 1149.81 g/mol) are: C 52.23, H 5.08, N 12.18, O 6.96, Cl 12.33, Cu 5.53, Zn 5.69; found: C 51.98, H 5.01, N 12.26, O 6.84, Cl 12.33, Cu 5.58, Zn 6.00. MS+: m/z 1148, 1149, 1150. MS-: m/z 1148, 1149.

CONCLUSION

New Cu(II) and Zn(II) complexes were synthesised and studied. Molar conductivity data shows that the complex [Cu(TAMEN)][Zn(NCS)₄] presents a 1:1 electrolyte type in acetonitrile solution and [Cu(TAMEN)ZnCl₄(H₂O)] a non-electrolyte type behavior. The visible absorption spectra of the complexes suggest that the copper(II) ions are in solution in a distorted octahedral ligand field. IR spectra have revealed that the ligand acts as a hexadentate donor in the case of [Cu(TAMEN)][Zn(NCS)₄], through the four oxygen atoms belonging to the antipyrine fragments and two nitrogen atoms of ethylenediamine and as bis-tridentate in the case of [Cu(TAMEN)ZnCl₄(H₂O)] through the O₂N donor set.

ACKNOWLEDGEMENTS

The authors would like to thank the Romanian and Hungarian Academies of Sciences for financial assistance. Thanks for financial support are also expressed to the "Fonds zur Förderung der Wissenschaftlichen Forschung in Österreich" (Project 19335-N17).

REFERENCES

1. C. H. Sayed, A. A. Hamed, G. A. Meligi, W. E. Boraie, M. Shafic, *Molecules*, **2003**, *8*, 322.
2. Y. Zhang, L. Yzhi, T. Hanbin, Z. Longgen, *Acta Crystallographica*, **2002**, *E58*, 24.
3. G. Turan-Zitouni, M. Sivaci, F. S. Kilic, K. Erol, *European Journal of Medicinal Chemistry*, **2001**, *36*, 685.
4. G. H. Sayed, A. Radwan, S. M. Mohamed, S. A. Shiba, M. Kalil, *Chinese Journal of Chemistry*, **1992**, *10*, 475.
5. M. Daoudi, N. B. Larbi, D. Benjelloun, A. Kerbal, J. P. Launaly, J. Bonvoisin, J. Jaud, M. Mimouni, J. Hadda, *Molecules*, **2003**, *8*, 269.
6. T. N. Sorrel, V. A. Vankai, M. L. Garrity, *Inorganic Chemistry*, **1991**, *30*, 207.
7. A. Togni, L. M. Venanzi, *Angewandte Chemie International Edition Eng.*, **1994**, *33*, 497.
8. A. Kandil, A. Hamid, *Journal of Drug Research*, **1980**, *12*, 27.
9. A. M. Farghlay, A. Hozza, *Pharmazie*, **1980**, *35*, 596.
10. H. Tronnier, *Acta Fac. Med. Univ. Brun*, **1972**, *40*, 211.
11. J. F. Cumming, *Clinical Pharmacology & Therapeutics*, **1976**, *19*, 486.
12. A. Doario, D. Craciunescu, C. Ghirvu, J. Nuno, *An. Quim*, **1977**, *73*, 1120.
13. N. T. Madhu, P. K. Radhakrishnan, M. Grunert, P. Weinberger, W. Linert, *Review in Inorganic Chemistry*, **2003**, *23*, 1 and references therein.
14. C. Mannich, W. Krösche, *Archiv der Pharmazie*, **1912**, *250*, 647. C. Mannich, B. Kather, *Archiv der Pharmazie*, **1919**, *18*, 257.
15. O. Costisor, A. Maurer, A. Tomescu, S. Policec, *Buletinul Stiintifico-Tehnic al Institutului Politehnic Timisoara, Seria Chimie*, **1981**, *26*, 93.
16. O. Costisor, A. Maurer, S. Policec, *Buletinul Stiintifico-Tehnic al Institutului Politehnic Timisoara, Seria Chimie*, **1981**, *26*, 87.
17. W. Linert, O. Costisor, R. Tudose, *Oriental Journal of Chemistry*, **1995**, *11*, 107.
18. Al. Stupariu, O. Costisor, E. Bedrosian, L. Radbea, E. Szabo, *Rev. Rom. Med. Veter.*, **1995**, *5*, 81.
19. R. Alexandrova, G. Rashkova, T. Popova, R. Tudose, E. M. Mosoarca, S. Slavov, O. Costisor, *Acta Morphologica and Anthropologica*, **2006**, *11*, 60.
20. R. Alexandrova, G. Rashkova, T. Popova, R. Tudose, E. M. Mosoarca, S. Slavov, O. Costisor, *Experimental Pathology and Parasitology*, **2005**, *8/2*, 93.
21. R. Alexandrova, A. Vacheva, M. Kirilova, G. Miloshev, E. M. Mosoarca, R. Tudose, O. Costisor, *Acta Morphologica and Anthropológica*, **2007**, *12*, 72.
22. O. Costisor, W. Linert, S. Deusch, C. Stanescu, *Journal of Coordination Chemistry*, **1994**, *33*, 229.
23. R. Tudose, I. Pantenburg, E. M. Mosoarca, G. Meyer, O. Costisor, *Zeitschrift für anorganische und allgemeine Chemie*, **2005**, *632*, 1491.

24. R. Tudose, I. Pantenburg, E. M. Mosoarca, G. Meyer, O. Costisor, *Zeitschrift für anorganische und allgemeine Chemie*, **2005**, 631, 2423.
25. E. M. Mosoarca, R. Tudose, R. Alexandrova, O. Costisor, *Chemical Bulletin of "Politehnica" University Timișoara*, **2004**, 63, 49.
26. I. Labadi, R. Tudose, I. Fejer, Z. Jori, O. Costisor, *Journal of Thermal Analysis and Calorimetry*, **1999**, 56, 553.
27. I. Labadi, Zs. Czibulya, R. Tudose, O. Costisor, *Journal of Thermal Analysis and Calorimetry*, **2004**, 77, 553.
28. I. Labadi, E. Pal, R. Tudose, O. Costisor, *Journal of Thermal Analysis and Calorimetry*, **2006**, 83, 681.
29. V. Sasca, E. M. Mosoarca, L. Avram, R. Tudose, O. Costisor, *Journal of Thermal Analysis and Calorimetry*, **2008**, 94(2), 355.
30. E. M. Mosoarca, V. Sasca, L. Avram, R. Tudose, O. Costisor, *Journal of Thermal Analysis and Calorimetry*, **2008**, 94(2), 361.
31. W. Geary, *Journal of Coordination Chemistry Review*, **1971**, 7, 81.
32. A.B.P. Lever, *Inorganic Electronic Spectroscopy*, Elsevier Publishing Company, Amsterdam, **1968**, 318.
33. N. T. Madhu, P. K. Radhakrishnan, *Transition Metal Chemistry*, **2000**, 25, 287.
34. N. Kalarani, S. Sangeetha, P. Kamalakannan and D. Venkappaya, *Russian Journal of Coordination Chemistry*, **2003**, 29 (12), 845.
35. M. Hesse, H. Meier, B. Zeeh, *Spektroskopische Methoden in der Organischen Chemie*, G. Thieme Verlag, Stuttgart, **1987**, 255.
36. K. Nakamoto, *Infrared and Raman Spectra of Inorganic and Coordination Compounds*, John Wiley & Sons, New York, **1986**, 283.
37. J. R. Ferraro, *Low-frequency vibration of inorganic and coordination compounds*, Plenum Press, New York, **1971**, 65.

Dedicated to the memory of Prof. dr. Ioan Silaghi-Dumitrescu marking 60 years from his birth

MICROWAVES ASSSITED N-ALKYLATION OF PHENOTHIAZINE

LUIZA GĂINĂ, TIMEA DALLOS, CASTELIA CRISTEA*,
TAMAS LOVASZ, IANI PERETEANU, MIHAI SURDUCAN
AND LUMINIȚA SILAGHI-DUMITRESCU

ABSTRACT. A *green chemistry* approach to the N-alkylation of phenothiazine is described. The chemical process was improved by applying the microwave assisted heating technique in closed vessel and by using safer solvents such as alcohol or PEG. Reaction conditions were optimized to give good yields in short reaction times.

Keywords: *Phenothiazine, N-alkylation, MAOS, green chemistry*

INTRODUCTION

N-alkyl-phenothiazine derivatives, proved to be extremely usefull substrates for the regioselective preparation of C-substituted phenothiazine derivatives *via* direct aromatic electrophilic substitution as well as by using organometallic intermediates [1-6]. N-methyl- and 10-ethylphenothiazines were prepared right at the begining of the phenothiazine chemistry by using the corresponding alcohols as alkylating agents [7] and the seeking for improved reaction conditions never stopped ever since. In alkaline conditions, alkyl halides proved to be excellent alkylating agents and large scale application were developed for the preparation of neuroleptic drugs containing this pharmacophore unit [8]. DMS [9] and oxalic acid esters [10] were also reported as alkylating agents.

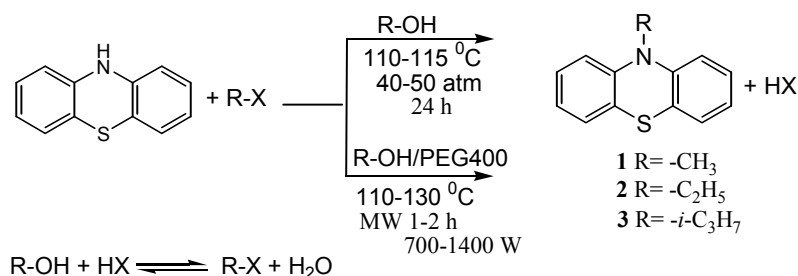
The tremendous development of microwave assisted organic synthesis (MAOS) during the last decades is supported by certain advantages such as: reaction rate acceleration, milder reaction conditions, lower energy input, usually higher reaction yields and sometimes different selectivity, which were observed after microwave irradiation, as compared to conventional convective heating of the reaction mixtures [11,12]. These advantages successfully integrate MAOS into the *green chemistry* principles, seeking for the development of cleaner, environmentally benign and energy efficient processes [13].

* *Universitatea Babeș-Bolyai, Facultatea de Chimie și Inginerie Chimică, Str. Kogălniceanu Nr. 1, RO-400084 Cluj-Napoca, Romania, castelia@chem.ubbcluj.ro*

The aim of this work is to describe our contribution to the improvement of the reaction conditions applied for the *N*-alkylation of phenothiazine with alkyl-halides, based on *green chemistry* principles and new technical possibilities offered by the use of modern *on-line* controlled microwave assisted reactors.

RESULTS AND DISCUSSION

A mixture of alkyl iodide and alcohol gave good yields of *N*-alkyl phenothiazine, when the reaction was performed at high temperatures (110-120 °C) in closed vessels (scheme 1). A volatile alcohol develops high internal pressures and may also participate to the *in situ* regeneration of alkyl iodide and for these reasons both the alkyl halide and the alcohol should contain the same alkyl chain. In these conditions, *N*-methyl-phenothiazine **1** was obtained more than 70% yield by using a mixture of methyl iodide and methanol, while a mixture of ethyl iodide and ethanol gave *N*-ethyl-phenothiazine **2** in lower yields (50-70%) [14,15]. 24 Hours of heating were required to complete these reactions and longer alkyl chains could not be attached to the heterocyclic nitrogen atom under these circumstances.



Scheme 1

Particularly efficient heating processes induced by the dielectric heating afforded shorter reaction times for the alkylation of phenothiazine with methyl iodide, ethyl iodide and *i*-propyl bromide respectively, in the presence of the proper alcohol, which is a solvent with medium absorbing properties of the microwave radiation (scheme 1). As it can be seen from table 1 which summarises the results obtained when different reaction conditions were applied, the best results were obtained when the corresponding alcohol was employed. Even though the recorded yields were decreasing with the increase of the alkyl chain, *N*-*i*-propyl-phenothiazine **3** could be obtained in 56% yields using an alkylating mixture of *i*-propyl bromide and isopropanol after 40 minutes of high power irradiation.

MICROWAVES ASSSITED *N*-ALKYLATION OF PHENOTHIAZINE

In our survey for safer solvents we selected PEG, a solvent capable to efficiently absorb microwave energy and thus to ensure a rapid heating of the reaction mixture by dipolar polarization mechanism.

However, as it can be seen in table 1, the yields in the methylation reaction were not improved neither when a mixture of alcohol and PEG (v/v 1:1), nor PEG was employed. Satisfactory yields were generated when catalytic amounts of were added Cs₂CO₃ to the PEG containing reaction mixture.

Table 1. Experimental conditions employed for the microwave assisted alkylation of phenothiazine with alkylhalides

| Cpd | Solvent v/v | Temp _{max} [°C] | Power/time [W]/[min] | Yield % |
|----------|---|-----------------------------|-------------------------------|---------|
| 1 | MeOH | 110 | 800W/20 min 1000W/90 min | 79 |
| | PEG400/CH ₃ OH 1/1 | 110 | 800W/20 min , 1000W/60 min | 20 |
| | PEG400 | 110 | 800W/20 min, 1000W/60 min | 16 |
| | <i>n</i> -BuOH, Cs ₂ CO ₃ | 130 | 700W/1 min 800W/15 min | 49 |
| | PEG400 Cs ₂ CO ₃ | 125 | 700W/2 min 800W/60 min | 44 |
| | BuOH, H ₂ O, Aliquat 336, KOH | 130 | 700W/90 min, 800W/15 min | 43 |
| 2 | EtOH | | 800W/20 min 1000W90 min | 65 |
| | PEG400/EtOH, 1/1 | 140 | 500W/40 min 800W/30 min | 54 |
| | PEG400 | 130 | 800W/2 min 500W/60 min | 17 |
| 3 | <i>i</i> -PrOH | 130 | 1400W/40 min | 56 |
| | PEG400, Cs ₂ CO ₃ | 120 | 700W/2 min 800 W/60 min | 10 |

Microwave irradiation was applied for the methylation of phenothiazine with methyl iodide under phase transfer catalysis conditions (using PTC catalyst Aliquat 336, butanol solvent and KOH base). Satisfactory yields were obtained in much shorter reaction time, as compared to classical PTC experiment which typically requires 48-72 hours of vigorous stirring.

CONCLUSIONS

MAOS can be successfully applied to the preparation of N-alkyl-phenothiazine with the advantage of a much shorter reaction time required in order to obtain comparable reaction yields with those resulted under conductive heating conditions. High power microwave irradiation of a mixture of phenothiazine, alkyl halide and alcohol may afford satisfactory yields of N-alkyl-phenothiazines containing more than 2 carbon atoms in the side chain.

EXPERIMENTAL SECTION

Microwave installation *Synthos 3000* equipped with temperature and pressure sensors, power control and software operation.

Merck reagents.

400 MHz NMR spectrometer Bruker Avance

Microwave assisted synthesis of N-alkyl-phenothiazine, general procedure:

The reaction mixture (phenothiazine, alkylhalide, as well as any starting materials required according to conditions listed in table 1) solved in the properly chosen solvent was introduced in the quartz reaction vessel, which was sealed and then subjected to microwave irradiation in the resonance cavity of the microwave power system. Samples temperatures were automatically monitored during the irradiation with the prescribed power level. Inside pressure was monitored during the experiment. After irradiation, the solvent was removed by filtration and the solid product was purified by recrystallization.

10-methyl-10H-phenothiazine 1

a) 5 mmol (1g) phenothiazine, 6.4 mmol (0.4 ml) methyl iodide, 10 ml MeOH were treated according to the general procedure and the parameters listed in table 1 were applied.

b) Microwave assisted PTC methylation

A mixture of 1.25 mmol (1g) phenothiazine, 1.6 mmol (0.1 ml) methyl iodide, 5 ml BuOH, 5 ml of 10% KOH aq. and catalytic amounts of Aliquat 336 was vigorously stirred in the closed vessel, while microwave irradiation was applied according to conditions described in table 1. The resulted reaction mixture was poured in water and the product was extracted in dichloromethane After solvent removal, the crude product was recrystallised from EtOH.

Recrystallization from EtOH. White crystals m.p.= 99,5°C, (lit. 99°C, 101-103 °C [14])

¹H-RMN 400MHz, CDCl₃: δ(ppm): 3,38ppm (s, 3H, H_a); 6,82ppm (d, 2H, ³J_{orto}= 8,4Hz, H₁); 6,93ppm (td, 2H, H₃); 7,14ppm (dd, 2H, ³J_{orto}= 7,1Hz, ⁴J_{meta}= 1,2Hz, H₄); 7,17ppm (td, 2H, ⁴J_{meta}= 1,2Hz, H₂) **¹³C-RMN**, CDCl₃: δ(ppm): 35,3ppm (CH₃, C_a); 114,0ppm (CH, C₁); 122,4ppm (CH, C₃); δ=123,4ppm (C_q, C_{4a}); 127,1ppm (CH, C₂); 127,4ppm (CH, C₄); 145,80ppm (C_q, C_{9a}).

10-ethyl-10H-phenothiazine 2

1.25 mmol (0.25g) phenothiazine, 1.6 mmol (0.2 ml) ethyl iodide, 10 ml EtOH were treated according to the general procedure and the parameters listed in table 1 were applied.

Recrystallization from EtOH. White crystals m.p.= 104.5°C (lit. 101-103°C [14])

¹H-RMN 400MHz, CDCl₃: δ(ppm): 1,38ppm (t, 3H, ³J= 6,8Hz, H_b); 3,88ppm (q, 2H, ³J= 6,8Hz, H_a); 6,83ppm (d, 2H, ³J_{orto}= 8,0Hz, H₁); 6,87ppm (t, 2H, H₃); 7,11ppm (m, 4H, ³J_{orto}= 7,6Hz, H_{2,4}) **¹³C-RMN**, CDCl₃: δ(ppm): 13,0ppm (CH₃, C_b); 41,7ppm (CH₂, C_a); 115,0ppm (CH, C₁); 122,2ppm (CH, C₃); 124,4ppm (C_q, C_{4a}); 127,2ppm (CH, C₂); 127,3ppm (CH, C₄); 144.9ppm (CH, C_{9a})

10-isopropyl-10H-phenothiazine 3

1.25 mmol (0.25g) phenothiazine, 1.6 mmol (0.15 ml) *i*-propyl bromide, 10 ml *i*-PrOH were treated according to the general procedure and the parameters listed in table 1 were applied.

Recrystallization from EtOH. m.p.= 60,5°C (lit 59-60 °C [14])

¹H-RMN 400MHz, CDCl₃: δ(ppm): 1,38ppm (d, 6H, ³J= 7,2Hz, H_b); 3,46ppm (m, 2H, ³J= 7,2Hz, H_a); 6,90ppm (t, 2H, H₃); 7,01ppm (d, 2H, ³J_{orto}= 8,2Hz, H₁); 7,17ppm (m, 4H, ³J_{orto}= 7,3Hz, H_{2,4}) **¹³C-RMN**, CDCl₃: δ(ppm): 16,5ppm (CH₃, C_b); 33,7ppm (CH, C_a); 115,0ppm (CH, C₁); 122,4ppm (CH, C₃); 123,4ppm (CH, C_{4a}); 127,2ppm (CH, C₂); 127,4ppm (CH, C₄); 145,1ppm (CH, C_{9a})

ACKNOWLEDGMENTS

Financial support from Roumanian Ministry of Education Research, Youth and Sports, grant PN-II-ID-564 is greatly acknowledged.

REFERENCES

1. T. Kline, E. Sieber-McMaster, W.F.Lau, S. Natarajan, *Bioorg. & Med. Chem. Lett.*, **1997**, 7(8), 1017.
2. S. Ebdrup, *Synthesis*, **1998**, 8, 1107.
3. T. J. J. Müller, *Tetrahedron Letters*, **1999**, 40, 6563.
4. Ng. Ph. Buu-Hoï, N. G. Hoán, *J. Chem. Soc.*, **1951**, 1834.

L. GĂINĂ, T. DALLOS, C. CRISTEA, T. LOVASZ, I. PERETEANU, M. SURDUCAN, L. SILAGHI-DUMITRESCU

5. G. Cauquil, E. Casadevall, R. Greze, *Bull. Soc. Chim. Fr.*, **1964**, 590.
6. V. Fărcășan, *Rev. Roum. Chim.*, **1970**, 15, 178.
7. A. Bernthsen, *Ann.*, **1885**, 230, 88.
8. R. R. Gupta, *Phenothiazines and 1,4-benzothiazines Chemical and Biomedical aspects in Bioactive Molecules*, Elsevier, **1988**, chapter 1.
9. Ng. Ph. Buu-Hoï, N. G. Hoán, *J. Chem. Soc.*, **1951**, 1834.
10. C. Lespagnol, *Bull. Soc. Chim. Fr.*, **1959**, 112.
11. A. Loupy (Ed), *Microwaves in Organic Chemistry*, Wiley-VCH Weinheim, **2002**.
12. P. Lidstrom, J. P. Tierney (Eds), *Microwave-Assisted Organic Synthesis*, Blackwell, Oxford, **2004**.
13. P. T. Anastas, J. C. Warner, "Green Chemistry Theory and Practice", Oxford Univ. Press, **1998**.
14. S. P. Massie, *Chem. Rev.*, **1954**, 54, 797.
15. H. Bernstein, L. Rothstein, *J. Am. Chem. Soc.*, **1944**, 66, 1886.

Dedicated to the memory of Prof. dr. Ioan Silaghi-Dumitrescu marking 60 years from his birth

**PURINE METABOLISM DYSHOMEOSTASIS AND THE
HETEROGENOUS NUCLEATION OF UROCONCREMENTS
NOTE I. ALKALINE AND ALKALINE-EARTH METALS
IN PURINE UROLITHIASIS**

**ZENO GARBAN^a, ADINA-ELENA AVACOVICI^b, GABRIELA GARBAN^c,
FRANCISC PETER^b, GEORGE-DANIEL GHIBU^a,
MIRCEA BOTOCA^d, ALIN CUMPĂNAȘ^d**

ABSTRACT. Biogenesis of lithiasic concrements constitutes a special domain when taking into account the location of lithiasis (currently named calculi or stones) in the organism, e.g.: sialolithiasis, rhinolithiasis, urolithiasis, flebolithiasis a.o. as well as the type of lithiasis.

In case of purine metabolites of endogenous (strictly metabolic) and exogenous (foods) origin the concrements formation in urine implies a heterogenous nucleation mechanism where metallic ions participate, too.

Problems concerning the purine uroconcrements (mainly with uric acid) and their content in alkaline and alkaline-earth metals were approached by investigations based on physico-chemical methods. Thus, by Fourier Transform - Infrared Spectroscopy the types of urolithiasis and by atomic absorption spectroscopy the metallogram (Na, K, Ca and Mg) of purine urolithiasis were established.

Keywords: *purine metabolism and uroconcrements; alkaline and alkaline-earth metals in purine uroconcrements*

INTRODUCTION

The problem of purine uroconcrements biogenesis is integrated in the modern approach of the complex aspects of proteomics and metallomics with application in the study of urolithiasis. Under the incidence of proteomics

^a *Department of Biochemistry and Molecular Biology, Faculty of Food Products Technology, University of Agricultural Sciences and Veterinary Medicine of Banat Timisoara, Calea Aradului Nr. 119, RO-300 645 Timișoara, Romania, zeno.garban@yahoo.com*

^b *Faculty of Industrial Chemistry and Environmental Engineering, University "Politehnica" of Timisoara*

^c *Laboratory of Environment and Nutrition, Institute of Public Health Timisoara*

^d *Clinic of Urology, Faculty of Medicine, University of Medicine and Pharmacy „Victor Babeș” Timișoara*

falls the nucleic acids (i.e. deoxyribonucleic acid - DNA and ribonucleic acid - RNA) biodegradation, resulting pyrimidine and purine derivatives Under the incidence of metallomics falls the metallic ions presence in blood and tissues as well as their capacity to generate in urine crystallization nuclei called „primers” or „starters” [1-4].

Commonly in the biogenesis of uroconcrements take part various metabolites like: purine derivatives (mostly uric acid), oxalic acid and oxalates, cystine, phosphates a.o. beside metallic ions ([5].

Nowadays the urolithiasis (kidney stones or urinary stones) represent about 1-2% of all diseases, about 12-40% among kidney diseases and affects about 3% of the acive people.

In the biochemical pathology of urolithiasis problems concerning the etiology, pathogenesis and composition of uroconcrements implies a complex inter- and multidisciplinary approach [6]. Efficient metaphylaxy and prophylaxy in case of urolithiasis can be achieved only by the exact knowledge of stone components [7].

The aim of the study was the determination of the qualitative composition of uroconcrements by Fourier Transform - Infrared Spectroscopy (abbreviated as FT-IR or FTIR) and thus the identification of the urolithiasis type as well as the determination, by atomic absorption spectroscopy (AAS), the concentration of alkaline and alkaline-earth metals in the purine urolithiasis.

RESULTS AND DISCUSSION

Free purines in the blood flow have the following sources: tissular purines - as a results of nucleic acid degradation; exogenous nucleoproteins - brought by food intake; newly synthetized purines in the organism - de novo biosynthesis [2, 8, 9].

Issues related to purine precursors of uroconcrements are integrated in the vast domain of proteomics. In this background there are discussed metabolic aspects, homeostasis and pathobiochemistry of purine metabolites.

In figure 1 there is presented the schematic degradation of nucleic acids with purine metabolites formation. Some of the resulted metabolites are precursor of purine uroconcrements.

As metal ions play an important role in the biogenesis of uroconcrements [3,10] the discussed subject of this study can be integrated also in metallomics, a consequential domain for environment, medicine and biology [11, 12]

It is known that between some purine derivatives and metallic ions occur the process named „heterogenous nucleation” where the starters become precursors of uroconcrements with a continuous growth. The presence of purine metabolites, of metallic ions as well as a protein and glycoprotein or mucoprotein "matrix" in the urine allow the "starters" or "primers" formation [10, 13-15].

These urolithiasis appear as the consequence of disturbances in purine nucleotides metabolism, homeostasis and excretion of the biodegraded end products, i.e. purine derivatives (uric acid, xanthine, 2,8-dihydroxyadenine).

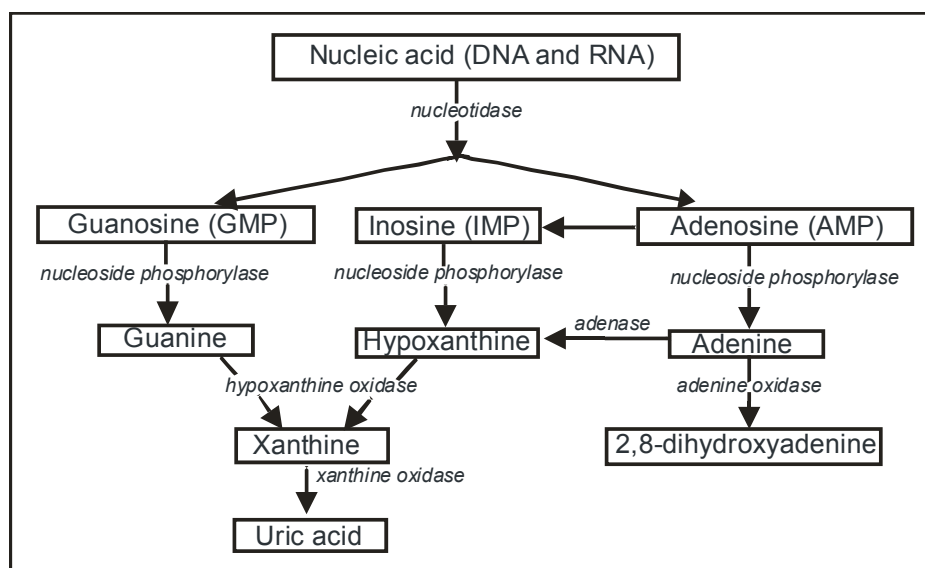


Figure 1. Main purine derivatives resulted from the biodegradation of nucleic acids

Uric acid is the end product of purine metabolism in man and is poorly soluble in biological fluids. It is excreted partly (2/3) by urinary tract and partly (1/3) eliminated by the gastrointestinal tract. Uric acid is filtered by the glomerulus and the filtered uric acid is almost completely reabsorbed in the proximal tubule. Further uric acid is secreted in to the lumen in the distal part of the proximal tubule and the daily urinary output of uric acid in a normal male on a purine-free diet is 1.6 - 3.6 mmoles (270 - 600 mg). The normal blood uric acid level is 40 ± 70 mg/L in man and 35 ± 60 mg/L in woman. Men tend to have higher values than women. Changes in the dietary intake of purines make relatively small differences to the blood plasma level of uric acid.

The in excess accumulation of uric acid in the urinary tract, alongside with other organic and inorganic substances (mainly metals) may lead - through coprecipitative processes - to starters formation in lithogenesis. This process is favored by a lower urine pH and by the low urine flow rate.

Uric lithiasis has a relatively low frequency among urolithiasis but the most increased among purine lithiasis. Most uric acid stones result by the precipitation of uric acid from supersaturated urine. Uric acid urolithiasis is often accompanied by uric acid crystals in the urine sediment. Excessive urinary uric acid excretion may result from increased filtration of uric acid (from excessive dietary purine intake, metabolic errors, myeloproliferative disorders, or hemolysis), from tubular effects such as an isolated defect in renal tubular uric reabsorption, or from generalized tubular dysfunction. Uric acid excretion is increased in as many as 10% of patients with hypercalciuria and urolithiasis. In endemic areas such as Southeast Asia and the Mediterranean region, uric acid stones are frequently not associated with hyperuricemia.

Xanthine lithiasis, rarely occurred, is difficult to be found. Sometimes is necessary to make use of differential spectrophotometry, X ray diffraction or chromatography in order to diagnose it. It appears as a consequence of a metabolic disturbances in which xanthine oxidase is implicated. This enzyme catalyses the hypoxanthine oxidation to xanthine and then of the xanthine to uric acid [16,17]. Often this dysmetabolism could be observed in childhood and is the consequence of an inherited xanthine oxidase deficiency.

The *2,8-dihydroxyadenine lithiasis* is very rare and in numerous cases may be confounded with uric lithiasis. At the origin is a defect in purine metabolism consisting in the deficiency of the adenine phosphoribosyl-transferase enzyme [18, 19]

Literature data concerning the purine derivatives concentration in urine, compiled by Altman and Dittmer [20] are presented in Table 1.

Table 1. Concentrations of purine nucleobases and other purine derivatives in urine

| Nr. | Purine metabolites | Values (mg/kg body) | |
|-----|--------------------------------|---------------------|---------------|
| | | Mean | Range |
| 1. | Adenine | 0.020 | 0.016 – 0.240 |
| 2. | Guanine | 0.006 | 0.003 – 0.009 |
| | 8-hydroxy-7-methyl-guanine | 0.020 | 0.016 – 0.030 |
| | 7-methyl-guanine | 0.090 | 0.080 – 0.110 |
| | N ² -methyl-guanine | 0.007 | 0.006 – 0.009 |
| 3. | Hypoxanthine | 0.140 | 0.080 – 0.190 |
| | 1-methyl-hipoxanthine | 0.006 | 0.003 – 0.010 |
| 4. | Xanthine | 0.090 | 0.070 – 0.120 |
| 5. | Uric acid | 2.000 | 0.800 – 3.000 |
| | 1,3-dimethyl-uric acid | traces | |
| 6. | Purine bases - total | | 0.200 – 1.000 |

The presence of oxypurines, end products of purine catabolism, is conditioned by pH level. Data presented by Klinenberg et al., cited by Watts [21] reveal the solubility of the purinic metabolites: hypoxanthine, xanthine and uric acid (Table 2). It is noticed that solubility differs in serum and urine conditioned by the purine metabolites and the pH of the medium.

In order to identify the chemical substances present in urolithiasis “standard spectra” of the appropriate chemically pure compounds were recorded and the specific FT-IR absorption bands for every compound have been identified, confirmed by the available literature data [22-25].

Table 2. Data concerning pH-solubility relationship of purine metabolites

| Medium | pH | Solubility (mg/ 100 mL) | | |
|--------|-----|-------------------------|----------|--------------|
| | | Uric acid | Xanthine | Hypoxanthine |
| Serum | 7.4 | 7 | 10 | 115 |
| Urine | 5.0 | 15 | 5 | 140 |
| | 7.0 | 200 | 13 | 150 |

Thus, there were recorded standard spectra for uric acid, xanthine, 2,8-dihydroxy-adenine, oxalates, phosphates, cystine, carbonates. Such a standard FT-IR spectrum for uric acid is given in figure 2.

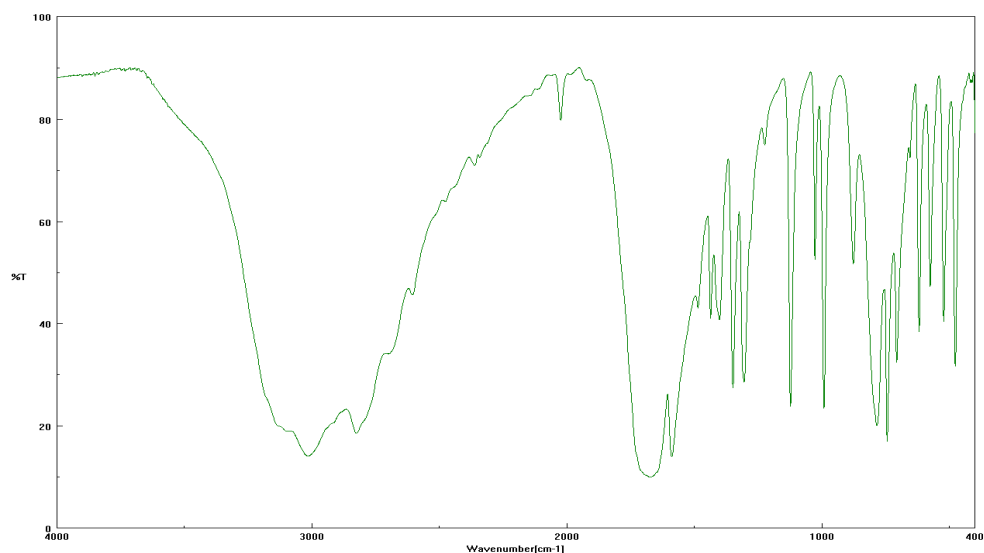


Figure 2. Standard spectrum of uric acid obtained by FT-IR

In the standard FT-IR spectrum of uric acid the significant bands were found: in the 2800-3300 cm^{-1} range for lactame and lactime O-H group stretching vibrations (with peaks at 2825 cm^{-1} and 3014 cm^{-1}); in the 990-1150 cm^{-1} range for the purine skeleton ring vibrations (with peaks at 992 cm^{-1} and 1122 cm^{-1}); in the 700-800 cm^{-1} range for the purine skeleton ring vibrations (with peaks at 706 cm^{-1} , 743 cm^{-1} and 783 cm^{-1}). Also, regarding the uric acid spectrum, the characteristic vibrations for C-N, N-H and C=O peaks will be presented below.

Spectra for two uroconcrements, one with simple and other with mixed composition, are given in figure 3. In the case of the simple urolithiasis the recorded spectrum presents specific IR bands corresponding to certain wave numbers which are characteristic for urates (U) - fig.3a. The bands presented peaks at 1036 cm^{-1} - for the vibration type C-N stretching; 3014 cm^{-1} - for the vibration type N-H stretching and 1672 cm^{-1} - for the vibration type C=O stretching.

In the case of the mixed urolithiasis, containing uric acid and oxalates (U-O) - fig.3b, there were found not only the bands with characteristic peaks and vibrations types specific for uric acid (mentioned above) but also specific bands with characteristic peaks for oxalates. Specific bands and types of vibrations for oxalates are: 1620 cm^{-1} and 1319 cm^{-1} for the C=O asymmetric and symmetric stretching, 781 cm^{-1} for the COO deformation and 518 cm^{-1} for the COO rocking (out-of-plane) vibrations.

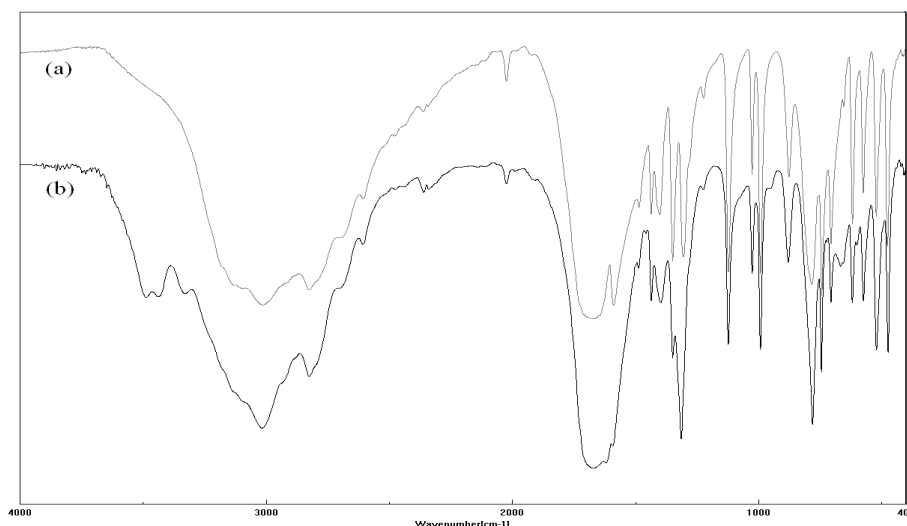


Figure 3. Spectra of some uroconcrements obtained by FT-IR :
(a) simple calculus with uric acid – urates (U); (b) mixed calculus with urates and oxalates (O-U)

In case of calculi with mixed composition there are selected the expressive peaks of the IR spectra of the uroconcrements. For the identification of substances present in such a mixture, e.g. uroconcrements with urates and oxalates, Estepa and Daudon [26] proposed the building of „calibration curves” used in the evaluation of peaks and the estimation of the prevailing component. Appliance of this method will permit the evaluation of mixed uroconcrements. In the present paper three characteristic peaks were taken into consideration in the evaluation of uroconcrements with mixed composition.

In the FT-IR spectra of uroconcrements one can mark out various non-specific peaks for the type of urolithiasis. The presence of those peaks can be explained by the heterogenous nucleation process where the different characteristic lithogenetic compounds (e.g. urates, oxalates, phosphates etc.) and metallic ions precipitate on a „matrix” support. The existence of the preliminary matrix in the biogenesis of calculi is known and accepted long time ago [13]. Recent data revealed that renal stones are concretions containing 97.5% polycrystalline aggregate and 2.5% glycoprotein or mucoprotein matrix [27].

Based on the „standard spectra” and the recorded spectra for each uroconcrements there were possible to establish the qualitative chemical composition of the uroconcrements and to classify them into simple and mixed (binary and ternary) ones. In table 3 there are presented the distribution of urolithiasis types according to their chemical composition and gender of the patients.

Table 3. Synopsis on the composition of the uroconcrements investigated by FT-IR

| Type of urolithiasis | Composition | | Number of cases | | |
|--------------------------------------|--------------------|---|-----------------|-----------|------------|
| | | | Total | Men | Women |
| Simple | Purine derivatives | Urates (U) | 34 | 14 | 20 |
| | | Xanthine (X) | -- | -- | -- |
| | | 2,8-dihydroxyadenine (2,8-DHA) | -- | -- | -- |
| | Oxalates (O) | 38 | 23 | 15 | |
| | Phosphates (P) | 19 | 6 | 13 | |
| | Cystine (C) | 6 | 2 | 4 | |
| Simple uroconcrements - total | | | 97 | 45 | 52 |
| Mixed | Binary | Oxalates-urates (O-U) | 11 | 3 | 8 |
| | | Urates-oxalates (U-O) | 6 | 2 | 4 |
| | | Oxalates-phosphates (O-P) | 31 | 13 | 18 |
| | | Oxalates-cholesterol (O-COL) | 3 | 2 | 1 |
| | | Phosphates-oxalates (P-O) | 15 | 3 | 12 |
| | | Phosphates-carbonates (P-CARB) | 2 | 1 | 1 |
| | Ternary | Oxalates-urates-phosphates (O-U-P) | 5 | 2 | 3 |
| | | Phosphates-oxalates-carbonates (P-O-CARB) | 2 | 2 | -- |
| Mixed uroconcrements – total | | | 75 | 27 | 50 |
| Total uroconcrements | | | 172 | 72 | 102 |

Metals are important components of human organism but they are not produced or destroyed by the body. Being present in our environment, i.e. food, water, air, soil they are introduced in the organism mainly by food and water.

The occurrence of the metals in uroconcrements is an outcome of their presence in urine where they initiate the co-precipitative processes. It was observed in the urine of the patients with calculosis an increase of Ca and Mg concentration, while the concentrations of Na and K displayed minor variations.

By means of AAS, we determined the concentration of alkaline metals in the simple and mixed purine urolithiasis. The results are presented in Table 4.

Table 4. Quantity of alkaline metals in the purine urolithiasis

| Type of urolithiasis | | Metals concentration ($\mu\text{g/g calculus}$) | | | |
|----------------------|------------|---|------------------|-----------|-----------------|
| | | Sodium | | Potassium | |
| | | n | X + SD | n | X + SD |
| Simple | Urates (U) | 34 | 586.12 + 251.64 | 34 | 193.81 + 125.18 |
| Mixed | O-U | 11 | 1722.31 + 503.17 | 11 | 497.72 + 184.16 |
| | U-O | 6 | 1364.05 + 414.17 | 6 | 322.57 + 156.74 |
| | O-U-P | 5 | 2249.33 + 516.64 | 5 | 912.43 + 206.17 |

n – number of cases; X- mean value; SD – standard deviation

Higher sodium concentration was found in case of mixed ternary and binary urolithiasis, more exactly in O-U-P and O-U lithiasis. Also, one can observe the indirect role of oxalates in the urolithiasis formation.

Regarding the alkaline-earth metals Ca and Mg their concentration was determined also by AAS. The results presented in table 5 revealed augmented quantities for Ca and Mg in the mixed purine urolithiasis O-U and O-U-P. Their quantity in the urolithiasis and especially that of Mg alkaline metals by the presence of phosphates, cases when result ammonio - magnesian phosphates.

Table 5. Quantity of alkaline-earth metals in the purine urolithiasis

| Type of urolithiasis | | Metals concentration ($\mu\text{g/g calculus}$) | | | |
|----------------------|------------|---|------------------------|-----------|-----------------|
| | | Calcium | | Magnesium | |
| | | n | X + SD | n | X + SD |
| Simple | Urates (U) | 34 | 611.43 + 270.33 | 34 | 137.61 + 91.27 |
| Mixed | O-U | 11 | 187 342.00 + 52 814.00 | 11 | 412.93 + 127.31 |
| | U-O | 6 | 121 416.00 + 47 200.00 | 6 | 376.14 + 102.19 |
| | O-U-P | 5 | 179 614.00 + 50 139.00 | 5 | 969.56 + 257.08 |

The analytical data of metallograms obtained by our investigations are similar with those in the literature [10, 28–31]. But, one must note that the composition of the uroconcrements and especially in metals is different from one patient to another and from one region to another. From these observations result that the difference is dependent not only on the purine metabolites (resulting from nucleoproteins) but also by the specific metallic composition of food nutrients and of the water. That is why metallomics - applied in the domain of uroconcrements biogenesis – integrate not only physiological and pathobiochemical aspects but also those related to the habitual environment (conditioned by geochemical peculiarities).

In the etiopathogeny of urolithiasis metals play an important role. They may intervene either indirectly as effectors (inhibitors-activators) of metabolic processes, or directly as substituents engaged in competing interactions owing to the difference in the solubility.

Urolithogenesis is a process which begins with the appearance of the so-called “primers” resulted by the heterogenous nucleation mechanism, involving the presence of specific lithogenic organic (urates, oxalates, cystine) or inorganic (phosphates, carbonates) components and metallic ions.

In the uroconcrement biogenesis can compete compounds with ion and/or non-ion structure. Beside these usually anionic structures there are ionic structures generated by some conditions: the pH, ionic strength, osmolality a.o. – situations in which such forms may generate hydroxylated derivatives of purines (uric acid, xanthine, 2,8 –DHA).

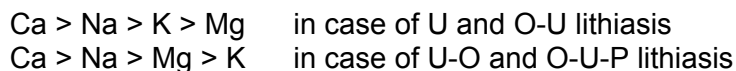
To organic or inorganic compounds of uroconcrements may bond metallic ions, such as Na^+ , K^+ , Ca^{2+} , Mg^{2+} , Zn^{2+} , Cu^{2+} , Fe^{2+} , Mn^{2+} , Pb^{2+} a.o. and non-metallic ions (NH_4^+). Though the metallic trace elements are in very small quantities they compete (obviously in a lesser degree) to the heterogenous nucleation mechanism of calculi. In the next paper (Note II) analytical data on the trace metals found in the uroconcrements studied by us will be presented.

Establishment of urolithiasis types and quantity of their metallic components are of interest not only for an accurate clinical guideline but also for the prophylaxy and metaphylaxy of urolithiasis.

CONCLUSIONS

By means of infrared spectroscopy there were established the following types of purine urolithiasis: simple - with urates (U); mixed - with oxalates-urates (O-U); urates-oxalates (U-O); oxalates-urates-phosphates (O-U-P).

The alkaline and alkaline-earth metals concentration in the simple and mixed purine urolithiasis, determined by atomic absorption spectroscopy, revealed a decrease as follows :



In mixed urolithiasis the concentration of Ca, Na, K and Mg was higher than in simple urolithiasis due to the presence of oxalates and phosphates which determine ionic bonds with the metals in uroconcrements.

EXPERIMENTAL SECTION

Samples obtainment. The study have been performed on the surgically removed or spontaneously eliminated urinary stones obtained from 172 patients admitted and treated in the Clinic of Urology Timișoara. The samples were collected during a period of 6 years.

Analytical determinations. First, in order to study the qualitative and quantitative composition of the kidney stones they were submitted to repeated washing with distilled water (to remove blood, mucous etc.), air-dried and finally powdered.

Next, the qualitative chemical composition of each urinary stone was determined by the Fourier Transform - Infrared Spectroscopy (FT-IR). For the spectra recording a JASCO FT-IR/410 spectrophotometer (Jasco, Japan), in the $400\text{-}4000\text{ cm}^{-1}$ wavenumber range at 4 cm^{-1} resolution, was used. The samples have been homogenized with KBr and converted in pellets using a manual 15 Ton Specac Pellet Press (Specac Ltd, U.K.). Initially there were recorded the FT-IR spectra of the chemically pure substances (presumed to be also in the composition of kidney stones) in order to create a database of „standard spectra” and afterwards the spectra of the powdered kidney stones (with unknown composition). Subsequently to the obtainment of FT-IR spectra of uroconcrements the types of urolithiasis were established.

Further on by means of atomic absorption spectroscopy (AAS) the quantity of the alkaline (Na, K) and alkaline-earth (Ca, Mg) metals in the simple and mixed (binary and ternary) purine urolithiasis was determined. The concentrations of Na, K, Ca and Mg were expressed in $\mu\text{g/g}$ calculus. For this investigation a PYE UNICAM apparatus Series SP 1900 was used.

Statistic evaluation. The analytical data were statistically processed by a computerized method. Mean values (X) and standard deviation (SD) of the metals concentration in the simple and mixed purine urolithiasis were determined.

REFERENCES

1. I.S. Williams, D.G. Chisholm, "Scientific Foundations of Urology", Vol. I, W. Heineman Medical Books Ltd., London, **1976**.
2. C. Borundel, A. Condacse, C.I. Rădulescu, "Hiperuricemiile", Ed. Medicală, București, **1976**.
3. L.A. Kaplan, A.J. Pesce, S.A. Kazmierczak, „Clinical Chemistry: Theory, Analysis and correlation”, 3th edition, Mosby Company, St. Louis-Baltimore-Boston-New York-London-Madrid-Toronto, **1996**.
4. F.L. Coe, A. Evan, E. Worcester, *Journal of Clinical Investigation*, **2005**, *115*, 2598.
5. F.L. Coe, J.H. Parks, "Nephrolithiasis. Pathogenesis and treatment", 2nd edition, Year Book Medical Publishers, Inc., Chicago-London-Boca Raton, **1988**.
6. P. Drăgan, Z. Garban, Gabriela Daranyi, F. Peter, Delia Popescu, *Timișoara Medicală*, **1993**, *37*, 43.
7. Z. Garban, Lucia Cristescu, Victoria Mihalca, P. Drăgan, *Timișoara Medicală*, **1981**, *26*, 54.
8. Z. Garban, Gabriela Garban, „Biochimie: Tratat Comprehensiv, Vol. III. Metabolisme”, ediția 3-a, Ed. Orizonturi Universitare, Timișoara, **2005**.
9. Y. Zhang, M. Morar, S.E. Ealick, *Cell. Mol. Life. Sci.*, **2008**, *65*, 3699.
10. W. Vahlensieck, G. Gasser (Eds.), „Pathogenese und Klinik der Harnsteine”, Vol. XIII, Steinkopff Verlag, Darmstadt, **1988**.
11. O.M. Rannert, W.Y. Chan (Eds.), „Metabolism of trace metals in man”, Vol.I, CRC Press Inc., Boca Raton, **1981**.
12. I. Silaghi-Dumitrescu, Z. Garban, P. Drăgan (Eds.), "Metal Elements in Environment, Medicine and Biology", Tome VIII, Publishing House Eurobit, Timișoara, **2008**.
13. W.H. Boyce, J.S. King, Jr. – *Ann. Rev. NY Acad.Sci.*, **1963**, *104*, 563.
14. Z. Garban, P. Drăgan, Gisela Nemes, Gabriela Daranyi, Doina Popeți, Livia Martoni - in "Meeting of the Federation of European Biochemical Societies: Metal ions, Proteins and Membranes", p.81, Algarve-Portugal, April 21-26, **1985**.
15. Adina Avacovici, Z. Garban, *Journal of Agroalimentary Processes and Technologies*, **2008**, *14*, 367.
16. J.E. Seegmiller, *Am. J. Med.*, **1968**, *45*, 780.
17. T. Gargah, A. Essid, A. Labassi, M. Hamzaoui, M.R. Lakhoua, *Saudi J. Kidney. Dis. Transpl.*, **2010**, *21*, 328.
18. H.A. Simmonds, *Clin. Nephrol.*, **1979**, *12*, 195.
19. P. Sreejith, K.L. Narasimhan, V. Sakhuja, *Indian. J. Nephrol.*, **2009**, *19*, 34.
20. P.L. Altman, S.D. Dittmer (Eds.), „Blood and other Body Fluids”, Publ. by Federation of American Societies for Experimental Biology, Washington, **1968**.
21. R.V.E. Watts, "Chemical Diagnosis of Disease" (Brown S.S., Mitchel F.L., Young D.S., Eds.), Elsevier Amsterdam, **1979**, pp.1059-1119.

22. A. Hesse, G. Sanders, „Atlas of infrared spectra for the analysis of urinary concrements”, George Thieme Verlag, Stuttgart, **1988**.
23. J. Bellanato, “Renal Tract Stone: Metabolic Basis and Clinical practice” (Wickham J.E.A., Colibuck A., Eds.), Churchill Livingstone, New York, **1990**.
24. Gabriela Daranyi, P. Drăgan, Z. Garban, Gr. Sigartău, Adina Avacovici, S. Sarafolean, "Metal Elements in Environment, Medicine and Biology", Tome II (Garban Z., Drăgan P., Eds.), Publishing House Eurobit, Timișoara, **1997**.
25. Y. Ning, “Structural Identification of Organic Compounds with Spectroscopic Techniques”, John Wiley and Sons, New York, **2005**.
26. L. Estepa, M. Daudon, *Biospectroscopy*, **1997**, 3, 347.
27. G.C.G. Koo – Renal colic-calculi, <http://sunzi.lib.hku.hk/hkjo/view/23/2300054.pdf>, **2010**.
28. A. Halabe, O. Sperling, *Miner.Electrolyte Metab.*, **1994**, 20, 424.
29. G. Capasso, P. Jaeger, W.G. Robertson, R.J. Unwin, *Curr. Pharm. Des.*, **2005**, 11, 4153.
30. D. Bazin, P. Chevallier, G. Matzen, P. Jungers, M. Daudon, *Urol. Res.*, **2007**, 35, 179.
31. I.A. Abboud, *Environ. Geochem Health*, **2008**, 30, 11.

Dedicated to the memory of Prof. dr. Ioan Silaghi-Dumitrescu marking 60 years from his birth

PHENOL CONTAMINATED WATER REMEDIATION USING COMMERCIAL IMMOBILIZED BENTONITES AS ADSORBENTS

MAJDIK CORNELIA, ANDRADA MĂICĂNEANU*,
CERASELLA INDOLEAN, SILVIA BURCĂ, MARIA STANCA

ABSTRACT. This work presents experimental results obtained in the process of phenol removal from model solutions using batch technique (magnetic stirring, 100 ml solution). As adsorbent we used five commercial bentonites immobilized in calcium alginate beads. Influences of bentonite provenience and quantity (2-10 grams), and phenol concentration (31-160 mg/L) over the process efficiency were studied. The adsorption capacity decreases in order B5 (Fort Benton) > B2 \cong B3 \geq B4 > B1 (BW200). Also, adsorption capacity increased with a decrease in the bentonite quantity and an increase of the initial phenol concentration. Maximum adsorption capacity was calculated to be 2.2013 mg phenol/g.

Keywords: *immobilized bentonite, alginate beads, phenol removal, adsorption*

INTRODUCTION

Water pollution is indeed of great concern since it is a major carrier of both organic and inorganic contaminants [1].

Aromatic compounds are a class of compounds regarded as ubiquitous pollutant. Many aromatic compounds exhibit carcinogenic, teratogenic or mutagenic properties [2].

Phenol is an aromatic compound that is one of common contaminants in wastewaters, being generated from petroleum and petrochemical, coal conversion, and phenol-producing industries [3].

Phenol are extensively used for the commercial production of a wide variety of resins including phenolic resins, which are used as construction materials for automobiles and appliances, epoxy resins and adhesives, and polyamides for various applications [4].

* *Universitatea Babeș-Bolyai, Facultatea de Chimie și Inginerie Chimică, Str. Kogălniceanu Nr. 1, RO-400028 Cluj-Napoca, România, andrada@chem.ubbcluj.ro*

According to Romanian legislation the maximum allowable concentration of phenol in surface waters and municipal sewer system is 0.3 and 30 mg/L, respectively [5], therefore elimination of phenol becomes a necessity in order to preserve water quality.

The most common methods used for removal of phenol from industrial effluents include stripping, solvent extraction, chemical oxidation (using O_3 , H_2O_2 and ClO_2), incineration, reverse osmosis and irradiation, ion exchange, biodegradation and adsorption methods [6-8]. Out of all these methods, adsorption has been known to be one of the most commonly used treatment methods for removal of phenol from industrial effluents, by virtue of its cost-effectiveness as well as efficiency [9].

Many of water contaminants can be removed by adsorption using natural and synthetic adsorbents. Due to their excellent adsorption properties, clay minerals are widely used in environmental applications. The removal of phenol is a good example for these applications [10].

There are a number of papers in the literature which deals with the removal of phenol by unmodified and modified (acid treated, organobentonites) clays [11-14]. All studies concluded that these types of materials can successfully remove phenol from aqueous solutions, due to their high specific surface area, and their chemical and mechanical stability.

Bentonite consists essentially of clay minerals of the smectite (montmorillonite) group and has a wide range of industrial applications including clarification of edible liquids (wine, for example) and mineral oils, paints, cosmetics and pharmaceuticals.

The abundance of bentonite in most continents of the world and its low cost make it a strong candidate as an adsorbent for the removal of many pollutants and wastewater remediation [3].

The aim of this work was to investigate, experimentally, the potential of five commercial bentonites used as beads (immobilized in calcium alginate) to adsorb phenol from aqueous solutions, in batch conditions.

RESULTS AND DISCUSSION

Bentonite provenience

In the first stage of the experiment, phenol adsorption was realised in a batch reactor with immobile phases using all five bentonites immobilized in calcium alginate beads. This experiment was performed in order to choose between the available bentonites the most effective one to continue the phenol adsorption study. The obtained results are presented in terms of phenol concentration evolution, figure 1, adsorption efficiency, figure 2, and adsorption capacity, figures 3 and 4, for the same quantity of bentonite present in the beads (8g) and the same phenol initial concentration (103.77 mg/L).

From figure 1 it can be observed that in the first 24 hours from the beginning of the experiment the highest quantity of phenol is removed. The highest drop in the concentration was observed for B5 sample, to 44 mg phenol/L from the initial 103.77 mg/L. The adsorption equilibrium was reached in 48 hours for all bentonite samples.

Figure 2 presents the evolution in time of adsorption efficiencies for all bentonite samples. Adsorption efficiency increases progressively until equilibrium is reached. Maximum values for adsorption efficiency are increasing from 12.12% obtained in case of B1 sample to 66.67% obtained in case of B5 sample. The adsorption efficiency decreases in order B5 > B2 \approx B3 \geq B4 > B1.

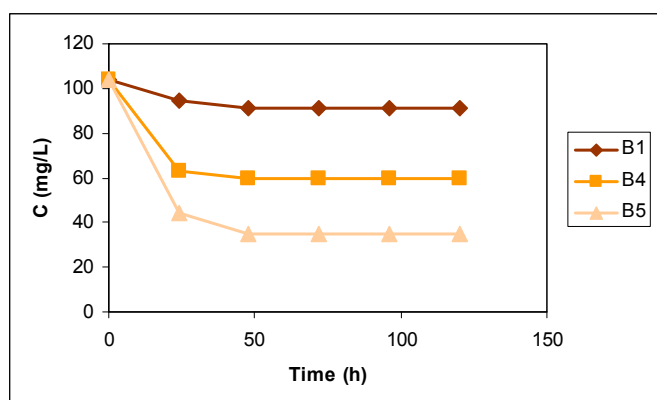


Figure 1. Time evolution of phenol concentration for three of the considered bentonites (8g bentonite, $C_i = 103.77$ mg phenol/L).

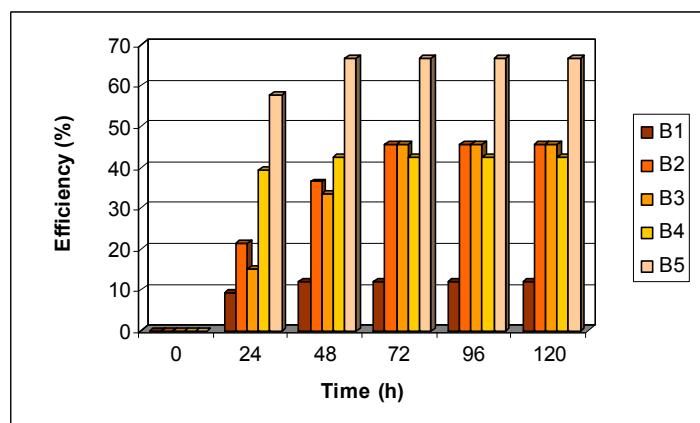


Figure 2. Influence of the bentonite type over the time evolution of adsorption efficiency for all considered bentonites (8g bentonite, $C_i = 103.77$ mg phenol/L).

Evolution of the adsorption process was also followed in terms of adsorption capacity, figure 3. Evolution of phenol adsorption capacity in time (not shown), follows a trend inverse proportional with concentration evolution. Therefore the adsorption capacity increases in time until equilibrium is reached, with a maximum increase after first 24 hours. Equilibrium adsorption capacities are presented in figure 3. Values between 0.1572 to 0.8648 mg phenol/g bentonite were calculated for B1 and B5 samples, respectively. The adsorption capacity decreases in the same order $B5 > B2 \cong B3 \geq B4 > B1$.

B5 bentonite sample, activated bentonite with an elevated montmorillonite content (up to 90%) and high specific surface area (around $750 \text{ m}^2/\text{g}$), was the most efficient sample by comparison with fibrous, powder and protein containing bentonite [15]. The activation procedure was not specified by the producer.

Taking into account the fact that B5 bentonite sample proved to be the most efficient one in the phenol adsorption process, this sample was next considered for the rest of adsorption experiments.

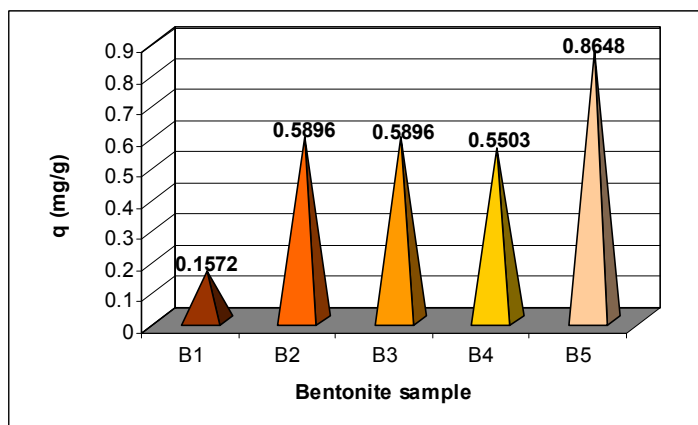


Figure 3. Adsorption capacity values for phenol removal in batch conditions (immobile phases) for all considered bentonites (8g bentonite, $C_i = 103.77 \text{ mg phenol/L}$).

For B5 bentonite sample were also performed experiments in batch conditions under magnetic stirring (mobile phases) using the same conditions (8g and 103.77 mg phenol/L). The adsorption capacity determined in this case was calculated to be the same, but in this case equilibrium was reached in 90 minutes by comparison with 48 hours for the previous experiment. All the experiments realised from now on are realised using a batch reactor and magnetic stirring.

Bentonite quantity

For a better use of the adsorbent (optimisation of the adsorbent quantity) the next stage of the experiment was to study the evolution of the adsorption process for different quantities of B5 bentonite immobilized in calcium alginate beads (2-10g) at different initial concentrations of phenol in solution (31-160 mg/L). In figures 5 and 6 are presented the results obtained for $C_i = 31.45$ mg phenol/L and all considered bentonite quantities – 2, 4, 8 and 10g.

To have a more complete image of the adsorption process on the chosen bentonite sample, adsorption capacities were calculated in order to include in the numerical results also the bentonite quantities we used, figure 4. From the values in figure 4, it is easy to observe that as the bentonite quantity increases, the adsorption capacity decreases. Therefore if an adsorption process of this type is considered for practical uses, it will be necessary to take into consideration the initial phenol concentration and water quantity that need to be treated, in order to establish the appropriate bentonite quantity. Also adsorption efficiency should be calculated and evaluated along with bentonite quantity from the economic point of view. As our results show, an increase of the bentonite quantity will lead to an increase of adsorption efficiency, which will lead to an increase of the operating cost.

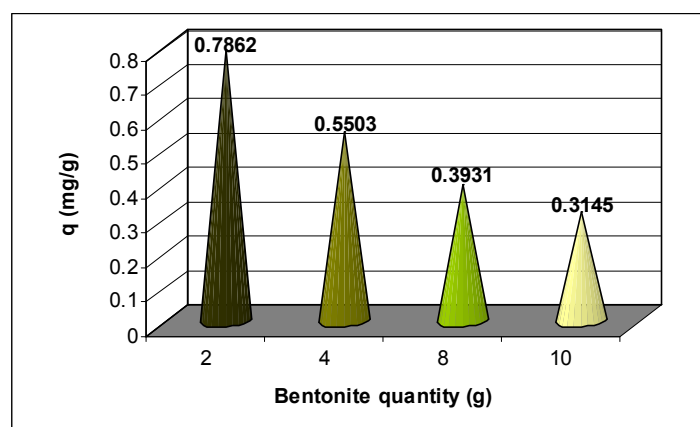


Figure 4. Adsorption capacity values for phenol removal in batch conditions (mobile phases) for different bentonite quantities (825 rpm, B5 bentonite, $C_i = 31.45$ mg phenol/L).

Phenol concentration in aqueous solution

In the final part of the study, the influence of the initial phenol concentration over the adsorption process was studied. Were used solutions containing between 31 and 160 mg phenol/L and as adsorbent 8g of B5 bentonite immobilized in calcium alginate beads.

Influence of phenol initial concentration over the evolution of phenol concentration in time is presented in figure 5. As the initial concentration decreases, the quantity of phenol retained in the first 15 minutes decreases also due to the smaller difference that exist between the concentration of phenol on the adsorbent surface and in the solution. Therefore the adsorption capacity of the immobilized B5, increases with an increase of the phenol initial concentration, from 0.5503 to 2.2013 mg phenol/L, figure 6. Equilibrium was reached after maximum 120 minutes for all five studied concentrations.

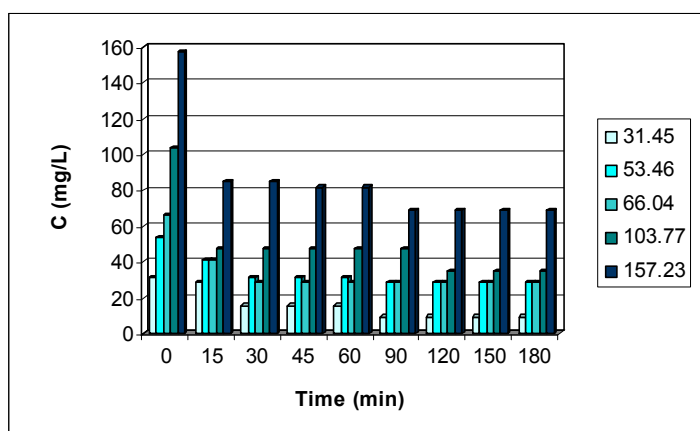


Figure 5. Influence of phenol initial concentration over the time evolution of the concentration (825 rpm, B5 bentonite, 8g).

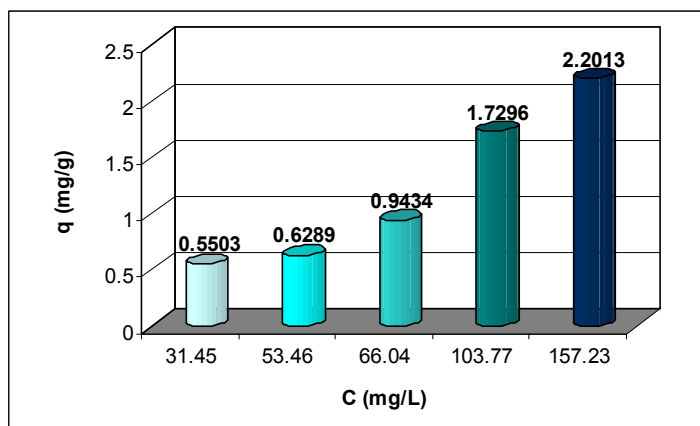


Figure 6. Adsorption capacity values for phenol removal in batch conditions (mobile phases) for different initial concentrations of phenol (825 rpm, B5 bentonite, 8g).

CONCLUSIONS

This work presents experimental results obtained in the process of phenol removal from model solutions using batch technique (magnetic stirring, 100 ml solution).

As adsorbent we used five commercial bentonites immobilized in calcium alginate beads. Influences of bentonite provenience and quantity (2-10 grams), and phenol concentration (31-160 mg/L) over the process efficiency were studied.

The adsorption capacity decreases in order B5 (Fort Benton) > B2 \cong B3 \geq B4 > B1 (BW200). Also, adsorption capacity increased with a decrease in the bentonite quantity and an increase of the initial phenol concentration. Maximum adsorption capacity was calculated to be 2.2013 mg phenol/g.

EXPERIMENTAL SECTION

We used five commercial sodium bentonites: BW 200 – powder sodium bentonite (B1), Gelbenton – purified fibrous bentonite (B2), Evergel – bentonite containing caseine, gelatine and egg albumine (B3), Nucleobent – powder sodium bentonite (B4) and Fort Benton Wyoming – activated bentonite (B5) purchased from Interker-wein Kft. (Hungary). The bentonite samples were used as powder, ($d < 0.2$ mm), without any chemical treatment. All chemicals used in this study were analytical reagent grade (phenol, alginic acid sodium salt, ethanol and CaCl_2).

In order to obtain the bentonite immobilized in alginate beads we used the cross-linking procedure with calcium alginate [16-19]. Thus, various quantities of bentonite (2, 4, 6, 8, 10 g) were suspended in 50-200 ml distilled water (water quantity increases with the bentonite quantity). This suspension was next blended with a mixture formed from 1 g Na-alginate and 2 ml ethanol. The mixture was then dropped with a peristaltic pump into a 0.2 M CaCl_2 solution. During this process, alginate-bentonite drops were gelled into beads with a diameter of 4.0 ± 0.2 mm. The Ca-alginate immobilized adsorbent beads were stored in 0.2 M CaCl_2 solution at 4°C for 1 hour to cure and to form the cross-linking bonds. The beads were rinsed with distilled water for remove excess of calcium ions and stored at 4°C prior to use.

For phenol adsorption study we used model solutions containing between 31 and 160 mg phenol/L. Concentration of phenol in solution was determined using a Jenway 6305 UV/VIS spectrophotometer (UV, 270 nm) after a preliminary centrifugation (14000 rpm, Mikro 200R Hettich centrifuge).

Phenol adsorption process was realized in a batch reactor with immobile and mobile phases (phenol aqueous solution – immobilized bentonite) using 100 ml phenol solution of different concentrations, in which Ca-alginate

bentonite beads obtained from the desired quantity of adsorbent were suspended. For the batch experiments realized with mobile phases, we used a magnetic stirrer operated at 825 rpm.

In order to determine the exact concentration of phenol and establish the evolution of the removal process, in batch conditions, samples of 0.5 mL (dilution in each case was 50) from the supernatant were collected at different time intervals, every 24 hours when we used immobile phases, and every 15 minutes for the first hour and next every 30 minutes when we used mobile phases, until equilibrium was reached.

We studied the influence of the bentonite type and quantity, and phenol concentration in solution over the process efficiency in batch conditions. The experiments were carried out at room temperature (20°C) and without any modification of the pH value of the phenol aqueous solution.

The amount of phenol adsorbed under different conditions was calculated as adsorption capacities Q , (mg/g), while the effectiveness of the adsorption process was expressed as adsorption efficiencies E ,(%); the calculated values of adsorption efficiencies and adsorption capacities should be regarded according to the precision of the determination methods we used [20].

REFERENCES

1. S. Froehner, R. Fernandez Martins, W. Furukawa, M.R. Errera, *Water Air and Soil Pollution*, **2009**, 199, 107.
2. G. Zhao, L. Zhou, Y. Li, X. Liu, X. Ren, X. G. Liu, *Journal of Hazardous Materials*, **2009**, 169, 402.
3. F.A. Banat, B. Al-Bashir, S. Al-Asheh, O. Hayajneh, *Environmental Pollution*, **2000**, 107, 391.
4. H.H. Fang, O. Chen, *Water Research*, **1997**, 31, 2229.
5. *** Romanian Government decisions, HG 188/2002 modified with HG 352/2005.
6. K.H. Lanouette, *Chemical Engineering*, **1977**, 84, 99.
7. J.K. Spiker, D.L. Crawford, E.J. Thiel, *Applied Microbiology and Biotechnology*, **1992**, 37, 518.
8. V. Srihari, S. Madhan Babu, A. Das, *Journal of Applied Science*, **2006**, 6, 47.
9. B. Subramanyam, A. Das, *Desalination*, **2009**, 249, 914.
10. S. Yapar, V. Özbudak, A. Dias, A. Lopes, *Journal of Hazardous Materials*, **2005**, B121, 135.
11. J.-Q. Jiang, C. Cooper, S. Ouki, *Chemosphere*, **2002**, 47, 711.

12. S. Al-Ashed, F. Banat, L. Abu-Aitah, *Separation and Purification Technology*, **2003**, 33, 1.
13. Y.-H. Shen, *Colloids and Surface A: Physicochemical and Engineering Aspects*, **2004**, 232, 143.
14. N. Yilmaz, S. Yapar, *Applied Clay Science*, **2004**, 27, 223.
15. http://www.aquatechnologies.com/info_bentonite_clay.htm
16. T.S. Pathak, J.-Ho Yun, J. Lee, K.-J. Paeng, *Carbohydrate Polymers*, **2010**, article in press, DOI:10.1016/j.carbpol.2010.03.025.
17. S. Peretz, O. Cintează, *Colloids and Surfaces A: Physicochemical and Engineering Aspects*, **2008**, 319, 165.
18. S.K. Papageorgiou, F.K. Katsaros, E.P. Kouvelos, J.W. Nolan, H. Le, *Journal of Hazardous Materials*, **2006**, 137, 1765.
19. P. Ferreira Almeida, A. J. Almeida, *Journal of Controlled Release*, **2004**, 97, 31.
20. H. Bedeleian, A. Măicăneanu, S. Burcă, M. Stanca, *Studia Universitatis Babeş-Bolyai, Geologia*, **2010**, 55, 9.

Dedicated to the memory of Prof. dr. Ioan Silaghi-Dumitrescu marking 60 years from his birth

GEOMETRY OPTIMIZATION AND COMPARATIVE DFT STUDY OF (DIETHYLENETRIAMINE)BIS(THEOPHYLLINATO)ZINC(II) DIHYDRATE

BÉLA MIHÁLY*, ATTILA-ZSOLT KUN, EDIT FORIZS,
ADRIAN PATRUT, IOAN SILAGHI-DUMITRESCU

ABSTRACT. The paper reports on the molecular modelling of $[Zn(th)_2(dien)] \cdot 2H_2O$, which serves as the model compound for assessing metal–nucleobase interactions. The X-ray crystallographic data was completed by *ab initio* density functional theory. Structural parameters of the complex were investigated by using different methods: the unrestricted Becke three-parameter hybrid exchange functional, combined with the Lee–Yang–Parr correlation functional (B3LYP), the 6-311G(d,p), LANL2DZ, CRENL, and DZVP basis sets applied for geometry optimizations.

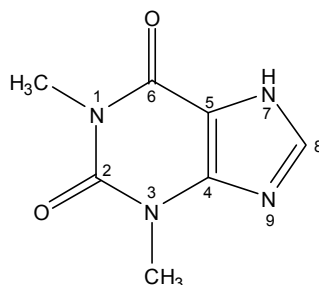
Keywords: *DFT, diethylenetriamine, theophylline, mixed ligand complexes, molecular modelling*

INTRODUCTION

The chemistry of metal complexes of theophylline (Scheme 1) has been extensively studied, mainly because of the capacity of these complexes to serve as model compounds for assessing the interaction between metal ions and oxopurine bases of nucleic acids. Previous research revealed that theophylline, *i.e.*, 1,3-dimethyl-2,6-dioxo-purine, is able to coordinate metal ions acting as a monodentate ligand *via* N7 in alkaline conditions [1–3] and *via* N9 in neutral conditions [4]; it can also form organometallic compounds *via* the C8 atom [5].

Several compounds in which theophylline acts as a bidentate ligand, forming N7/O6 chelates well also reported [6].

* Babeș-Bolyai University, Faculty of Chemistry and Chemical Engineering, RO-400028 Cluj-Napoca, Romania, E-mail: mb15@chem.ubbcluj.ro



Scheme 1

In our research on coordination compounds with theophylline and various amines we reported the synthesis and characterization of several new mixed ligand complexes of Cu(II), Co(II) and Ni(II), containing the theophyllinato anion and 2-aminoethanol or benzylamine as co-ligands [7–10]. The synthesis of $[\text{Zn}(\text{th})_2(\text{dien})]\cdot 2\text{H}_2\text{O}$ and the corresponding X-Ray structure was also presented [11].

The aim of this work was the calculation of $[\text{Zn}(\text{th})_2(\text{dien})]\cdot 2\text{H}_2\text{O}$, at different levels of theory, in order to evaluate their accuracy by comparing them to experimental data. Results of geometry optimizations were in good agreement with the experimental values.

RESULTS AND DISCUSSION

Computational details

Geometry optimizations were performed by using the density functional theory (DFT) using the unrestricted Becke three-parameter hybrid exchange functional, combined with the Lee–Yang–Parr correlation functional (B3LYP). The 6-311G(d,p) [12] full electron and LANL2DZ (Los Alamos National Laboratory 2 Double Zeta) [13, 14] effective core potential (ECP) basis sets are internal, while the CRENL ECP (Christiansen's effective core potential) [15, 16] and DZVP (Double Zeta Valence with Polarization) [17] full electron basis sets were obtained from the Basis Set Exchange webpage [18]. The *Gaussian09* electronic structure program package was used for calculations [19]. Optimizations were performed with the standard convergency criteria of *Gaussian09*, followed by vibrational analysis to make certain that the obtained geometries are true minima.

Optimized geometries

In the complex under study, the geometry around the pentacoordinated Zn(II) is a distorted trigonal bipyramide, consisting of three N atoms of the diethylenetriamine ligand and the N7 atom of each of the two theophyllinate

moieties. The Zn–N_a distance found in the complex is longer than the Zn–N_e bond, corresponding to the typical appropriate distances found in trigonal bipyramidal structures. One of the two water molecules is positioned on the coordination axis, but relatively far from the central Zn(II) atom; consequently, it can be considered as being located outside the proper coordination sphere of Zn(II).

The molecular structure of [Zn(th)₂(dien)] with the water molecule, closer to the metal ion, was optimized in the gaseous phase. The final geometries and the structure determined by X-Ray diffraction are displayed in Figure 1. In all cases there are two hydrogen bonds present in the optimized structures; one between the C6=O of the equatorial theophylline and the N₂–H of dien moiety and the other formed between the C6=O of the axial theophylline and the water molecule.

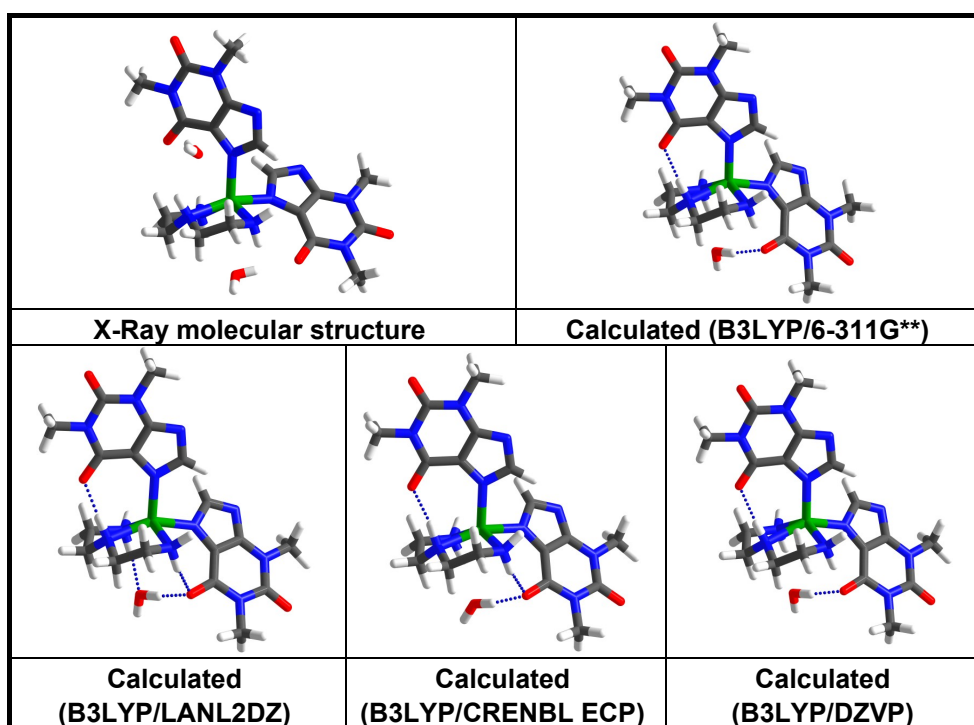


Figure 1. X-Ray molecular structure of [Zn(th)₂(dien)]·2H₂O, and the corresponding optimized structures.
(Color code: C – grey, N – blue, O – red, H – white, Zn – green)

The main geometrical parameters, optimized at different levels of theory, are listed in Table 1. Theoretical calculations revealed that the majority of optimized bond lengths are slightly longer than the experimental values.

This can be also considered as a consequence of having performed the theoretical calculations for an isolated molecule in gaseous phase, while the experimental results were recorded for the compound in solid state. Hydrogen bonds formation also contributes to the changes in geometry.

Our results suggest that the differences of bond lengths and bond angles between the experimental data and the predicted values are greater when using the DZVP basis set. According to the calculated values, the water molecule considered for optimization is located outside the coordination sphere. This statement is valid for all calculation techniques employed. Therefore, the Zn(II) atom is pentacoordinated, having distorted trigonal bipyramide geometry; hence, it cannot be considered as being hexacoordinated.

The mean error for angle values is greater, when using the DZVP basis set (see Table 1).

Table 1. Experimental and calculated geometry parameters.

| | X-Ray | 6-311G(d,p) | LANL2DZ | CRENBL ECP | DZVP |
|-----------------------------------|-------|-------------|---------|---------------|-------|
| Distances (Å) | | | | | |
| Zn–N _a | 2.120 | 2.087 | 2.159 | 2.127 | 2.110 |
| Zn–N _e | 2.074 | 2.031 | 2.097 | 2.142 | 2.049 |
| Zn–N ₁ | 2.084 | 2.161 | 2.183 | 2.204 | 2.199 |
| Zn–N ₂ | 2.220 | 2.215 | 2.242 | 2.246 | 2.244 |
| Zn–N ₃ | 2.092 | 2.175 | 2.201 | 2.231 | 2.207 |
| Zn–O _w | 3.190 | 3.735 | 3.639 | 3.592 | 3.819 |
| Angles (°) | | | | | |
| N _a –Zn–N _e | 95.5 | 104.2 | 102.0 | 96.1 | 105.3 |
| N _a –Zn–N ₁ | 93.3 | 91.2 | 90.8 | 92.1 | 90.8 |
| N _a –Zn–N ₂ | 165.1 | 151.9 | 154.1 | 161.7 | 149.6 |
| N _a –Zn–N ₃ | 97.2 | 94.0 | 92.9 | 95.2 | 93.9 |
| N _e –Zn–N ₁ | 119.6 | 114.9 | 118.5 | 116.9 | 115.5 |
| N _e –Zn–N ₃ | 101.9 | 101.2 | 101.8 | 96.8 | 101.8 |
| N ₁ –Zn–N ₃ | 135.9 | 140.9 | 137.8 | 144.6 | 139.5 |
| N _e –Zn–O _w | 171.6 | 166.7 | 170.0 | 171.8 | 167.0 |

N_a and N_e represent the N7 donor atom of theophylline ligands. The terminal N₁ and N₃ atoms of the dien ligand are in the equatorial plane, while the middle N₂ atom is located in an axial position. O_w designates the O atom of the nearer water molecule, opposite to the N_e position.

Reported data are in good agreement with the experimental ones, revealing that the CRENBL ECP and the B3LYP/LANL2DZ level of theory are suitable for the theoretical study of the system described above.

Vibrational analysis

Vibrational frequencies, calculated at the B3LYP/6-311G(d,p) level, were scaled by the typical factor 0.96. Several selected primary calculated harmonic frequencies are listed in Table 2, in comparison with the experimental data. The Gabedit program [20] was used for assigning the calculated harmonic frequencies.

The calculated values of the predicted harmonic vibrational frequencies are relatively close to the frequencies found in the experimental FTIR spectrum of the complex. The largest deviations occur for the B3LYP/CRENBL level of the theory.

It can be stated that the scaled frequencies of the DFT calculation are close to the corresponding FTIR vibration values, and that the DFT B3LYP method can predict accurately the vibrational frequencies for the system reported here.

Table 2. Comparison of the observed and calculated vibrational spectra.

| Assignment | Exp. IR (KBr) | Calcd. (B3LYP/6-311G(d,p)) | Calcd. (B3LYP/LANL2DZ) | Calcd. (B3LYP/CRENBL ECP) | Calcd. (B3LYP/DZVP) |
|------------|-------------------------------|----------------------------|---|--|---|
| O-H str. | 3496.31 | 3879.32 3528.82 | 3807.36 | 4216.31 3595.80 | 3828.73 3507.71 |
| N-H str. | 3353.6 3318.89 3272.61 | 3398.88 3391.68 | 3563.28 3559.56 3364.38 3298.10 3275.40 | 3739.65 3737.18 3492.71 3492.71– 3451.96 | 3548.90 3548.64 3405.40 3393.47 3359.62 |
| C-H str. | 2940.91 | 3232.66– 3005.89 | 3306.03 3296.73 3216.05– 3022.41 | 3207.59– 3058.50 | 3254.30– 3027.60 |
| C=O str. | 1685.48 1664.27 1635.34 | 1758.63 1755.57 | 1668.08 1663.69 | 1864.99 1861.81 1787.50 | 1747.37 1744.49 |

CONCLUSIONS

Our calculations revealed that the utilized techniques were efficient in optimizing structural geometries of systems based on organic molecules and transition metal ions, such as Zn(II). The best calculation precision of the geometry parameters was obtained for the B3LYP/CRENBL ECP and B3LYP/LANL2DZ level of the theory.

ACKNOWLEDGMENTS

Calculations were performed at the Centre for Molecular Modelling and Quantum Computational Chemistry (CMMCCC) facilities in the framework of the CAPACITATI, 130/14.09.07 Category I, P1 Programme.

REFERENCES

1. N. S. Begum, H. Manohar, *Polyhedron*, **1994**, *13*, 307.
2. W. J. Birdsall, M. S. Zitzman, *J. Inorg. Nucl. Chem.*, **1979**, *41*, 116.
3. W. J. Birdsall, *Inorg. Chim. Acta*, **1985**, *99*, 59.
4. E. M. Griffith, E. L. Amma, *J. Chem. Soc., Chem. Commun.*, **1979**, 322.
5. A. Romerosa, J. Suarez-Varela, M. A. Hidalgo, J. C. Avila-Roson, E. Colacio, *Inorg. Chem.*, **1997**, *36*, 3784.
6. D. J. Szalda, T. J. Kistenmacher, L. G. Marzilli, *J. Am. Chem. Soc.*, **1976**, *98* (26), 8371.
7. P. Bombicz, J. Madarász, E. Forizs, I. Foch, *Polyhedron*, **1997**, *16*, 3601.
8. S. Gál, J. Madarász, E. Forizs, I. Labádi, V. Izvekoy, G. Pokol, *J. Therm. Anal. Cal.*, **1998**, *53*, 343.
9. E. Forizs, L. David, O. Cozar, V. Chiş, G. Damian, J. Csibi, *J. Mol. Struct.*, **1999**, *482*, 143.
10. B. Mihály, E. Forizs, I. Silaghi-Dumitrescu, *Studia Univ. Babeş-Bolyai, Chemia*, **2007**, *LII*, *4*, 111.
11. B. Mihály, E. Forizs, A.-Z. Kun, I. Silaghi-Dumitrescu, *Acta Cryst.*, **2009**, *E65*, m579.
12. L. A. Curtiss, M. P. McGrath, J-P. Blandeau, N. E. Davis, R. C. Binning, Jr. L. Radom, *J. Chem. Phys.*, **1995**, *103*, 6104.
13. T. H. Dunning Jr., P. J. Hay, "Methods of Electronic Structure Theory", Ed. H. F. Schaefer III., Plenum, New York, **1977**.
14. P. J. Hay, W. R. Wadt, *J. Chem. Phys.*, **1985**, *82*, 284.
15. M. M. Hurley, L. F. Pacios, P. A. Christiansen, R. B. Ross, W. C. J. Ermler, *Chem. Phys.*, **1986**, *84*, 6840.
16. L. A. LaJohn, P. A. Christiansen, R. B. Ross, T. Atashroo, W. C. J. Ermler, *Chem. Phys.*, **1987**, *87*, 2812.
17. N. Godbout, D. R. Salahub, J. Andzelm, E. Wimmer, *Can. J. Chem.*, **1992**, *70*, 560.
18. K. L. Schuchardt, B. T. Didier, T. Elsethagen, L. Sun, V. Gurumoorthi, J. Chase, J. Li, T. L. Windus, *J. Chem. Inf. Model.*, **2007**, *47*(3), 1045. <https://bse.pnl.gov/bse/portal>

19. M. J. Frisch, G. W. Trucks, H. B. Schlegel, G. E. Scuseria, M. A. Robb, J. R. Cheeseman, G. Scalmani, V. Barone, B. Mennucci, G. A. Petersson, H. Nakatsuji, M. Caricato, X. Li, H. P. Hratchian, A. F. Izmaylov, J. Bloino, G. Zheng, J. L. Sonnenberg, M. Hada, M. Ehara, K. Toyota, R. Fukuda, J. Hasegawa, M. Ishida, T. Nakajima, Y. Honda, O. Kitao, H. Nakai, T. Vreven, J. A. Montgomery, Jr., J. E. Peralta, F. Ogliaro, M. Bearpark, J. J. Heyd, E. Brothers, K. N. Kudin, V. N. Staroverov, R. Kobayashi, J. Normand, K. Raghavachari, A. Rendell, J. C. Burant, S. S. Iyengar, J. Tomasi, M. Cossi, N. Rega, J. M. Millam, M. Klene, J. E. Knox, J. B. Cross, V. Bakken, C. Adamo, J. Jaramillo, R. Gomperts, R. E. Stratmann, O. Yazyev, A. J. Austin, R. Cammi, C. Pomelli, J. W. Ochterski, R. L. Martin, K. Morokuma, V. G. Zakrzewski, G. A. Voth, P. Salvador, J. J. Dannenberg, S. Dapprich, A. D. Daniels, O. Farkas, J. B. Foresman, J. V. Ortiz, J. Cioslowski, D. J. Fox, Gaussian 09, Revision A.02, Gaussian, Inc., Wallingford CT, **2009**.
20. A. R. Allouche, Gabedit 2.2.11., <http://gabedit.sourceforge.net>

Dedicated to the memory of Prof. dr. Ioan Silaghi-Dumitrescu marking 60 years from his birth

STUDIES ON THE EUROPIUM AND PALLADIUM EXTRACTION WITH SOME CALIX[6]ARENE DERIVATIVES

ALINA SAPONAR^{a, *}, ELISABETH-JEANNE POPOVICI^a,
IOANA PERHAIȚA^a, NICOLAE POPOVICI^a AND
IOAN SILAGHI-DUMITRESCU^b

ABSTRACT. The capability of *p-tert*-butyl calix[6]arene functionalized at the lower rim with 2-butenyl, ethyl acetate and/or N,N-diethylacetamide groups to extract Pd²⁺ and Eu³⁺ ions from aqueous medium have been investigated. Good extraction yield was obtained for calix[6]arene derivatives functionalized with *tri*- and *hexa*- ethylacetate and *tri*- and *hexa*- N,N-diethylacetamide groups. It was revealed that the half or total substituted *p-tert*-butyl calix[6]arene ester derivatives present interest as liquid-liquid extraction reagents for precious metal and rare earth ions.

Keywords: Calixarene, liquid-liquid extraction, metal ions.

INTRODUCTION

The development of efficient extraction agents to remove metal ions from both organic and aqueous effluents for either safe disposal or recycling has motivated research into the coordination properties of calixarene-based ligands.

Calixarenes are macrocycles made up of phenolic units linked by methylene bridges with host-guest properties. They are known as inexpensive, chemically stable molecular networks/systems utilizable as selective complexing agents for neutral molecules and ions [1-10]. Functionalised calix[n]arene (n = 4, 6, 8) have received much attention because of their increased molecular and ion binding capability revealed also by their ability to transport metal cations across organic membranes and to behave as metal carriers.

^a Raluca Ripan Institute for Research in Chemistry, Babes Bolyai University, 400294, Cluj-Napoca, Romania, * salina@chem.ubbcluj.ro

^b Faculty of Chemistry and Chemical Engineering, Babes-Bolyai University, 400084, Cluj-Napoca, Romania.

Selective and efficient cation receptors can be prepared by functionalization of the parent calixarene with metal coordinating groups. Usually, this is performed at the “narrow rim”, because of the easy synthesis of a great number of derivatives, which allows comparing the impact of some factors on the extraction behavior (i.e. cavity size, conformation, functional groups) and the flexibility to design a proper ligand to selectively recognize metal ions [11-23]. Liquid-liquid extraction experiments were carried out to recover metals from aqueous solution using as extractants calix[6]arene derivatives dissolved in organic solvents (i.e. chloroform, dichloromethane, toluene, acetonitrile), allowing the exploitation of the calixarene’s cone-shape and the chelating ring of oxygen, nitrogen and phosphorus donor atoms that encircle the guests.

Herein we present our studies referring to the extraction of some rare earth and precious metals, using the parent calix[6]arene and some new calix[6]arene derivatives obtained by functionalization at the narrow rim with ester and/or amido and/or alkenyl donor groups.

In this respect, ten calixarene- based compounds were used as extracting agents i.e. *p-tert*-butyl calix[6]arene and *p-tert*-butyl calix[6]arene grafted with two, three and four *E*-2-butenyl groups, three and six ethylacetate groups, three and six *N,N*-diethylacetamide groups, three 2-butenyl and three ethylacetate groups and three 2-butenyl and three *N,N*-diethylacetamide groups, respectively. Their capability to act as extraction reagents for Pd²⁺ and Eu³⁺ ions was investigated.

RESULTS AND DISCUSSION

A series of nine ester, amido and/or alkenyl calix[*n*]arene derivatives were tested as extracting reagent for precious metal and rare earth ions, in comparison with the parent calixarene (Figure 1).

The following calixarene-based compounds were used as extracting reagents: *p-tert*-butyl-calix[6]arene (**C6**), *bis*-2-butenyl-calix[6]arene (**C6Cr2**), *tris*-2-butenyl-calix[6]arene (**C6Cr3**), *tetra*-2-butenyl-calix[6]arene (**C6Cr4**), *tris*-ethylacetate-calix[6]arene (**C6Es3**), *tris*-*N,N*-diethylacetamide-calix[6]arene (**C6Am3**), *hexa*-ethylacetate-calix[6]arene (**C6Es6**), *hexa*-*N,N*-diethylacetamide-calix[6]arene (**C6Am6**), *tris*-*N,N*-diethylacetamide-*tris*-2-butenyl-calix[6]arene (**C6Am3Cr3**) and *tris*-ethylacetate-*tris*-2-butenyl-calix[6]arene (**C6Es3Cr3**).

Extraction was performed using 5-10 x10⁻⁴ M aqueous solution of PdCl₂ or Eu(NO₃)₃ and 1x10⁻³ M solution of calixarene (Cx) in CHCl₃. Extraction yield was determined by monitoring the concentration of palladium or europium from the aqueous solutions, using Inductively Coupled Plasma Optical Emission Spectrometry.

Extraction of Pd^{2+} ions

The capability of *p*-*tert*-butyl calix[6]arene derivatives to extract Pd^{2+} ions was determined by liquid-liquid extraction experiments that were performed using equal volumes and equal concentrations of metal ions and calixarenes ($Pd^{2+}:Cx = 1:1$), and a variable pH of the aqueous medium (Figure 2).

The extraction capability of the different calixarene-based compounds, at pH=2.5, varies between ~54 % for **C6Am6** and ~73% for **C6Es6**. *p*-*tert*-butyl calix[6]arene **C6** shows an extraction yield of 65%.

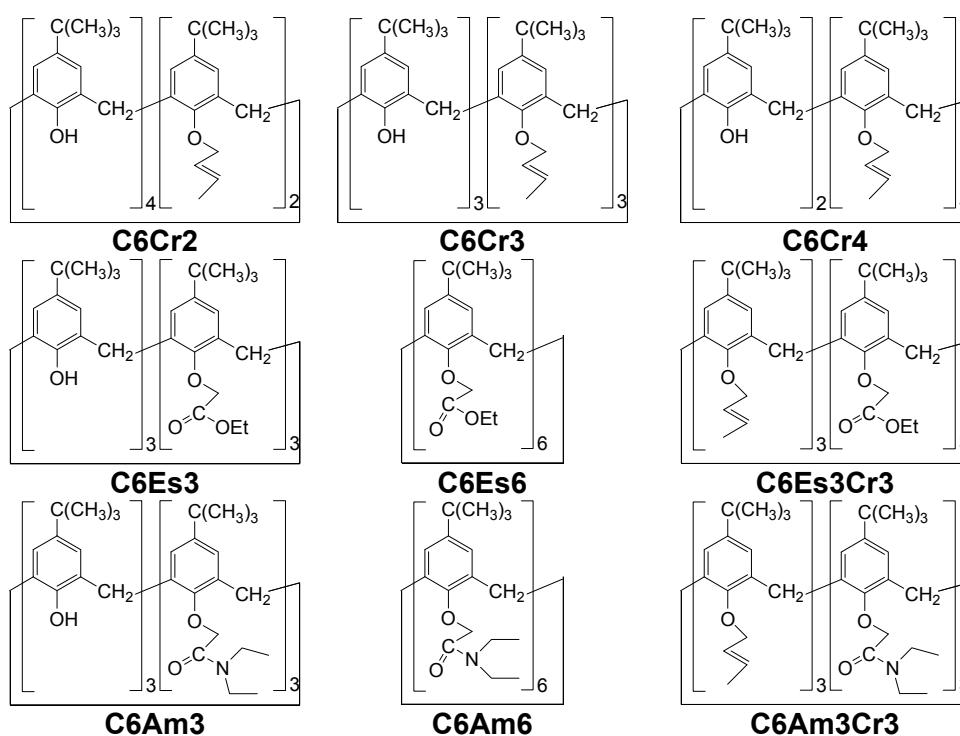


Figure 1. The calixarene derivatives used as extracting agents

The grafting of two or three alkenyl- as well as four or six amido-groups decreases the yield as compared with the parent calixarene. Favourable effect is shown by the functionalisation with ester groups. The highest extraction yield i.e. over 70 % is shown by calixarene-derivatives with the highest level of functionalisation i.e. compounds **C6Am3Cr3**, **C6Cr4** and **C6Es6**.

The extraction yield of the Pd²⁺ ions with calixarene-based compounds depends on the acidity of the aqueous medium. Excepting the *hexa*-ester calix[6]arene derivative, extraction yield from aqueous solutions with pH=4.1 is relatively low (under 60%). The highest extraction yield was obtained for **C6Es6** derivatives, namely 72.6% at pH=2.5 and 75.8% at pH = 4.1, respectively.

By comparing the total functionalized calixarene with the half substituted compounds, it can be concluded that, at pH=2.5, the *hexa* functionalized ester derivative (**C6Es6**) is more efficient as extractant than the *tri* functionalized one (**C6Es3**).

The capability of calixarene-based compounds to extract palladium ions in well defined extraction conditions can be estimated by the ratio *r* representing the ratio between the mol number of metal ion and calixarene.

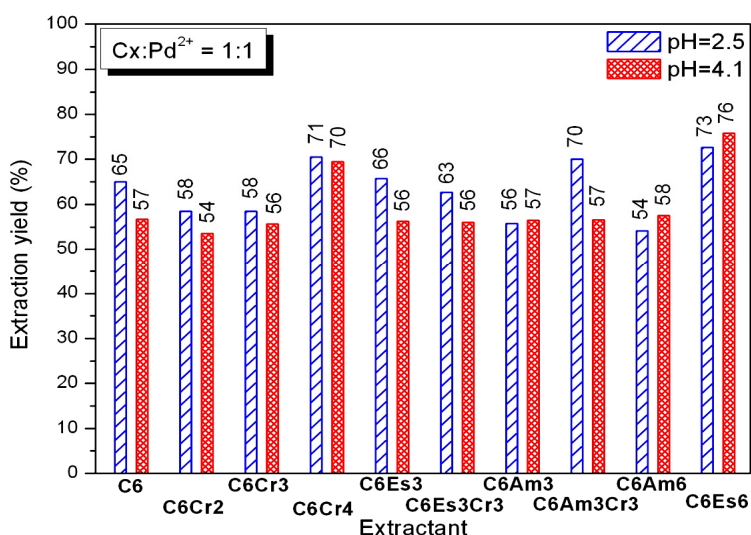


Figure 2. Variation of the extraction yield of Pd²⁺ from solutions with variable pH, using different calixarene-based compounds ($C_{Cx}=1 \times 10^{-3}$ mol/l; $C_{PdCl_2}= 1 \times 10^{-3}$ mol/l)

In our extraction conditions, for the ester calix[6]arene derivatives, the maximum *r* value was obtained at pH =2.5 for **C6Es3** (0.657) and at pH=4.1 for **C6Es6** (0.758) whereas for amido calix[6]arene derivatives, at pH =4.1 for both **C6Am3** (0.565) and **C6Am6** (0.575) compounds.

Extraction of Eu³⁺ ions

The capability of *p-tert*-butyl calix[6]arene derivatives to extract Eu³⁺ ions was determined by liquid-liquid extraction experiments that were performed using variable volumes with equal concentrations of metal ions and calixarenes so that Cx :Eu ratio be varied between 2:1 and 1:2, and variable pH of the aqueous medium.

The extraction yield (η) and the ratio (r) representing the mol number of Eu³⁺ extracted by 1 mol of calixarene-based compounds, at pH=2.8 are shown in Table 1. Extraction experiments were performed for 1:1, 2:1 and 1:2 ratio between the extractant (Cx) and the extracted species (Eu).

The *p-tert*-butyl calix[6]arene **C6** shows an extraction yield of only 23.9%, when working with calixarene: metal ratio equal to 1:1. The grafting of two alkenyl-groups slowly increases the yield as compared with the parent calixarene whereas the attaching of three or four alkenyl-groups decreases it. Opposite results were obtained in the case of experiments with calixarene: metal ratio equal to 2:1. The grafting of three or six ester groups increase the yield as compared with the parent calixarene or the other calixarene derivatives. Favorable effect is shown by the functionalization with ester groups, whatever the calixarene: metal ratio.

Table 1. The extraction data for europium ions, using different calixarene-based compounds (pH=2.8; $C_{Cx}=1 \times 10^{-3}$ mol/l; $C_{Eu(NO_3)_3}=1 \times 10^{-3}$ mol/l)

| Calixarene-based compounds | Ratio Cx:Eu=1:1 | | Ratio Cx:Eu = 2:1 | | Ratio Cx:Eu = 1:2 | |
|----------------------------|-----------------|-------|-------------------|-------|-------------------|-------|
| | η (%) | r | η (%) | r | η (%) | r |
| C6 | 23.9 | 0.238 | 26.1 | 0.130 | 13.2 | 0.263 |
| C6Cr2 | 31.9 | 0.319 | 21.3 | 0.106 | 20.4 | 0.408 |
| C6Cr3 | 18.7 | 0.187 | 42.6 | 0.213 | 23.8 | 0.475 |
| C6Cr4 | 12.5 | 0.124 | 38.6 | 0.193 | 29.6 | 0.592 |
| C6Es3 | 57.1 | 0.570 | 58.3 | 0.291 | 44.6 | 0.891 |
| C6Es3Cr3 | 34.2 | 0.342 | 55.2 | 0.276 | 61.1 | 1.222 |
| C6Am3 | 38.7 | 0.386 | 13.4 | 0.067 | 25.0 | 0.500 |
| C6Am3Cr3 | 29.9 | 0.298 | 16.8 | 0.083 | 20.3 | 0.405 |
| C6Am6 | 50.1 | 0.500 | 18.3 | 0.091 | 27.9 | 0.557 |
| C6Es6 | 51.9 | 0.519 | 48.5 | 0.242 | 26.2 | 0.523 |

The extraction yield of Eu(III) ions from aqueous solution (pH=2.8) varies between 12.5% for **C6Cr4** and 57.1% for **C6Es3**, in experiments with calixarene: metal ratio Cx:Eu= 1:1, between 13.4% for **C6Am3** and 58.3% for **C6Es3** for Cx:Eu= 2:1 and 13.2% for **C6** and 61.1% for **C6Es3Cr3** for Cx:Eu= 1:2.

Unexpectedly, the highest extraction yield for europium ions (61.1%) was obtained for **C6Es3Cr3** derivatives, when calixarene: metal ratio was 1:2. The grafting of alkenyl-groups alone or together with ester ones improve the calixarene capability to extract Eu(III) ions.

The extraction yield of the Eu^{3+} ions with calixarene-based compounds depends on the calixarene: metal ratio (Figure 3). In this case, the total functionalised ester calix[6]arene derivative is less efficient than the half substituted compound, contrary to the palladium situation. The maximum efficiency appears at **C6Es3** derivatives, for Cx:Eu= 2:1.

The capability of calixarene-based compounds to extract europium ions in well defined extraction conditions was estimated by the ratio r representing the mol number of metal ion extracted by 1 mol of calixarene. In our extraction conditions, for the ester substituted calix[6]arene, the maximum r value was obtained for Cx:Eu = 1:2, namely 0.891 for **C6Es3** and 0.523 for **C6Es6**. The additional grafting of three butenyl-groups to the **C6Es3** compound increases the r value to 1.222 thus suggesting that for **C6Es3Cr3** compound, a more complicated Eu^{3+} sequestration process is involved.

The capability of *p-tert*-butyl calix[6]arene derivatives to extract Eu^{3+} ions was also determined at pH=4.6, using europium nitrate solutions with different concentrations.

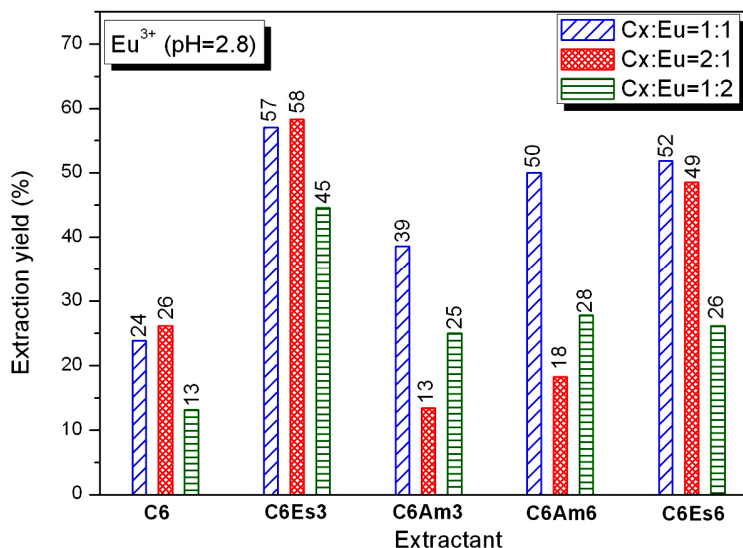


Figure 3. Variation of the extraction yield of Eu^{3+} using variable calixarene-to-europium ratios and different calixarene-based compounds ($c_{\text{Cx}}=1 \times 10^{-3}$ mol/l; $c_{\text{Eu}(\text{NO}_3)_3}=1 \times 10^{-3}$ mol/l)

The extraction yield (η) and the ratio (r) representing the mol number of Eu^{3+} extracted by 1 mol of calixarene for different calixarene-based compounds, at pH=4.6 are shown in Table 2. Extraction experiments were performed for 1:1 ratio between the extractant (Cx) and the extracted species (Eu).

Table 2. The extraction data for europium ions, using different calixarene-based compounds and Eu^{3+} solutions with variable concentration (pH=4.6; Cx:Eu=1:1; $c_{\text{Cx}}=1 \times 10^{-3}$ mol/l)

| Calixarene-based compounds | 1×10^{-3} mol Eu^{3+} /L | | 5×10^{-4} mol Eu^{3+} /L | |
|----------------------------|--|-------|--|-------|
| | η (%) | r | η (%) | r |
| C6 | 32.4 | 0.324 | 23.2 | 0.231 |
| C6Cr2 | 26.8 | 0.268 | 26.0 | 0.260 |
| C6Cr3 | 30.3 | 0.303 | 25.3 | 0.253 |
| C6Cr4 | 30.2 | 0.301 | 22.1 | 0.220 |
| C6Es3 | 32.2 | 0.321 | 20.8 | 0.208 |
| C6Es3Cr3 | 29.0 | 0.290 | 21.1 | 0.210 |
| C6Am3 | 30.5 | 0.304 | 24.8 | 0.247 |
| C6Am3Cr3 | 25.0 | 0.250 | 25.9 | 0.258 |
| C6Am6 | 34.8 | 0.347 | 19.9 | 0.198 |
| C6Es6 | 37.4 | 0.374 | 41.9 | 0.419 |

The extraction capability of the different calixarene-based compounds to extract Eu^{3+} ions in solutions with pH=4.6 is low. *p-tert-butyl* calix[6]arene **C6** shows an extraction yield of only 32.4% and 23.2% when working with 1×10^{-3} mol Eu^{3+} /L and 5×10^{-4} mol Eu^{3+} /L, respectively. In the first case, almost all calixarene-derivatives show a lower extraction capability than the parent calixarene. The only exceptions are the total substituted calix[6]arene with ester- and amido- groups (**C6Es6**; **C6Am6**).

With the exception of **C6Es3** and **C6Am3Cr3** derivatives, the best extraction results were obtained when working with 1×10^{-3} M solutions.

In order to investigate whether the concentration of europium solutions influences also the extraction yield in more acidic medium, liquid-liquid extraction experiments were performed for some of the *hexa* substituted calix[6]arene, using diluted europium solutions (5×10^{-4} mol Eu^{3+} /L) and variable Cx:Eu ratio (Figure 4)

The extraction of europium from diluted solution with pH=2.7 take place with a yield that varies between ~41% (**C6Am6**) and ~77 (**C6Es6**) for Cx:Eu=2:1 and ~26% (**C6Am3Cr3**) and 31% (**C6Am6**) for Cx:Eu=2:1. Although the extraction yield obtained with *hexa* ester calix[6]arene derivative is high (77%), in our experimental conditions, the ratio r representing the mol number of Eu^{3+} extracted by 1 mol of calixarene is only 0.191.

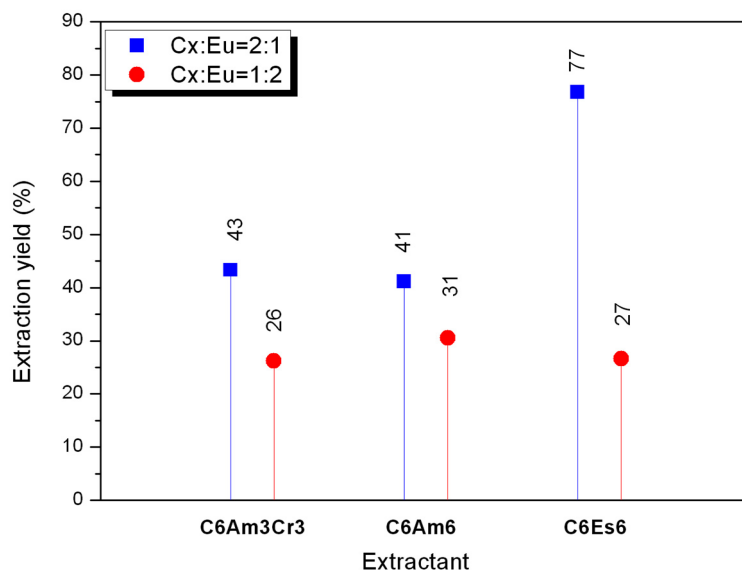


Figure 4. Variation of the extraction yield of Eu^{3+} using different calixarene-to-europium ratios and different calixarene-based compounds ($\text{pH}=2.7$; $c_{\text{Cx}}=1 \times 10^{-3} \text{ mol/L}$; $c_{\text{Eu}(\text{NO}_3)_3}=5 \times 10^{-4}$)

CONCLUSIONS

The capability of *p-tert*-butyl calix[6]arene functionalised at the lower rim with 2-butenyl, ethyl acetate and/or N,N-diethylacetamide groups to extract precious or rare earth metallic ions have been investigated by liquid-liquid extraction experiments. Partial or total substituted calix[6]arenes with alkenyl and/or ester and/or amido donor groups were used to extract Pd^{2+} and Eu^{3+} ions from aqueous medium, in different experimental conditions i.e. pH, cation concentration, calixarene/metal ratio.

The best extraction capability was shown by calix[6]arene derivatives functionalized with *tri*- and *hexa*- ethylacetate groups. For palladium ions, the total functionalized calixarene derivative is more efficient as extractant than the half substituted compound; opposite results were obtained for europium extraction. The highest extraction yield is achieved at $\text{pH}=2\text{...}3$ for europium and $4\text{...}5$ for palladium. In general, the capability of *p-tert*-butyl calix[6]arene derivatives to extract Eu^{3+} ions is smaller than for Pd^{2+} , whatever the pH value.

The extraction yield can be considerably improved by modifying the extraction conditions: ratio between calixarene derivatives and metallic ions,

solutions concentration, the number of the extraction cycles, etc. The extraction yield of europium could be increased with 20-30% when the calixarene: metal ratio is modified from 1:1 to 2:1.

The *p-tert*-butyl calix[6]arene derivatives functionalized with *tri*- and *hexa*- ethyl acetate groups present great interest as liquid-liquid extraction reagents for precious metal and rare earth ions.

EXPERIMENTAL SECTION

Chemical reagents

All the calixarene-base compounds were synthesized according to the described methods [25-27]: *hexa-t*-butylcalix[6]arene (abbreviated **C6**), *hexa-t*-butyl-bis[(but-2-enyloxy)- *tetra*hydroxy calix[6]arene (**C6Cr2**), *hexa-t*-butyl-*tris*[(but-2-enyloxy)-*tri*hydroxy-calix[6] arene (**C6Cr3**), *hexa-t*-butyl-*tetrakis*-[(but-2-enyloxy)- dihydroxy calix[6] arene (**C6Cr4**), *hexa-t*-butyl-*tris*-[(ethoxycarbonyl)methoxy]-*tri*hydroxy-calix[6]arene(**C6Es3**), *hexa-t*-butyl-*tris* [(N,N-diethylamino carbonyl) methoxy]- *tri*hydroxy-calix[6] arene (**C6Am3**), *hexa-t*-butyl-*hexakis*-[(ethoxycarbonyl)methoxy]-calix[6]arene(**C6Es6**), *hexa-t*-butyl-*hexakis* [(N,N-diethylamino-carbonyl)methoxy] calix[6]arene (**C6Am6**), *hexa-t*-butyl-*tris*[(N,N-diethylamino-carbonyl)methoxy]- *tris*-(but-2-enyloxy)-calix[6]arene (**C6Am3Cr3**) and *hexa-t*-butyl-*tris* [(ethoxycarbonyl)methoxy]-*tris*-(but-2-enyloxy)-calix[6]arene (**C6Es3Cr3**).

Analytical-grade chloroform and deionized water were employed as solvents in the liquid-liquid extraction experiments. All others inorganic and organic reagents were standard grade and used without further purification.

Instrumentation and analysis

The metal concentration in aqueous medium was determined before and after extraction with ICP-OES - Spectroflame D Spectrophotometer ($\lambda=340,458$ nm and detection limit=0,01919 mg/l for palladium; $\lambda=381,966$ nm and detection limit=0,0081 mg/l for europium).

Liquid-liquid extraction of metal ions

The organic solutions were prepared by dissolving the required amount of calixarene derivative, in chloroform, to obtain a solution with 1×10^{-3} M concentration.

The aqueous solutions of metals were prepared by dissolving the required amount of PdCl₂ or Eu(NO₃)₃·5H₂O in acidulated water to obtain $5 \dots 10 \times 10^{-4}$ mol/L solutions. The acidity of the aqueous medium was monitored with a pH-instrument. The pH was adjusted to pH 2.5 and 4.1 with HCl, for Pd²⁺ solution and to pH 2.7-2.8 or 4.6 with HNO₃, for Eu³⁺ solutions.

Liquid-liquid extraction experiments were carried out by introducing the organic and aqueous solutions (1:1, 2:1 and 1:2 volumetric ratios) into extraction funnels and vigorously shaking them, for 30 minutes, using a mechanical shaker. The aqueous phase was left to settle, washed with CHCl_3 , separated and analysed.

The measurements were carried out with an ICP-OES instrument, using standard conditions calibration. The extraction yield ($\eta\%$) was calculated from the equation [28]:

$$\eta = (A_0 - A) / A_0 \times 100 \%$$

where A_0 and A are the initial and the final concentration (mg/L) of the metal salt before and after extraction, respectively.

ACKNOWLEDGEMENTS

The financial support of the Romanian Ministry of Education and Innovation under the project PNII 71-062 is gratefully appreciated.

REFERENCES

1. S. Erdemir, M. Bahadir, M. Yilmaz, *Journal of Hazardous Materials*, **2009**, *168*, 1170.
2. M.C. Semedo, A. Karmali, P.D. Barata, J.V. Prata, *Journal of Molecular Catalysis B: Enzymatic*, **2010**, *62*, 97.
3. M. Bayrakci, S. Ertul, M. Yilmaz, *Tetrahedron*, **2009**, *65*, 7963.
4. M. Atanassova, V. Lachkova, N. Vassilev, S. Varbanov, I. Dukov, *Polyhedron*, **2010**, *29*, 655.
5. M. A. Kamboh, I. B. Solangi, S. T. H. Sherazi, S. Memon, *Journal of Hazardous Materials*, **2009**, *172*, 234.
6. L. Elsellami, V. Chartron, F. Vocanson, P. Conchon, C. Felix, C. Guillard, L. Retailleau, A. Houas, *Journal of Hazardous Materials*, **2009**, *166*, 1195.
7. K. Ohto, H. Ishibashi, H. Kawakita, K. Inoue, T. Oshima, *Journal of Inclusion Phenomena and Macrocyclic Chemistry*, **2009**, *65*, 111.
8. F. Yang, Y. Wang, B. Hong, X. Chai, *Journal of Inclusion Phenomena and Macrocyclic Chemistry*, **2009**, *64*, 67.
9. E. A. Shokova, V. V. Kovalev, *Russian Journal of Organic Chemistry*, **2009**, *45(9)*, 1275.
10. A. Hamdi, R. Souane, L. Kim, R. Abidi, L. Mutihac, J. Vicens, *Journal of Inclusion Phenomena and Macrocyclic Chemistry*, **2009**, *64*, 95.

11. G. Daneshvar, A. Jabbari, Y. Yamini, D. Paki, *Journal of Analytical Chemistry*, **2009**, 64(6), 602.
12. M. S. Gidwani, H. Kaur, U. Pal, S. K. Menon, *Journal of Analytical Chemistry*, **2009**, 64(2), 104.
13. M. Surowiec, R. Custelcean, K. Surowiec, R. A. Bartsch, *Tetrahedron*, **2009**, 65, 7777.
14. N. Iki, *Journal of Inclusion Phenomena and Macrocyclic Chemistry*, **2009**, 64, 1.
15. O. H. Altshuler, N. V. Malysenko, G. J. Shkurenko, H. N. Altshuler, *Theoretical Foundations of Chemical Engineering*, **2009**, 43(1), 43.
16. R. Nie, X. Chang, Q. He, Z. Hu, Z. Li, *Journal of Hazardous Materials*, **2009**, 169, 203.
17. U. Ocak, M. Ocak, K. Surowiec, R. A. Bartsch, M. G. Gorbunova, C. Tu, M. A. Surowiec, *Journal of Inclusion Phenomena and Macrocyclic Chemistry*, **2009**, 63, 131.
18. X. Liu, K. Surowiec, R. A. Bartsch, *Tetrahedron*, **2009**, 65, 5893.
19. Y. de Gaetano, I. Clarot, J.-B. Regnouf-de-Vains, *Tetrahedron Letters*, **2009**, 50, 5793.
20. M. Surowiec, R. Custelcean, K. Surowiec, R. A. Bartsch, *Tetrahedron*, **2009**, 65, 7777.
21. X. Liu, K. Surowiec, R. A. Bartsch, *Tetrahedron*, **2009**, 65, 5893.
22. O. O. Karakus, H. Deligoz, *Analytical Letters*, **2010**, 43(5), 768.
23. N. Singh, D. Jang, *Supramolecular Chemistry*, **2009**, 21(5), 351.
24. T. A. Halgren, *J. Comput. Chem.*, **1999**, 20, 720.
25. A. Saponar, E.-J. Popovici, N. Popovici, E. Bica, G. Nemes, P. Petronela, I. Silaghi-Dumitrescu, *Rev.Chim.*, **2009**, 60(3), 278.
26. A. Saponar, I. Silaghi-Dumitrescu, E.-J. Popovici, N. Popovici, *Studia Universitatis Babes-Bolyai, Chemia*, **2007**, LII (4), 67.
27. A. Saponar, E.-J. Popovici, R. Grecu, I. Silaghi-Dumitrescu, N. Popovici, *Studia Universitatis Babes-Bolyai, Chemia*, **2009**, LIV (4), 203.
28. N. Toumi, F. Kajo, D. Fournier, F. Vocanson, R. Lamartine, I. Dumazet-Bonnamour, *Materials Science and Engineering C*, **2008**, 28, 645.

Dedicated to the memory of Prof. dr. Ioan Silaghi-Dumitrescu marking 60 years from his birth

THE INFLUENCE OF COAGULANTS IN COLLOIDAL PARTICLES REMOVAL FROM DISPERSIONS

ADINA GHIRIȘAN*, SIMION DRĂGAN

ABSTRACT. This study describes the physicochemical treatment applied to colloidal dispersion of carboxymethylcellulose (CMC) in order to improve the removal of colloidal particles from aqueous solution by sedimentation and pressure filtration. The physicochemical treatment consists in coagulation/flocculation with different coagulants/flocculants at different concentrations. By coagulation-sedimentation combination the optimal parameters were established to be 5.9 for pH and 200 mg/g (FeCl₃/CMC) for coagulant concentration. By coagulation-filtration the best result were obtained with the coagulant concentration of 200 mg/g (FeCl₃/CMC) and pressure difference of 4 bar.

Keywords: *physicochemical treatment, coagulation, flocculation, sedimentation, pressure filtration, carboxymethylcellulose.*

INTRODUCTION

The application of physicochemical treatment in removing micron-size or colloidal particles is widespread in wastewater treatment, before sedimentation and membrane (micro-, ultra- and nano-) filtration when the fouling of filtering surface occurs [1].

Coagulation by chemical additives and flocculation by natural or synthetic materials are the most important physicochemical pretreatment steps in industrial wastewater used to reduce the suspended and colloidal materials responsible for color and turbidity of the wastewater. A well-chosen pretreatment process can change the structure of the system improving the sedimentation and membrane filtration processes.

Removal of colloidal and micro-size particles by coagulation/flocculation, precipitation and neutralization involves particle destabilization and particle transport [2, 3]. Coagulants destabilize colloidal suspensions allowing particles to agglomerate into microflocs, while flocculants bring the microflocs into contact with each other forming large flocs.

* *Universitatea Babeș-Bolyai, Facultatea de Chimie și Inginerie Chimică, Str. Kogălniceanu Nr. 1, RO-400084 Cluj-Napoca, Romania, ghirisan@chem.ubbcluj.ro*

Experimental determination have shown that destabilization in filtration is similar to destabilization in coagulation; effective coagulants/ flocculants are observed to be effective “filter aids”. In the same time, particles transport in filtration is analogous to transport in coagulation/ flocculation processes [4].

A great variety of destabilizing chemicals is currently available for this purpose, including metal salts (e.g., salts of Al(III), Fe(III)) and natural and synthetic polymers, which may be organic or inorganic.

The effect of a coagulation/flocculation treatment depends on the pH, the type and concentration of the used additives, and the characteristics of the feed suspension [5].

The objectives of the present work are: a). evaluation of the physicochemical pretreatment procedure in removal of colloidal particles of carboxymethylcellulose by filtration; b). optimization of pH and coagulant concentration by jar test apparatus; and c). determination of filtration kinetics by pressure filtration tests.

RESULTS AND DISCUSSION

a). Carboxymethylcellulose (CMC) solution contains colloidal particles that not settle if no coagulant is added, causing turbidity. In order to destabilize the system and to remove the colloidal particles of CMC from solution, preliminary tests are conducted in this work using different coagulants as ferric chloride FeCl_3 , calcium chloride CaCl_2 , and polyacrilamide (PAA) as flocculant, and a combination of these.

Considering the mean filtration rate of coagulated/flocculated 5 g/L CMC solutions as performance parameter, the best results obtained by vacuum filtration are shown in Table 1.

Table 1. Results of preliminary tests

| Sample | Coagulant concentration [mg/g] | V_f [m^3/m^2] | τ [s] | $w_f \cdot 10^6$ [m/s] | Observation |
|-------------------------------------|--------------------------------|-----------------------------------|------------|------------------------|---------------|
| Solution CMC 3% | 0 | - | - | - | Rapid fouling |
| Solution CMC 1% | 0 | 0.00071 | 900 | 0.79 | Rapid fouling |
| Solution CMC 0.5% | 0 | 0.00116 | 900 | 1.29 | Rapid fouling |
| Solution CMC 0.5% + FeCl_3 | 75 | 0.0174 | 900 | 16.4 | Small flocs |

THE INFLUENCE OF COAGULANTS IN COLLOIDAL PARTICLES REMOVAL FROM DISPERSIONS

| Sample | Coagulant concentration [mg/g] | V_f [m^3/m^2] | τ [s] | $w_f \cdot 10^6$ [m/s] | Observation |
|------------------------------------|--------------------------------|---------------------|------------|------------------------|----------------------------|
| Solution CMC 0.5% + $FeCl_3$ | 150 | 0.0358 | 900 | 39.4 | Large flocs |
| Solution CMC 0.5% + $CaCl_2$ | 2980 | 0.0076 | 900 | 8.43 | No structural modification |
| Solution CMC 0.5% + $CaCl_2$ | 5960 | 0.0063 | 900 | 7.03 | No structural modification |
| Solution CMC 0.5% + PAA | 120 | 0.0093 | 900 | 10.3 | Small flocs |
| Solution CMC 0.5% + PAA | 240 | 0.0109 | 900 | 12.18 | Small flocs |
| Solution CMC 0.5% + $FeCl_3$ + PAA | 75 120 | 0.0542 | 900 | 60.22 | Large flocs |
| Solution CMC 0.5% + $FeCl_3$ + PAA | 75 240 | 0.035 | 900 | 38.88 | Gelling aggregates |

As Table 1 shows, the filtration of initial samples (with CMC concentration 0.5 %, 1% or 3 %) leads to the rapid fouling of filter medium, without the possibility to measure the filtration rate for 3% CMC solution sample. The rapid fouling of filtering surface caused by blocking and internal clogging justifies the pretreatment of CMC solution using coagulants and/or flocculants.

Comparing the values of obtained filtration rate it was concluded that, in spite that addition of polyacrylamide (PAA) can accelerate the filtration process, for the next experiments only $FeCl_3$, which is friendlier with the environment than (PPA), will be used as coagulant.

b). In order to optimize the pH and the FeCl_3 dosage, considering coagulation procedure before a conventional sedimentation, the methods of A. Koohestanian [6] and S. W. Krasner [7] were applied. The variation of supernatant turbidity after sedimentation in jar test apparatus for different pH values and constant coagulant concentration of 200 mg/g plotted in Figure 1 shows the minimal values for pH of 5.9.

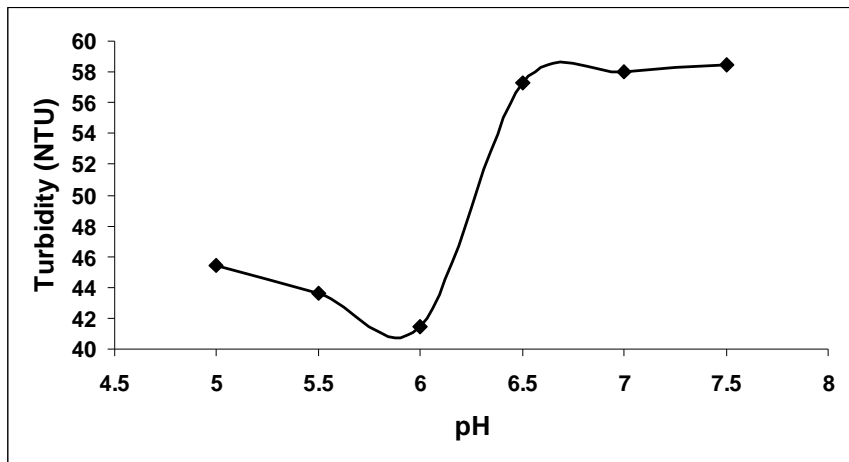


Figure 1. pH effect on the turbidity removal for 5 g/L CMC dispersion.

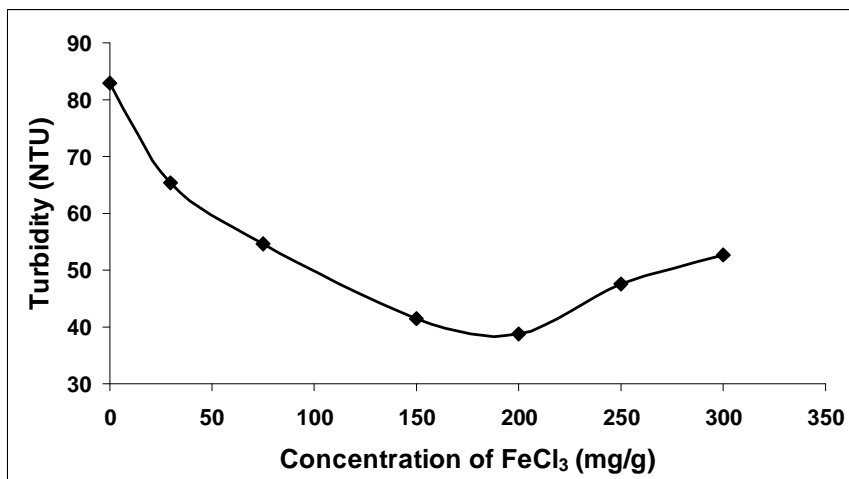


Figure 2. Coagulant concentration effect on the turbidity removal for 5 g/L CMC dispersion.

The influence of different concentrations of FeCl₃ added to CMC solution at constant pH = 5.9 is presented in Figure 2. As can be seen, by increasing the coagulant concentration, the supernatant turbidity decreases until the experimental concentration of coagulant is equal to 200 mg/g (FeCl₃/CMC). After this concentration the turbidity increases again. This means that for a concentration higher than 200 mg/g (FeCl₃/CMC) a re-dispersing of the flocs occurs, enhancing in this way the turbidity of solution.

Considering the combination coagulation-sedimentation at 200 mg/g (FeCl₃/CMC), the turbidity decreases from 83 NTU in initial solution to 38.76 NTU in supernatant, which means a turbidity removal with more than 53 %.

The progress of sedimentation, at optimal concentration of FeCl₃ equal to 200 mg/g (FeCl₃/CMC) and pH equal to 5.9 is shown in Figure 3. The mean settling rate of 0.63 mm/min was obtained by the typical curve.

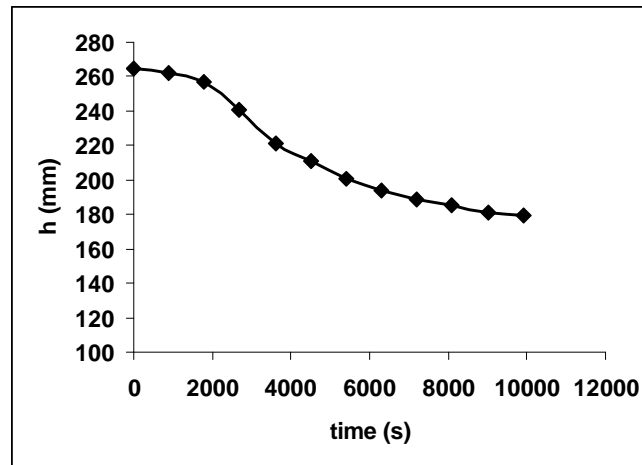


Figure 3. Sedimentation curve at optimal conditions.

c). To describe the pressure filtration, Darcy's law written as Equation 1, is proposed:

$$\frac{dV}{A \cdot dt} = \frac{\Delta p}{\eta \left(r_c \cdot c \cdot \frac{V}{A} + R_m \right)} \quad (1)$$

where V is the volume of filtrate (m³), Δp – pressure difference (Pa), A - filtering surface (m²), η - the liquid viscosity (Pa.s), r_c - specific resistance of the filter cake (m/kg), R_m - the resistance of the filter medium (m⁻¹), c – weight of solids/volume of filtrate (kg solid/m³ filtrate).

Considering $V/A = V_f$ (m^3/m^2) the specific filtrate volume, and integrating Equation (1) with the assumption of constant pressure, a linear dependence of t/V_f versus V_f is resulting (Equation 2):

$$\frac{t}{V_f} = \frac{\eta \cdot r_c \cdot c}{2 \cdot \Delta p} \cdot V_f + \frac{\eta \cdot R_m}{\Delta p} \quad (2)$$

The mean value of cake resistance r_c and the resistance of the filter membrane R_m determined from the slope a and the intercept b of linear plot t/V_f versus V_f are given by Equations (3) and (4):

$$r_c = \frac{a \cdot 2 \cdot \Delta p}{\eta \cdot c} \quad (3)$$

$$R_m = \frac{\Delta p \cdot b}{\eta} \quad (4)$$

Considering the results obtained by the combination coagulation-sedimentation procedure, pressure filtration tests were conducted after the coagulation with ferric chloride concentration between 150 mg/g and 200 mg/g (FeCl_3/CMC). Figures 4a and 4b show the influence of coagulant concentration on the filtration kinetics of 5 g/L CMC solution.

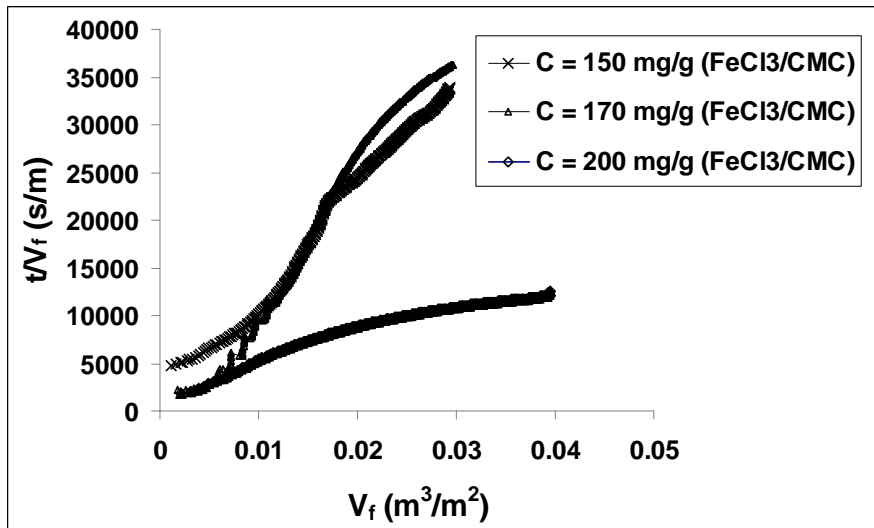


Figure 4a. Comparison of filtration behavior at 2 bar and different FeCl_3 dosage.

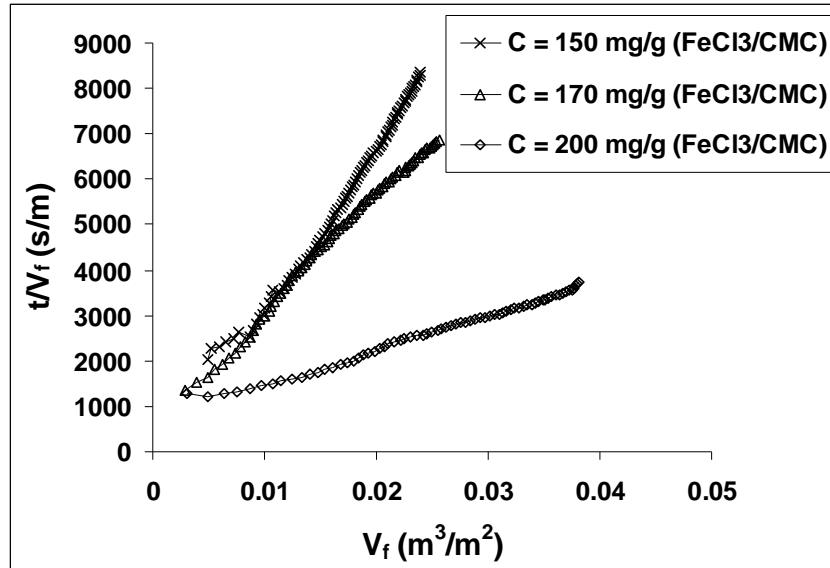


Figure 4b. Comparison of filtration behavior at 4 bar and different $FeCl_3$ dosage.

As it can be seen, an acceleration of the filtration process with the increase of the coagulant concentration is observed for experimental measurements at 2 bar and at 4 bar. In both cases a lower slope of the curves t/V_f vs. V_f was obtained when before pressure filtration a coagulant concentration of 200 mg/g ($FeCl_3/CMC$) was used.

Considering the effect of the coagulant concentration on the pressure filtration of 5 g/L CMC solutions, next results were determined from experimental data, using Equations (3) and (4): specific filter cake resistance of $r_c \approx 13.0 \cdot 10^{13}$ m/kg for coagulant concentration of 150 mg/g ($FeCl_3/CMC$), $r_c \approx 8.3 \cdot 10^{13}$ m/kg for 170 mg/g ($FeCl_3/CMC$), and $r_c \approx 2.0 \cdot 10^{13}$ m/kg for 200 mg/g ($FeCl_3/CMC$), and a mean medium resistance of $R_m \approx 3.0 \cdot 10^{11}$ m^{-1} , when the experiments were conducted at $\Delta p = 4$ bar.

Coagulant effect on turbidity removal by pressure filtration has shown a decrease from 83 NTU in initial samples to 6 - 8 NTU in filtrate, which means a turbidity removal with more than 90 %. This can be explained by adsorption phenomena and the retention of small particles on filter cake.

The influence of the pressure difference on the filtration test at coagulant concentration of 200 mg/g ($FeCl_3/CMC$) is shown in Figure 5. It can be seen an acceleration of filtration process with the increase of pressure difference from 1 bar to 4 bar.

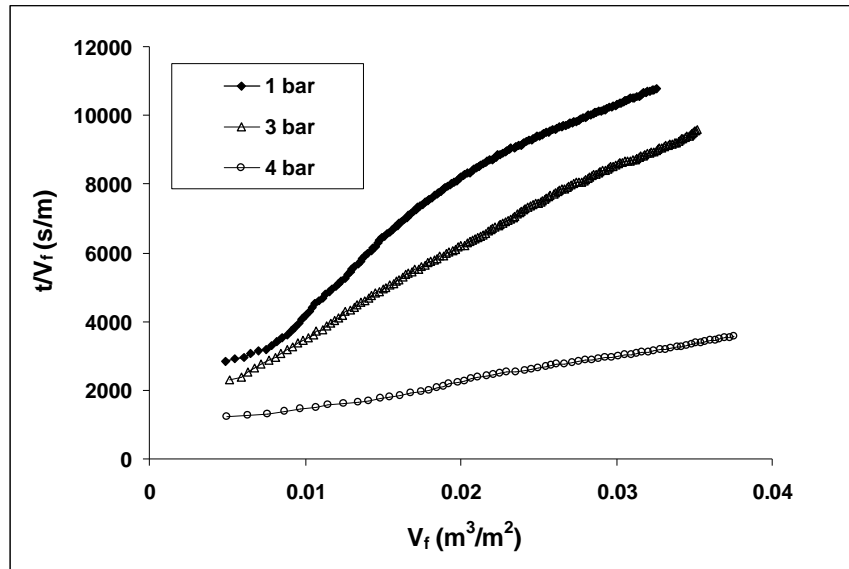


Figure 5. Comparison of filtration behavior at different pressure.

Specific filter cake resistances of $r_c \approx 6.0 \cdot 10^{13}$ m/kg for a difference pressure $\Delta p = 1$ bar, $r_c \approx 4.8 \cdot 10^{13}$ m/kg for $\Delta p = 3$ bar and $r_c = 2.0 \cdot 10^{13}$ m/kg for $\Delta p = 4$ bar were calculated considering experimental data at different pressures and constant coagulant concentration of 200 mg/g.

The results show that the specific filter cake resistance decreases with the increase of coagulant dosage and with the increase of pressure difference.

Considering the combination coagulation-filtration the best results were obtained for coagulant concentration of 200 mg/g (FeCl_3/CMC) and $\Delta p = 4$ bar. The mean filtration rate for these conditions, considering the calculated cake resistance, is $w_f = 20.5 \cdot 10^{-5}$ m/s, which is 3.5 times higher than filtration rate obtained for coagulant concentration of 150 mg/g (FeCl_3/CMC) and $\Delta p = 4$ bar ($w_f = 6.0 \cdot 10^{-5}$ m/s), and 10 times higher than filtration rate obtained for 200 mg/g (FeCl_3/CMC) and $\Delta p = 1$ bar ($w_f = 2.0 \cdot 10^{-5}$ m/s).

CONCLUSIONS

In this study coagulation with ferric chloride as physicochemical pretreatment before conventional sedimentation and before pressure filtration was applied to 5 g/L CMC solution samples in order to improve the removal of colloidal particles and to avoid membrane-fouling.

The optimal experimental parameters were obtained combining coagulation with settling in a jar test apparatus and coagulation with pressure filtration in Filtratest.

By coagulation-sedimentation combination the optimal parameters were established to be 5.9 for pH and 200 mg/g (FeCl_3/CMC) for coagulant concentration. The influence of coagulant concentration and pressure on filtration has shown an acceleration of filtration kinetics with the increase of the concentration of FeCl_3 from 150 mg/g to 200 mg/g and with the increase of pressure from 1 bar to 4 bar, by the reduction of the specific cake resistance.

After coagulation the turbidity of carboxymethylcellulose solution was found to be reduced by more than 53 % considering the combination coagulation-sedimentation and by more than 90% for the combination coagulation-filtration. This means that the procedure coagulation-filtration is more efficient for the removal of CMC particles due to adsorption phenomena and better retention of small particles on filter cake.

EXPERIMENTAL SECTION

Colloidal synthetic solutions of carboxymethylcellulose 5 g/L were obtained dissolving sodium carboxymethylcellulose, a white powder, in cold distilled water (initial turbidity was equal to 83 NTU).

Preliminary tests have been made using the laboratory vacuum equipment ($\Delta p = 400 \text{ mm Hg}$).

A jar test apparatus model JLT 6 was used for the optimization of pH and dosage of coagulants/flocculants. Samples of 500 mL of 5 g/L CMC solution were placed in six beakers. To optimize the pH, solutions of 1.0 N NaOH and 1.0 N H_2SO_4 were added in each beaker containing the CMC solution and 200 mg/mg (FeCl_3/CMC), determined by preliminary tests.

After pH adjustment different concentrations of ferric chloride (30, 75, 150, 200, 250, 300 mg/g) were tested by stirring at 100 rpm for 1 min, and then at 30 rpm for 15 min. Then, the stirrer was turned off in order to let the sample to settle for 30 min. Supernatant was sampled 10 mm below the water surfaces, and the turbidity and pH were measured. The procedures were repeated at fixed dosage to examine the optimum pH.

Turbidity was measured by an Analytic turbidimeter Hanna type C-102 with a range of 0 – 100 FTU.

The pH was measured with a pH/mV meter type Orion 4 STAR from Thermo Electron Corporation.

Pressure filtration tests were performed with the laboratory filtration equipment FITRATEST from BOKELA GmbH having a pressure filter cell of steel with the capacity of 400 mL and the filtering surface of 20 cm^2 . For each

experiment sample of 100 mL 5g/L CMC solution was tested. FILTRATEST apparatus was operated at constant pressure; pressure difference Δp was chosen between 1 bar and 4 bar. The cumulative filtrate weight was recorded online by the computer and analyzed using Excel software. Three replicate experiments were carried out for each set of experimental conditions. The reproducibility of experiments was higher than 95 %. A SEFAR filter medium with pore size of 1.0 microns was tested during the pressure filtration.

REFERENCES

1. J. Bratby, "Coagulation and Flocculation in Water and Wastewater Treatment", IWA Publishing, London, 2nd Edition, **2007**, chapters 3-5.
2. A. Ghirișan, „Separarea fizico-mecanică a sistemelor eterogene solid-lichid”, Ed. Casa Cărții de Știință, Cluj-Napoca, **2005**, chapter 3.
3. A. Ghirișan, S. Drăgan, A. Pop, M. Simihăian, V. Miclăuș, *Canadian Journal of Chemical Engineering*, **2007**, *85*, 900.
4. H. Stechemesser, B. Dobias, *Coagulation and Flocculation, Surfactant Science Series, CRC Press*, **2006**, 126, 969.
5. A. Ghirișan, Al. Pop, M. Moceanu, V. Miclăuș, *Studia Universitatis Babeș-Bolyai, Chemia*, **2005**, *50(1)*, 97.
6. A. Koohestanian, M. Hosseini, Z. Abbasian, *American-Eurasian Journal of Agriculture & Environment Science*, **2008**, *4(2)*, 226.
7. S.W. Krasner, G. Amy, *Journal of American Water Works Association*, **1995**, *87(10)*, 93.

Dedicated to the memory of Prof. dr. Ioan Silaghi-Dumitrescu marking 60 years from his birth

KINETICS OF THE PHENOL OXIDATION BY PERMANGANATE IN ACIDIC MEDIA. THE INTERMEDIATE OXIDIZED SPECIES 4,4'-BIPHENOQUINONE EVOLUTION

LUCIAN COPOLOVICI^{a,*} AND IOAN BALDEA^b

ABSTRACT. The kinetics of phenol oxidation by permanganate has been carried out in relative strong acidic media, in the presence and in absence of manganese (II) as catalyst. Formation of an intermediate colored species that absorbs light at 400 nm has been observed during the course of reaction. Its formation and decay has been followed spectrophotometrically. The intermediate has been assigned as 4,4'-biphenolquinone. Kinetic laws for the formation and consumption of this intermediate have been established. Complicate rate equations of the *one-plus* form were deduced either for building up or for decomposition of the intermediate. Rate constants, pre-equilibrium constants and experimental activation energies were determined. Some mechanistic considerations were made.

Keywords: phenol, permanganate, kinetics, 4,4'-biphenolquinone.

INTRODUCTION

The kinetic study of oxidation by permanganate has received a considerable attention because of its importance in analytical [1,2] and organic chemistry [3-5]. Nevertheless, there are still unsolved aspects of the mechanisms of many permanganate oxidation reactions [6]. The reaction mechanisms of oxidation of various substrates, including phenols [7-15], in alkaline solutions are better understood [16-19], but they are more complex in acidic solutions due to ability of manganese to exist in various oxidation states between VII and II, as well as to the auto-catalytic character of numerous permanganate oxidations [20-25]. Knowledge of the phenol oxidation has applications in water purification [26] and some organic syntheses [3,4]. In this paper we report information obtained from a kinetic study by monitoring

^a Estonian University of Life Sciences, Institute of Agricultural and Environmental Sciences, Kreutzwaldi 1, Tartu 51014, Estonia. * E-mail: lucian.copolovici@emu.ee

^b Babes-Bolyai University of Cluj, Faculty of Chemistry and Chemical Engineering, 11 Arany Janos Str. Cluj-Napoca, 400028 Romania, e-mail: ibaldea@chem.ubbcluj.ro

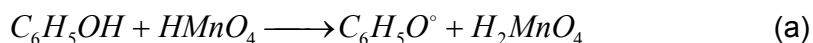
the evolution of 4,4'-biphenoquinone intermediate during the phenol oxidation in acidic solution, either in the absence or in the presence of manganese (II) at the start of reaction.

RESULTS AND DISCUSSION

Spectra and mechanistic considerations. Substantial evidence has been obtained for the formation of an intermediate species that absorbs light within the region 350–450 nm, with a peak located at 400 nm. The mixing of aqueous phenol and permanganate in acidic media leads to solution color changes within an interval of several minutes. It starts purple-violet, rapidly turns yellowish-brown and faded to colorless in a slower pace. When phenol and permanganate were mixed and spectra recorded at 1 second intervals by a diode –array spectrophotometer, an absorption band emerge and then falls to zero around 400 nm. The permanganate ion peak at 525 nm decreases steadily from the start of the process [27]. No isosbestic points have been noticed on time-dependent spectra, suggesting the involvement of some consecutive steps. The same peak position was obtained when the reaction was carried out in the presence of Mn(II) in the reaction mixture. The spectra were presented previously [27] where we performed the reduction of MnO_4^- by Mn^{2+} in large excess. Mn(III) is the single species formed [28]. After complete decay of permanganate ion, a phenol solution was injected into the mixture to achieve a large excess concentration. A yellowish-brown color suddenly appeared during the mixing that further faded to colorless, as time elapses. Successive spectra were recorded and position of the peak is the same as when permanganate was the oxidizing agent. Because Mn(III) is a strong oxidizing agent (redox potential for the Mn(III)/Mn(II) couple of 1.5 - 1.6 V [29]), one can assume it reacts more rapidly with phenol than Mn(VII) does. Such a reaction rate also explains the catalytic effect of Mn(II) in permanganate oxidations. On the other hand, this system involves the same intermediate species as in the case of phenol - permanganate system.

A comparison of the spectra obtained with those of $\text{Mn}_{\text{aq}}^{3+}$, and $\text{Mn}(\text{OH})^{2+}$ ions [30], Mn(IV) with a peak at 418 nm [31–33], identified by Insausti and co-workers [22,23] reveals that the intermediate is an oxidation product of phenol rather than an intermediate valence state of manganese. The spectra of *ortho*- and *para*-quinone differ from the one in discussion. A supplementary argument for the formation of such an intermediate is brought by the oxidation of *ortho*-cresol, when a similar intermediate with an absorption peak at 408 nm is formed. In the case of *para*-cresol oxidation either by permanganate or Mn(III), no absorption peak was found in this range of wavelength.

We consider that the intermediate is 4,4'-biphenoquinone formed by oxidative coupling of phenoxy radicals that is the primary oxidation product of phenol by Mn(VII) or Mn(III). Such a relative long-lived intermediate has been found in the case of phenol oxidation by ferrate (VI) in phosphate buffered solutions [34]. Similar behavior has been found by hexacyanoferrate(III) [35a], *trans*-dioxoruthenium(VI) [35b], oxochromium(IV) ion [35c] in acidic media oxidation. Lee and Sebastian [14] showed that phenoxy radicals undergo further coupling and oxidation reactions, which eventually produce a mixture of *ortho* and *para*-diphenoquinone, the final products of alkaline oxidation. Hay and co-workers described oxidative coupling with 2,6-disubstituted phenols [36]. D.T Yiu and co-workers [35b] showed that either by a hydrogen abstraction or by an electron transfer, the phenoxy radical is produced with ruthenium complex. It undergoes two rapid concurrent reactions. The first is a further three-electron oxidation to give *p*-benzoquinone and other organic products. The second is a coupling and oxidation process to give 4,4'-biphenoquinone, followed by a decay step. Therefore, we consider that the formation of 4,4'-biphenoquinone requires the following sequence of steps:



In the step (b) phenoxy radical switches to a carbon radical. The formation of a covalent bond between one of the limiting structures of the phenoxy radical and the oxidation can take place successively. The involvement of free radicals during the permanganate oxidation of phenols or other organic substrates is supported by the induced polymerization of ethylacrylate [24]. It has been mentioned previously in the case of other phenol oxidation [4,37,38].

Kinetics. Under large hydrogen ion concentration the final reduction product is Mn(II). No MnO₂ precipitate is formed. Our kinetic measurements were carried out under experimental conditions where the induction period was either imperceptible short or it was missing. At least three replicate runs were carried out for each set of experimental conditions, which yield rate constants that do not differ to more than 3 %. Under the excess of phenol, all absorbance recordings could be described by linear kinetics, regardless the absorbance was monitored at 525 nm for Mn(VII), or at 400 nm for the intermediate.

At 400 nm the evolution of absorbance against time, a biphasic curve, obeys the following equation:

$$A = [Mn(VII)]_0 \varepsilon_0 e^{-k'_{obsd}t} + s[Mn(VII)]_0 \varepsilon_1 \frac{k'_{obsd}}{k''_{obsd} - k'_{obsd}} (e^{-k'_{obsd}t} - e^{-k''_{obsd}t}) + \varepsilon_2 [C_6H_5OH]_0 \quad (2)$$

where k'_{obsd} and k''_{obsd} are pseudo-first-order rate coefficients for the formation and decay of the intermediate. ε_0 , ε_1 and ε_2 stand for molar absorptivities of all three absorbing species (permanganate, biphenolquinone intermediate and phenol, respectively), s is a stoichiometry factor. $A_\infty = \varepsilon_2 [C_6H_5OH]_0$ is the final absorbance. Since phenol and permanganate absorb light very weakly in this region of electronic spectrum and $\varepsilon_0, \varepsilon_2 \ll \varepsilon_1$, the first and the last terms in eq. (2) have an insignificant contribution. Therefore,

$$A - A_\infty = C \cdot (e^{-k'_{obsd}t} + e^{-k''_{obsd}t}) \quad (3)$$

The constant C is the factor in front of the parenthesis of the second term in eq. (2).

A non-linear regression of equation (3) was used for the data recorded at 400 nm and has fitted well with R^2 between 0.990 and 0.999 and χ^2 of the order of magnitude smaller than 10^{-6} . At constant hydrogen ion concentration, the dependence of the observed first-order rate constants on phenol concentration is presented in Table 1. These data were obtained in the absence and the presence of Mn(II) as catalyst.

Table 1. Observed first-order rate constants (mean values) for the two-step sequence at $[MnO_4^-] = 1.30 \cdot 10^{-4}$, $[HClO_4] = 0.38$, $\mu = 0.4$ and $T = 298K$ in absence and presence of $3.33 \cdot 10^{-4} \text{ mol.L}^{-1}$ Mn(II)

| $[C_6H_5OH]$ mmol.L ⁻¹ | k'_{obsd} s ⁻¹ | k'_{obsd} s ⁻¹ Mn(II) | k''_{obsd} s ⁻¹ | k''_{obsd} s ⁻¹ Mn(II) |
|--------------------------------------|-----------------------------|---------------------------------------|------------------------------|--|
| 0.33 | 0.0180 | 0.032 | 0.00203 | 0.0015 |
| 0.67 | 0.0383 | 0.055 | 0.00315 | 0.0024 |
| 1.00 | 0.0526 | - | 0.00511 | - |
| 1.33 | - | 0.091 | - | 0.0041 |
| 1.67 | 0.074 | 0.125 | 0.00663 | 0.0050 |
| 2.00 | 0.087 | 0.150 | 0.00702 | 0.0057 |
| 2.67 | 0.120 | 0.180 | 0.00782 | - |
| 3.33 | 0.133 | 0.200 | 0.00864 | 0.0075 |
| 4.00 | 0.155 | 0.224 | - | - |
| 5.00 | 0.179 | 0.231 | 0.0091 | 0.0081 |
| 6.67 | 0.196 | 0.244 | 0.0096 | 0.0087 |
| 8.33 | 0.217 | - | 0.0100 | - |

In this paper we focused the attention on the formation and decay of 4,4'-biphenoquinone intermediate that has been followed at 400 nm and exhibits a biphasic behavior concerning the absorbance evolution. Its formation involves a total loss of four electrons from two phenol molecules. On the behalf of permanganate ions it means that 1.25 moles of this condensed compound are formed for each mole of permanganate reduced to Mn(II). Therefore it can be formed at least 1.25 times faster than permanganate consumption. Because of the involvement of the intermediate valence state of Mn, more reactive than Mn(VII), the building of such a species in the early stages of reaction can outpace the rate of disappearance of Mn(VII) reported previously [27].

The rate coefficient for the intermediate formation k'_{obsd} (s^{-1}) exhibits a tendency of leveling off towards larger concentration of phenol as shown in Figure 1. The curve can be described by the following equation:

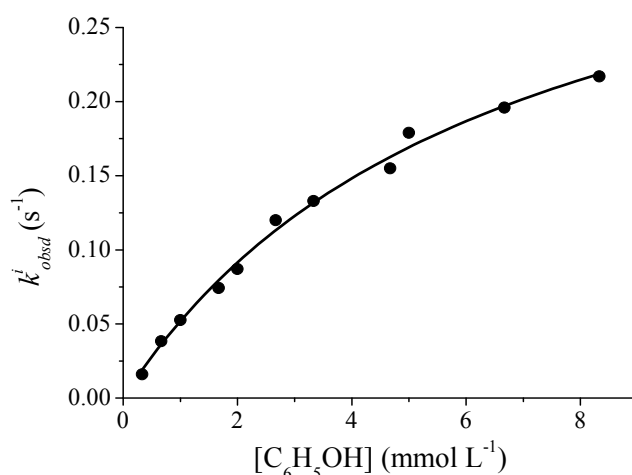


Figure 1. The first-order rate constant dependence on phenol concentration for the formation of intermediate.

$$k'_{obsd} = \frac{a_1[C_6H_5OH]}{1 + b_1[C_6H_5OH]} = \frac{(57.5 \pm 2.5)[C_6H_5OH]}{1 + (125 \pm 11)[C_6H_5OH]} \quad (4)$$

with $\chi^2 = 0.000001 \text{ s}^{-1}$ and $R^2 = 0.996$. In the presence of Mn(II) ion, the same pattern has been observed and the equation is:

$$k'_{obsd(Mn)} = \frac{a'_1[C_6H_5OH]}{1 + b'_1[C_6H_5OH]} = \frac{(102 \pm 5)[C_6H_5OH]}{1 + (227 \pm 20)[C_6H_5OH]} \quad (5)$$

The acceleration of reaction rate by Mn(II), which causes a supplementary decrease of Mn(VII) concentration, is due to the intermediate oxidation states of manganese that react faster with reducing organic species. For the case of Mn(II) initially added to the reaction mixture, data presented in columns 3 of Table 1 reveals also that k'_{obsd} increases strongly at smaller concentration of phenol and not so pronounced at higher concentration. A similar tendency of leveling off also appears.

The linear form of this one-plus type equation as a double reciprocal of (4) and (5) also permits the determination of the coefficients.

$$\frac{1}{k'_{obsd}} = \frac{1}{a[C_6H_5OH]} + \frac{b}{a} \quad (6)$$

The effect of the acidity on these rate coefficients was investigated within the range 0.07 – 0.7 mole·L⁻¹ HClO₄. The mean rate coefficients obtained from at least three individual runs are given in Table 2. Data in the second and third columns fitted well with a linear dependence:

$$k'_{obsd} = (3.0 \pm 8,5) \cdot 10^{-3} + (0.34 \pm 0.02)[H^+] \quad (7)$$

with R²= 0.999 and SD = 0.004 in the absence of Mn(II), and

$$k'_{obsd(Mn)} = (1.9 \pm 2.0) \cdot 10^{-2} + (0.52 \pm 0.05)[H^+] \quad (8)$$

in the case of the initial presence of Mn(II) species in the mixture.

Table 2. The effect of acid concentration on the rate. [C₆H₅OH]=3.33·10⁻³, [MnO₄⁻] = 1.30·10⁻⁴, μ = 0.4 and T = 298K in absence and presence of 3.33·10⁻⁴ mol·L⁻¹ Mn(II)

| [HClO ₄] mol·L ⁻¹ | k'_{obsd} s ⁻¹ | k'_{obsd} s ⁻¹ Mn(II) | k''_{obsd} s ⁻¹ | k''_{obsd} s ⁻¹ Mn(II) |
|---|-----------------------------|---------------------------------------|------------------------------|--|
| 0.0773 | 0.0249 | 0.065 | 0.00316 | 0.00319 |
| 0.155 | 0.0559 | 0.1046 | 0.0046 | 0.0049 |
| -0.232 | 0.0884 | 0.139 | 0.00662 | 0.00572 |
| 0.387 | 0.133 | 0.200 | 0.00846 | 0.00746 |
| 0.541 | 0.189 | 0.288 | 0.0098 | 0.0089 |
| 0.619 | 0.207 | 0.340 | 0.0101 | 0.00908 |
| 0.773 | 0.267 | 0.428 | 0.0110 | 0.00928 |

The linear dependence of k'_{obsd} as described by eqs (6) and (7) indicates a first-order with respect to hydrogen ion, the intercept of the lines being not statistically different from zero.

By combining equations (4) and (7), the rate coefficient for the intermediate formation can be written as dependent of both phenol and acid concentrations as:

$$k'_{obsd} = \frac{\alpha_1 [C_6H_5OH][H^+]}{1 + \beta_1 [C_6H_5OH]} \quad \text{or} \quad \frac{[H^+]}{k'_{obsd}} = \frac{1}{\alpha_1 [C_6H_5OH]} + \frac{\beta_1}{\alpha_1} \quad (9)$$

The parameters are: $\alpha_1 = (144 \pm 8) \text{ L}^2 \text{ mol}^{-2} \text{ s}^{-1}$ $\beta_1 = (125 \pm 13) \text{ L} \cdot \text{mol}^{-1}$ and $R^2 = 0.997$. By using additionally the data in column 1 of Table 2 in the linear form of eq. (9), the parameters of the line are: slope = 0.0066, the intercept = 0.8696 and $R^2 = 0.9962$ corresponding to $\alpha_1 = (144 \pm 8) \text{ L}^2 \text{ mol}^{-2} \text{ s}^{-1}$, $\beta_1 = (132 \pm 12) \text{ L} \cdot \text{mol}^{-1}$.

It is obvious that the *p*-diphenoquinone intermediate is formed on the account of permanganate in the early stages of the reaction. Therefore, in the initial absence of Mn(II) ion, its formation is caused by the oxidation of phenol by permanganate, or when considering the first-order with respect to hydrogen ion, by permanganic acid. Indeed, when the process was followed at 400 nm and various initial concentrations of permanganate were used, always as limiting reactant, a linear dependence of k'_{obsd} on permanganate has been found:

$$k'_{obsd} = (9.2 \pm 5.4) \cdot 10^{-3} + (9.1 \pm 0.4) \cdot 10^2 [MnO_4^-] \quad (10)$$

Note that in the early stages of reaction, under the larger concentration of oxidizing agent, the larger concentration of phenoxy free radicals is formed and the larger rate of biphenoquinone would be. The intercept is quite small and can be considered zero. It clearly justifies the use of equation (4), which is first order with respect to the colored oxidizing agent. Another possibility of the proton involvement could be its rapid bounding to phenol.

If one compares k_{obsd} at the permanganate consumption ($\lambda = 525 \text{ nm}$), as obtained previously [27], with the apparent first-order rate coefficient k'_{obsd} , the latter is greater than $1.25 \cdot k_{obsd}$. The stoichiometric factor of 1.25 comes out from the need of 4-electron removal from reducing species to form a molecule of biphenoquinone. The involvement of intermediate valence-state of Mn, which react faster than Mn(VII) is apparent. The dependence in Table 1 proves the involvement of at least Mn(III) species revealing the autocatalysis/catalysis by Mn(II). On the other hand, the involvement of two terms in the denominator of rate equation (9) indicates also the presence of a fast reversible process.

The effect of temperature on the apparent first-order rate constant k'_{obsd} in the range of 15 – 40°C yielded an experimental activation energy of 67 ± 2 kJ.mol⁻¹. A comparison with the smaller value of 12.5 ± 1.9 kJ.mol⁻¹ when permanganate consumption was monitored [27], indicates that the step of formation of phenoxy radical is not the rate-determining step for 4,4'-biphenoquinone formation, but its further oxidation or coupling. The switch from oxy free radical to a carbon free radical (eq. 1.b) seems also to take place rapidly within the π -conjugated electronic system. The coupling and further oxidation (or further oxidation of C-free radical and coupling) could also justify the linear dependence of k^i_{obsd} on permanganate.

Concerning the decay of the intermediate species, the same pattern of the one-plus type rate law has been found as dependent of the substrate concentration. The apparent first-order rate constant is:

$$k''_{obsd} = \frac{a_2[C_6H_5OH]}{1 + b_2[C_6H_5OH]} = \frac{(7.1 \pm 0.3)[C_6H_5OH]}{1 + (547 \pm 33)[C_6H_5OH]} \quad (11)$$

with $\chi^2 = 1.5 \cdot 10^{-7}$ s⁻¹ and $R^2 = 0.997$ for the consumption of the intermediate in the absence of Mn(II) ion. The linear form of eq.(10), as a double reciprocal, is presented in Figure 2.

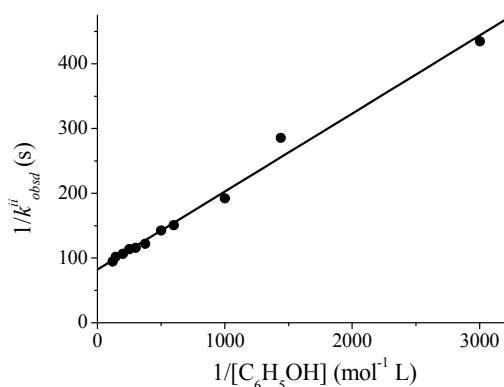


Figure 2. Double reciprocal plot of equation (5) with the data in Table 1

The parameters of the line are: slope = $1/a_2 = 0.141$, intercept = $b_2/a_2 = 77.1$, $R^2 = 0.9877$. The constants are $a_2 = 7.1 \pm 0.3$ L.mol⁻¹s⁻¹ and $b_2 = 547 \pm 33$ L.mol⁻¹ (errors statistically counted). On the other hand, as presented in the last two columns of table 1, a small decline of k''_{obsd} , as compared to

the values in the absence of Mn(II) in the mixture has been noticed for the disappearance of the biphenoquinone intermediate.

A more complex behavior has been found at the decay of the intermediate as dependent on the mineral acid in solution as compared to that of the intermediate formation. A one-plus type equation describes hydrogen ion effect on the observed rate. It infers the involvement of a rapid protonation pre-equilibrium. The apparent first-order rate constant is:

$$k_{obsd}'' = \frac{a_2'[H^+]}{1 + b_2'[H^+]} = \frac{(0.051 \pm 0.0023)[H^+]}{1 + (3.47 \pm 0.25)[H^+]} \quad \frac{1}{k_{obsd}''} = \frac{1}{a_2'[H^+]} + \frac{b_2'}{a_2'} \quad (12)$$

It is characterized by $\chi^2 = 3.68 \cdot 10^{-8}$, $R^2 = 0.998$ and $R^2 = 0.9968$ for the line. In the presence of Mn(II) the corresponding values are: $a_2' = (5.6 \pm 0.3) \cdot 10^{-2} \text{ L} \cdot \text{mol}^{-1} \cdot \text{s}^{-1}$, $b_2' = 4.79 \pm 0.23 \text{ L} \cdot \text{mol}^{-1}$ and $R^2 = 0.993$. These last values are not far from those in the absence of Mn(II), suggesting the interaction between phenol and 4,4'-biphenoquinone is not significantly influenced by the catalyst.

When combining equations (11) and (12), the decay rate of the intermediate is described by the following rate equation:

$$-\frac{d[OC_6H_4 = C_6H_4O]}{dt} = \frac{\alpha_2[C_6H_5OH][H^+]}{1 + \beta_2[C_6H_5OH][H^+]} [OC_6H_4 = C_6H_4O] \quad (13)$$

and the first-order rate coefficient is:

$$k_{obsd}'' = \frac{\alpha_2[C_6H_5OH][H^+]}{1 + \beta_2[C_6H_5OH][H^+]} \quad (14)$$

with the parameters $\alpha_2 = (17.9 \pm 0.7) \text{ L}^2 \cdot \text{mol}^{-2} \cdot \text{s}^{-1}$ and $\beta_2 = (1.32 \pm 0.12) \cdot 10^3 \text{ L}^2 \cdot \text{mol}^{-2}$. It can be assigned to the reaction of the protonated *p*-diphenoquinone with the excess phenol molecule.

If this equation describes well the data, it should be applied to both series of measurements, when either phenol, or the acid has been maintained constant and the other was varied. Indeed, we obtained such a correlation in the linear form, as presented in Figure 3.

$$\frac{1}{k_{obsd}''} = \frac{1}{\alpha'''} \frac{1}{[C_6H_5OH][H^+]} + \frac{\beta'''}{\alpha'''} \quad (15)$$

with $R^2 = 0.993$, $(\beta_2 / \alpha_2 = 74 \pm 4)$ and $(1 / \alpha_2 = 0.056 \pm 0.002) \text{ mol}^2 \cdot \text{s} \cdot \text{L}^{-2}$.

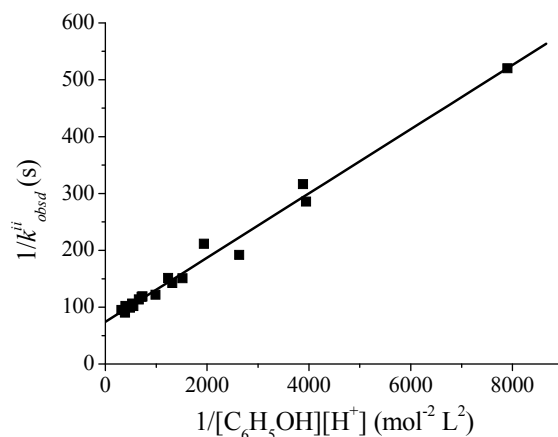
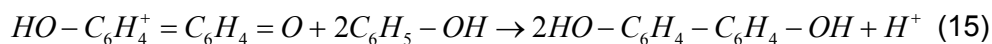


Figure 3. Linear presentation of all data (eq.14) of the two series of measurements (Tables 1 and 2) in the absence of Mn(II).

Accounting for the acid effects, interaction of protonated 4,4'-biphenoquinone is involved in the phenol oxidation to generate biphenols [39] with the stoichiometry:



It could proceed by two successive one-equivalent electron-transfer yielding free oxy radicals from phenol and biphenol. The apparent activation energy determined over the same range of temperature by the effects on k_{obsd}'' is $50 \pm 1 \text{ kJ}\cdot\text{mol}^{-1}$, a value smaller than that of the intermediate formation, and could be attributed to the first one- equivalent electron-transfer step (or first hydrogen abstraction from phenol by protonated 4,4'-biphenoquinone). The second step involves a free oxy radical of biphenol, which would react faster with the second phenol molecule.

The overall stoichiometry of phenol – permanganate reaction found previously [27] implies that the partial oxidized products of phenol react further, and probably faster, up to the ring rupture, even in the presence of phenol excess with any oxidizing species in relative strong acid solution. A possible route could be by means of traces of benzoquinone formed by phenoxy radical oxidation. All intermediate oxidation states of manganese are able to bring about oxidative ring breakage of *o*- or *p*-benzoquinone. The complexity of the system needs more data for a better elucidation of the elementary steps network.

CONCLUSIONS

The formation and decay of 4,4'-biphenoquinone, as an active intermediate, has been followed and the corresponding rate laws have been determined.

The presence of Mn(II) in the solution has a catalytic effect on the formation and practically no influence on the consumption of intermediate.

The one-plus rate laws revealed complex mechanisms with the involvement of some pre-equilibrium concerning the proton intervention. Third-order rate constants α and equilibrium constants β were estimated from the kinetics.

The apparent activation energies were also obtained, which argue the rate determining steps implied in the formation and redox consumption of 4,4'-biphenoquinone.

EXPERIMENTAL SECTION

Materials. Chemicals of analytical grade and ultra-pure water (de-ionised and tetra-distilled) were used throughout this study. A stock solution of HClO₄ was prepared from Merk's 70 % HClO₄ and standardized by titration. Stock solution of NaClO₄ was prepared from Merk's NaClO₄·H₂O and standardized by titration after passing a measured volume over Vionit –100C (H-form) cationic resin. Working solution of KMnO₄ was prepared before each set of runs and standardized by titration with oxalic acid. The phenol solution was also prepared freshly from purified staff (distillation under low pressure; m.p. 40.5 – 41.5°C).

Kinetic measurements. Electronic absorption spectra were recorded either by using a M-40 Diode-Array Spectrophotometer or a Jasco UV-VIS V-530 spectrophotometer. A conventional spectrophotometrical method was used to monitor the progress of the reaction at constant temperature. Two wavelengths could be used: either at 525 nm, where permanganate ion exhibits an absorption peak and its disappearance was recorded, or 400 nm, where a biphasic plot has been obtained, the formation and the decay of a yellowish-brown colored intermediate species. The reaction was performed in a quartz 5-cm path length cuvette. It was started by injecting of 5 mL permanganate solution over the mixture of the other reactants. The mixing time does not exceed 1 second. Pseudo-first-order conditions were employed. Both the phenol and mineral acid were taken in excess as compared to permanganate oxidizing agent. Kinetic measurements were also carried out in the presence of Mn(II) ions, in a small excess as compared to permanganate.

ACKNOWLEDGMENT

Financial support of Romanian National University Research Council (CNCSIS) is gratefully acknowledged by the authors.

REFERENCES

1. P. Berka, Z. Zavesky, *Mikrochim. Acta*, **1974**, *3*, 493.
2. D. A. Skoog, D. M. West, *Fundamentals of Analytical Chemistry*, 1-st Ed. Holt, Reinhart and Winston, New-York, **1963**.
3. W. I. Taylor, A. R. Battersby, *Oxidative coupling of phenols*, Ed. Dekker, New York, **1967**.
4. L. K. Liu, C. S. Lin, *J. Chin. Chem. Soc.*, **1996**, *43*, 61.
5. S. Dash, S. Patel, B. K. Mishra, *Tetrahedron*, **2009**, *65*, 707.
6. F. Freeman, C. O. Fuselier, C. R. Armsted, C. E. Dalton, P. A. Davidson, E. M. Karchesfski, D. E. Krochman, M. N. Johnson, N. K. Jones, *J. Am. Chem. Soc.*, **1981**, *103*, 1154.
7. F. Freeman, *Rev. React. Species Chem. React.*, **1976**, *1*, 179.
8. R. Stewart, *Oxidation in Organic Chemistry*, Ed. K. B. Wiberg, Academic Press, New York, Part A, **1965**.
9. L. I. Simandi, M. Jaky, F. Freeman, C. O. Fuselier, E. M. Karchesfski, *Inorg. Chim. Acta*, **1978**, *31*, 457.
10. D. Benson, *Mechanisms of Oxidation by Metal Ions*, Elsevier, Amsterdam, **1976**.
11. L. I. Simandi, M. Jaky, N. T. Son, J. Hagedus-Vajda, *J. Chem. Soc. Perkin Trans 2*, **1977**, *10*, 1794.
12. R. H. Simoyi, P. de Kepper, I. R. Epstein, K. Kustin, *Inorg. Chem.*, **1986**, *25*, 538.
13. P. Bhatia, K. K. Banerji, *J. Chem. Soc. Perkin Trans 2*, **1983**, 1577.
14. D. G. Lee, C. F. Sebastian, *Can. J. Chem.*, **1981**, *59*, 2776.
15. D. G. Lee, C. F. Sebastian, *Can. J. Chem.*, **1981**, *59*, 2780.
16. R. G. Panari, R. B. Chougale, S. T. Nadibewoor, *J. Phys. Org. Chem.*, **1998**, *11*, 448.
17. R. G. Panari, R. B. Chougale, S. T. Nadibewoor, *Polish Journ. Chem.*, **1998**, *72*, 99.
18. M. Jaky, J. Szammer, *J. Phys. Org. Chem.*, **1997**, *10*, 420.
19. B. K. Satsangi, S. Kothari, *J. Ind. Chem. Soc.*, **1980**, *74*(1), 16.
20. J. W. Landbury, C. F. Cullis, *Chem. Rev.*, **1958**, *58*, 403.
21. M. J. Insausti, F. Mata-Perez, M. P. Alvarez-Macho, *An. Quim.*, **1991**, *87*, 877.
22. M. J. Insausti, F. Mata-Perez, M. P. Alvarez-Macho, *Collect. Czech. Chem. Commun.*, **1994**, *59*, 528.
23. M. J. Insausti, F. Mata-Perez, M. P. Alvarez-Macho, *Collect. Czech. Chem. Commun.*, **1996**, *61*, 232.
24. S. Vivekanandan, K. Venkatarao, M. Santappa, S. Shanmuganathan, *Indian J. Chem., Sect. A*, **1980**, *19*, 364; Alexandra Csavdari, I. Baldea, *Studia Univ. Babeş-Bolyai, Chem.*, **2007**, *52*(1), 35.

KINETICS OF THE PHENOL OXIDATION BY PERMANGANATE IN ACIDIC MEDIA

25. M.S. Manhas, F. Mohasmmmed, Z. Khan, *Colloids and Surface. A. Physicochemical and Engineering Aspects*, **2007**, 253, 165.
26. N. Kang, D. S. Lee, J. Yoon, *Chemosfere*, **2002**, 47, 915.
27. L. Copolovici, I. Baldea, *Rev. Roum. Chim.*, **2007**, 52, 1045.
28. G. Davies, *Coordin. Chem. Rev.*, **1969**, 4, 199.
29. A. McAuley, *Coordin. Chem. Rev.*, **1970**, 5, 245.
30. F. Well, G. Davies, *Nature*, **1965**, 205, 692; F. Well, G. Davies, *J. Chem. Soc. A*, **1967**, 1858; J. P. Fackler, I. D. Chawla, *Inorg. Chem.*, **1964**, 3, 1130.
31. L. I. Simandi, M. Jaky, C. R. Savage, Z. A. Schelly, *J. Am. Chem. Soc.*, **1985**, 107, 4220.
32. F. Mata, J. Perez-Bendito, A. Arranz, *Z. Phys. Chem. (Leipzig)*, **1983**, 135, 141.
33. M. I. Hussain, F. Ahmad, *Transition Met. Chem.*, **1990**, 15, 185.
34. H. Huang, D. Sommerfeld, B. C. Dunn, E. M. Eyring, C. R. Lloyd, *J. Phys. Chem. A*, **2001**, 105, 3536.
35. a) M. Bhattacharjee, M.K. Mahanti, *Int. J. Chem. Kinet.*, **1983**, 15, 197; b) T.Y. Douglas Yiu, F.W.Mendy Lee, W.Y. William Lam, Tai-Chu Lau, *Inorg.Chem.*, **2003**, 42, 1225; c) A. Alajlouni, A. Bakac, J.H. Espenson, *Inorg. Chem.*, **1993**, 32, 5792.
36. A. S. Hay, *J.Org.Chem.*, **1969**, 34, 1160; G.F.Endres, A.S.Hay, J. W. Eustance, *J. Org. Chem.*, **1963**, 28, 1300; A. S. Hay, *J.Polym Sci.*, **1962**, 88, 581; A. S. Hay, *Tetrahedron Lett.*, **1965**, 4341.
37. J. D. Rush, J. E. Cyr, Z. Zhao, B. H. Bielski, *J. Free Radical Res.*, **1995**, 22, 349.
38. A. Al-Ajlouni, K. Shawakfeh, R. Rajal, *Kinetics and Catalysis*, **2009**, 50, 88.
39. F. M. Menger, D. W. Carnahan, *J. Org. Chem.*, **1985**, 50, 3927.

Dedicated to the memory of Prof. dr. Ioan Silaghi-Dumitrescu marking 60 years from his birth

SYNTHESIS OF TUNGSTEN TRIOXIDE MESOPOROUS POWDERS PREPARED BY INORGANIC SOL-GEL ROUTE

ECATERINA BICA^{a,b}, ELISABETH-JEANNE POPOVICI^a, MARIA ȘTEFAN^a, IOANA PERHAIȚA^a AND IONEL CĂTĂLIN POPESCU^b

ABSTRACT. Powders of mesoporous tungsten trioxide (WO₃) have been synthesized by an inorganic sol-gel route, in presence of polyethylene glycol PEG as porosity regulating agent. The influences of PEG addition and calcination regime on powder properties were investigated. Samples characterization was performed by thermal analysis, UV-Vis spectroscopy, as well as by surface area and porosity measurements.

Keywords: *Tungsten trioxide powders, sol-gel method, porosity, optical properties.*

INTRODUCTION

Tungsten trioxide (WO₃) is a semiconductor with special optical and electrical properties which explain its use as photoanode in electrochemical hydrogen production or as photocatalyst in pollutants photodegradation [1-4]. The energy band gap of 2.3 - 2.8 eV allows hole generation and quick formation of electron-hole pairs under UV light irradiation, which confer WO₃ a good photocatalytic activity [5, 6]. The morpho-structural properties of the powder, i.e. crystalline structure, porosity, surface morphology, particles size and optical characteristics are strongly influenced by the synthesis route and subsequent treatment conditions [7, 8].

Among the preparation methods, the sol-gel route offers many advantages such as molecular-scale homogeneity, high purity and reactivity, as well as controlled particles size and shape of the obtained product [9-12]. By this synthesis route, mesoporous WO₃ powders could be obtained in special preparation conditions. Their high photocatalytic activity in oxidation

^a Babeș-Bolyai University, "Raluca Ripan" Institute for Research in Chemistry, Fantanele 30, Cluj-Napoca, Romania, ebica@chem.ubbcluj.ro

^b Babeș-Bolyai University, University, Faculty of Chemistry and Chemical Engineering, Arany Janos 11, Cluj-Napoca, Romania

processes is correlated with a large surface area, with many active sites, which can adsorb water, molecular oxygen or hydroxyl group in order to produce active oxidizing species [13].

The present paper continues our studies concerning the preparation of WO_3 powders and thin films, with well defined properties [14-17]. In this context, tungsten trioxide powders were prepared by sol-gel method, in presence of polyethylene glycol (PEG), as porosity regulating agent. The influences of polymer additive and calcination regime on WO_3 powder properties were also investigated. Because the main goal of our studies is the preparation of WO_3 -based materials with good photocatalytic properties, special attention was given to the powder porosity control.

RESULTS AND DISCUSSIONS

Tungsten trioxide powders were obtained from tungstic acid precursors ($WO_3 \cdot xH_2O$) prepared by sol-gel method, in the presence of polyethylene glycol with variable polymerization degree (PEG200, PEG400, PEG600). The thermal treatment was performed at $550^\circ C$ for 30 - 90 minutes (Table 1).

Table 1. Synthesis conditions of WO_3 samples

| Precursor code | Polymer additive | Sample code | Thermal treatment |
|----------------|------------------|-------------|--------------------------------|
| Pr_SG1 | - | SG1-30 | $550^\circ C / 30 \text{ min}$ |
| | | SG1-90 | $550^\circ C / 90 \text{ min}$ |
| Pr_SG2 | PEG200 | SG2-30 | $550^\circ C / 30 \text{ min}$ |
| | | SG2-90 | $550^\circ C / 90 \text{ min}$ |
| Pr_SG3 | PEG400 | SG3-30 | $550^\circ C / 30 \text{ min}$ |
| | | SG3-90 | $550^\circ C / 90 \text{ min}$ |
| Pr_SG4 | PEG600 | SG4-30 | $550^\circ C / 30 \text{ min}$ |
| | | SG4-90 | $550^\circ C / 90 \text{ min}$ |

In order to establish the optimal calcination regime, the tungstic acid precursors were investigated by thermal analysis. Thermogravimetric (TGA), differential thermogravimetric (DTG) and differential thermal analysis (DTA) results illustrate the difference between the thermal behavior of $WO_3 \cdot xH_2O$ precursors prepared with or without polymer additive (Fig.1).

The sample with no polymer additive (Pr-SG1) shows a total weight loss of ~12%. The two main decomposition steps are associated with the removal of physically ($25-200^\circ C$) and chemically bonded water ($200-400^\circ C$). The endothermic effect observed at $305^\circ C$ corresponds to the tungstic acid decomposition.

The thermal behavior of all PEG containing precursors was similar, the major difference being the total weight loss. Between 25-150°C, there are two steps of weight loss, associated with the removal of physical adsorbed water and alcohol. The weight loss step noticed at 150-250°C was related with PEG decomposition. DTG curves illustrate that the maximum weight loss is at ~215°C (Pr_SG2), ~201°C (Pr_SG3) and ~191°C (Pr_SG4). On DTA curves, the corresponding endo-thermal peaks can be noticed at ~220°C (Pr_SG2), ~207°C (Pr_SG3) and ~201°C (Pr_SG4). For PEG containing powders, one additional small exo-thermal effect can be observed at ~250°C (Pr_SG2), ~246°C (Pr_SG3) and 242°C (Pr_SG4) that could be ascribed to the self-ignition of the residual polyalcohol.

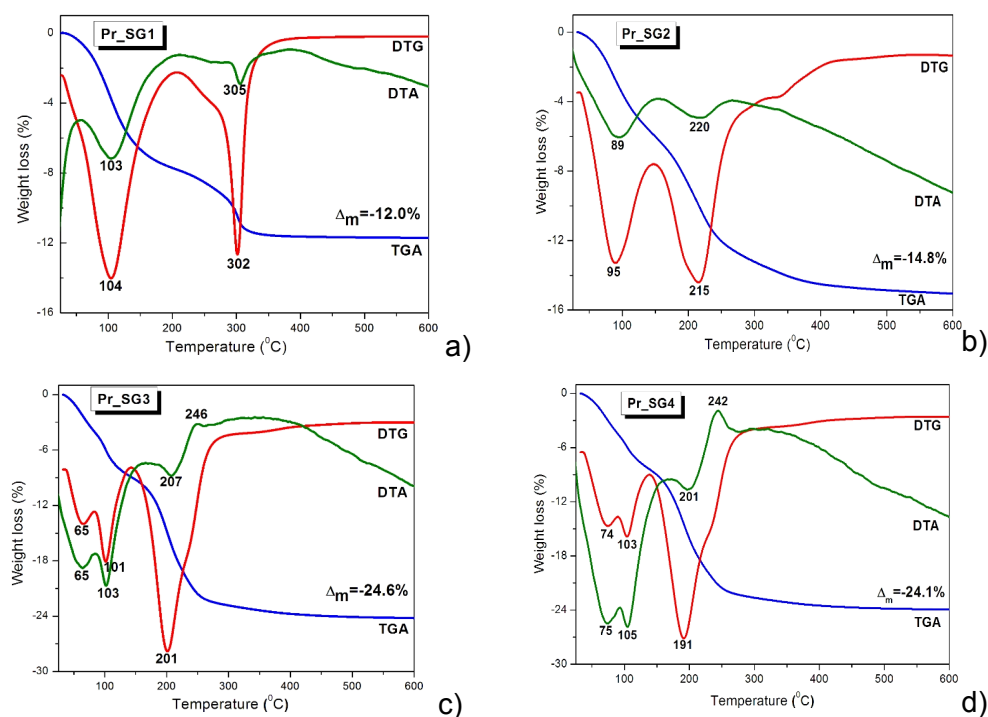


Figure 1. TGA/DTG/DTA curves of precursors with no polymer (a), PEG200 (b), PEG400 (c) and PEG600 (d) additive

According to the thermal analysis results, the conversion of precursors with or without polymer addition into tungstic oxide powders is finalized at 500°C.

In order to obtain WO₃ powders with controlled porosity properties, the thermal treatment regime was investigated. For this reason, precursor

samples were thermally treated for 30 min (short thermal treatment) and 90 min (long thermal treatment) at 550°C. Subsequently, the specific surface area and porosity were determined using the nitrogen adsorption isotherms (Fig. 2).

The BET (Brunauer, Emmett & Teller) specific surface area was calculated by determining the monolayer volume of adsorbed gas (Table 2). The micro-pores ($d < 2\text{nm}$) volume and area were calculated from the t-plot (thickness curve) using the Broekhoff-de Boer equation, involving the thickness evaluation of the monolayer of adsorbed gas. The mesopore ($d = 2 - 50\text{nm}$) and macropore ($d > 50\text{nm}$) volume and area distribution were determined using BJH (Barett, Joyner & Halenda) calculation, based on the variation of the thickness of both the adsorbate layer and the condensed liquid, with porosity [18].

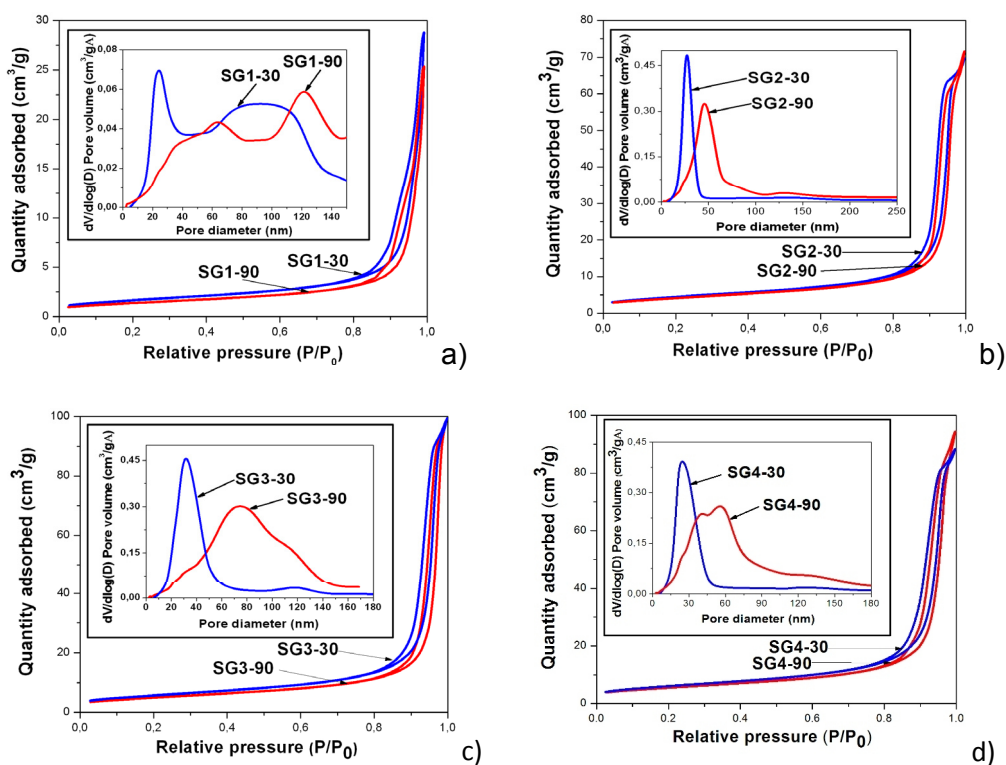


Figure 2. Adsorption-desorption isotherms of WO_3 samples and the volume pores distribution curve in function of pore diameter (inset): a) SG1 (WO_3); b) SG2 ($\text{WO}_3/\text{PEG200}$); c) SG3 ($\text{WO}_3/\text{PEG400}$); d) SG4($\text{WO}_3/\text{PEG600}$)

Table 2. The surface area and porosity characteristics of WO₃ samples

| Sample code | Specific surface area BET (m ² /g) | Micro-pores (t-plot) | | Meso and Macro-pores (BJH-desorption) | | |
|-------------|---|-----------------------------------|--------------------------------|---------------------------------------|--------------------------------|-----------------------|
| | | Total volume (cm ³ /g) | Total area (m ² /g) | Total volume (cm ³ /g) | Total area (m ² /g) | Average diameter (nm) |
| SG1-30 | 5.9 | 0.0003 | 2.1 | 0.0453 | 5.7 | 103.7 |
| SG1-90 | 4.9 | 0.0004 | 2.0 | 0.0400 | 4.8 | 33.7 |
| SG2-30 | 16.2 | 0.0007 | 5.6 | 0.1121 | 18.5 | 123.1 |
| SG2-90 | 15.0 | 0.0013 | 6.6 | 0.1132 | 16.5 | 27.5 |
| SG3-30 | 20.3 | 0.0013 | 7.8 | 0.1577 | 22.7 | 108.8 |
| SG3-90 | 17.6 | 0.0014 | 7.2 | 0.1545 | 18.6 | 33.2 |
| SG4-30 | 21.7 | 0.0009 | 7.4 | 0.1409 | 24.9 | 116.5 |
| SG4-90 | 19.6 | 0.0018 | 8.4 | 0.1498 | 22.4 | 26.7 |

The distribution curve of the no polymer containing WO₃ is multimodal which accounts for the heterogeneous porosity of the powder (Fig. 2a).

The increase of the calcination time decreases the surface area (from 5.9 to 4.9 m²/g), at same time with the decrease of the meso- and macropore volume and area. Additionally, the average pore diameter decreases from ~103.7 nm to ~33.7 nm.

The addition of polyethylene glycol determines the regularization of pore dimensions, for both types of thermally treated samples. All distribution curves become unimodal (Fig. 2b-d). At the same time, the surface area of WO₃ powders increases in direct relation with the enlargement of the pore volume and area. The effect is stronger for polyalcohol with high polymerization degree. It can be concluded that PEG additive acts as porosity regulator.

The prolongation of the thermal treatment shifts the maximum of the distribution curve from mesopore to macropore domain. This suggests that the small size pores coalesced under the thermal treatment.

Tungsten trioxide powders prepared with PEG additive are mesoporous and show a relative homogeneous porosity as compared with no polymer containing WO₃ powder. The effect was stronger for sample prepared with PEG200.

The use of PEG with higher molecular weight increases the pore volume and area and consequently enlarges the BET specific surface area. The prolongation of the thermal treatment determines a slow displacement of pores size toward macropore domain, due to the complete removal of the organic material.

All tungsten trioxide powders absorb light in the visible domain and have a lime-fruit color. The influence of the polymer addition and thermal synthesis regime on the WO₃ powder color was put in evidence by the diffuse reflectance spectra depicted in Fig. 3. The no polymer containing WO₃ powder (SG1-30) presents a good reflection in the yellow-green spectral domain with a maximum at 519 nm. Moreover, the powder reflection is improved with about 15% by the thermal treatment (SG1-90).

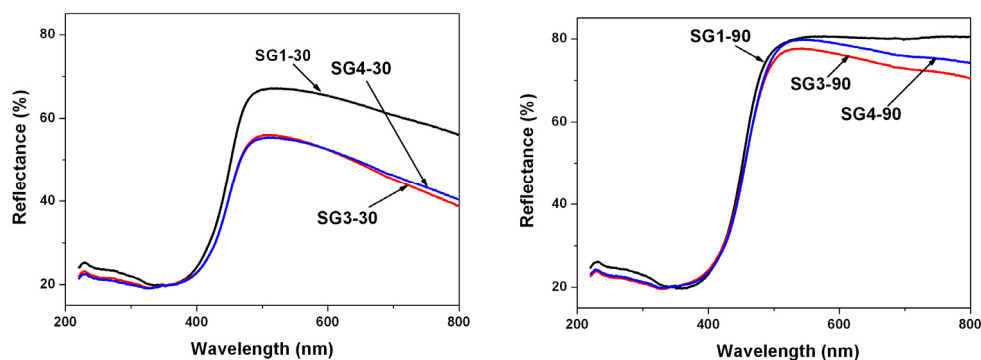


Figure 3. Diffuse reflectance spectra of WO_3 powders with no polymer containing (SG1), PEG400 (SG2) and PEG600(SG3) addition

The PEG addition seems to a blue-shift of the maximum reflectance and to decrease the reflectivity of WO_3 powders. The prolongation of the thermal treatment improves the powder reflectivity with about 20%.

Some of the optical characteristics of WO_3 powders, determined on the basis of the diffuse reflectance spectra, are summarized in Table 3. The optical band gap (E_g) was evaluated from the absorption spectra obtained by conversion of the diffuse reflectance spectra.

Table 3. Optical characteristics of WO_3 powders

| Code probe | Maximum reflectance (R_{\max}) | | Wavelength cut-off $\lambda_{\text{cut-off}}$ (nm) | E_g (eV) |
|------------|------------------------------------|----------------------|---|---------------|
| | Wavelength λ (nm) | Reflectance R (%) | | |
| SG1-30 | 519 | 67 | 481.5 | 2.58 |
| SG1-90 | 563 | 81 | 488.9 | 2.54 |
| SG3-30 | 512 | 56 | 490.8 | 2.53 |
| SG3-90 | 543 | 78 | 496.1 | 2.50 |
| SG4-30 | 510 | 55 | 482.9 | 2.57 |
| SG4-90 | 545 | 80 | 494.1 | 2.51 |

According to the literature data, the band gap energy of semiconductors can be estimated from the wavelength cut-off ($\lambda_{\text{cut-off}}$) representing the intersection point between the tangent at the absorption curve and the x axis [19, 20]. The band gap energy is calculated using the relation E_g (eV) = $1240 / \lambda_{\text{cut-off}}$ (nm).

The calculated values of the band gap energy are in 2.50 - 2.58 eV range, in good agreement with the literature data [21]. The band gap tends to decrease with both the polymer addition and the annealing duration.

The use of a relative longer thermal treatment is favorable for the obtaining of WO_3 powders with improved optical properties. The effect is stronger for samples prepared with PEG additive, probable in association with a more complete removal of organics.

Some of the tungsten trioxide powders were tested for photocatalytic activity in the dye degradation. For these preliminary tests, SG1-30 (WO_3) and SG3-30 (WO_3 /PEG400) samples were used for the methylene blue photo-degradation. The efficiency values were 90% for SG1-30 and 40% for SG3-30, illustrating that WO_3 samples show significant photocatalytic activity. The incomplete removal of the organic material dramatically damages the photocatalytic activity for dye oxidative degradation.

CONCLUSIONS

Tungsten trioxide powders were prepared following an inorganic sol-gel route, in presence of polyethylene glycol i.e. PEG200, PEG400 and PEG600. The surface area and porosity as well as the optical properties of WO_3 powders are influenced by thermal treatment regime and PEG addition.

Tungsten trioxide powders prepared with PEG additive are mesoporous and show a relative homogeneous porosity as compared with the no polymer containing WO_3 powder. The effect is stronger for sample prepared with PEG200. The use of PEG with higher molecular weight increases the pore volume and area and consequently, enlarges the BET specific surface area. The increase of the thermal treatment time determines a slow displacement of pores dimensions toward the macropore domain, due to a better removal of the organic material.

As evidenced by the diffuse reflectance spectroscopy, the polymer addition and the thermal synthesis regime influence the color of WO_3 powder. The PEG addition exerts a blue-shift of the maximum reflectance and decreases the reflectivity of WO_3 powders. The use of a relative longer time for thermal treatment favors obtaining of WO_3 powders with improved optical properties. The calculated band gap energies are in good agreement with the literature data and decrease with both polymer addition and the annealing duration.

Some of the mesoporous tungsten trioxide powders were used as photocatalysts for a reference dye photodegradation. Thus, the tested WO_3 samples show a significant photocatalytic activity for the oxidative degradation of methylene blue. The incomplete removal of the organic material, associated with a short thermal treatment, damages the photocatalytic activity.

EXPERIMENTAL SECTION

Sample preparation

Tungsten trioxide (WO_3) powders were prepared from tungstic acid solution obtained by dissolving 8 g tungsten powder (Merck) into 60 ml 30% hydrogen peroxide (Merck). The dissolution process was conducted under magnetic stirring, at 0 -10⁰C (exothermic reaction) and the H_2O_2 excess was removed by catalytic decomposition on Pt black [22]. In order to obtain powders with controlled porosity, polyethylene glycol (Carlo Erba) with variable molecular weight i.e. PEG200, PEG400 or PEG600 was used as additive. The yellow-translucent sol was dried at 70⁰C, in air. The as obtained tungstic acid precursors were annealed at 550⁰C, in air, for 30 or 90 minutes.

Sample characterization

The tungstic acid precursors were investigated by thermal analysis (Mettler Toledo TGA/SDTA851; heating rate 5⁰C/min; N_2 atmosphere).

WO_3 powders were characterized by surface area measurements (Micromeritics Tristar II 3020 instrument, N_2 adsorption; BET method for surface area; the BJH method/desorption branch for pores size distribution) and UV-Vis spectroscopy/diffuse reflectance spectra (Jasco Spectrometer V650, with ILV 724 integrating sphere accessory, light source D2/WI). The photocatalytic activity was evaluated for methylene blue degradation (1g WO_3 powder was used for 100 ml aqueous 0.125 mM solution of methylene blue).

ACKNOWLEDGEMENTS

This work was supported by the Romanian Ministry of Education, Research and Innovation (Contract PNII 71-047).

REFERENCES

1. H. Wang, P. Xu, T. Wang, *Thin Solid Films*, **2001**, *388*, 68.
2. A. Watcharenwong, W. Chanmanee, N. R. Tacconi, C. R. Chenthamarakshan, P. Kajitvichyanukul, K. Rajeshwar, *Journal of Electroanalytical Chemistry*, **2008**, *612*, 112.
3. H. Liu, S. Huang, L. Zhang, S. Liu, W. Xin, L. Xu, *Catalysis Communications*, **2009**, *10*, 544.
4. A. Cremonesi, Y. Djaoued, D. Bersani, P.P. Lottici, *Thin Solid Films*, **2008**, *516*, 4128.

5. M. G. Hutchins, O. Abu-Alkhair, M.M. El-Nahass, K. Abd El-Hady, *Materials Chemistry and Physics*, **2006**, *98*, 401.
6. J. Sun, Y. Wang, R. Sun, S. Dong, *Materials Chemistry and Physics*, **2009**, *115*, 303.
7. M. Deepa, M. Kar, D.P. Singh, A.K. Srivastava, S. Ahmad, *Solar Energy Materials & Solar Cells*, **2008**, *92*, 170.
8. A. Cremonesi, Y. Djaoued, D. Bersani, P.P. Lottici, *Thin Solid Films*, **2008**, *516*, 4128.
9. J. Livage, M. Henry, C. Sanchez, *Progress in Solid State Chemistry*, **1988**, *18*, 259.
10. I. Jimenez, J. Arbiol, A. Cornet, J.R. Morante, *IEEE Sensors Journal*, **2002**, *2*, 329.
11. H. I.S. Nogueira, A.M.V. Cavaleiro, J. Rocha, T. Trindade, J.D. Pedrosa de Jesus, *Materials Research Bulletin*, **2004**, *39*, 683.
12. H. Liu, T. Peng, D. Ke, Z. Peng, C. Yan, *Materials Chemistry and Physics*, **2007**, *104*, 377.
13. Z. Lixia, Z. Qin, L. Qingcheng, *Journal Of Rare Earths*, **2006**, *24*, 60.
14. M. Stefan, E. Bica, L. Muresan, R. Grecu, E. Indrea, M. Trif, E. J. Popovici, *Journal of Optoelectronics and Advanced Materials – Symposia*, **2010**, *2*, 115.
15. E. Bica, M. Stefan, L. E. Muresan, E. Indrea, I. C. Popescu, E. J. Popovici, *Journal of Optoelectronics and Advanced Materials – Symposia*, **2009**, *1*, 1011.
16. E. Bica, M. Stefan, I. C. Popescu, L. Muresan, M. Trif, E. Indrea, E. J. Popovici, *Journal of Optoelectronics and Advanced Materials – Symposia*, **2010**, *2*, 107.
17. E. Bica, L. E. Muresan, L. Barbu-Tudoran, E. Indrea, I. C. Popescu, E. J. Popovici, *Studia Universitatis Babeş-Bolyai, Chemia*, **2009**, *LIV*, 15.
18. P. A. Webb, C. Orr, "Analytical Methods in Fine Particle Technology", Micromeritics Instrument Corporation, U.S.A., **1997**, chapter 3.
19. J. Portier, H.S. Hilal, I. Saadeddin, S.J. Hwang, M.A. Subramanian, G. Campet, *Progress in Solid State Chemistry*, **2004**, *32*, 207.
20. S. Gorai, P. Guha, D. Ganguli, S. Chaudhuri, *Materials Chemistry and Physics*, **2003**, *82*, 974–979.
21. G. R. Bamwenda, H. Arakawa, *Applied Catalysis A: General*, **2001**, *210*, 181.
22. M. Stefan, E. Bica, L.E. Muresan, E. Indrea, E.J. Popovici, *Journal of Optoelectronics and Advanced Materials – Symposia*, **2009**, *1*, 1004.

Dedicated to the memory of Prof. dr. Ioan Silaghi-Dumitrescu marking 60 years from his birth

GROWTH RATE OF HYDROXYAPATITE CRYSTALS OBTAINED BY PRECIPITATION

**VALENTINA ROXANA DEJEU*, BARABÁS REKA, ANA-MARIA CORMOȘ,
BOGYA ERZSÉBET SÁRA, PAUL-ȘERBAN AGACHI**

ABSTRACT. Identification of a precipitation process consists in the formulation of a mathematical model which describes the real system characteristics. The model parameters have physical significance in terms like growth rate, nucleation rate or population density of particles. In the present work, the precipitation kinetics of hydroxyapatite (HAP) was studied at the laboratory scale using a 0.5 L batch reactor. The vessel was operated continuously at 25 °C and 50 °C at different feed concentrations. A methodology already known for other systems was applied to determine the kinetic parameters (growth rate) from the crystal size distribution (CSD) in the preparation of hydroxyapatite. Predicted particle size characteristics shown reasonable agreement with experimental data collected. The influence of feed concentration on particle size of hydroxyapatite was discussed too.

Keywords: *hydroxyapatite, growth rate, population balance, precipitation, particle formation, mathematical*

INTRODUCTION

The study of precipitation processes using chemical reaction engineering is based on a direct correlation between the processes kinetic (chemical reaction rates, nucleation and growth rates) and the final product quality (crystal shape and CSD). The way that this estimation is made is essential in the critical analysis of the accuracy and model validity. Several authors have presented methods for the simultaneous estimation of crystal growth and nucleation kinetics from batch crystallizations. In an early study, Bransom and Dunning (1949) derived a crystal population balance to analyse batch CSD for growth and nucleation kinetics. Misra and White (1971), Ness and White (1976) and McNeil et al. (1978) applied the population balance

* *Universitatea Babeș-Bolyai, Facultatea de Chimie și Inginerie Chimică, Str. Kogălniceanu Nr. 1, RO-400084 Cluj-Napoca, Romania, vdejeu@chem.ubbcluj.ro*

to obtain both nucleation and crystal growth rates from the measurement of crystal size distributions during a batch experiment. In a refinement, Tavaré and Garside (1986) applied the laplace transformation to the population balance. Qui and Rasmusson (1991) and Nvlt (1989), respectively, measured solution concentration during seeded batch cooling crystallizations and determined the crystal size distribution from which growth and nucleation rates were determined. Witkowski et al. (1990) used a non-linear parameter estimation technique to estimate nucleation and growth rates based on solution concentration and light obscuration measurements. Gutwald and Mersmann (1990) estimated growth and nucleation rates from constant supersaturation controlled batch crystallization. Qui and Rasmuson (1994) proposed a direct optimization method based on solution concentration and product CSD data from seeded batch experiments. Aoun et al. (1999) reviewed methods for determining precipitation kinetics and also presented a method for the simultaneous determination of growth and nucleation kinetics from batch experiments [1].

The precipitation of calcium phosphates has attracted the interest of many researches because of its importance in industrial water system scale formation (e.g. heat exchangers, cooling towers, boilers, etc.), in water treatment processes, in catalysis as supporting material, in agriculture as fertilizers, and basically in bio-mineralization processes [2, 3, 4]. Hydroxyapatite, thermodynamically the most stable calcium phosphate at pH > 5, is the main inorganic compound of hard tissues in vertebrates. Although the precipitation of HAP is of particular importance in the bio-mineralization processes, very little is known about the crystal growth mechanism [5].

In the present work, the precipitation kinetics and the influence of feed concentration on particle size of hydroxyapatite was studied at the laboratory scale. Kinetic parameters identification was realized using an optimization algorithm based on a least squares minimization.

Precipitation kinetics

For a global treatment of the growing phenomena is necessary to model the crystal size distribution using the population balance equation (PBE) [6, 7]. General form of PBE described by Randolph and Larson [8] is:

$$\frac{\partial n}{\partial t} + G \frac{\partial n}{\partial L} = B_{aggl} + B_{disr} - D_{aggl} - D_{disr} - \frac{nQ}{V} \quad (1)$$

where the birth terms for agglomeration and disruption are:

$$B_{aggl} + B_{disr} = \frac{L^2}{2} \int \frac{K_{aggl} n(L_u) n(L_v) dL_u}{L_v^2} + \int K_{disr} S(L_u, L_v) n(L_u) n(L_v) dL_u \quad (2)$$

and the death terms for agglomeration and disruption are:

$$D_{aggl} + D_{disr} = n(L) \int K_{aggl} n(L_u) dL_u + K_{disr} n(L) \quad (3)$$

The expression for the supersaturation was found to be:

$$S = \left(\frac{C_A^{v_A} C_B^{v_B}}{K_{sp}} \right)^{1/(v_A+v_B)} \quad (4)$$

Crystal growth rate data from industrial crystallizers are usually correlated empirically with environmental conditions, such as concentration and temperature using a power law model of the form:

$$G = k_g (\sigma + 1)^g \quad (5)$$

The power coefficient g in the growth equation does not depend on the form of the equation used and is normally a number between 1 and 2. The constants g and k_g are temperature-dependent and are usually fit to the Arrhenius equation to obtain a general expression for growth rate as a function of temperature. The Arrhenius equation can be written as:

$$k_g = A \exp(-E_a / RT) \quad (6)$$

where A is a constant and E_a is the activation energy. The activation energy can be used to obtain information of whether the rate-controlling step is diffusion or surface integration. A complete crystal growth expression that includes both the effect of temperature and supersaturation on the growth rate would, therefore, be written as:

$$G = A \exp(-E_a / RT) (\sigma + 1)^g \quad (7)$$

The agglomeration and disruption kernels are also assumed to depend on the supersaturation in power law form:

$$K_{aggl} = \beta_{aggl} f(\varepsilon) \sigma^g \quad (8)$$

$$K_{disr} = \beta_{disr} g(\varepsilon) \sigma^g \quad (9)$$

and the mean crystal residence time is:

$$\tau = \frac{Q}{V} \quad (10)$$

The method of moments, described by Hulburt and Katz [9], was used to solve PBE (a partial integro-differential equation). Using the method of moments, equation (1) becomes a set of ordinary differential equations in the moments. The j moment is:

$$\mu_j = \int_0^{\infty} L^j n(L) dL \quad (11)$$

The lower order moments (i.e., $j = 0, 1, 2, 3$) are related to the physical description of the particle size distribution, i.e. μ_0 is related to the total number of particles, μ_1 is related to the total particle diameter, μ_2 is related to the total particle surface area and μ_3 is related to the total particle volume.

For a well-mixed batch reactor in which crystal breakage and agglomeration may be neglected, the population balance equation leads to the partial differential equation which describes the crystal size distribution $n(L, t)$ as a function of both crystal size and time, where G is the overall linear growth rate (dL/dt); equation (1) becomes:

$$\frac{\partial n}{\partial t} + \frac{\partial(Gn)}{\partial L} = 0 \quad (12)$$

For example, if the crystal growth rate is invariant with size and in the absence of particle breakage and agglomeration, after the moment transformation equation (12) is represented by a set of ordinary differential equations (ODEs) in terms of the moments:

$$\begin{aligned} \frac{\partial \mu_0}{\partial t} &= 0 \\ \frac{\partial \mu_1}{\partial t} &= G\mu_0 \end{aligned} \quad (13)$$

$$\begin{aligned} \frac{\partial \mu_2}{\partial t} &= 2G\mu_1 \\ \frac{\partial \mu_3}{\partial t} &= 3G\mu_2 \\ c(t) &= c(0) - \rho_c k_v \mu_3(t) \end{aligned} \quad (14)$$

In order to model the time-dependent behavior of a continuous system, the mass balance (eq. 14) was solved together with eq. (5) over an interval of time. The values for g and k_g were obtained from a least – squares optimization.

RESULTS AND DISCUSSION

In Table 1 is presented the variation of the final particle mean diameter with concentration and temperature. When precipitation takes place at lower concentrations, the nucleation rate is slowly, the growth rate is faster (the diffusion phenomena become important in the process) and the particles grow. At higher concentrations the nucleation rate is faster, stable nuclei are formed and no changes in the particle diameter are observed.

GROWTH RATE OF HYDROXYAPATITE CRYSTALS OBTAINED BY PRECIPITATION

In a precipitation process, crystal size distribution depends on the $\frac{\text{growth rate}}{\text{nucleation rate}}$ ratio. At 20 °C the growth rate is slower, in the first stage many critical nuclei are formed, and then they simply redissolve because they are extremely unstable. At 50 °C the growth rate is faster, the number of the critical nuclei formed is insignificant so that the nuclei grow beyond a certain critical size and become stable.

The analysis of CSD (Figure 1 – (a) and (b)) using the population density data from the Counter Coulter exhibits almost oscillating behavior due to the agglomeration and particle disruption.

Table 1. Mean particle diameter at different work conditions

| $C_{Ca_3(NO_3)_2}$ [mol/l] | $C_{(NH_4)_2HPO_4}$ [mol/l] | Mean particle diameter [μm] | |
|----------------------------|-----------------------------|--|-------|
| | | 20 °C | 50 °C |
| 1.25 | 0.46 | 0.02 | 0.02 |
| 1 | 0.4 | 0.02 | 0.02 |
| 0.67 | 0.3 | 4.61 | 0.02 |
| 0.5 | 0.24 | 5.33 | 0.02 |
| 0.29 | 0.15 | 6.13 | 0.02 |
| 0.15 | 0.09 | 6.17 | 0.02 |

First it increases to a maximum and then decreases, eventually approaching steady state after 22 hours. This behavior could be observed for all concentrations and temperatures (only the representative concentrations were presented in this article).

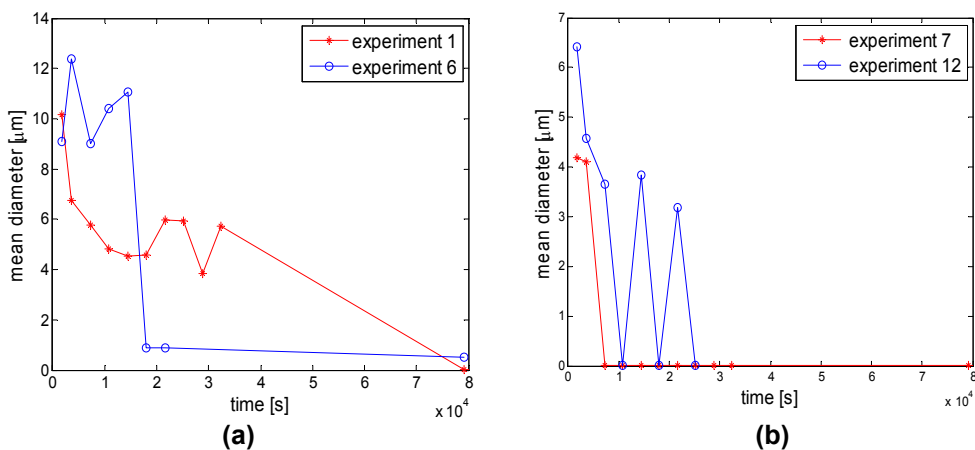


Figure 1. Mean particle diameter vs time at 20 °C (a) and 50 °C (b)

According to the first law of precipitation, with progressively increasing concentration of the reacting solutions, the mean magnitude of the individual crystals of precipitates will pass through a maximum. As the time becomes greater, this maximum is displaced to the left side and upwards [10]. Figure 2 shows the initial particle size distribution and the distribution after 5 h of stirring (a semi-log graph, defined by a logarithmic scale on the x axis, and a linear scale on the y axis). The distribution gradually shifts to smaller sizes as large particles are reduced in size by breakage or attrition.

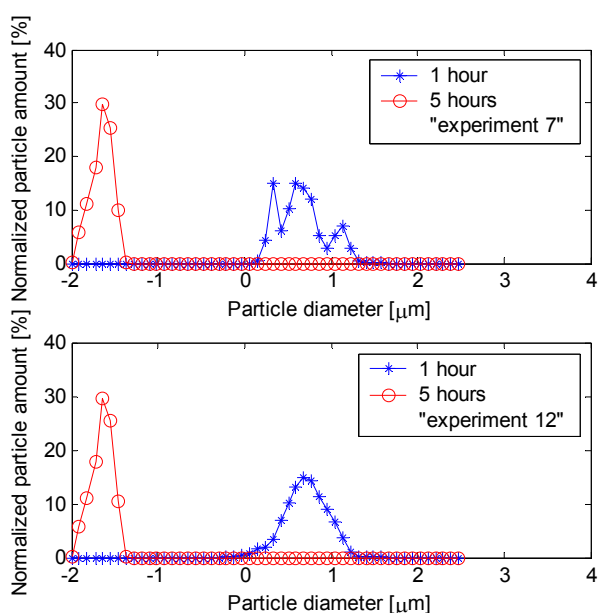


Figure 2. Number density

Furthermore, the measured total number of particles increases as each breakage event leads to a number of daughter particles (this behavior was observed at all range on concentration presented in Table 1).

The growth rate can be directly determined from the third moment, assuming that size-independent growth and the third moment (mass) is conserved in the agglomeration and disruption process. Knowing the moments of the distribution, growth rate G can be calculated from:

$$G = \frac{\mu_3}{3\mu_2\tau} \quad (15)$$

In Figure 3 – (a) and (b), the growth rate was plotted versus the time for 2 concentrations and 2 temperatures.

GROWTH RATE OF HYDROXYAPATITE CRYSTALS OBTAINED BY PRECIPITATION

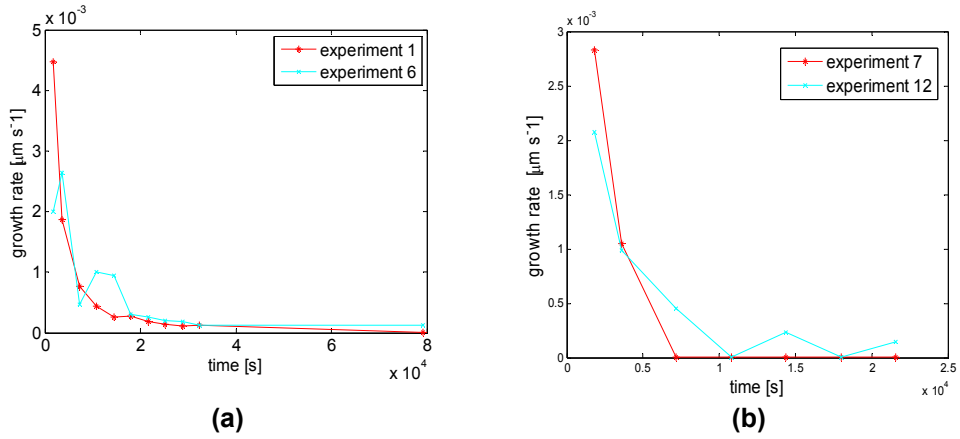


Figure 3. Growth rate vs time at 20 °C (a) and 50 °C (b)

First an increase of the growth rate with time was observed for all conditions. The particles are agglomerating, as can be expected from the higher levels of supersaturation in the precipitation reactor. These aggregates continue to agglomerate by forming interparticle bonds. Then, due to breakage or attrition processes, a decrease was observed.

By combining the process model with an optimization algorithm the growth kinetics mechanism and parameters can be extracted from the experimental data. In Figure 4 –(a) and (b), the experimental growth rates were correlated with the growth rates obtained from the model predictions. It could be observed that the values obtained from the experiments were within the range of the simulation data. It should be considered that direct comparison of the kinetic data is not always possible.

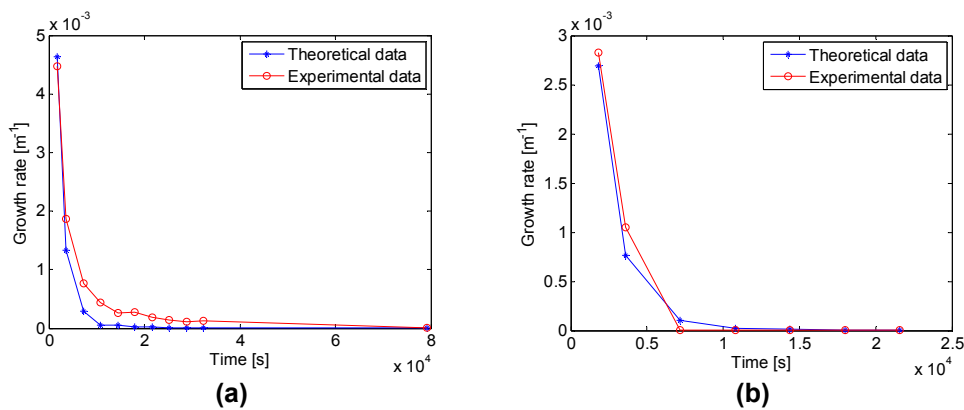


Figure 4. Experimental and simulated growth rate vs time at (a) 20°C and (b) 50°C

Table 2. The values for the growth parameters

| Experiment | g | k_g |
|------------|------|----------------------|
| 1 | 1.79 | $9.0 \cdot 10^{-13}$ |
| 2 | 1.68 | $4.1 \cdot 10^{-12}$ |
| 3 | 1.92 | $3.0 \cdot 10^{-13}$ |
| 4 | 1.95 | $3.0 \cdot 10^{-13}$ |
| 5 | 1.95 | $3.0 \cdot 10^{-13}$ |
| 6 | 1.98 | $3.0 \cdot 10^{-13}$ |
| 7 | 1.74 | $1.1 \cdot 10^{-12}$ |
| 8 | 2 | $1.0 \cdot 10^{-13}$ |
| 9 | 1.90 | $3.0 \cdot 10^{-13}$ |
| 10 | 1.54 | $1.0 \cdot 10^{-13}$ |
| 11 | 1.83 | $9.0 \cdot 10^{-13}$ |
| 12 | 1.98 | $3.0 \cdot 10^{-13}$ |

Using an optimization algorithm based on a least squares minimization the growth parameters g and k_g from equation (5) were determined and the values are presented in Table 2. From the theoretical considerations, for diffusion controlled growth $g = 1$, for crystal growth originating from screw dislocations $g = 1 - 2$ and for polynuclear growth $g > 2$.

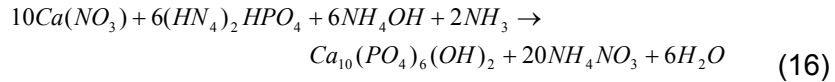
CONCLUSIONS

For the obtaining process of hydroxyapatite, a technique already known for other systems was used to determine the growth kinetics from experimental precipitation data (CSD). The model was able to predict reasonably well the growth rates for different work conditions (concentrations and temperatures) and can also be used to analyze experimental data from crystallization.

The results presented demonstrate that in the batch precipitation experiments is a strong dependence of the crystal size distributions on the feed concentrations and temperature. Due to this fact, small particles could be obtained at higher temperatures and supersaturations. Because the aggregation/growth rate increases with the supersaturation and the disruption rate increases with higher rotational speeds, further experiments are needed in order to show the dependence of the crystal size distribution on the mode of mixing.

EXPERIMENTAL SECTION

Hydroxyapatite was precipitated from reacting supersaturated solutions of calcium nitrate and bi-ammonia phosphate, at $pH = 11$ [11], according to the following equation:



To investigate the precipitation kinetics, the experiments were carried out under different feed concentrations and two temperatures (the values are presented in Table 3). At different preset times (see the plots), samples were taken and analyzed by laser light scattering technique using a Counter Coulter WING-SALD 7101.

Table 3. Experimental conditions (temperatures and feed concentrations)

| Experiment | | $C_{Ca_3(NO_3)_2}$ [mol/l] | $C_{(NH_4)_2HPO_4}$ [mol/l] |
|------------|-------|-------------------------------|--------------------------------|
| 20 °C | 50 °C | | |
| 1 | 7 | 1.25 | 0.46 |
| 2 | 8 | 1 | 0.4 |
| 3 | 9 | 0.67 | 0.3 |
| 4 | 10 | 0.5 | 0.24 |
| 5 | 11 | 0.29 | 0.15 |
| 6 | 12 | 0.15 | 0.09 |

NOTATIONS

| | |
|------------|--|
| B_{aggl} | birth rate due to agglomeration, $m^{-4} s^{-1}$ |
| B_{disr} | birth rate due to disruption, $m^{-4} s^{-1}$ |
| C | concentration of the reactant, g, mol m^{-3} |
| D_{aggl} | death rate due to agglomeration, $m^{-4} s^{-1}$ |
| D_{disr} | death rate due to disruption, $m^{-4} s^{-1}$ |
| g | kinetic order of growth, dimensionless |
| G | molecular growth rate, $m s^{-1}$ |
| k_v | volumetric shape factor |
| K_g | growth rate coefficient, $m s^{-1}$ |
| K_{aggl} | agglomeration rate, $m^3 s^{-1}$ |
| K_{disr} | disruption rate, s^{-1} |
| K_{sp} | solubility product, $mol^2 m^{-6}$ |
| L | particle size, m |
| n | population density, $\# m^{-4}$ |
| Q | flow rate, $m^3 s^{-1}$ |
| S | (relative) supersaturation, dimensionless |
| t | time, s |
| V | reactor volume, m^3 |

Greek letters

| | |
|-----------------------|--|
| μ_j | j^{th} moment of distribution, m^3 |
| β_{aggl} | agglomeration kernel |
| β_{disr} | disruption kernel |
| ε | power input per unit volume, W kg^{-1} |
| ρ | suspension density, g/l |
| σ | (absolute) supersaturation (S-1), dimensionless |
| τ | mean residence time, s |

REFERENCES

1. R. Barabás, A. Pop, E. Fazakas, V. Dejeu, *Proc. 10th ECerS Conf.*, Göller Verlag, Baden-Baden, **2007**, 925.
2. N. Ellis, A. Margaritis, C.L. Briens, M.A. Bergougnou, *AIChE Journal*, **1996**, *42*, 87.
3. H.M. Hulburt, S. Katz, *Chem. Eng. Sci.*, **1964**, *19*, 555.
4. A. Jones, "Crystallization Process Systems", **2002**, chapter 5.
5. S. Koutsopoulos, *Langmuir*, **2001**, *17(26)*, 8092.
6. C.L. Kibby, W.K. Hall, "The Chemistry of Biosurfaces Vol. 2", M.L. Hair ed., Dekker, New York, **1972**, 663.
7. J.O. Leckie, W. Stumm, "In the changing chemistry of the oceans", D. Dyrssen and D. Jagner, Eds. Almquist and Wiksell, Stockholm, **1972**.
8. P.P. von Weimarn, *Chem. Rev.*, **1926**, *2*, 217.
9. D. Ramkrishna, *Reviews in Chemical Engineering*, **1985**, *3(1)*, 49.
10. A.D. Randolph, M.A. Larson, "Theory of Particulate Processes, 2nd ed."; Academic Press: San Diego, CA, **1988**.
11. R. Zauner, A. Jones, *Chem. Eng. Sci.*, **2000**, *55*, 4219.

Dedicated to the memory of Prof. dr. Ioan Silaghi-Dumitrescu marking 60 years from his birth

KINETIC INVESTIGATION IN TROLOX-DPPH• SYSTEM

LIDIA VARVARI, GABRIELLA SZABÓ, ADRIAN NICOARĂ*

ABSTRACT. A kinetic study using voltammetry and spectrophotometric measurements on the Trolox/DPPH•, in hydro-ethanolic and ethanolic medium is presented. The heterogenous electrochemical rates were obtained from the peak parameters in quasireversible and irreversible conditions and the homogenous rate constant and partial reaction orders were obtained using reaction half-life.

Keywords: *Antioxidants, Trolox, DPPH•, voltammetry, spectrophotometry, kinetics*

INTRODUCTION

A free radical is a chemical species able of independent existence, possessing one or more unpaired electrons. Biologically important free radicals are thus highly unstable molecules that have electrons available to react with various organic substrates, generated by oxidative stress that can lead to a series of biochemical alterations through chain radical reactions. The natural defence against the oxidative stress is based on the action of antioxidant compounds, also known as radical scavengers. They usually act by neutralising the unstable free radical molecules by supplying them with electrons, thus preventing or at least limiting the chain reactions that cause tissue damage [1-2]. There are several categories of substances acting as antioxidants, including vitamins, inorganic compounds, essential amino acids and polyphenols. Their capacity to scavenge free radicals is now universally recognised although the true mechanism by means of which they act is still not fully understood [3].

Several methods have been proposed for the detection of antioxidants, based on photometric, fluorimetric, chromatographic and electrochemical approaches. Inherent limitations of the analysis differ from method to method (low sensitivity, interferences, slow detection and cost of equipment) and have

* *Universitatea Babeș-Bolyai, Facultatea de Chimie și Inginerie Chimică, Str. Kogălniceanu Nr. 1, RO-400084 Cluj-Napoca, Romania, anicoara@chem.ubbcluj.ro*

stimulated the study of simple, fast and sensitive methods for the characterization of antioxidants. In the past two decades the electrochemical methods, especially the amperometric ones, have been intensively used for antioxidant detection mostly because are fast and less expensive [4].

One of the most employed method of antioxidant activity determination uses a stable free radical 2,2-diphenyl-1-picrylhydrazyl (DPPH•). Having intense colour, which changes from violet to pale yellow during reaction with antioxidants, this free radical is suitable for spectrophotometric determination [5]. Because DPPH• free radical can exchange electrons at an electrode interface, its reaction with antioxidants is suitable also for electrochemical detection. In both mentioned cases, the antioxidants activity can be determined by following the consumption of DPPH• free radical. Correlating to free radical consumption when using a standard antioxidant, like 6-hydroxi-2,5,7,8,-tetramethyl-chroman-2-carboxylic acid (Trolox), it is possible to calculate the antioxidant activity of a complex natural matrix of antioxidants in terms of Trolox equivalent antioxidant activity [6].

The present study aims to investigate the elementary processes that occur during operation of an amperometric sensor for antioxidant activity determination. It is of interest to study the electrochemical behaviour of Trolox and DPPH• independently and in mixtures, employing spectrophotometric techniques for those processes that do not take place at electrode interface. After the obtaining of kinetic and thermodynamic information, it is possible to operate the amperometric detection in condition in which a judicious balance between desired performance descriptors can be more easily achieved.

RESULTS AND DISCUSSION

A detailed knowledge of the redox processes that occur in Trolox/DPPH• system during amperometric detection of antioxidant activity requests a preliminary investigation of electrochemical behavior of isolated components of the system.

Cyclic voltamograms of Trolox (Figure 1a) show the presence of one pair of voltammetric peaks, indicating chemically reversible nature for Trolox reduction. The asymmetry of the peaks, with the anodic one smaller and broader, corroborated with the significant peak separation is the indication of a relative slow charge transfer. Figure 1b and 1c contain the influence of scan rate on the peak parameters. Presented data indicate transition between quasireversible and irreversible behavior when increasing the scan rate, as can be evidenced by deviation from linearity of the representations from Figure 1b and 1c.

Attempting to obtain physico-chemical information, one can use the peak parameters to calculate some thermodynamic and kinetic parameters.

KINETIC INVESTIGATION IN TROLOX-DPPH SYSTEM

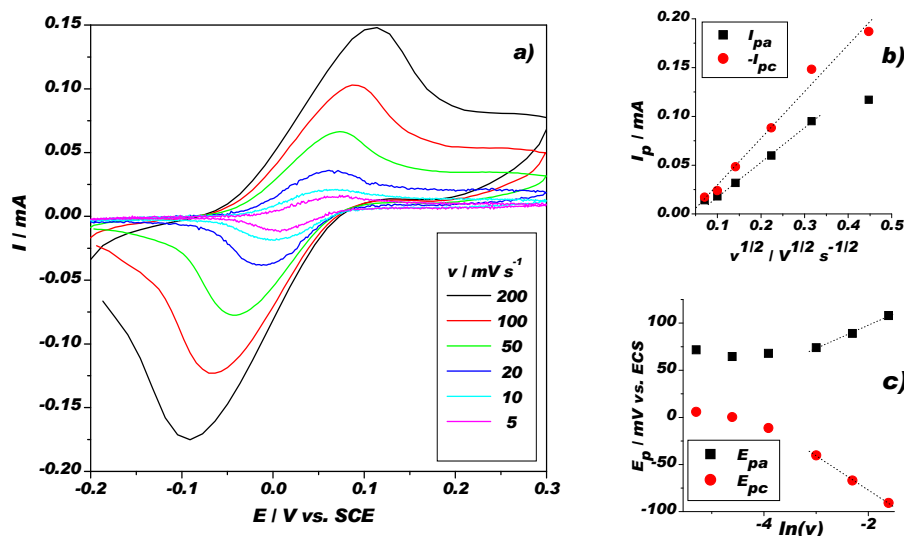


Figure 1. Voltammetric response of Trolox 4 mM hydro-ethanolic solution; the influence of the scan rate on cyclic voltammograms, in a), on peaks current, in b), and on peaks potential, in c).

To simplify the requested analysis, in the present work the formal standard potential was calculated using the data from quasireversible domain, by simple mediation of the anodic and cathodic potentials, whereas calculation of the other parameters was performed using the data from irreversible domain. In these circumstances, the formal standard potential was found to be $E^{o'} = 0.03$ V vs. SCE.

For an irreversible behavior, the peak parameters are given by:

$$\begin{aligned}
 I_{p,a} &= 2.99 \cdot 10^5 n [(1-\alpha)n_a]^{1/2} AD^{1/2} C^* v^{1/2} \\
 I_{p,c} &= -2.99 \cdot 10^5 n (\alpha n_a)^{1/2} AD^{1/2} C^* v^{1/2} \\
 E_{pa} &= E^{o'} - \frac{0.02569}{(1-\alpha)n_a} \left[0.78 - \ln\left(\frac{\sqrt{D_R}}{k^o}\right) - \ln\left(\sqrt{\frac{(1-\alpha)n_a}{0.02569} v}\right) \right] \\
 E_{pc} &= E^{o'} - \frac{0.02569}{\alpha n_a} \left[0.78 + \ln\left(\frac{\sqrt{D_O}}{k^o}\right) + \ln\left(\sqrt{\frac{\alpha n_a}{0.02569} v}\right) \right]
 \end{aligned} \tag{1}$$

where n is the (total) number of exchanged electrons, n_a the number of electrons involved in the rate determining step, α the transfer coefficient, A the surface, v the scan rate, C^* the concentration, D the diffusion coefficient

of the reacting species (when mentioned, O denotes the oxidized and R, the reduced; otherwise denotes the reacting species) and k^0 the standard rate constant [7].

In order to perform the parameter calculation, the peak parameters were plotted on convenient coordinates (I_p vs. $v^{1/2}$ and E_p vs. $\ln(v)$, as can be seen in Figure 1b and 1c, respectively) to ensure linearization. Using the slopes obtained by linear fitting of data presented in Figure 1c - 0.0246 ± 0.0015 and 0.0364 ± 0.0012 for anodic and, respectively, cathodic peaks - one can first calculate $n_a \approx 1$ and $\alpha = 0.60 \pm 0.02$, values consistent to mentioned peak asymmetry. The next step employs the I_p vs. $v^{1/2}$ dependence, described by the slopes of linear correlation found to be $(3.56 \pm 0.07)10^{-4}$ and $(4.79 \pm 0.29)10^{-4}$, respectively. Assuming $n=1$, one can calculate $D = 1.2 \cdot 10^{-6} \text{ cm}^2 \text{ s}^{-1}$, value corresponding to the reduced form of Trolox. To calculate the standard rate constant, the intercepts of Figure 1c (0.147 ± 0.004 and 0.150 ± 0.003 , respectively) lead to calculation of $k^0 = (2.9 \pm 0.2) \cdot 10^{-4} \text{ cm s}^{-1}$.

Cyclic voltammograms of DPPH• (Figure 2a) show in the domain of potential employed of the Trolox study the presence of one pair of voltammetric peaks that reveal a chemically reversible nature of electron exchange of studied free radical. An additional chemical irreversible oxidation peak, not presented here, is not important for the present study, since it occurs at potentials well above the interest domain, where both Trolox and DPPH• exchange electrons [8]. As in Figure 1, the shape of the peaks and relative proportional influence of square root of scan rate on the peak currents suggest a redox process involving soluble species, without contribution of adsorbed species.

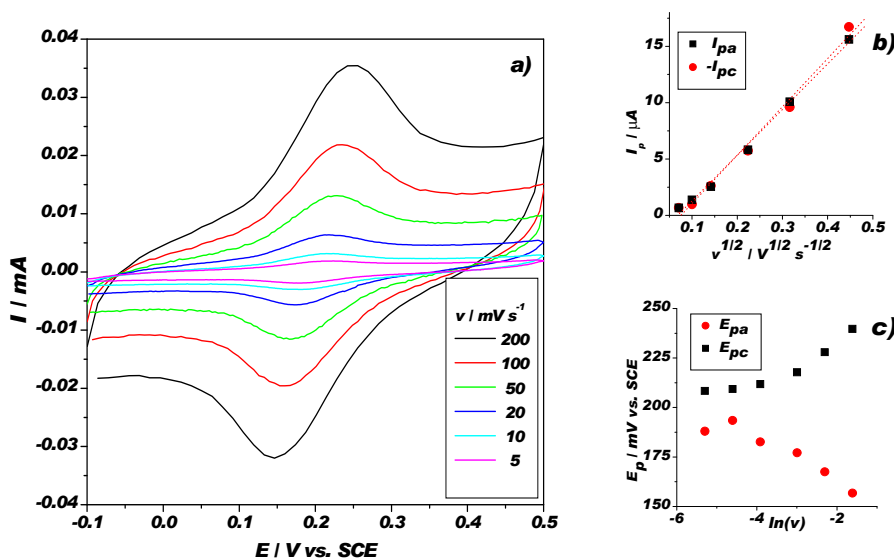


Figure 2. Voltammetric response of DPPH• 0.2 mM hydro-ethanolic solution; the influence of the scan rate on cyclic voltammograms, in a), on peaks current, in b), and on peaks potential, in c).

As compared to Trolox, DPPH• presents more symmetric peaks, less separated, denoting a significant faster rate. Consequently, the linearization correlation between peak potential and $\ln(v)$ takes place on higher scan rates, as can be seen in Figure 2c. In these circumstances, the voltammetry was performed under quasireversible behavior, and mathematical analysis aiming calculation of physico-chemical information must be performed accordingly. The standard formal potential was calculated as above, being found $E^{o'}=0.19$ V vs. SCE. For a quasireversible system Matsuda and Ayabe proposed a diagram that correlates the peak separation with an *ad hoc* kinetic term

$$\Lambda = k^o \sqrt{\frac{0.02569}{D_O^{1-\alpha} D_R^\alpha v}} \quad (2)$$

and links up the peak current to scan rate by using a second *ad hoc* kinetic term Ψ , both *ad hoc* kinetic terms being correlated through another diagram [9]. Under these assumptions, we found $n \approx 2$, $D_{\text{DPPH}\cdot} = 5.9 \cdot 10^{-6} \text{ cm}^2 \text{ s}^{-1}$, $k^o = 1.3 \cdot 10^{-2} \text{ cm s}^{-1}$.

For a full kinetic description of Trolox-DPPH• system a final voltammetric investigation was performed in order to describe the homogenous redox process. As can be seen in Figure 3, during addition of Trolox the peaks corresponding to DPPH• couple is marginally influenced, mostly due to modification of base line current. Moreover, the peak currents of Trolox couple are direct proportional to added Trolox concentration.

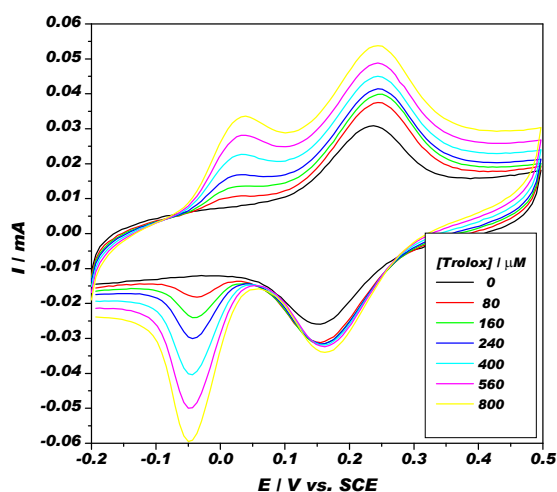


Figure 3. Voltammetric response of DPPH• 0.2 mM hydro-ethanolic solution with Trolox of concentration indicated in legend. Scan rate is 0.1 V s^{-1} .

All these suggest that, under studied experimental condition, the so-called homogenous coupled reaction cannot be evidenced. To obtain some kinetic information about this reaction, spectrophotometric measurements were further performed.

The reaction between DPPH• and Trolox in hydro-ethanolic mixtures was completed in few seconds, which prohibits kinetic measurement using employed instrumentation. For such fast systems, kinetic investigations can be made only in stopped-flow system. However, using ethanolic solution reaction is significant slower, allowing a preliminary insight into the kinetics in investigated system. Even if the values found in ethanolic solution could be related to previously found heterogeneous rate constants only with large precautions, the spectrophotometric measurements were further restricted to alcoholic solutions.

Ethanolic solutions of DPPH• obey Lambert-Beer law up to $2 \cdot 10^{-4}$ M, absorption maximum was found at 516 nm with a molar extinction coefficient of $19 \cdot 10^4 \text{ M}^{-1}\text{cm}^{-1}$. Reaction between ethanolic solutions of DPPH• and Trolox was reported as 1 mol of this antioxidant reduces 2 mol of free radical [6].

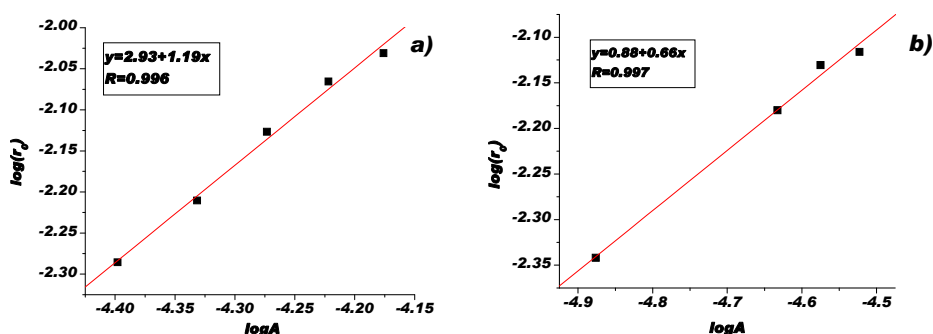


Figure 4. Dependence of initial rate on the DPPH• absorbance at constant Trolox concentration, a), and at constant DPPH• concentration, b).

Using different initial concentration of both species, on the basis of the rate law having the following expression, $r_0 = k c_{0DPPH}^a c_{0Trolox}^b$, partial reaction orders of 0.7 and 1.2 with respect to Trolox and DPPH•, respectively, were determined from the initial rates of the reaction, see Figure 4. As suggested by Brand-Williams and Bondet [5], the rate constant was determined from the half-life of the reaction:

$$t_{1/2} = \left((2^{a+b-1} - 1) / k_e \right) \times C_{DPPH}^{1-a-b} \quad (3)$$

where $\sigma=2$ represents the DPPH• number of mol reduced by the antioxidant and k_e is related to the rate constant by:

$$k_e = (a + b - 1) \frac{k}{\sigma^b} \quad (4)$$

The values of the rate constant determined at two different temperatures are presented in the table 1.

Table 1. The rate constant determined at different temperatures.

| T (K) | $10^5 \cdot C_{0DPPH}$ (M) | $t_{1/2}$ (s) | k_e ($M^{-1} \cdot s^{-1}$) | k ($M^{-1} \cdot s^{-1}$) | \bar{k} ($M^{-1} \cdot s^{-1}$) |
|-------|-------------------------------|---------------|---------------------------------|-------------------------------|-------------------------------------|
| 298 | 6 | 48 | 113.8 | 206.0 | 203.3 |
| | 4 | 71 | 110.8 | 200.6 | |
| 293 | 6 | 55 | 99.3 | 180.6 | 184.7 |
| | 4 | 75 | 104.9 | 189.8 | |

CONCLUSIONS

The stable free radical DPPH•, which can be amperometrically detected, is consumed by the antioxidants from analysed sample allowing to evidence the antioxidants by quantifying the decrease of the DPPH• concentration. Trolox is further employed to quantify the activity of the natural antioxidants present in an analysed sample. We will further investigate the way in which the experimental finds endorse the utilisation of an amperometric sensor based on investigated system.

The results prove that the DPPH• free radical can be reduced during a reversible process, on a relative positive potential ($E^{\circ} = 0.19$ V vs. SCE). There are two positive consequences: the value of formal standard potential contributes to a good selectivity as analytes with more negative formal standard potential would not interfere, and de reversible nature of this process allows increasing of the sensibility as the oxidation product is available to re-reduction during a homogenous coupled chemical process. Another important original find is the kinetic constant of this heterogeneous reaction; the reasonable high value, of $k^{\circ} = 1.3 \cdot 10^{-2} \text{ cm s}^{-1}$, is beneficial for the detection as the fast rates is a prerequisite for a low response time of detection.

The electrochemical investigation of Trolox revealed a reversible process at a more cathodic formal standard potential ($E^{\circ} = 0.03$ V vs. SCE). The difference of mentioned formal standard potentials constitute the driving force of reaction between Trolox and DPPH• in the investigated conditions. A smaller value would give a certain degree of reversibility, with detrimental reducing of linearity of the amperometric sensor. More important, the voltammetric peaks of Trolox are clearly separated from those of DPPH• free radical, allowing the use of analytical techniques that request the presence of Trolox in the investigated sample with antioxidants.

The last attempt was to investigate the homogenous redox reaction between Trolox - DPPH•. As the catalytic coupling was not evidenced by voltammetry, spectrophotometric techniques were employed. Yet again the kinetics was favourable, too fast to even evaluate the rate constant with utilized instrumentation when the reaction was investigated in hydro-ethanolic solution. Even in pure ethanolic solution the homogenous rate constant was reasonable large, of $203 \text{ M}^{-1} \text{ s}^{-1}$, ensuring a small measuring time for the amperometric detection. The only draw-back is given by subunit value, of 0.7, for DPPH• free radical reaction order; poor linearity should be expected for the samples containing Trolox if the measurements are performed without reaching the equilibrium.

EXPERIMENTAL SECTION

Instrumentation

The voltammetric measurements were performed using a Computer controlled (via an AT-MIO-16F-5, National Instruments, USA, data acquisition board) analogical potentiostat (PS3, Meinsberg, Germany). A standard three-electrode electrochemical cell configuration was employed for the measurements. The working electrode was glassy carbon ($A=0.0314 \text{ cm}^2$) reference electrode was a double-junction saturated calomel electrode (SCE) and the counter electrode was a spiralled Pt wire. Voltammetric measurements were performed at a temperature of $25 \pm 1 \text{ }^\circ\text{C}$.

Spectrophotometric measurements were carried out on a Jasco V-530 UV/VIS spectrophotometer connected to a computer for data acquisition. Standard (1 cm x 1 cm x 4.5 cm) glass spectroscopic cuvette was used for visible absorbance measurement. Temperature was controlled by using an M 20 Lauda thermoregulating system. DPPH• spectrum was recorded in the range of 800 and 400 nm. Time course measurements were recorded at 516 nm wavelength at $25 \pm 0.5 \text{ }^\circ\text{C}$. Ultrasonication of stock solutions was performed with Transsonic T 420, Elma.

Reagents and solutions

Commercially available chemicals were obtained from Sigma-Aldrich. DPPH• stock solutions were prepared in absolute ethanol and ultrasonicated for about 30 minutes. In order to avoid thermal decomposition and by light the solutions were kept in refrigerator. Trolox was dissolved in absolute ethanol and in hydro-alcoholic phosphate buffer. The hydro-ethanolic solutions (25% vv ethanol) were prepared by adding ethanol to the buffer solution with desired pH of 7.4. All the solutions contained 0.1 M KCl as supporting electrolyte.

ACKNOWLEDGMENTS

The authors acknowledge for the financial support granted by the National Research Council, project SENSALIM, PN II Nr. 71/098-2007.

REFERENCES

1. A. Somogyi, K. Rosta, P. Pusztai, Z. Tulassay, G. Nagy, *Physiological Measurements*, **2007**, *28*, R41.
2. L. Campanella, E. Martini, M. Tomassetti, *Talanta*, **2005**, *66*, 902.
3. L. Campanella, A. Bonanni, D. Bellantoni, G. Favero, M. Tomassetti, *Journal of Pharmaceutical and Biomedical Analysis*, **2004**, *36*, 91.
4. Ignatov, S. Ignatov, D. Shishniashvili, B. Ge, F.W. Scheller, F. Lisdat, *Biosensors and Bioelectronics*, **2002**, *17*, 191.
5. V. Bondet, W. Brand-Williams, C. Berset, *Lebensmittel-Wissenschaft und Technologie/ Food Science and Technology*, **1997**, *30*, 609.
6. S. Mildradovic, D. Ivekovic, B. Grabaric, *Bioelectrochemistry*, **2006**, *68*, 175.
7. R. Nicholson, I. Shain, *Analytical Chemistry*, **1964**, *36*, 706.
8. Mildradovic, D. Ivekovic, V. Rumenjak, B. Grabaric, *Electroanalysis*, **2005**, *17*, 1847.
9. A.J. Bard, L.R. Faulkner, *Electrochemical methods. Fundamentals and applications* 2nd ed., Wiley, **2001**, chapter 6.3.

